Lepton flavor violation from low scale seesaw neutrinos with masses reachable at the LHC

Memoria de tesis doctoral realizada por
Xabier Marcano Imaz
presentada ante el Departamento de Física Teórica
de la Universidad Autónoma de Madrid
para optar al Título de Doctor en Física

Trabajo dirigido por la
Dra. María José Herrero Solans
Profesora Catedrática del Departamento de Física Teórica
Universidad Autónoma de Madrid

Departamento de Física Teórica
Universidad Autónoma de Madrid

Instituto de Física Teórica
UAM-CSIC

Madrid, junio de 2017

Nire aitxitxari,
honaino bere erruz heldu naizelako.

Contents

Introducción

El 4 de julio de 2012, los experimentos ATLAS y CMS, situados en el gran colisionador de hadrones (LHC) del CERN, anunciaron el descubrimiento [1, 2] del eslabón perdido en el Modelo Estándar (SM) [3–6] de las interacciones fundamentales, el bosón de Higgs. Este descubrimiento completó una de las teorías más exitosas en los anales de la Física, un modelo predictivo capaz de describir con extraordinaria precisión la mayoría de los fenómenos conocidos en la Física de Partículas. Sin embargo, existen algunas evidencias experimentales, como las masas de los neutrinos, la materia oscura o la asimetría bariónica del universo, y ciertos problemas teóricos, tales como el problema de las jerarquías, el problema de CP fuerte o el puzzle de sabor, que el SM no es capaz de explicar, invitándonos a un viaje hacia nueva física más allá del SM.

El SM es una teoría cuántica de campos basada en el grupo de simetría gauge $SU(3)_C \times SU(2)_L \times U(1)_Y$, que describe tres de las cuatro interacciones fundamentales que conocemos entre las partículas elementales, conocidas como interacción fuerte, débil y electromagnética. En su espectro de partículas podemos encontrar a los fermiones, constituyentes de la materia, a los bosones de espín uno, mensajeros de las fuerzas, y al bosón escalar de Higgs, el remanente del proceso que genera la masa de las partículas elementales, el mecanismo de Brout-Englert-Higgs (BEH) [7–10]. Este mecanismo explica cómo la ruptúra espontánea de la simetría electrodébil (EWSB) genera las masas que observamos para los bosones gauge W y Z, así como para todos los fermiones salvo los neutrinos, que son tratados como partículas sin masa por el SM.

Históricamente, los experimentos dedicados a la búsqueda de procesos con violación de sabor han sido una pieza fundamental en los avances teóricos en la Física de Partículas, tales como el mecanismo de Glashow-Iliopoulos-Maiani (GIM) [11] para explicar por qué no se veían las corrientes neutras con cambio de sabor, o la matriz de Cabibbo-Kobayashi-Maskawa (CKM) [12, 13] de mezcla de los quarks para las corrientes cargadas. Asímismo, la evidencia experimental más clara de la existencia de nueva física proviene de la física del sabor, en concreto de la observación de violación de sabor leptónico (LFV) en el sector de los neutrinos. Tal y como acabamos de decir, el SM se construyó asumiendo que los neutrinos no tenían masa. Sin embargo, las evidencias experimentales de LFV en las oscilaciones de neutrinos, observadas por primera vez por las colaboraciones de Super-Kamiokande [14] y

SNO [15, 16], han demostrado que los neutrinos sí tienen masa, estableciendo así la necesidad de modificar el SM para explicar tal hecho. Del mismo modo, si alguno de los experimentos actuales o futuros detectase alguna señal de los procesos con LFV en el sector cargado, todavía no observados en la naturaleza, se abriría una nueva venta a la física más allá del SM, más allá incluso de la física de la masa de los neutrinos.

Estudiando el espectro de partículas del SM, puede comprobarse que la ausencia de neutrinos dextrógiros (RH) en la teoría prohíbe que los neutrinos interactúen con el campo de Higgs y, por lo tanto, que adquieran masa después del EWSB. Así, la manera más simple de introducir masas para los neutrinos en el SM sería añadir los neutrinos RH, ν_R, que le faltan. De esta forma, los neutrinos podrían interactuar con el campo de Higgs a través de un acoplamiento de tipo Yukawa, Y_ν, y obtener una masa de Dirac $m_D = vY_\nu$ tras el EWSB, como el resto de fermiones, siendo ésta proporcional al valor esperado del vacío del Higgs, cuya normalización tomamos como $v = 174$ GeV. Sin embargo, esta extensión mínima del SM plantea nuevas preguntas: ¿Por qué son los neutrinos tan diferentes a los demás fermiones? ¿Por qué son sus masas tan pequeñas comparadas con el resto de las masas de los otros fermiones? Además, dado que los neutrinos no tienen carga de color ni carga eléctrica, podrían ser fermiones de Majorana, i.e., podrían ser sus propias antipartículas. De ser éste el caso, supondría una gran novedad para la Física de Partículas.

Escudriñando más profundamente los nuevos campos ν_R, podemos darnos cuenta de que son singletes bajo todo el grupo de simetría gauge del SM y, por tanto, no existe nada que prohíba escribir un término de masa Majorana, m_M, para ellos. Estas dos masas distintas, m_D y m_M, son los ingredientes básicos del bien conocido modelo del seesaw de tipo-I [17–21], que normalmente asume una escala para la masa de Majorana m_M mucho más pesada que m_D y que la escala electrodébil v. En tal caso, el espectro de neutrinos físicos consistiría en un neutrino de Majorana pesado y otro ligero por cada generación, con masas del orden de m_M y m_D^2/m_M, respectivamente. Así, el seesaw de tipo-I explica de forma elegante por qué la masa de los neutrinos que observamos es tan pequeña, ya que ésta surgiría del cociente entre dos escalas muy distantes, m_D y m_M. Analizando la escala de la masa ligera $m_\nu \sim m_D^2/m_M$, puede comprobarse que para tener $m_\nu \sim \mathcal{O}(\text{eV})$ con acoplamientos Yukawa grandes $Y_\nu \sim \mathcal{O}(1)$, se necesitan masas pesadas del orden de $m_M \sim \mathcal{O}(10^{14} \text{ GeV})$. Por otro lado, masas de neutrinos dextrógiros en el rango de los TeV requerirían acoplamientos muy pequeños $Y_\nu \sim \mathcal{O}(10^{-5})$. De una manera o de otra, la mayor parte de la fenomenología en el seesaw tipo-I está muy suprimida. Por tanto, la simplicidad de este argumento es lo que hace este modelo atractivo y, a su vez, difícil de testar en otros observables de baja energía más allá de la propia masa de los neutrinos ligeros.

Los modelos seesaw de baja escala son variaciones interesantes del seesaw tipo-I que ofrecen una fenomenología mucho más rica. En este tipo de modelos, se recurre a alguna nueva simetría con el objetivo de evitar que los neutrinos ligeros adquieran una masa demasiado grande, permitiendo por tanto que los neutrinos pesados puedan tener masas más

ligeras y acoplamientos Yukawa grandes al mismo tiempo. Una realización particular de este tipo de modelos, y en el que se centra esta Tesis, es el seesaw inverso (ISS) [22–24], que asume una simetría aproximada de conservación de número leptónico (LN). En el límite en el que el LN está conservado de forma exacta, los neutrinos ligeros no tienen masa. Sin embargo, si esta simetría está rota por cierto parámetro de masa, los neutrinos adquieren una pequeña masa de Majorana proporcional a este parámetro de violación del LN. Por otro lado, podemos esperar que este parámetro sea pequeño de forma natural, en el sentido de 't Hooft [25], ya que si fuese cero la simetría del modelo sería mayor. Por lo tanto, en el modelo ISS la ligereza de los neutrinos está relacionada con una pequeña violación del LN.

En el modelo ISS, la condición de que la violación del LN sea pequeña se cumple introduciendo nuevos singletes fermiónicos en pares (ν_R, X) con LN opuesto, y asumiendo que la conservación del LN se viola sólo por un pequeña masa de Majorana μ_X para los campos X. De este modo, el espectro físico consiste en neutrinos de Majorana ligeros con masas suprimidas por el pequeño valor de μ_X, y dos neutrinos de Majorana pesados y casi degenerados por generación. Éstos últimos forman pares de fermiones pseudo-Dirac y de hecho se comportan prácticamente como fermiones de Dirac, al contrario que los neutrinos pesados del seesaw de tipo-I. De forma interesante, como la escala μ_X asegura la ligereza de los neutrinos observados, los neutrinos pesados pueden tener grandes acoplamientos de Yukawa a los neutrinos del SM y al mismo tiempo masas del orden de varios TeV o menores, siendo así accesibles en el LHC. Esto hace del ISS un modelo atractivo e interesante con una fenomenología muy rica que puede ser estudiada en experimentos presentes y del futuro cercano. Esto incluye, entre otros, estudios de violación de universalidad de sabor leptónico en desintegraciones leptónicas y semileptónicas de mesones [26, 27], momentos dipolares eléctricos de leptones cargados [28, 29], momentos magnéticos de los leptones [30], producción de neutrinos pesados en colisionadores [31–38], materia oscura [39], leptogénesis [40, 41] y procesos con LFV en el sector cargado [42–52].

Desde el punto de vista teórico, el SM también posee algunas propiedades indeseadas, como el llamado problema de las jerarquías. Este problema se refiere a la inestabilidad del sector de Higgs frente a correcciones radiativas en presencia de nueva física a una escala muy grande. Para ilustrar esta idea, podemos considerar la masa del bosón de Higgs, m_H, y calcular sus correcciones radiativas bajo la hipótesis de que no hay nueva física hasta la masa de Planck $M_P \sim 10^{19}$ GeV, donde los efectos gravitacionales empiezan a desempeñar un papel importante. Haciendo esto, encontramos que las correcciones cuánticas Δm_H^2 crecen como el cuadrado de la escala de la nueva física, lo que proporciona un valor muy alejado del medido experimentalmente $m_H = 125.09 \pm 0.21(\text{stat.}) \pm 0.11(\text{syst.})$ GeV [53]. Así. para obtener una predicción compatible con el experimento, se requiere un ajuste muy fino en la cancelación entre la masa desnuda y las correcciones cuánticas, un hecho que no resulta muy natural sin una nueva explicación o simetría.

Una de las soluciones más populares y elegantes a este problema la proporciona la

supersimetría (SUSY) [54–56], una nueva simetría que relaciona fermiones y bosones. En la extensión más simple y mínima del SM, conocida como *Minimal Supersymmetric Standard Model* (MSSM) [57–59], cada fermión del SM tiene un compañero de espín cero, llamado sfermión, con la misma masa y los mismos números cuánticos que el fermión original; de la misma manera, todos los bosones del SM tienen su compañero de espín un medio. El hecho de que existan fermiones y bosones con los mismos acoplamientos y masas cancela completamente las peligrosas correcciones cuánticas a la masa del bosón de Higgs, proporcionando así una solución elegante al problema de las jerarquías. Obviamente, duplicar el espectro de partículas del SM es una predicción fenomenológica muy importante, pues supone la existencia de nuevas partículas que deberían observarse en los experimentos. Por desgracia, éstos no han sido capaces de encontrar ningún miembro supersimétrico del MSSM todavía. Este hecho implica que, si la SUSY existe en la naturaleza, ésta no puede ser una simetría exacta, debe estar rota, de tal forma que las partículas SUSY sean más pesadas que sus compañeras del SM. Esta ruptura, sin embargo, no puede arruinar completamente la solución al problema de las jerarquías, por lo que la SUSY debe estar rota de manera suave [60], i.e., las correcciones a Δm_H^2 que dependen cuadráticamente con la escala de la nueva física han de seguir cancelándose, aunque podría quedar todavía una dependencia logarítmica.

Una vez añadidos estos términos que rompen la SUSY de manera suave, el MSSM es una teoría viable con consecuencias fenomenológicas muy interesantes. Sin embargo, al estar construída a partir del SM, todavía requiere de un mecanismo que explique la generación de la masa de los neutrinos. Retomando la discusión anterior, podemos considerar de nuevo el modelo ISS y adaptarlo al contexto SUSY, añadiendo al espectro del MSSM nuevos neutrinos y sneutrinos, cuyas masas puedan estar en el entorno del TeV y, al mismo tiempo, sus acoplamientos ser grandes. Así, este modelo SUSY-ISS combina las cualidades más interesantes de ambos contextos, tanto de la SUSY como del ISS.

La forma óptima de demostrar experimentalmente la validez de cualquier modelo más allá del SM sería detectando las nuevas partículas que predice. No obstante, esta tarea puede ser muy tediosa en muchos casos, sobre todo si estas nuevas partículas son demasiado pesadas como para producirlas directamente en los experimentos actuales, por lo que un primer indicio sobre su existencia prodría venir de sus implicaciones indirectas sobre observables de baja energía. En el caso particular de los modelos de generación de masas para los neutrinos, los procesos con LFV podrían ser de nuevo los observables idóneos para ver tales implicaciones indirectas, concretamente en el sector de leptones cargados, pues podrían ser inducidos cuánticamente por loops de neutrinos pesados.

Los procesos con LFV en el sector cargado (cLFV) están prohídos en el SM si los neutrinos no tienen masa, y extremamente suprimidos en el caso de añadir *ad-hoc* las pequeñas masas de los neutrinos necesarias para explicar las oscilaciones de neutrinos. Por tanto, una señal positiva en cualquiera de los experimentos en busca de procesos con cLFV implicaría automáticamente la existencia de nueva física más allá del SM incluso con la masa de los

neutrinos añadida de manera mínima. A pesar de que ningún proceso de este estilo ha sido observado todavía, se trata de un campo muy activo, explorado continuamente por un gran número de experimentos que han sido capaces de poner cotas superiores a la probabilidad de que este tipo de procesos con cLFV puedan ocurrir. A día de hoy, las cotas más estrictas han sido encontradas para las transiciones del tipo μ-e, como la desintegración radiativa $\mu \to e\gamma$ o la conversión μ-e en núcleos pesados, cuyas probabilidades de desintegración han sido acotadas por las colaboraciones de MEG [61] y SINDRUM II [62], respectivamente, a ocurrir menos del 4.2×10^{-13} y 7.0×10^{-13} de las veces. Además, se espera que la siguiente generación de experimentos sean capaces de mejorar la sensibilidad a estas transiciones μ-e, alcanzando el impresionante rango de 10^{-18} para la conversión μ-e en núcleos en el experimento PRISM en el J-PARC [63]. Por otro lado, las cotas actuales a las transiciones en los sectores τ-μ y τ-e son mucho más suaves, siendo, por ejemplo, del orden de 10^{-8} para las desintegraciones radiativas del tau según el experimento BABAR [64]. Esto quiere decir que existe algo más de espacio para transiciones LFV en estos sectores que en el de μ-e, que podrán ser exploradas en un futuro cercano por el experimento BELLE-II [65].

Asímismo, en la actualidad el LHC está en funcionamiento y también tiene mucho que decir sobre procesos con cLFV. En primer lugar, el hecho de haber descubierto una nueva partícula, el bosón de Higgs, abre una nueva ventana a posibles desviaciones del SM que definitivamente debe ser explorada. En particular, este descubrimiento añade al mercado tres nuevos canales con cLFV, las desintegraciones LFV del bosón de Higgs a dos leptones de distinto sabor, $H \to \ell_k \bar{\ell}_m$, que de hecho ya han sido buscadas por los experimentos de CMS [66, 67] y ATLAS [68]. Aunque CMS observó un pequeño pero interesante exceso en el canal $H \to \tau\mu$ tras analizar los datos de la etapa-I [69], éste no ha sido confirmado con los nuevos datos de la etapa-II y, actualmente, han sido capaces de imponer una cota superior a este proceso de 2.5×10^{-3} [67]. Estas búsquedas de las desintegraciones con LFV del Higgs, al igual que otras exploraciones del sector de Higgs, seguirán en el LHC y seguro que serán mejoradas con más datos.

Otros observables interesantes que el LHC también está buscándo son las desintegraciones con LFV del bosón Z en dos leptones de diferente sabor, $Z \to \ell_k \bar{\ell}_m$ [68, 70]. Es interesante destacar que, tras la etapa-I, ATLAS ha conseguido alcanzar ya las sensibilidades anteriores del experimento LEP [71, 72], e incluso de mejorar las cotas para el canal $Z \to \mu e$. Al igual que las búsquedas del Higgs, las desintegraciones con LFV del Z también continuarán durante las nuevas etapas, por lo que podemos esperar nuevos resultados interesantes por parte de ATLAS y CMS. Aún así, la mejor sensibilidad a las desintegraciones con LFV del Z se espera que la provea la siguiente generación de colisionadores de leptones, dado que pueden operar como factorías de producción de bosones Z en un entorno muy limpio. En particular, en los futuros colisionadores lineales, que esperan alcanzar sensibilidades de hasta 10^{-9} [73, 74], o en los futuros colisionadores circulares e^+e^- (como el FCC-ee (TLEP) [75]), donde se estima que se podrían producir un total de 10^{13} bosones de Z y que

las sensibilidades a las desintegraciones LFV del Z podrían ser mejoradas hasta 10^{-13} [49].

La motivación principal de esta Tesis es, por tanto, la de explorar la conexión entre la existencia de nuevos neutrinos dextrógiros con masas en el entorno del TeV, accesibles en el LHC, y la LFV en el sector de los leptones cargados. Estamos particularmente interesados en los dos modelos descritos anteriormente, el ISS y el SUSY-ISS, ya que contienen precisamente neutrinos dextrógiros con masas en el rango del TeV y, al mismo tiempo, con acoplamientos grandes. La fenomenología asociada al cLFV en modelos con neutrinos masivos ha sido estudiada anteriormente [76–92] y también en el ISS [42–52]. En esta Tesis, nos concentramos mayormente en el estudio de las predicciones a las desintegraciones con LFV de los bosones de Higgs y Z, procesos que, como decíamos, son extremadamente oportunos de estudiar a la luz de los nuevos datos del LHC. Además, también realizamos nuevas predicciones para otros procesos con cLFV, tales como $\ell_m \to \ell_k \gamma$ o $\ell_m \to \ell_k \ell_k \ell_k$, junto con otros procesos que preservan el sabor leptónico y que serán relevantes en el contexto de los modelos que consideramos.

Estudiamos, de manera completa y por primera vez, las desintegraciones con LFV del bosón de Higgs en presencia de neutrinos dextrógiros en el modelo ISS, así como en presencia de sneutrinos en el modelo SUSY-ISS. Realizamos este estudio siguiendo dos estratégias diferentes. Primero presentamos, basándonos en los resultados de la Ref. [82] para el modelo seesaw de tipo-I, los resultados para el cálculo completo a nivel de un *loop* realizado en la base de masa de los neutrinos físicos. Segundo, usamos la técnica de la aproximación de inserción de masa (MIA), que se basa en trabajar en la base electrodébil y permite obtener fórmulas útiles y simples para las desintegaciones con LFV del Higgs. En la evaluación numérica, demostramos que es posible obtener tasas de desintegración grandes para los procesos con LFV en direcciones partículares del espacio de parámetros donde las transiciones μ-e, las más acotadas experimentalmente, están muy suprimidas. Siguiendo esta línea, proponemos una nueva forma para construir este tipo de escenarios fenomenológicamente interesantes que suprimen las transiciones en el sector μ-e. Estos escenarios están basados en la parametrización μ_X, que también es una nueva y genuína contribución de esta Tesis. Por otro lado, las desintegraciones con LFV del bosón Z en el modelo ISS han sido estudiadas previamente en la Ref. [49]. Así pues, en este caso nos centramos directamente en el estudio de los escenarios particulares con las transiciones μ-e suprimidas, ya que sabemos que las predicciones para los tasas de desintegración son mayores. En este sentido, realizamos un estudio complementario al hecho con anterioridad en la literatura.

Tal y como hemos dicho antes, nuestro interés en los modelos con neutrinos dextrógiros con masas del orden del TeV radica en el hecho de que podrían ser producidos en el LHC. En el modelo ISS, debido al carácter pseudo-Dirac de los neutrinos pesados, las búsquedas estándares de neutrinos de Majorana [93–96], basadas en procesos con violación de número leptónico en el estado final de dos leptones con la misma carga, no son eficientes. Por tanto, aquí proponemos el uso alternativo de estados finales con violación de sabor leptónico para

discriminar los eventos de producción y desintegración de neutrinos de modelos de seesaw de baja escala. En particular, nos centramos en eventos exóticos con estados finales de $\tau^{\pm}\mu^{\mp}jj$ o $\tau^{\pm}e^{\mp}jj$ y sin energía transversa perdida, que podrían ser producidos en escenarios en el que los ν_R tienen masas en y por debajo de la escala del TeV y donde la LFV está favorecida en el sector τ-μ o τ-e, respectivamente.

Esta Tesis está organizada de la siguiente manera. En el Capítulo 1 repasamos la física de las oscilaciones de neutrinos y su conexión con la necesidad de introducir masas para los neutrinos. Discutimos algunos de los modelos de generación de masas de neutrinos más populares, centrándonos especialmente en los modelos con neutrinos dextrógiros con masas en el entorno del TeV, como es el caso del modelo del seesaw inverso y de su versión SUSY. Estos son los modelos que consideraremos para explorar en detalle su fenomenología con LFV en los Capítulos posteriores. Además, durante el estudio del sector de los neutrinos en estos modelos, presentamos una nueva parametrización, a la que nos referimos como la parametrización μ_X, que resultará extremadamente útil a la hora de explorar el espacio de parámetros del modelo asegurando siempre el acuerdo con los datos de las oscilaciones de neutrinos.

En el Capítulo 2 abordamos la importancia de la búsqueda de nueva física en los procesos con LFV en el sector cargado y resumimos el estado experimental actual. Posteriormente, repasamos las desintegraciones con LFV de los leptones, en concreto las radiativas $\ell_m \to \ell_k \gamma$ y las de tres cuerpos $\ell_m \to \ell_k \ell_k \ell_k$, con $k \neq m$. El estudio de estos procesos nos permitirá aprender sobre el comportamiento de la LFV con los parámetros del ISS, así como resaltar las ventajas a la hora de usar nuestra parametrización μ_X. Como resultado de este estudio, encontraremos algunos escenarios fenomenológicamente interesantes, motivados por las cotas experimentales actuales, en los que se favorece las transiciones con LFV en el sector τ-μ o τ-e a la vez que se suprimen las del sector μ-e, y que nos resultarán muy útiles a la hora de explorar las desintegraciones con LFV del H y el Z. Además, en este Capítulo también discutimos las implicaciones de los neutrinos dextrógiros con masas del orden del TeV a otros observables de baja energía, los que acotarán nuestras búsquedas en los siguientes Capítulos de las tasas de desintegración máximas permitidas por los datos experimentales actuales.

El Capítulo 3 está dedicado al estudio de las desintegraciones con LFV del Higgs (LFVHD) en los modelos del ISS y SUSY-ISS. En él presentamos los resultados del cálculo completo a nivel de un loop de las tasas de LFVHD en el modelo ISS y estudiamos sistemáticamente su dependencia con los parámetros de este modelo. Con el fin de entender mejor estos resultados, realizamos un cálculo completo e independiente de estas tasas de desintegración usando la aproximación de inserción de masa, lo que nos permitirá obtener una fórmula muy simple para el vértice efectivo $H\ell_k\ell_m$ con LFV, extremadamente útil para quien desee realizar una estimación rápida de las LFVHD en este tipo de modelos. Igualmente, exploramos estos procesos en el modelo SUSY-ISS, demostrando que los nuevos *loops* SUSY que incluyen sleptones y sneutrinos pueden aumentar notablemente los valores máximos

permitidos, llegando a valores cercanos a las sensibilidades experimentales actuales.

En el Capítulo 4 estudiamos las desintegraciones con LFV del bosón Z (LFVZD) en el modelo ISS. Centramos nuestro análisis en los escenarios fenomenológicos introducidos previamente, donde pueden obtenerse tasas de desintegración con LFV grandes en los sectores τ-μ y τ-e. Comparamos nuestros resultados con los trabajos previos en la literatura y demostramos que, en estas interesantes direcciones del espacio de parámetros del ISS, se pueden conseguir tasas de desintegración altas, perfectamente alcanzables por la siguiente generación de experimentos en busca de las LFVZD.

En el Capítulo 5 nos centramos en la producción en el LHC de los neutrinos de los modelos seesaw de baja escala. Estudiamos la posibilidad de detectar la producción y desintegración de los neutrinos pesados del ISS buscando eventos exóticos con LFV, $\ell_k^\pm \ell_m^\mp jj$ con $k \neq m$, y sin energía perdida transversa. De forma alternativa a las búsquedas estándares de neutrinos de Majorana en los colisionadores, que no son eficientes en el modelo ISS, nuestra propuesta trata de aprovechar el hecho de que los nuevos neutrinos pesados pueden tener una estructura de sabor no trivial, produciendo así este tipo de señales interesantes con LFV. Concretamente, aplicaremos esta idea a la producción de eventos exóticos $\tau\mu jj$ en los escenarios introducidos anteriormente, encontrando resultados prometedores para las futuras etapas del LHC.

Finalmente, resumiremos las conclusiones más relevantes de este trabajo en la parte final de este documento.

Los contenidos presentados en esta Tesis, contemplados a lo largo de los Capítulos 1-5, las Conclusiones y los Apéndices, son trabajos originales que han sido publicados en las Refs. [97–101] y en el los artículos de conferencia [102–105].

Introduction

The 4th of July of 2012, the ATLAS and CMS experiments at the CERN Large Hadron Collider (LHC) announced the discovery [1, 2] of the last missing piece of the Standard Model (SM) [3–6] of fundamental interactions, the Higgs boson. This discovery completed one of the most successful theories in the annals of Physics, a predictive model able to describe with an extraordinary precision most of the known phenomena in Particle Physics. Nevertheless, there are at present some experimental evidences, as neutrino masses, dark matter or the baryon asymmetry of the universe, and theoretical issues, like the hierarchy problem, the strong-CP problem or the flavor puzzle, that the SM fails to explain, inviting us to a journey towards new physics beyond the SM (BSM).

The SM is a quantum field theory based on the $SU(3)_C \times SU(2)_L \times U(1)_Y$ gauge symmetry that describes three of the four known fundamental interactions among elemental particles, i.e, the strong, weak and electromagnetic interactions. To its particle spectrum belong the fermions, constituents of matter, the spin one bosons, force carriers, and the Higgs scalar boson, the remnant of the mass generation procedure via the Brout-Englert-Higgs (BEH) mechanism [7–10]. This mechanism explains how the spontaneous electroweak symmetry breaking (EWSB) generates the observed masses for the gauge W and Z bosons, as well as for all the fermions but the neutrinos, which remain massless in the SM.

Historically, experimental searches for flavor violating processes have been essential for the theoretical developments in Particle Physics, as the Glashow-Iliopoulos-Maiani (GIM) mechanism [11] for explaining the lack of signal from flavor changing neutral currents or the Cabibbo-Kobayashi-Maskawa (CKM) quark mixing matrix [12, 13] for the flavor changing charged currents. Likewise, the most clear experimental evidence for new physics at present comes from lepton flavor violation (LFV) in the neutrino sector. As we just said, neutrinos are massless by construction in the SM. However, experimental evidences of LFV in neutrino oscillations, first observed by the Super-Kamiokande [14] and SNO [15, 16] collaborations, have showed that neutrinos do have masses, implying that the SM needs to be modified. Moreover, if ongoing or future experiments could detect a positive signal from the yet not observed LFV processes in the charged sector, a new window to physics beyond the SM and beyond neutrino masses would be opened.

Looking at the SM particle spectrum, we see that the absence of right-handed (RH) neutrino fields in the theory forbids the neutrinos from interacting with the Higgs field and, thus, from acquiring a mass after the EWSB. Therefore, the simplest way of incorporating neutrino masses to the SM would be adding the missing RH neutrino fields, ν_R. This way, neutrinos can interact with the Higgs field via a Yukawa coupling Y_ν and obtain, after the EWSB, a Dirac mass $m_D = vY_\nu$, as the rest of SM fermions, being proportional to the Higgs vacuum expectation value which we normalize as $v = 174$ GeV. Nonetheless, this minimal extension of the SM sets out further questions: why are neutrinos so different than the rest of the fermions? why are their masses much smaller with respect to other fermion masses? Moreover, since neutrinos have no color nor electric charge, they could be Majorana fermions, i.e., could they be their own antiparticles. If true, this would be certainly a novelty in Particle Physics.

Having a closer look to the new added ν_R fields, we realize that they are singlets under the full SM gauge group and, therefore, there is nothing that forbids them from having a Majorana mass m_M. These two different masses, m_D and m_M, are the basic ingredients of the well known type-I seesaw model [17–21], which usually assumes that the Majorana mass scale m_M is much heavier than m_D and than the electroweak scale v. In such case, the physical neutrino spectrum consists on one heavy and one light Majorana neutrino per generation, with masses of the order of m_M and m_D^2/m_M, respectively. Therefore, the type-I seesaw elegantly explains the smallness of the observed light neutrino masses as the ratio of two very distinct mass scales m_D and m_M. Looking at the light neutrino mass scale $m_\nu \sim m_D^2/m_M$, we also see that in order to have $m_\nu \sim \mathcal{O}(\text{eV})$ with large Yukawa couplings $Y_\nu \sim \mathcal{O}(1)$, we need very heavy type-I seesaw masses of $m_M \sim \mathcal{O}(10^{14} \text{ GeV})$. On the other hand, lighter right-neutrino masses at the TeV range would demand small couplings $Y_\nu \sim \mathcal{O}(10^{-5})$. One way or the other, most of the phenomenology is suppressed in this type-I seesaw model. Therefore, the simplicity of this argument is what makes this model appealing and, at the same time, what makes it difficult to be tested in other low energy observables beyond the light neutrino masses themselves.

Interesting variations of this simple type-I seesaw model that have a much richer phenomenology are the low scale seesaw models. In this kind of models, some new symmetry is invoked with the aim of protecting the light neutrinos of having a large mass and, therefore, allowing the new heavy neutrinos to have lower masses and large Yukawa couplings at the same time. A particular realization of these low scale seesaw models, on which we will focus this Thesis, is the inverse seesaw (ISS) model [22–24], which assumes an approximately conserved total lepton number (LN) symmetry. In the limit of exact LN conservation, light neutrinos will be massless. However, if this symmetry is broken by some mass parameter, neutrinos will have a small Majorana mass proportional to this LN breaking parameter. On the other hand, we can expect this parameter to be naturally small, in the sense of 't Hooft [25], since setting it to zero increases the symmetry of the model. Therefore, in the

ISS model the lightness of the neutrino masses is related to the smallness of a LN symmetry breaking mass parameter.

In the ISS model, the above demanded small LN breaking is obtained by introducing new fermionic singlets in pairs (ν_R, X) of opposite LN, and assuming that the LN conservation is only violated by a small Majorana mass term μ_X for the X fields. Then, the physical spectrum consists of light Majorana neutrinos with masses suppressed by the smallness of μ_X, and two heavy nearly degenerate Majorana neutrinos per generation, which form pseudo-Dirac pairs and indeed behave almost as Dirac fermions, contrary to the heavy neutrinos of the standard type-I seesaw. Interestingly, since the μ_X scale ensures the smallness of light neutrino masses, the heavy neutrino states can have, at the same time, both large Yukawa couplings to the SM neutrinos and masses of the order of a few TeV or below, being therefore reachable at the LHC. This makes the ISS model an appealing model, with a rich phenomenology that can be tested at present or near-future experiments. These include, among others, studies of lepton flavor universality violation in meson leptonic and semileptonic decays [26, 27], lepton electric dipole moments [28, 29], lepton magnetic moments [30], heavy neutrino production at colliders [31–38], dark matter [39], leptogenesis [40, 41] and charged LFV processes [42–52].

On the theoretical size, the SM also suffers from some undesired properties, as the so-called hierarchy problem. This problem refers to the instability of the Higgs sector under radiative corrections if some new physics at a large scale is introduced. In order to illustrate this idea we can consider the Higgs boson mass, m_H, and compute its radiative corrections under the assumption that there is no new physics until the Planck mass $M_\mathrm{P} \sim 10^{19}$ GeV, where the gravitational effects start playing a role. By doing this, we find that the quantum corrections Δm_H^2 grow as the square of new physics scale, which gives a value very far from the experimentally measured value $m_H = 125.09 \pm 0.21(\mathrm{stat.}) \pm 0.11(\mathrm{syst.})$ GeV [53]. Thus, in order to obtain a prediction that is compatible with this experimental value, a very fine tunned cancellation among the bare mass and the quantum corrections is needed, which is not very natural without any further explanation nor extra symmetry.

One of the most popular and elegant solution to this problem is provided by supersymmetry (SUSY) [54–56], a new symmetry that relates fermions and bosons. In its simplest and minimal extension of the SM, known as the Minimal Supersymmetric Standard Model (MSSM) [57–59], each fermion of the SM has a spin-zero partner, called sfermion, with the same mass and quantum numbers as the original fermion; equivalently, all the SM bosons have spin one-half partners. The fact that there are fermions and bosons with the same couplings and masses gives the needed cancellation of the dangerous quantum corrections to the Higgs boson mass, providing an elegant solution to the hierarchy problem. Of course, doubling the SM spectrum is a strong prediction that experiments have tested and, unfortunately, the SUSY part of the MSSM spectrum has not been founded yet. This means that, if SUSY exists in Nature, cannot be an exact symmetry, it must be broken, such that the SUSY

particles must be heavier than the SM ones. This breaking, however, cannot spoil completely the nice solution to the hierarchy problem, so SUSY needs to be softly broken [60], i.e, the dominant quadratic dependence on the new physics scale of Δm_H still cancels out, although a logarithmic dependence remains.

Once these soft SUSY breaking terms are included, the MSSM is still a viable model with a very appealing phenomenology. Nevertheless, since it is constructed from the SM, it also demands a mechanism for neutrino mass generation. Following the previous discussion, we can consider again the ISS model and embed it in a supersymmetric context, adding to the MSSM spectrum new neutrinos and sneutrinos which can have both masses at a few TeV scale or below and with large couplings. This way, this SUSY-ISS model combines the appealing features of both frameworks, the SUSY and the ISS ones.

The best way of experimentally proving that any beyond the SM model is correct would be directly detecting the new particles that it predicts. Nevertheless, this task can in many cases be very difficult if these new particles are too heavy as to be directly produced in present experiments, so a first indication of their existence could come from their indirect implications to some other low energy observables. In the particular case of neutrino mass models, one of the optimal places for this purpose is again looking for LFV processes, concretely in the charged lepton sector, which can be quantumly induced via heavy neutrino loop effects.

Processes involving charged lepton flavor violation (cLFV) are forbidden in the SM if neutrinos are massless, and extremely suppressed if the small neutrino masses from oscillation data are *ad-hoc* added to the SM. Consequently, a positive signal in any of the experimental searches for cLFV processes would automatically imply the existence of new physics, and it must be indeed beyond the SM with minimally added neutrino masses. Although no such processes have been observed yet, this is a very active field that is being searched by many experiments which have set upper bounds to this kind of cLFV processes. At present, the strongest bounds have been found in the μ-e transitions, as the radiative $\mu \to e\gamma$ decay or μ-e conversion in heavy nuclei, which have been bounded to be below 4.2×10^{-13} and 7.0×10^{-13} by the MEG [61] and SINDRUM II [62] collaborations, respectively. Moreover, next generation of experiments are expected to improve in several orders of magnitude the sensitivities for LFV μ-e transitions, reaching the impressive range of 10^{-18} for μ-e conversion in nuclei by the PRISM experiment in J-PARC [63]. On the other hand, present bounds on transitions in the τ-μ and τ-e sectors are less constraining, with, for example, upper bounds of about 10^{-8} for LFV radiative tau decays from BABAR [64]. Therefore, there is some more room in these sectors than in the μ-e one for having large LFV signals that new experiments as BELLE-II [65] would be able to test in the near future.

Additionally, the currently running LHC has also many things to say about cLFV. First of all, the fact that a new particle, the Higgs boson, has been discovered opens a new window for possible deviations from the SM that definitely needs to be explored. In particular, three new cLFV channels are introduced in the cLFV market, the LFV Higgs boson decays into

two leptons of different flavor, $H \to \ell_k \bar{\ell}_m$, $k \neq m$, which have already been searched by the CMS [66, 67] and ATLAS [68] experiments. Even though CMS saw a small but intriguing excess in the $H \to \tau\mu$ channel after run-I [69] , it has not been confirmed yet with run-II data and, at present, they have been able to set an upper bound of 2.5×10^{-3} [67]. These searches of LFV Higgs decays, as well as other explorations of the Higgs sector, will continue and surely be improved with more data after new LHC runs.

Other interesting observables that the LHC is also looking for are the LFV Z boson decays into two leptons of different flavors $Z \to \ell_k \bar{\ell}_m$ [68, 70]. Interestingly, after the run-I, ATLAS has already reached the previous sensitivities from the LEP experiment [71, 72], even improving the bound for the $Z \to \mu e$ channel. As for the Higgs searches, LFV Z decays will certainly continue during the new runs, so hopefully new interesting data will come from ATLAS and CMS. Nevertheless, the best expected sensitivities for LFV Z decays are expected from next generation of lepton colliders, as long as they can work as Z factories with a very clean environment. In particular, at future linear colliders, with an expected sensitivity of 10^{-9} [73, 74], or at a Future Circular e^+e^- Collider (such as FCC-ee (TLEP) [75]), where it is estimated that up to 10^{13} Z bosons would be produced and the sensitivities to LFV Z decay rates could be improved up to 10^{-13} [49].

The main motivation of this Thesis, therefore, is to explore the connection between the existence of new right-handed neutrino particles with masses of a few TeV or below, reachable at the LHC, and LFV in the charged lepton sector. We are particularly interested in the two models above described, the ISS and the SUSY-ISS model, which are very appealing models since they can provide right-handed neutrino states with masses at the TeV range and, at the same time, with large couplings. Charged LFV phenomenology within massive neutrino models has been studied before [76–92] and also in the ISS [42–52]. In this Thesis, we concentrate mainly in studying the predictions for the LFV Higgs and Z boson decays, which as we said are extremely timely to explore in the light of the recent discovery of the Higgs boson and the new LHC data on the LFV Z decays. In addition, we also make new predictions for other cLFV processes like $\ell_m \to \ell_k \gamma$ and $\ell_m \to \ell_k \ell_k \ell_k$, as well as for other lepton flavor preserving observables that will be also relevant in the context of the model we consider here.

We fully study for the first time the LFV H decays in presence of right-handed neutrinos in the ISS model, as well as in presence of sneutrinos in the SUSY-ISS model. We perform this study following two different approaches. First we present, based on the results for the type-I seesaw model in Ref. [82], the results for the full one-loop computation done in the physical neutrino mass basis. Second, we use the mass insertion approximation technique, which works in the electroweak basis and allow us to obtain useful and simple formulas for the LFV H decay rates. For the numerical evaluation, we show that large LFV rates can be obtained focusing in particular directions of the parameter space where μ-e transitions, the experimentally most constrained ones, are highly suppressed. In this line, we provide a new

proposal for the building of these phenomenologically interesting scenarios with suppressed μ-e transitions. These scenarios are based on the μ_X parametrization, which also a new genuine contribution proposed in this Thesis. On the other hand, LFV Z decay rates in the ISS model have been first explored in Ref. [49]. Therefore, in the case of these observables, we directly present a more specific study in those particular directions of the parameters space with suppressed μ-e transitions, that give large allowed ratios. In this sense, we perform a complementary study of that previously done.

As we said, we are interested in models with right-handed neutrinos at the TeV range, since they belong to the scale of energies that the LHC is now probing. In the ISS model, due to the pseudo-Dirac character of the heavy neutrinos, standard collider searches looking for lepton number violating final states with two same-sign leptons, the 'smoking gun' signature of Majorana fermions [93–96], are not efficient. Therefore, here we propose to use instead lepton flavor violating final states in order to discriminate events from the production and decay of the low scale seesaw heavy neutrinos. In particular, we focus on exotic $\tau^{\pm}\mu^{\mp}jj$ or $\tau^{\pm}e^{\mp}jj$ final states with no missing transverse energy, which could be produced in scenarios with ν_R masses at and below the TeV range and where LFV is favored in the τ-μ or τ-e sector, respectively.

This Thesis is organized as follows. In Chapter 1 we review neutrino oscillation physics and its connection with the need of introducing neutrino masses. We discuss some popular neutrino mass models, paying special attention to models with right-handed neutrinos with TeV range masses, as the inverse seesaw model and its SUSY version. These are the two models that we will consider for exploring in detail the LFV phenomenology in the following Chapters. Moreover, when studying the neutrino sector of these models, we present a new parametrization, which we refer to as the μ_X parametrization, that will turn out to be very useful for exploring the parameter space while being always in agreement with neutrino oscillation data.

In Chapter 2 we address the importance of charged LFV processes in the search of new physics and summarize the experimental status. Then, we revisit the LFV lepton decays in the ISS model, meaning the radiative $\ell_m \to \ell_k \gamma$ and three-body $\ell_m \to \ell_k \ell_k \ell_k$ decays with $k \neq m$. This new study of these processes will allow us to learn about the behavior of the LFV with respect to the ISS parameters, as well as to emphasize the advantages of using our μ_X parametrization. As a result of this study, we will find some interesting phenomenological scenarios, well motivated by present experimental bounds, where LFV τ-μ or τ-e transitions are favored while keeping the μ-e transitions highly suppressed, which will be useful for exploring LFV H and Z decays. Furthermore, we also discuss in this Chapter the implications of right-handed neutrinos with TeV masses to other relevant low energy observables, which we will consider as constraints when looking for maximum allowed rates in the next Chapters.

Chapter 3 is devoted to the study of the LFV Higgs decay (LFVHD) rates in the

ISS and SUSY-ISS models. We present the results of the full one-loop calculation of the LFVHD rates in the ISS model and systematically study their dependence with the different parameters of this model. In order to better understand the results, we perform a complete and independent calculation of these rates using the mass insertion approximation, which will allow us to derive a simple expression for an effective LFV $H\ell_k\ell_m$ vertex, very useful for any author that wishes to make a fast estimation of the LFVHD rates in this kind of models. This complete analysis will serve as to conclude on the maximum LFVHD rates allowed by present experimental constraints. Moreover, we explore these rates in the SUSY-ISS model, showing that the new SUSY loops including sleptons and sneutrinos may considerably enhance the maximum allowed rates, reaching values close to the present experimental sensitivities.

In Chapter 4 we study the LFV Z boson decays (LFVZD) in the ISS model. We focus our analysis in the previously introduced phenomenological scenarios, where large allowed LFV rates in the τ-μ and τ-e sector can be achieved. We compare our finding to previous works in the literature and show that, in these interesting directions of the ISS parameter space, large allowed rates can be obtained, well within the reach of next generation of experimental LFVZD searches.

In Chapter 5 we focus on low scale seesaw neutrino production at the LHC. We study the possibility of detecting the production and decay of the ISS heavy neutrinos searching for exotic LFV $\ell_k^\pm \ell_m^\mp jj$ events, with $k \neq m$, and with no missing transverse energy. Alternatively to standard Majorana neutrino searches at colliders that are not relevant for the ISS model, our proposal explotes the fact that the new heavy neutrino states can have non-trivial flavor structure, leading to this kind of interesting LFV signals. Concretely, we will apply this idea to the production of exotic $\tau\mu jj$ events within the previously introduced scenarios, finding promising results for the future LHC runs.

Finally, we summarize the main conclusions at the end of this document.

The contents presented in this Thesis, summarized along the Chapters 1-5, the Conclusions and the Appendices, are original works that have been published in Refs. [97–101] and in the conference proceedings [102–105].

Chapter 1

Seesaw models with heavy neutrinos at the TeV energy range

In this Chapter we motivate the need of going beyond the Standard Model for explaining lepton flavor changing neutrino oscillation data and review some of the most popular models for this task, the seesaw models. We will concentrate specially in the so-called low scale seesaw models, one of which will be of special relevance for this Thesis: the Inverse seesaw model. Finally, we will introduce a Supersymmetric version of the latter, the SUSY-ISS, an interesting model that combines the appealing features of the Minimal Supersymmetric Standard Model and the Inverse seesaw model. Along this Chapter, we derive the μ_X parametrization in Section 1.3, useful for accommodating neutrino oscillation data, which is a genuine contribution of this Thesis and was first published in Ref. [97]. The implementation of the ISS model in the SUSY framework, as given in Eqs. (1.64)-(1.74), and the derivation of the interaction Lagrangian in the physical SUSY-ISS basis in Eq. (1.77) and in App. D are original works of this Thesis that have been published in Ref. [98].

1.1 Neutrino oscillations

In the Standard Model (SM) the neutrinos, and antineutrinos, come in three different flavors. When they are produced by the standard charged current, they are always produced together with a charged lepton, which is the one that labels them: if the neutrino is produced with an e^+ or e^-, we name it as electron-neutrino (ν_e) or electron-antineutrino ($\bar{\nu}_e$), respectively; if it is produced with a μ^+ or μ^-, we have a ν_μ or $\bar{\nu}_\mu$; and if it is produced with τ^+ or τ^-, it is a ν_τ or $\bar{\nu}_\tau$. This one-to-one identification with the charged lepton sector is, at the same time, what allows us to detect and identify these elusive particles. These three neutrino flavor states $\nu_\ell \equiv \left(\nu_e, \nu_\mu, \nu_\tau\right)$ form a basis that we will refer to as the interaction basis.

17

Neutrinos only suffer from weak interactions and, consequently, they can travel long distances without interacting with anything. Their evolution is given by the Schrödinger equation, whose solutions are plane waves with energies defined by the eigenvalues of the 3×3 neutrino mass matrix. These stationary solutions define a new basis, the so-called mass or physical basis $\nu_\alpha \equiv (\nu_1, \nu_2, \nu_3)$, which in general does not coincide with the above introduced interaction basis. This misalignment is the origin of the neutrino oscillation phenomena.

The relation between the two basis can be written as:

$$\nu_\ell = \sum_{\alpha=1}^{3} (U_{\text{PMNS}})_{\ell\alpha} \nu_\alpha \,, \tag{1.1}$$

where the U_{PMNS} is a unitary 3×3 rotation matrix, analogous to the CKM matrix in the quarks sector, whose name comes from Pontecorvo, who proposed neutrino oscillations [106], and from Maki-Nakagawa-Sakata, who introduced the mixing matrix [107].

When a neutrino is produced, it is in a specific flavor state, which can be expressed as a superposition of the mass eigenstates. If neutrinos were massless or degenerate in mass, all the mass eigenstates would have the same time evolution and, consequently, the initial flavor state would remain unchanged. In such a situation, we could say that the individual lepton flavor numbers, i.e., L_e, L_μ and L_τ, were preserved. On the contrary, if physical neutrinos had non-degenerate masses, each of the mass eigenstates would evolve differently in time, modifying the initial superposition and therefore the flavor of the initial neutrino state. This process, which is a direct consequence of non-degenerate neutrino masses, is known as neutrino oscillation and implies that individual lepton flavor numbers are not conserved. In the ultrarelativistic limit, the oscillation probability in vacuum from a flavor ν_ℓ to a flavor $\nu_{\ell'}$ is given by [108]:

$$\mathcal{P}_{\nu_\ell \to \nu_{\ell'}}(L, E) = \sum_{\alpha,\beta=1}^{3} U_{\ell\alpha}^* U_{\ell'\alpha} U_{\ell\beta} U_{\ell'\beta}^* exp\left(-i\frac{\Delta m_{\alpha\beta}^2 L}{2E}\right) \,, \tag{1.2}$$

where we have used $U \equiv U_{\text{PMNS}}$ to shorten the notation, $E \sim |\boldsymbol{p}|$ is the neutrino energy, L is the distance between the source and the detector, and $\Delta m_{\alpha\beta}^2 \equiv m_\alpha^2 - m_\beta^2$ is the squared mass difference.

Several experiments involving solar, atmospheric, reactor and accelerator neutrinos have established the evidences for neutrino oscillations and, therefore, for neutrino masses (see Ref. [109] for a review). Nevertheless, and despite this experimental effort, there are still open issues related with neutrino oscillations and masses. First of all, we do not know the absolute neutrino mass scale, although we know that it is at the eV scale or below from the upper limits on the effective electron neutrino mass in β decays, given by the Mainz [110]
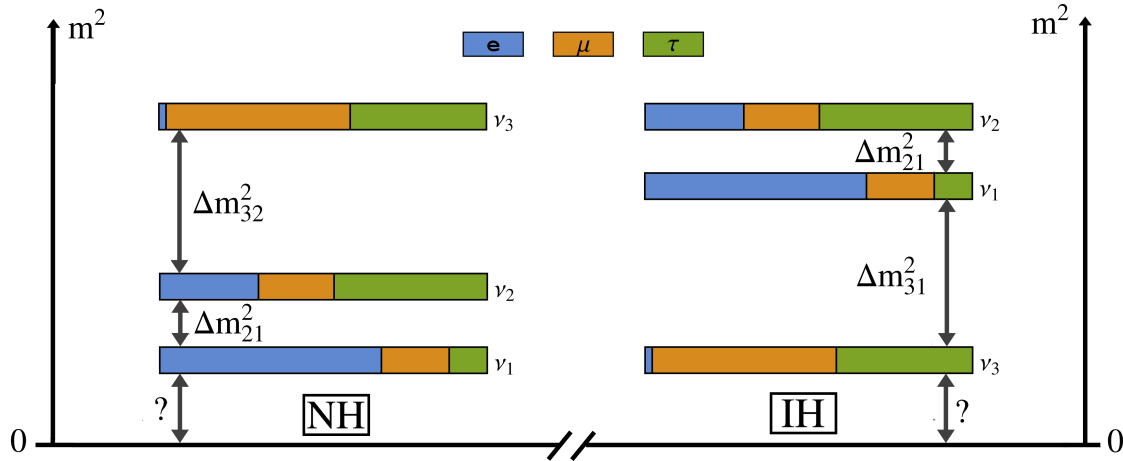
Figure 1.1: The two possible neutrino mass orderings, known as normal (left) and inverted (right) hierarchies. The colors represent the flavor composition of each of the physical neutrinos: blue for ν_e, orange for ν_μ and green for ν_τ.

and Troitsk [111] experiments:

$$m_\beta < 2.05 \text{ eV} \quad \text{at 95\% C.L.} \tag{1.3}$$

Additional information on the absolute neutrino mass scale, can be obtained from cosmological observations, which has set bound to the sum of the light neutrino masses. At present, there are only upper bounds on this quantity, being the most constraining ones provided by the Planck collaboration [112]:

$$\sum m_\nu < 0.23 \text{ eV}. \tag{1.4}$$

Measuring neutrino oscillations in vacuum allows us to know the mass differences $|\Delta m_{21}^2|$ and $|\Delta m_{31}^2|$, but it does not tell us anything about neither the absolute neutrino mass scale nor the neutrino mass hierarchy. Additional measurements of matter effects or the Mikheev-Smirnov-Wolfenstein (MSW) effects [113–117] in neutrino oscillations can help solving the sign degeneracies. Nowadays, matter effects in the sun have made possible to know that $\Delta m_{21}^2 > 0$, but the sign of Δm_{31}^2 is a mystery yet. Therefore, two orderings are still possible, as shown if Fig. 1.1: a Normal Hierarchy (NH) where $m_{\nu_1} < m_{\nu_2} < m_{\nu_3}$ and an Inverted Hierarchy (IH) where $m_{\nu_3} < m_{\nu_1} < m_{\nu_2}$. Solving this degeneracy is one of the most important open issues in neutrino physics.

Second, being neutrinos the only electrically neutral fermions in the SM, they could be Majorana particles, i.e, they could be their own antiparticles. This would be in contrast to the rest of the SM model Dirac fermions, for which their antiparticle is a different state.

This hypothetical Majorana character of the neutrinos, although very common in theoretical models as we will see later, does not have any impact on neutrino oscillations and, therefore, new observables to discern between Majorana and Dirac fermions need to be considered. The fact that a lepton can be its own antiparticle is directly related to the conservation of the total Lepton Number (LN) violation, since a Majorana mass terms breaks LN in two units. Consequently, LN violating processes, like neutrinoless double beta decay, are usually considered as the smoking gun signatures for Majorana neutrinos (for a review on $0\nu\beta\beta$, see for instance Refs. [118, 119]). Unfortunately, no experimental evidence has been found yet for any LN violating processes, so knowing if neutrinos are Majorana or Dirac fermions is still an open issue.

Third, massive neutrinos add new CP-violating phases to the SM parameters. For the case of three massive neutrinos, the PMNS matrix in Eq. (1.1) introduces one CP-violating phase, known as the Dirac CP phase, if neutrinos are Dirac fermions, and two extra Majorana CP-violating phases if neutrinos are Majorana fermions. However, neutrino oscillations are only sensitive to the Dirac phase and this dependence appears via a particular combination of several oscillation parameters, known as the Jarlskog invariant [120] $J_{CP} = \mathrm{Im}\big(U_{\mu3}U_{e3}^*U_{e2}U_{\mu2}^*\big)$. This fact makes difficult to measure the Dirac phase in oscillation experiments, but experiments as T2K, NOνA, or future Hyper-K or Dune, may be able to do it in the next years. On the other hand, the extra Majorana phases do not play any role in neutrino oscillations. Nevertheless, they can be important for trying to explain the matter-antimatter asymmetry of the universe though the mechanism known as Baryogenesis via Leptogenesis (for a review see, for instance, Ref. [121]).

Finally, we may wonder how many neutrinos do exist in Nature. Despite the fact that there are some anomalies [122–130] pointing towards the existence of eV-KeV scale sterile neutrinos, we will assume in this Thesis that there are only three light neutrinos, which is the minimal requirement to fit neutrino oscillation observations. In this situation, the unitary PMNS matrix in Eq. (1.1) can be parametrized in its standard form as:

$$
U_{\mathrm{PMNS}} = \begin{pmatrix} c_{12}c_{13} & s_{12}c_{13} & s_{13}e^{-i\delta} \\ -s_{12}c_{23}-c_{12}s_{23}s_{13}e^{i\delta} & c_{12}c_{23}-s_{12}s_{23}s_{13}e^{i\delta} & s_{23}c_{13} \\ s_{12}s_{23}-c_{12}c_{23}s_{13}e^{i\delta} & -c_{12}s_{23}-s_{12}c_{23}s_{13}e^{i\delta} & c_{23}c_{13} \end{pmatrix} \cdot P \,, \qquad (1.5)
$$

where $c_{ij} = \cos\theta_{ij}$, $s_{ij} = \sin\theta_{ij}$, δ being the CP-violating Dirac phase and the diagonal matrix $P = \mathrm{diag}(1, e^{i\phi_1}, e^{i\phi_2})$ accounts for the two extra CP-phases that do not play any role in neutrino oscillations, as we said before. In order to consider all the experimental neutrino oscillation data in a consistent way, we will take the results from the global fit analysis done by the NuFIT group [131]. Assuming a Normal Hierarchy, they obtain at the 1σ level:

$$
\sin^2\theta_{12} = 0.306^{+0.012}_{-0.012} \,, \qquad\qquad \Delta m^2_{21} = 7.50^{+0.19}_{-0.17} \times 10^{-5}\mathrm{eV}^2 \,,
$$
$$
\sin^2\theta_{23} = 0.441^{+0.027}_{-0.021} \,, \qquad\qquad \Delta m^2_{31} = 2.524^{+0.039}_{-0.040} \times 10^{-3}\mathrm{eV}^2 \,,
$$

$$\sin^2 \theta_{13} = 0.02166^{+0.00075}_{-0.00075}, \qquad\qquad \delta = 261^{+51}_{-59}, \qquad\qquad (1.6)$$

while for the Inverted Hierarchy they give

$$\sin^2 \theta_{12} = 0.306^{+0.012}_{-0.012}, \qquad\qquad \Delta m^2_{21} = 7.50^{+0.19}_{-0.17} \times 10^{-5} \text{eV}^2,$$
$$\sin^2 \theta_{23} = 0.587^{+0.020}_{-0.024}, \qquad\qquad \Delta m^2_{32} = -2.514^{+0.038}_{-0.041} \times 10^{-3} \text{eV}^2,$$
$$\sin^2 \theta_{13} = 0.02179^{+0.00076}_{-0.00076}, \qquad\qquad \delta = 277^{+40}_{-46}. \qquad\qquad (1.7)$$

1.2   Seesaw models for neutrino masses

At the time that the SM was built, there were no evidences for neutrino masses. Moreover, experiments showed that neutrinos produced in charged weak interactions were left-handed (LH) fields, while antineutrinos were right-handed (RH). These facts were minimally satisfied in the SM by a chiral LH flavor field $\nu_{\ell_L} \equiv (\nu_\ell)_L$, which together with the LH charged lepton field forms a $SU(2)_L$ doublet, as required by the SM gauge symmetry. As a result, right-handed neutrino fields were left out and neutrinos were treated as massless fields by the SM.

Nowadays the status has changed. The strong experimental evidences of neutrino oscillations, as mentioned in the previous section, have established that neutrinos do have masses, claiming for new physics beyond the SM to accommodate this new situation. In a very simple and minimalistic choice, one could reconsider the addition of RH neutrino fields to the SM, in such a way that neutrinos could obtain their masses via their Yukawa interaction with the Higgs field, mimicking the mass generation for the rest of the SM fermions,

$$\mathcal{L}_{\text{Yuk}} = -Y^{ij}_\nu \overline{L_i} \widetilde{\Phi} \nu_{R_j} + h.c. \qquad\qquad (1.8)$$

where Y_ν is the neutrino Yukawa coupling matrix, $L = (\nu_L\ \ell_L)$ is the $SU(2)_L$ lepton doublet and $\widetilde{\Phi} = i\sigma_2 \Phi$ with Φ the Higgs $SU(2)_L$ doublet:

$$\Phi = \begin{pmatrix} G^+ \\ v + \dfrac{1}{\sqrt{2}}(H + iG^0) \end{pmatrix} \quad , \quad \widetilde{\Phi} = i\sigma_2 \Phi = \begin{pmatrix} v + \dfrac{1}{\sqrt{2}}(H - iG^0) \\ -G^+ \end{pmatrix}. \qquad (1.9)$$

After the Electroweak Symmetry Breaking (EWSB), this Lagrangian term leads to a Dirac mass term for neutrinos $m_\nu = m_D = vY_\nu$, with $v = 174$GeV. In order this mass to be at the eV scale, as suggested by neutrino oscillations, the Yukawa coupling needs to be very small, of the order of 10^{-11}. This value would extremely suppress any kind of phenomenology beyond neutrino oscillations. Moreover, such a tiny neutrino Yukawa coupling is five orders of magnitude smaller than the electron Yukawa coupling and eleven orders with respect

to the top, so it would make even worse the flavor puzzle problem of understanding the hierarchy of the fermion masses.

On the other hand, having a closer look to the new added ν_R fields, we realize that they are singlets under the full SM gauge group and, therefore, there is nothing that protects them from having a Majorana mass term. In that situation, physical neutrinos will be Majorana particles.

In order to work with Majorana fermions, it is very useful to introduce the particle-antiparticle conjugation operator $\hat{C}$, which is defined as [108, 132]:

$$\hat{C} : \psi \to \psi^C = \mathcal{C}\bar{\psi}^T \,. \tag{1.10}$$

This matrix $\mathcal{C}$ fulfills:

$$\mathcal{C}^{-1}\gamma_\mu\mathcal{C} = -\gamma_\mu^T \,, \quad \mathcal{C}^{-1}\gamma_5\mathcal{C} = \gamma_5^T \,, \quad \mathcal{C}^\dagger = \mathcal{C}^{-1} = -\mathcal{C}^* \,, \tag{1.11}$$

which, in the Weyl representation, can be satisfied by chosing $\mathcal{C} = i\gamma_2\gamma_0$. Consequently, this operator $\hat{C}$ flips the chirality of chiral fields:

$$\hat{C} : \psi_L \to (\psi_L)^C = (\psi^C)_R \,, \quad \psi_R \to (\psi_R)^C = (\psi^C)_L \,, \tag{1.12}$$

meaning that the antiparticle of a LH field is a RH field. Moreover, the fact that Majorana fermions coincide with their antiparticle can be expressed in terms of this operator as:

$$\psi^C = \psi \,. \tag{1.13}$$

These relations will be very useful when considering models with Majorana neutrinos, as the standard seesaw models.

On a more model independent ground, we could make use of the effective Lagrangians formalism in order to try a bottom up approach to the neutrino mass problem. In this formalism, we assume that the SM is an effective theory of a more complete but unknown theory, which in general will contain new symmetries and fields at a heavy scale Λ. If we knew the complete theory at high energies, we could integrate out all the heavy fields with masses above the electroweak scale and obtain a low energy Lagrangian in terms only of the SM fields. The modifications with respect to the SM Lagrangian would then be a series of new non-renormalizable operators suppressed by the heavy scale Λ, which encode all the new physics effects at low energy. Unfortunately, we do not know the complete theory to follow this top down way. Therefore, with the aim of covering any possible high energy theory for neutrino physics, we can alternatively write the most general non-renormalizable $SU(2)_L \times U(1)_Y$ invariant Lagrangian that involves neutrino and other SM fields, the low energy fields. This will lead us to an effective Lagrangian that generically can be written as the SM Lagrangian extended with a series of higher order non-renormalizable operators

$$\mathcal{L}_{\text{eff}} = \mathcal{L}_{\text{SM}} + \delta\mathcal{L}_{d=5} + \delta\mathcal{L}_{d=6} + \dots \tag{1.14}$$

where d stands for the dimension of the operators in $\delta\mathcal{L}_d$, which will be suppressed by $d-4$ inverse powers of the heavy scale Λ.

It is illustrative to look at the $d=5$ Lagrangian. Since neutrinos are members of a $SU(2)_L$ doublet, there is only one possible operator, first written by Weinberg [133], contributing to $\delta\mathcal{L}_5$, given by:

$$\delta\mathcal{L}_{d=5} = \frac{1}{2}\frac{c_{ij}}{\Lambda}\left(\overline{L_i^C}\widetilde{\Phi}^*\right)\left(\widetilde{\Phi}^\dagger L_j\right), \tag{1.15}$$

where c_{ij} are dimensionless complex coefficients and $i,j = 1..3$. After the EWSB, this operator gives a Majorana mass term for the neutrinos:

$$\delta\mathcal{L}_{d=5} \to \frac{v^2 c_{ij}}{2\Lambda}\left(\overline{\nu_i^C}\nu_j + h.c.\right). \tag{1.16}$$

Interestingly, this Majorana mass term is naturally small, suppressed by the new physics scale. The higher the scale Λ, the lower the neutrino mass, as if they were playing with a seesaw. This is the idea behind the seesaw models, the simplest renormalizable models leading to this relation after integrating out the new heavy particles responsible of generating neutrino masses at the tree level.

Looking at the Weinberg operator, we can learn some properties about the new particles of the seesaw models. In order to be gauge invariant, these new particles can be either singlets or triplets of $SU(2)_L$, since they need to couple to two $SU(2)$ doublets in an invariant way. On the other hand, they can be either fermions or scalar, so we can define three[1] possible seesaw models according to which new type of fields they add to the SM: fermionic singlets (type-I), scalar triplets (type-II) or fermionic triplets (type-III).

Before going to the details of these seesaw models, we want to emphasize that any high energy theory that introduces a Majorana mass term for the neutrinos leads to the Weinberg operator in Eq. (1.15) when integrating out the heavy fields, as it is the only one that can be written at lowest order. This implies that, in order to distinguish between the different neutrino theories, we need to consider their implications beyond the neutrino mass generations. In terms of the effective Lagrangian in Eq. (1.14), this means looking for the effect of the $d=6$ operators [134] or higher. As we will see later, lepton flavor violating phenomenology is one of the optimal places for studying this task.

Type-I Seesaw Model

The type-I seesaw model [17–21] extends the SM with right-handed neutrinos ν_R, which are fermionic singlets under the full SM gauge group. As mentioned above, these new fields

---

[1]The choice of a scalar singlet is not possible due to the structure of the Weinberg operator.

allow the neutrinos to have a Yukawa interaction with the Higgs field, as well as a Majorana mass term for themselves. The Lagrangian of the type-I seesaw can be thus written as:

$$\mathcal{L}_{\text{type-I}} = -Y_\nu^{ij}\overline{L_i}\widetilde{\Phi}\nu_{Rj} - \frac{1}{2}m_M^{ij}\overline{\nu_{Ri}^C}\nu_{Rj} + h.c. \tag{1.17}$$

where the first term is the Yukawa Lagrangian as in Eq. (1.8) and in the second term m_M is a symmetric Majorana mass matrix. If we assign to the ν_R fields the same lepton number than to the L fields, we realize that the Yukawa interaction conserves LN, while the Majorana mass term breaks it in two units. Therefore, this model introduces a new scale that explicitly breaks LN. After the EWSB, Eq. (1.17) leads to a neutrino mass Lagrangian that, in the electroweak interaction basis reads as:

$$\mathcal{L}_{\text{type-I}}^{\text{mass}} = -m_D^{ij}\overline{\nu_{Li}^C}\nu_{Rj} - \frac{1}{2}m_M^{ij}\overline{\nu_{Ri}^C}\nu_{Rj} + h.c. = -\frac{1}{2}\overline{N_L}\begin{pmatrix} 0 & m_D \\ m_D^T & m_M \end{pmatrix}N_L^C + h.c. \tag{1.18}$$

where we have defined the LH fields as a vector column $N_L = (\nu_{Li}, \nu_{Ri}^C)^T$. From this mass Lagrangian, we identify the neutrino Majorana mass matrix in the EW basis:

$$M_{\text{type-I}}^\nu = \begin{pmatrix} 0 & m_D \\ m_D^T & m_M \end{pmatrix}. \tag{1.19}$$

It is illustrative to consider first the case where there is only one generation of neutrinos. In that context, all the parameters in Eq. (1.19) are just numbers and $M_{\text{type-I}}^\nu$ is a 2×2 mass matrix which, in the seesaw limit, defined by choosing the two involved scales very distant, $m_D \ll m_M$, has the following two eigenvalues:

$$m_\nu \simeq -\frac{m_D^2}{m_M} = -\frac{v^2 Y_\nu^2}{m_M}, \quad m_N \simeq m_M. \tag{1.20}$$

One of the physical neutrino is then a heavy state N with a mass close to the LN breaking scale m_M, while the other is a light state ν with a small mass m_ν suppressed by m_M^{-1}. This desired suppression is a particular realization of Eq. (1.16), and can be understood as the tree level processes in the left plot of Fig. 1.2.

For a more realistic model, we can add three[2] RH fields to the SM spectrum. In that case, $M_{\text{type-I}}^\nu$ is a 6×6 matrix which, again in the seesaw limit, can be block-diagonalized by the following 6×6 approximate unitary matrix:

$$U_\xi^\nu = \begin{pmatrix} (\mathbb{1} - \frac{1}{2}\xi^*\xi^T) & \xi^*(\mathbb{1} - \frac{1}{2}\xi^T\xi^*) \\ -\xi^T(\mathbb{1} - \frac{1}{2}\xi^*\xi^T) & (\mathbb{1} - \frac{1}{2}\xi^T\xi^*) \end{pmatrix} + \mathcal{O}(\xi^4), \tag{1.21}$$

---

[2]Although the addition of two neutrinos is enough for explaining neutrino oscillation data.

where we have introduced the seesaw matrix parameter $\xi = m_D m_M^{-1}$. This rotation leads to two separated 3×3 mass matrices, given by:

$$U_\xi^{\nu T} M_{\text{type}-I}^\nu U_\xi^\nu \simeq \begin{pmatrix} -m_D m_M^{-1} m_D^T & 0 \\ 0 & m_M \end{pmatrix} \equiv \begin{pmatrix} m_\nu & \\ & m_N \end{pmatrix} . \tag{1.22}$$

We see again that there are two sectors, one light sector whose mass m_ν is suppressed by m_M^{-1} and a heavy sector with masses close to m_M.

Without lost of generality, we can decide to work in the basis where m_M is already diagonal and, therefore, we only need to diagonalize the light mass matrix. In order to be in agreement with neutrino oscillation data, we can impose this light matrix to be diagonalized by the proper U_{PMNS} matrix and to have the right eigenvalues. This can be done by requiring:

$$m_\nu \simeq -m_D m_M^{-1} m_D^T \equiv U_{\text{PMNS}}^* m_\nu^{\text{diag}} U_{\text{PMNS}}^\dagger. \tag{1.23}$$

In this equation, m_ν^{diag} contains the masses of the physical light neutrino states and the U_{PMNS} matrix the mixing angles, as explained in the previous section. Eq. (1.23) can be solved for m_D, leading to the Casas-Ibarra parametrization [135] of the Dirac mass matrix:

$$m_D^T = i\sqrt{m_N^{\text{diag}}} R \sqrt{m_\nu^{\text{diag}}} U_{\text{PMNS}}^\dagger , \tag{1.24}$$

where we have used the relation $m_N^{\text{diag}} \simeq m_M$ so as to express everything in terms of the physical masses. This parametrization allow us to use as input parameters the physical masses, the experimentally measured mixing angles and an unknown 3×3 complex orthogonal matrix R.

As we said, the type-I seesaw model is a simple extension of the SM that explains the smallness of the neutrino masses as a ratio of two very distant scales, the low Dirac mass and the high Majorana mass scales. In order to accommodate light neutrino masses in the eV scale, this ratio needs to be very small. Following Eq. (1.20), we see that large $Y_\nu \sim 1$ couplings imply GUT scale Majorana masses of $m_M \sim 10^{14}$ GeV. On the other hand, TeV scale heavy neutrinos require very small Yukawa couplings, of the order of 10^{-8}. As a consequence, one way or the other, most of the new phenomenology related with these new heavy neutrinos, as well as their direct production at colliders, will be then very suppressed.

Type-II Seesaw Model

The type-II seesaw model [21, 136–139] adds a new scalar $SU(2)_L$ triplet with hypercharge 2 to the SM for generating neutrino masses. In contrast with the fermionic singlets of the type-I seesaw, this new triplet does not interact only with the neutrino fields, but also with the rest of the SM fields, so the full Lagrangian is more involved. Nevertheless, for the
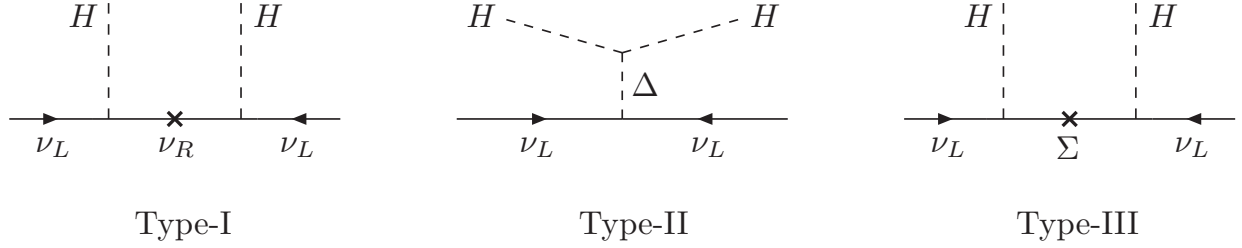
Figure 1.2: Diagrams for the tree level light Majorana mass generation in the type-I (left), type-II (middle) and type-III (right) seesaw models.

purpose of our discussion of neutrino mass generation, it is enough to consider the following relevant terms:

$$\mathcal{L}_{\text{type-II}} = -\frac{1}{2} Y_\Delta^{ij} \overline{L_i^C} \, \widetilde{\Delta} L_j - \mu \Phi^T i\sigma_2 \Delta^\dagger \Phi - \frac{1}{2} M_\Delta^2 \text{Tr}\big(\Delta^\dagger \Delta\big) + h.c. \tag{1.25}$$

Here, Δ stands for the new scalar $SU(2)$ triplet, defined as:

$$\Delta = \begin{pmatrix} \Delta^+/\sqrt{2} & \Delta^{++} \\ \Delta^0 & -\Delta^+/\sqrt{2} \end{pmatrix} . \tag{1.26}$$

The first term in Eq. (1.25) is a Yukawa like interaction between the SM $SU(2)_L$ leptonic doublet L and the scalar triplet, with coupling Y_Δ and $\widetilde{\Delta} = i\sigma_2\Delta$. The other two terms are part of the new scalar potential in this model, with M_Δ the mass of the triplet and μ a coupling of the triplet scalar with two Higgs doublets. The full scalar potential, given in Ref. [140] for instance, sets the vacuum expectation values for the neutral components of both the doublet and triplet scalars. In the limit where the triplet is heavy, $M_\Delta \gg v$, its *vev* is given by,

$$v_\Delta \simeq \mu \frac{v^2}{M_\Delta^2} , \tag{1.27}$$

which then gives a Majorana mass for the neutrinos of

$$m_\nu \simeq v_\Delta Y_\Delta . \tag{1.28}$$

Diagrammatically, this mass term can be understood as the tree level process in the middle of Fig. 1.2.

We can now understand how the type-II seesaw can explain the smallness of the neutrino masses. Looking at these equations, we see that, on the one hand, large Yukawa couplings or heavy triplet masses is a possibility, as in the type-I seesaw. On the other hand, in these equations there is an extra scale μ, which being small can explain the smallness of

m_ν even for large Y_Δ and low M_Δ. Furthermore, assigning to the triplet a leptonic number $L = 2$, we see that the only LN violating term is precisely the one proportional to this μ parameter and, therefore, it is natural to consider μ to be small, as setting it to zero would increase the symmetry of the model [25]. As a result, the smallness of neutrino masses is related somehow to a small breaking of a symmetry.

However, the addition of a new scalar to the SM spectrum will in general modify the Higgs sector or contribute to electroweak precision observables, which are constrained by experiments. For instance, precision measurements of the electroweak ρ parameter set an upper bound on the new scalar triplet vev of $v_\Delta \lesssim 3$ GeV. Fortunately, such a small v_Δ can be again explained by a small LN violating mass scale μ. Additionally, the (double) charged components of the scalar triplet could also induce potentially large tree level flavor changing processes, not observed yet by any experiment.

Type-III Seesaw Model

The type-III seesaw model [141] explains the neutrino masses by adding a new fermionic $SU(2)_L$ triplet to the SM spectrum, which is defined as:

$$\Sigma = \begin{pmatrix} \Sigma^0/\sqrt{2} & \Sigma^+ \\ \Sigma^- & \Sigma^0/\sqrt{2} \end{pmatrix}. \tag{1.29}$$

As the ν_R of the type-I seesaw model, this Σ couples to the LH neutrinos and to the Higgs doublet, with a Lagrangian given by

$$\mathcal{L}_{\text{type-III}} = -Y_\Sigma^{ij}\overline{L_i}\widetilde{\Phi}\Sigma - \frac{1}{2}M_\Sigma^{ij}\text{Tr}\left(\overline{\Sigma_i^C}\Sigma_j\right) + h.c. \tag{1.30}$$

This Lagrangian is very similar to Eq. (1.17), with the Yukawa coupling Y_Σ and the Majorana mass M_Σ. Consequently, in the seesaw limit $M_\Sigma \gg vY_\Sigma$, the obtained light neutrino mass matrix is equivalent to the one in Eq. (1.23):

$$m_\nu \simeq -vY_\Sigma M_\Sigma^{-1}vY_\Sigma^T. \tag{1.31}$$

The tree level diagram generating this mass neutrino mass is shown in the right panel of Fig. 1.2, which is the same as in the type-I seesaw with Σ instead of ν_R. Actually, in this model the neutral component of Σ behaves like the right-handed neutrino of the type-I seesaw. Nevertheless, being the Σ a $SU(2)_L$ triplet, it also has gauge couplings to the SM. This fact can lead to new phenomenology, such as tree-level flavor changing currents mediated by the charged components $\Sigma^\pm$, which so far have not been observed experimentally.

These three types of seesaw models are some examples of models for generating light neutrino masses. There are many other models proposed in the literature, which try different

approaches to explain the lightness of neutrino masses. For instance, in the models known as radiative seesaw models, the tree level neutrino masses are forbidden, so they need to be generated at the loop level and, therefore, they are naturally suppressed with respect to the rest of fermion masses. This is the case in the Zee-Babu model [142, 143]. Another option could be to assume that there is a symmetry protecting the neutrinos from having a tree level mass term, which is spontaneously broken with a small *vev* that generates small neutrino masses, as some R-parity violating supersymmetric models [144–146]. For a review of neutrino mass models, see for instance Refs. [147, 148].

In this Thesis, we are interested in the phenomenology of right-handed neutrinos with masses at the TeV scale, such that they can lead to not very suppressed low energy effects. We are also interested in the possibility of producing them at colliders. As we said, the type-I seesaw model introduces ν_R fields that can indeed be at the TeV, although in this case their Yukawa coupling is so small than it suppresses most of the phenomenological implications. An interesting way out of this situation is to invoke a symmetry that protects the light neutrino masses even in the case of low right-handed masses and large Yukawa couplings. This is the main idea behind low scale seesaw models, as the inverse seesaw model, that we describe in full detail in the following.

1.3   The Inverse Seesaw model and its parametrizations

As we discussed above, the original type-I seesaw model cannot have right-handed neutrinos with masses at the TeV scale and large Yukawa couplings and, at the same time, accommodate light neutrino masses at the eV range. In low scale seesaw models this interesting situation is accomplished by making use of extra symmetries, for instance a common assumption is global lepton number conservation. In order to better understand this idea, we can first consider the simplified situation of one generation, where there is only one left-handed neutrino as in the SM and add two extra fermionic singlets, ν_R and X. The ν_R field is like in the type-I seesaw model, a right-handed partner of the ν_L, singlet under the full SM group and with lepton number $L = -1$, while the new singlet X has the opposite lepton number $L = 1$. In the limit where LN is conserved, the only terms that we can add to the SM Lagrangian are:

$$\mathcal{L} = -Y_\nu \overline{L}\widetilde{\Phi}\nu_R - M_R \overline{\nu_R^C}X \,, \tag{1.32}$$

which, after the EWSB, leads to the following neutrino Majorana mass matrix in the EW (ν_L, ν_R^C, X^C) basis:

$$M^\nu = \begin{pmatrix} 0 & m_D & 0 \\ m_D & 0 & M_R \\ 0 & M_R & 0 \end{pmatrix} \,. \tag{1.33}$$

Diagonalizing this matrix we obtain two degenerate Majorana neutrinos, which form one single Dirac neutrino, and one massless neutrino. This means that imposing exact LN conservation gives rise to massless neutrinos and, therefore, we need to include a LN breaking in order to generate neutrino masses. If this breaking is small, the neutrino mass will be small. As a result, in these low scale seesaw models the smallness of neutrino masses is related to a small breaking of a symmetry, which is natural in the sense of 't Hooft [25].

Different models can be defined following this idea, depending where we introduce the small LN violating scale that generates the masses for the light neutrinos. Including a Majorana mass term for the X fields, we end up with the inverse seesaw model [22–24], whereas a LN violating interaction between the ν_L and X fields defines the linear seesaw model [149, 150]. In this Thesis, we will work in the framework of the inverse seesaw model, although most of our results will also apply to other models as the linear seesaw, since we will see that they can be easily related.

We consider a realization of the inverse seesaw model adapted to three generations where three[3] pairs of fermionic singlets (ν_R, X) are added to the SM. The ISS Lagrangian in this case is given by

$$\mathcal{L}_{\text{ISS}} = -Y_\nu^{ij}\overline{L_i}\widetilde{\Phi}\nu_{Rj} - M_R^{ij}\overline{\nu_{Ri}^C}X_j - \frac{1}{2}\mu_R^{ij}\overline{\nu_{Ri}^C}\nu_{Rj} - \frac{1}{2}\mu_X^{ij}\overline{X_i^C}X_j + h.c.\,, \qquad (1.34)$$

with the favor indices i,j running from 1 to 3. Here, Y_ν is the 3×3 neutrino Yukawa coupling matrix, as in Eq. (1.17), M_R is a lepton number conserving complex 3×3 mass matrix, and μ_R and μ_X are Majorana complex 3×3 symmetric mass matrices that violate LN conservation by two units. As we said, these two LN violating scales are naturally small in this model, as setting them to zero would restore the conservation of LN, thus enlarging the symmetry of the model. After the EWSB, we obtain the complete 9×9 neutrino mass matrix, which again in the EW (ν_L, ν_R^C, X^C) basis, reads,

$$M_{\text{ISS}}^\nu = \begin{pmatrix} 0 & m_D & 0 \\ m_D^T & \mu_R & M_R \\ 0 & M_R^T & \mu_X \end{pmatrix}. \qquad (1.35)$$

Since this complex mass matrix is symmetric, it can be diagonalized using a 9×9 unitary matrix U_ν according to

$$U_\nu^T M_{\text{ISS}}^\nu U_\nu = \text{diag}(m_{n_1}, \ldots, m_{n_9})\,, \qquad (1.36)$$

where n_i are the nine physical neutrino Majorana states, with masses m_{n_i}, respectively, and

---

[3]Although the minimal realization of the ISS model that accounts for oscillation data only needs two fermionic pairs [151], usually referred to as the (2,2)-ISS, we prefer to add one pair for each SM family, usually denoted by (3,3)-ISS.
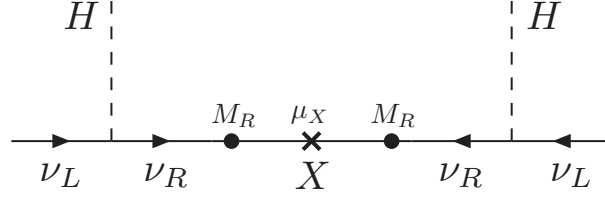
Figure 1.3: Diagram for the tree level light Majorana mass generation in the ISS model.

related to the electroweak eigenstates through the rotation U_ν as:

$$
\begin{pmatrix} \nu_L^C \\ \nu_R \\ X \end{pmatrix} = U_\nu P_R \begin{pmatrix} n_1 \\ \vdots \\ n_9 \end{pmatrix} \quad , \quad \begin{pmatrix} \nu_L \\ \nu_R^C \\ X^C \end{pmatrix} = U_\nu^* P_L \begin{pmatrix} n_1 \\ \vdots \\ n_9 \end{pmatrix} .
\tag{1.37}
$$

As we did for the type-I seesaw, it is interesting to consider first the simplified scenario where there is only one generation of (ν_L, ν_R, X). In that case, all the parameters in Eq. (1.35) are just numbers and M_{ISS}^ν is a 3×3 mass matrix which, in the $\mu_X \ll m_D, M_R$ limit of approximate LN conservation, has the following three eigenvalues:

$$
m_\nu \simeq \frac{m_D^2}{m_D^2 + M_R^2} \mu_X ,
\tag{1.38}
$$

$$
m_{N_1, N_2} \simeq \pm \sqrt{M_R^2 + m_D^2} + \frac{M_R^2 \mu_X}{2(m_D^2 + M_R^2)} + \frac{\mu_R}{2} .
\tag{1.39}
$$

We see that the mass m_ν of one of the states is small, since it is proportional to the small parameter μ_X, and, therefore, it can be associated to the light neutrino states observed in neutrino oscillations. Notice that, contrary to the type-I seesaw model where the lightness of m_ν is related to a suppression of a large LN breaking scale, here it is proportional to a small LN breaking scale, μ_X, motivating the model name of inverse seesaw. In the seesaw limit $m_D \ll M_R$, it can be further simplified to $m_\nu \sim \mu_X m_D^2 / M_R^2$, which can be understood as the result of the diagram in Fig. 1.3. The other two mass eigenstates have almost degenerate heavy masses, m_{N_1, N_2}, which combine to form a pseudo-Dirac pair. Notice that the μ_R Majorana mass term for the ν_R fields does not enter in Eq. (1.38), meaning that μ_R does not generate light neutrino masses at the tree level. The effects of this new scale appear only at one-loop level in the light neutrino masses and are, consequently, more suppressed. Therefore, we will set μ_R to zero for the rest of this Thesis and consider a small μ_X as the only Lepton Number violating parameter leading to the light neutrino masses.

A similar pattern of neutrino masses occurs in our three generations case, with one light and two nearly degenerate heavy neutrinos per generation. In the masses range of interest
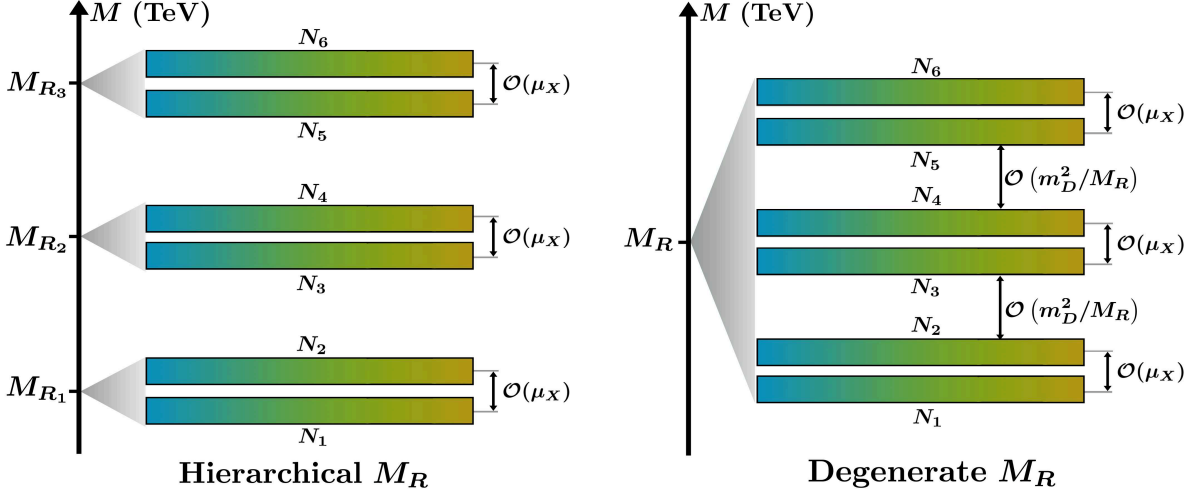
Figure 1.4: Schematic distribution for the mass spectrum of the six ISS heavy neutrinos, $N_{i=1,\ldots,6}$ with $m_{N_1} < \cdots < m_{N_6}$. For hierarchical M_R, with $M_{R_1} < M_{R_2} < M_{R_3}$ here, there are three quasidegenerate states with masses $m_{N_1} \simeq m_{N_2} \simeq M_{R_1}$, $m_{N_3} \simeq m_{N_4} \simeq M_{R_2}$ and $m_{N_5} \simeq m_{N_6} \simeq M_{R_3}$. For degenerate M_R, meaning $M_{R_{1,2,3}} \equiv M_R$, all the heavy neutrino masses are close to M_R, with small separations between the pairs of $\mathcal{O}(m_D^2/M_R)$. In both cases, there are small $\mathcal{O}(\mu_X)$ splittings between the quasidegenerate neutrinos. We demand that the light neutrino sector is as in Fig. 1.1 by using the parametrizations described in this section. The color code represents the fact that heavy neutrinos have a non-trivial flavor structure, which we will further study in Chapter 5.

with $\mu_X \ll m_D \ll M_R$, the mass matrix M_{ISS}^ν can be diagonalized by blocks [152], leading to six heavy neutrinos that form quasidegenerate pairs with masses approximately given by the eigenvalues of M_R and with splittings of order $\mathcal{O}(\mu_X)$. We display schematically the heavy neutrino mass spectrum in Fig. 1.4. Regarding the light neutrino sector, it contains three light Majorana neutrinos, whose 3×3 mass matrix is as follows:

$$M_{\mathrm{light}} \simeq m_D M_R^{T^{-1}} \mu_X M_R^{-1} m_D^T. \tag{1.40}$$

In the same manner as we did in Eq. (1.23), we can ensure the agreement with neutrino oscillation data by demanding:

$$M_{\mathrm{light}} \equiv U_{\mathrm{PMNS}}^* m_\nu^{\mathrm{diag}} U_{\mathrm{PMNS}}^\dagger. \tag{1.41}$$

Then, we can solve this equation for m_D, as we did before to obtain the Casas-Ibarra parametrization. In fact, this can be easily done by analogy with the type-I seesaw. Defining a new 3×3 mass matrix as

$$M = M_R \mu_X^{-1} M_R^T, \tag{1.42}$$

the light neutrino mass matrix can be written similarly to Eq. (1.23):

$$M_{\text{light}} \simeq m_D M^{-1} m_D^T \,. \tag{1.43}$$

Therefore, we can modify the Casas-Ibarra parametrization in Eq. (1.24) to define a new version for the ISS given by:

$$m_D^T = V^\dagger \sqrt{M^{\text{diag}}} R \sqrt{m_\nu^{\text{diag}}} U_{\text{PMNS}}^\dagger \,, \tag{1.44}$$

where V is a unitary matrix that diagonalizes M according to $M = V^\dagger M^{\text{diag}} V^*$ and, as before, R is an unknown complex orthogonal matrix that can be written as

$$R = \begin{pmatrix} c_2 c_3 & -c_1 s_3 - s_1 s_2 c_3 & s_1 s_3 - c_1 s_2 c_3 \\ c_2 s_3 & c_1 c_3 - s_1 s_2 s_3 & -s_1 c_3 - c_1 s_2 s_3 \\ s_2 & s_1 c_2 & c_1 c_2 \end{pmatrix} \,, \tag{1.45}$$

with $c_i \equiv \cos\theta_i$, $s_i \equiv \sin\theta_i$ and θ_1, θ_2, and θ_3 are arbitrary complex angles.

The Casas-Ibarra parametrization has been extensively used in the literature for accommodating light neutrino data in this type of models. We propose here an alternative parametrization that we find very useful to ensure the agreement with oscillation data in the ISS model[4]. The main idea is to use precisely the new scale μ_X as to codify light neutrino masses and mixings. This can be done by solving Eq. (1.41) for μ_X instead of m_D, which defines our μ_X parametrization:

$$\mu_X = M_R^T \; m_D^{-1} \; U_{\text{PMNS}}^* m_\nu U_{\text{PMNS}}^\dagger \; m_D^{T-1} M_R \,. \tag{1.46}$$

Notice that we have assumed that the Dirac mass matrix, or equivalently the Yukawa coupling matrix, is not singular so it can be inverted.

Of course, physics does not depend on the parametrization one chooses, however the efficiency in exploring the model parameter space does. When using this new parametrization, we see two important advantages. First, Eq. (1.41) is quadratic in m_D, so solving it leads to a redundancy reflected as the orthogonal matrix R that introduces six new unknown parameters to scan over. In contrast, Eq. (1.41) is linear in μ_X, and therefore the μ_X parametrization does not introduce any new parameter and the parameter space can be easily explored. Second, the μ_X parametrization considers Y_ν and M_R as input parameters, while the Casas-Ibarra parametrization works with μ_X as input instead of Y_ν. As we will see, the relevant parameters for the LFV and related phenomenology in these models are the interaction Yukawa coupling and source of the LFV, Y_ν, and the heavy mass scale M_R. Therefore, being able to treat them as independent input parameters is important for

---

[4]Nevertheless, this idea could be generically applied to any model with a new scale responsible of explaining the smallness of neutrino masses.

studying the LFV phenomenology in these models. Furthermore, this later point will be also important in order to understand the decoupling behavior of the different observables in the limit of very heavy right-handed neutrinos. All these points will become clear in the following Chapters.

In order to complete the theoretical set up of the model, we specify next all the relevant neutrino interactions in their mass basis. These include the neutrino Yukawa couplings, the gauge couplings of the charged and neutral gauge bosons, $W^\pm$ and Z, and the couplings of the corresponding Goldstone bosons, $G^\pm$ and G^0:

$$\mathcal{L}_W = -\frac{g}{\sqrt{2}} \sum_{i=1}^{3} \sum_{j=1}^{9} W_\mu^- \bar{\ell}_i B_{\ell_i n_j} \gamma^\mu P_L n_j + h.c., \tag{1.47}$$

$$\mathcal{L}_Z = -\frac{g}{4c_W} \sum_{i,j=1}^{9} Z_\mu \bar{n}_i \gamma^\mu \Big[C_{n_i n_j} P_L - C^*_{n_i n_j} P_R \Big] n_j, \tag{1.48}$$

$$\mathcal{L}_H = -\frac{g}{2m_W} \sum_{i,j=1}^{9} H \bar{n}_i C_{n_i n_j} \Big[m_{n_i} P_L + m_{n_j} P_R \Big] n_j, \tag{1.49}$$

$$\mathcal{L}_{G^\pm} = -\frac{g}{\sqrt{2}m_W} \sum_{i=1}^{3} \sum_{j=1}^{9} G^- \bar{\ell}_i B_{\ell_i n_j} \Big[m_{\ell_i} P_L - m_{n_j} P_R \Big] n_j + h.c\,, \tag{1.50}$$

$$\mathcal{L}_{G^0} = -\frac{ig}{2m_W} \sum_{i,j=1}^{9} G^0 \bar{n}_i C_{n_i n_j} \Big[m_{n_i} P_L - m_{n_j} P_R \Big] n_j, \tag{1.51}$$

where $P_{R,L} = (1 \pm \gamma^5)/2$ are the usual chirality projectors and,

$$B_{\ell_i n_j} = U_{ij}^{\nu*}, \tag{1.52}$$

$$C_{n_i n_j} = \sum_{k=1}^{3} U_{ki}^\nu U_{kj}^{\nu*}\,. \tag{1.53}$$

These coupling matrices follow the following interesting identities [93]:

$$\sum_{k=1}^{N} B_{\ell_1 n_k} B^*_{\ell_2 n_k} = \delta_{\ell_1 \ell_2}\,, \quad \sum_{k=1}^{N} B_{\ell n_k} C_{n_k n_i} = B_{\ell n_i}\,, \quad \sum_{k=1}^{N} C_{n_i n_k} C^*_{n_j n_k} = \sum_{k=1}^{3} B^*_{\ell_k n_i} B_{\ell_k n_j} = C_{n_i n_j}\,,$$

$$\sum_{k=1}^{N} m_{n_k} C_{n_i n_k} C_{n_j n_k} = 0\,, \quad \sum_{k=1}^{N} m_{n_k} B_{\ell n_k} C^*_{n_k n_i} = 0\,, \quad \sum_{k=1}^{N} m_{n_k} B_{\ell_1 n_k} B_{\ell_2 n_k} = 0\,, \tag{1.54}$$

where N stands for the total number of neutrinos, i.e., $N = 9$ for the ISS realization we are considering.

1.3.1 The linear seesaw model

Finally, we want to briefly comment on the other low scale seesaw model above mentioned, the linear seesaw model (LNN), and its relation with the ISS model. As we said, in the LSS model the LN violating mass scale is introduced via a Yukawa coupling, $\widetilde{Y}_\nu$, between the ν_L and the X singlets, in contrast to the ISS model, where the LN violating scale is introduced via the Majorana mass terms. For simplicity, we focus this discussion on the one generation case, although it can be easily generalized to more generations. Then, the neutrino mass matrix in the linear seesaw, in the same EW basis (ν_L, ν_R^C, X^C), reads as:

$$M_{\text{LSS}}^\nu = \begin{pmatrix} 0 & m_D & \widetilde{m}_D \\ m_D & 0 & M_R \\ \widetilde{m}_D & M_R & 0 \end{pmatrix}, \tag{1.55}$$

with $\widetilde{m}_D = v\widetilde{Y}_\nu$ and the other parameters are as before. Assuming an approximate LN symmetry, this new Yukawa interaction will be small, leading to a light neutrino mass. This is given, for $\widetilde{m}_D \ll m_D \ll M_R$, by,

$$m_\nu \simeq -2\widetilde{m}_D \frac{m_D}{M_R}, \tag{1.56}$$

which is linear in m_D, motivating the name of the model.

In order to show the relation between the linear and inverse seesaw models, first we notice that they are identical in the limit of massless neutrinos, i.e, in the limit of exact LN conservation. When LN is violated in the linear seesaw model via a non-zero $\widetilde{m}_D$, we can redefine the fermionic singlets in such a way that $\widetilde{m}_D$ is rotated away. This can be done by performing a rotation [153] of $\tan\theta = \widetilde{m}_D/m_D$ between the (ν_R, X) fields. Then

$$\begin{pmatrix} 1 & 0 & 0 \\ 0 & c & s \\ 0 & -s & c \end{pmatrix} \begin{pmatrix} 0 & m_D & \widetilde{m}_D \\ m_D & 0 & M_R \\ \widetilde{m}_D & M_R & 0 \end{pmatrix} \begin{pmatrix} 1 & 0 & 0 \\ 0 & c & -s \\ 0 & s & c \end{pmatrix} = \begin{pmatrix} 0 & m_D/c & 0 \\ m_D/c & M_R s_2 & M_R c_2 \\ 0 & M_R c_2 & -M_R s_2 \end{pmatrix}, \tag{1.57}$$

where $c = \cos\theta$, $s = \sin\theta$, $c_2 = \cos 2\theta$ and $s_2 = \sin 2\theta$. Since $\widetilde{m}_D \ll m_D$, $\tan\theta$ is small and, therefore, the mass matrix in this rotated basis has the same pattern as the ISS mass matrix in Eq. (1.35). Given this relation, we emphasize again that the results and general conclusions of this Thesis, computed and studied for the particular case of the ISS model, could be applicable to other low scale seesaw models, like the linear seesaw model.

It is important to notice that this kind of low scale seesaw models, in contrast to the standard type-I seesaw, there are three different scales which play different roles. In the particular case of the ISS model, μ_X controls the smallness of the light neutrino masses, M_R the masses of the new heavy neutrinos and $m_D = vY_\nu$ the interaction between the new added neutrino sector and the SM ν_L fields. Since they are independent, we can have at the

same time large Yukawa couplings, $Y_\nu^2/4\pi \sim \mathcal{O}(1)$, and right-handed neutrinos in the TeV range, i.e, reachable at present experiments like the LHC. These two properties make the ISS model in particular, and low scale seesaw models in general, interesting models with a rich phenomenology that we wish to explore further in this Thesis.

1.3.2   The SUSY Inverse Seesaw model

The Higgs mechanism of the SM introduces a fundamental scalar particle, the recently found Higgs boson, whose mass has been set experimentally to $m_H = 125.09 \pm 0.21(\text{stat.}) \pm 0.11(\text{syst.})$ GeV [53]. Being a fundamental scalar, it will receive huge contributions via quantum corrections if a new heavy scale associated to some new physics is introduced, for instance, if gravitational effects are introduced at the Planck mass scale $M_P \sim 10^{19}$ GeV. This instability of the Higgs sector under radiative corrections is known as the hierarchy problem and it is one of the main theoretical problems of the SM. One of the most popular and elegant solutions to this problem is provided by supersymmetry (SUSY) [54–56]. This is a new symmetry that relates fermions with bosons, such that their contributions to the radiative corrections to the Higgs boson mass cancels exactly. Therefore, it introduces a new symmetry that protects the scalar sector from unnaturally large radiative corrections.

The minimal SUSY extension of the SM model is the Minimal Supersymmetric Standard Model (MSSM) [57–59]. We can understand the way this model extends the SM in two steps. First, for consistency reasons, it adds a second scalar $SU(2)_L$ doublet to the SM, in a way that one of the doublets is responsible of giving masses to the up-type fermions and the other one to the down-type fermions. Then, it doubles all the particles in the spectrum introducing a SUSY partner for each field. For a full review of SUSY and the MSSM, we refer the reader to Refs. [154, 155]. However, in this minimal extension of the SM, neutrinos remain massless as in the SM and, therefore, it needs to be extended in order to explain neutrino oscillation data. In this section we shortly summarize the most relevant aspects of the simplest SUSY version of the inverse seesaw model, introducing the new neutrino and sneutrino sectors needed for our forthcoming phenomenological studies, in particular for the LFV Higgs decay computations in Section 3.2.

In the simplest supersymmetric realization of the ISS model, the SUSY-ISS model in short, the MSSM superfield content is supplemented by three pairs of gauge singlet chiral superfields $\widehat{N}_i$ and $\widehat{X}_i$ with opposite lepton numbers ($i = 1, 2, 3$). As in the original ISS model, this allows to write a Yukawa interaction term for the neutrinos, with coupling Y_ν, a heavy mass term $\widetilde{M}_R$ between the extra singlets, and a Majorana mass term $\widetilde{\mu}_X$ for the X fields. The SUSY-ISS model is then defined by the following superpotential:

$$W = W_{\text{MSSM}} + \varepsilon_{ab}\widehat{N}Y_\nu\widehat{H}_2^b\widehat{L}^a + \widehat{N}\widetilde{M}_R\widehat{X} + \frac{1}{2}\widehat{X}\widetilde{\mu}_X\widehat{X}, \tag{1.58}$$

with $\varepsilon_{12} = 1$ and

$$W_{\text{MSSM}} = \varepsilon_{ab} \left[\widehat{E} Y_e \widehat{H}_1^a \widehat{L}^b + \widehat{D} Y_D \widehat{H}_1^a \widehat{Q}^b + \widehat{U} Y_U \widehat{H}_2^b \widehat{Q}^a - \mu \widehat{H}_1^a \widehat{H}_2^b \right] . \tag{1.59}$$

Here, all chiral superfields are taken to be left-handed. This means that $\widehat{Q}, \widehat{L}$ are the chiral superfields involving the left-handed $SU(2)_L$ doublets Q_L and L_L, respectively, as well as their SUSY partners. For instance, the the spin 0 and spin $\frac{1}{2}$ components of $\widehat{L}$ are $(\widetilde{\nu}_L, \widetilde{e}_L)$ and (ν_L, e_L). On the other hand, the chiral superfields $\widehat{D}, \widehat{U}, \widehat{E}$ contains the d_R^c, u_R^c and e_R^c fields and their partners, for example, we have $\widehat{E} = \left[(\widetilde{e_R})^*, (e_R)^c \right]$. The down- and up-type Higgs bosons, $\widehat{H}_1$ and $\widehat{H}_2$ respectively, are defined as

$$\widehat{H}_1 = \begin{pmatrix} \hat{h}_1^0 \\ \hat{h}_1^- \end{pmatrix}, \quad \widehat{H}_2 = \begin{pmatrix} \hat{h}_2^+ \\ \hat{h}_2^0 \end{pmatrix}, \tag{1.60}$$

and μ is the Higgs superfield mass parameter. The coupling $Y_{e,D,U}$ are the Yukawa coupling matrices. The generation indices have been suppressed for simplicity and it should be understood in a tensor notation as $\widehat{N} Y_\nu \widehat{H}_2^b \widehat{L}^a = \widehat{N}_i (Y_\nu)_{ij} \widehat{H}_2^b \widehat{L}_j^a$.

Exact SUSY invariance requires any particles to have the same mass of its SUSY partner, meaning that the SM spectrum should have a SUSY copy with the same corresponding masses. Nevertheless, the lack of any signal from such new particles in the experiments has excluded this situation and, therefore, if SUSY exists in Nature, it must be broken. This breaking, however, cannot spoil the above commented solution to the hierarchy problem, so it needs to be softly broken.

Even if we do not know the SUSY breaking mechanism, we can parametrize it by introducing a set of well established soft SUSY breaking terms [60]. In the SUSY-ISS model, this soft SUSY breaking Lagrangian is given by

$$-\mathcal{L}_{\text{soft}} = -\mathcal{L}_{\text{soft}}^{\text{MSSM}} + \widetilde{\nu}_R^T m_{\widetilde{\nu}_R}^2 \widetilde{\nu}_R^* + \left[\widetilde{\nu}_R^\dagger (A_\nu Y_\nu) \widetilde{\nu}_L h_2^0 - \widetilde{\nu}_R^\dagger (A_\nu Y_\nu) \widetilde{e}_L h_2^+ + h.c. \right]$$

$$+ \widetilde{X}^T m_{\widetilde{X}}^2 \widetilde{X}^* + \left[\widetilde{X}^\dagger (B_X \widetilde{\mu}_X) \widetilde{X}^* + \widetilde{\nu}_R^\dagger (B_R \widetilde{M}_R) \widetilde{X}^* + h.c. \right], \tag{1.61}$$

with

$$-\mathcal{L}_{\text{soft}}^{\text{MSSM}} = \widetilde{e}_R^T m_{\widetilde{e}}^2 \widetilde{e}_R^* + \widetilde{d}_R^T m_{\widetilde{d}}^2 \widetilde{d}_R^* + \widetilde{u}_R^T m_{\widetilde{u}}^2 \widetilde{u}_R^* + m_{H_1}^2 |H_1|^2 + m_{H_2}^2 |H_2|^2$$

$$+ \delta_{ab} (\widetilde{Q}^a)^\dagger m_{\widetilde{Q}}^2 \widetilde{Q}^b + \delta_{ab} (\widetilde{L}^a)^\dagger m_{\widetilde{L}}^2 \widetilde{L}^b + \frac{1}{2} \left[M_1 \bar{\lambda}_b \lambda_b + M_2 \bar{\lambda}_W^\alpha \lambda_W^\alpha + M_3 \bar{\lambda}_g^\alpha \lambda_g^\alpha + h.c. \right]$$

$$+ \varepsilon_{ab} \left[(\widetilde{u}_R^\dagger (A_u Y_u) \widetilde{Q}^a H_2^b + \widetilde{d}_R^\dagger (A_d Y_d) \widetilde{Q}^b H_1^a + \widetilde{e}_R^\dagger (A_e Y_e) \widetilde{L}^b H_1^a + B\mu H_2^a H_1^b + h.c. \right]. \tag{1.62}$$

These SUSY breaking Lagrangians introduces a set of new unknown parameters to the SUSY-ISS model. From the MSSM Lagrangian, we have the squark and slepton soft masses, $m^2_{\tilde{e},\tilde{d},\tilde{u},\tilde{Q},\tilde{L}}$, the Higgs sector soft masses $m^2_{H_{1,2}}$ and $B\mu$, the gaugino soft masses $M_{1,2,3}$ and the trilinear couplings for squarks and sleptons, $A_{u,d,e}$. In the SUSY-ISS model, there are some extra soft parameters related to the new added fields, in particular, the soft masses $m^2_{\tilde{\nu}_R,\tilde{X}}$, $B_X\widetilde{\mu}_X$ and $B_R\widetilde{M}_R$, and the trilinear coupling A_ν.

All these new parameters could, in principle, have a non-trivial flavor structure. Nevertheless, when studying the SUSY-ISS model, and for the sake of simplicity, we will take all soft SUSY breaking masses, as well as the lepton number conserving mass term $\widetilde{M}_R$, to be flavor diagonal. This way, the only sources of flavor violation are the neutrino Yukawa coupling Y_ν, and the lepton number violating mass term $\widetilde{\mu}_X$. The only exception will be $m^2_{\tilde{L}}$, which receives radiative corrections via the renormalization group equations (RGE), from a heavy scale M with universal soft SUSY breaking parameters down to the heavy neutrino scale M_R. These corrections are also governed by Y_ν and, for phenomenological purposes, can be described as [156]:

$$(\Delta m^2_{\tilde{L}})_{ij} = -\frac{1}{8\pi^2}(3M_0^2 + A_0^2)(Y_\nu^\dagger \log \frac{M}{M_R} Y_\nu)_{ij}\,. \tag{1.63}$$

After the EWSB, the neutrino sector is as in the previous ISS model, therefore the analysis of the mass matrix diagonalization and the discussion about using the Casas-Ibarra or the μ_X parametrization for accommodating oscillation data is as before. Hence, it is enough to describe the new SUSY sector, and the sneutrino mass matrix $M^2_{\tilde{\nu}}$, which is defined by

$$-\mathcal{L}^{\tilde{\nu}}_{\text{mass}} = \frac{1}{2}\left(\tilde{\nu}_L^\dagger, \tilde{\nu}_L^T, \tilde{\nu}_R^T, \tilde{\nu}_R^\dagger, \tilde{X}^T, \tilde{X}^\dagger\right) M^2_{\tilde{\nu}} \begin{pmatrix} \tilde{\nu}_L \\ \tilde{\nu}_L^* \\ \tilde{\nu}_R^* \\ \tilde{\nu}_R \\ \tilde{X}^* \\ \tilde{X} \end{pmatrix}, \tag{1.64}$$

where $\tilde{\nu}_L$, $\tilde{\nu}_R$ and $\tilde{X}$ are vectors made of 3 weak eigenstates each and they are defined in a similar fashion, e.g. $\tilde{\nu}_L = (\tilde{\nu}_L^{(e)}, \tilde{\nu}_L^{(\mu)}, \tilde{\nu}_L^{(\tau)})^T$. The complete 18×18 sneutrino mass matrix is then expressed in terms of 3×3 submatrices, giving:

$$M^2_{\tilde{\nu}} = \begin{pmatrix} M^2_{LL} & 0 & 0 & M^2_{LR} & m_D M_R^* & 0 \\ 0 & (M^2_{LL})^T & (M^2_{LR})^* & 0 & 0 & m_D^* M_R \\ 0 & (M^2_{LR})^T & M^2_{RR} & 0 & M_R\mu_X^* & (B_R M_R^*)^* \\ (M^2_{LR})^\dagger & 0 & 0 & (M^2_{RR})^T & B_R M_R^* & M_R^*\mu_X \\ M_R^T m_D^\dagger & 0 & \mu_X M_R^\dagger & (B_R M_R^*)^\dagger & M^2_{XX} & 2(B_X\mu_X^*)^\dagger \\ 0 & M_R^\dagger m_D^T & (B_R M_R^*)^T & \mu_X^* M_R^T & 2(B_X\mu_X^*) & (M^2_{XX})^T \end{pmatrix}, \tag{1.65}$$

with

$$M^2_{LL} = m_D m^\dagger_D + m^2_{\tilde{L}} + \mathbb{1} \frac{m_Z}{2} \cos 2\beta \,, \tag{1.66}$$

$$M^2_{LR} = -\frac{\mu}{\tan\beta} m_D + m_D A^\dagger_\nu \,, \tag{1.67}$$

$$M^2_{RR} = m^T_D m^*_D + M_R M^\dagger_R + m^2_{\tilde{\nu}_R} \,, \tag{1.68}$$

$$M^2_{XX} = M^T_R M^*_R + \mu_X \mu^*_X + m^2_{\tilde{X}} \,. \tag{1.69}$$

Then, the sneutrino mass matrix is diagonalized by using:

$$\tilde{U}^\dagger M^2_{\tilde{\nu}} \tilde{U} = M^2_{\tilde{n}} = \text{diag}(m^2_{\tilde{n}_1}, ..., m^2_{\tilde{n}_{18}}) \,, \tag{1.70}$$

which corresponds to the following rotation between the interaction and mass basis

$$\begin{pmatrix} \tilde{\nu}_L \\ \tilde{\nu}^*_L \\ \tilde{\nu}^*_R \\ \tilde{\nu}_R \\ \tilde{X}^* \\ \tilde{X} \end{pmatrix} = \tilde{U} \begin{pmatrix} \tilde{n}_1 \\ \vdots \\ \vdots \\ \vdots \\ \tilde{n}_{18} \end{pmatrix} . \tag{1.71}$$

Notice that the basis used in Eq. (1.64) uses the sneutrino electroweak eigenstates and their complex conjugate states and they fulfill:

$$\tilde{\nu}_i = \tilde{U}_{i,j} \tilde{n}_j \,, \tag{1.72}$$

$$\tilde{\nu}^*_i = \tilde{U}_{3+i,j} \tilde{n}_j \,, \tag{1.73}$$

but at the same time:

$$(\tilde{\nu}_i)^* = \tilde{U}^*_{i,j} \tilde{n}_j \,, \tag{1.74}$$

since the physical sneutrinos are real scalar fields. While both Eqs. (1.73) and (1.74) are equally valid, we choose Eq. (1.73).

The mass matrices of the other SUSY particles, namely the charginos, neutralinos, and charged sleptons, are the same as in the SUSY type I seesaw studied in Ref. [82], so we will use their definitions of the corresponding rotation matrices, which in turn were based on the conventions of Ref. [58] for the charginos and neutralinos. Specifically, U and V will be the matrices that rotate the chargino states and N the one that rotates the neutralino states. In addition, combinations of rotation matrices for the neutralinos are defined as

$$N'_{a1} = N_{a1} \cos\theta_W + N_{a2} \sin\theta_W \,,$$
$$N'_{a2} = -N_{a1} \sin\theta_W + N_{a2} \cos\theta_W \,. \tag{1.75}$$

As for the charged sleptons, they are diagonalized by

$$\tilde{\ell}' = R^{(\ell)}\tilde{\ell}\,, \tag{1.76}$$

where $\tilde{\ell}' = (\tilde{e}_L, \tilde{e}_R, \tilde{\mu}_L, \tilde{\mu}_R, \tilde{\tau}_L, \tilde{\tau}_R)^T$ are the weak eigenstates and $\tilde{\ell} = (\tilde{\ell}_1, \dots, \tilde{\ell}_6)^T$ are the mass eigenstates.

Finally, we introduce the relevant interaction terms from the Lagrangian that will be needed later in the study of the LFV Higgs decays. Following again the notation in Ref. [82], these terms are given in the mass basis by

$$
\begin{aligned}
\mathcal{L}_{\tilde{\chi}_j^- \ell \tilde{\nu}_\alpha} &= -g\,\bar{\ell}\left[A_{L\alpha j}^{(\ell)} P_L + A_{R\alpha j}^{(\ell)} P_R \right] \tilde{\chi}_j^- \tilde{\nu}_\alpha + h.c.\,, \\
\mathcal{L}_{\tilde{\chi}_a^0 \ell \tilde{\ell}_\alpha} &= -g\bar{\ell}\left[B_{L\alpha a}^{(\ell)} P_L + B_{R\alpha a}^{(\ell)} P_R \right] \tilde{\chi}_a^0 \tilde{\ell}_\alpha + h.c.\,, \\
\mathcal{L}_{H_x \tilde{s}_\alpha \tilde{s}_\beta} &= -iH_x\left[g_{H_x \tilde{\nu}_\alpha \tilde{\nu}_\beta}\tilde{\nu}_\alpha^* \tilde{\nu}_\beta + g_{H_x \tilde{\ell}_\alpha \tilde{\ell}_\beta}\tilde{\ell}_\alpha^* \tilde{\ell}_\beta \right]\,, \\
\mathcal{L}_{H_x \tilde{\chi}_i^- \tilde{\chi}_j^-} &= -gH_x \bar{\tilde{\chi}}_i^-\left[W_{Lij}^{(x)} P_L + W_{Rij}^{(x)} P_R \right] \tilde{\chi}_j^-\,, \\
\mathcal{L}_{H_x \tilde{\chi}_a^0 \tilde{\chi}_b^0} &= -\frac{g}{2}H_x \bar{\tilde{\chi}}_a^0\left[D_{Lab}^{(x)} P_L + D_{Rab}^{(x)} P_R \right] \tilde{\chi}_b^0\,, \\
\mathcal{L}_{H_x \ell \ell} &= -gH_x \bar{\ell}\left[S_{L,\ell}^{(x)} P_L + S_{R,\ell}^{(x)} P_R \right] \ell\,.
\end{aligned}
\tag{1.77}
$$

The coupling factors here are given in terms of the SUSY-ISS model parameters in App. D.

Summarizing, in this Chapter we have seen that the experimental evidences for neutrino masses have established the need of new physics in order to add neutrino masses to the SM. We have reviewed some popular neutrino mass generation models, paying special attention to two low scale seesaw models, the ISS and the SUSY-ISS models, which add heavy neutrinos with masses at the reach of the LHC. We have discussed in detail the neutrino sector of these models and introduce a new parametrization, the μ_X parametrization, that allows to accommodate neutrino oscillation data while choosing as input parameters the Yukawa coupling matrix and the heavy neutrino mass matrix M_R, which are the most relevant parameters for our forthcoming study of the charged LFV observables.

Chapter 2

Phenomenological implications of low scale seesaw neutrinos on LFV

In this Chapter we revisit some of the relevant phenomenological implications of right-handed neutrinos with TeV scale masses, paying special attention to their lepton flavor violating consequences. After reviewing the experimental status of charged LFV searches, we discuss in detail the LFV radiative and three-body lepton decays in presence of right-handed neutrinos at the TeV scale. Furthermore, we also study other observables that are modified by the new neutrino sector, such as electroweak precision observables, or processes with lepton number violation or lepton flavor universality violation. This Chapter will be very useful and illustrative to learn the general ideas about LFV from TeV right-handed neutrinos and to describe the main points of our analysis, as well as to introduce the set of observables that we will consider as potential constraints when studying maximum allowed predictions for LFV Higgs and Z decays in the forthcoming Chapters. The content of this Chapter, except Section 2.1, is original work of this Thesis. It includes the proposal of new scenarios with suppressed μ-e transitions, the geometrical interpretation of the associated neutrino Yukawa coupling matrix, as well as the phenomenological consequences of these mentioned scenarios. All these new contributions have been published in Refs. [97, 100].

2.1 Experimental status of charged LFV and constraints

Lepton flavor violating processes are forbidden in the SM due to the assumption of massless neutrinos, therefore any observation of lepton flavor violation would automatically imply the presence of new physics beyond the SM. This was the case when LFV was observed in neutrino oscillations, what led to the need of extending the SM to include neutrino masses, as we discussed in Chapter 1. Interestingly, if neutrino masses and mixings are minimally added
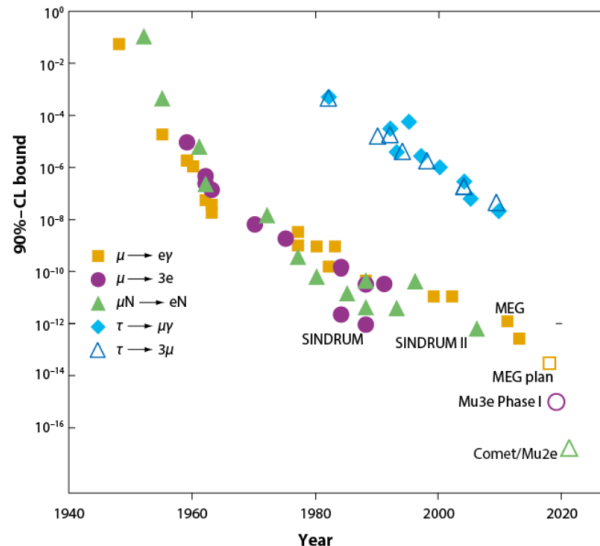
Figure 2.1: Evolution of cLFV transitions upper limits from several experiments, including expected sensitivities for some next generation experiments. Figure borrowed from Ref. [157].

to the SM, they radiatively induce LFV in the charged lepton sector (cLFV), although with extremely small ratios, suppressed by the smallness of the neutrino masses. For instance, using neutrino oscillation data in Eq. (1.6), the predictions for the $\mu \to e\gamma$ ratio are of the order of 10^{-50}. Consequently, a positive experimental signal for cLFV would open a new window for BSM physics and could also help throwing light on the question of what is the mechanism that generates the neutrino masses.

Unfortunately, cLFV has not been observed yet in Nature, although there is an extensive experimental program developing different strategies to look for new physics signals in the charged lepton sector and, indeed, there are already very competitive upper bounds on several cLFV processes. One of the standard searches focuses on the radiative decay of a muon into a electron and a photon, concretely on the $\mu^+ \to e^+\gamma$ channel, which has impressively evolved from the first bound of less than a 10% by Hincks and Pontecorvo [158] in 1947, to the latest upper bound by the MEG collaboration [61] of 4.2×10^{-13} in 2016. We schematically show this evolution in Fig. 2.1, borrowed from Ref. [157]. For a complete historical review see, for instance, Refs. [159, 160]. In the next few years, the upgrade from MEG to MEG-II [161] is expected to improve the sensitivity for this cLFV channel in one order of magnitud. Another possible LFV decay channel of the muon is $\mu \to 3e$, complementary to the $\mu \to e\gamma$ channel and very interesting for many BSM models. The best current upper bound is provided by SINDRUM [162] which sets $\mathrm{BR}(\mu^+ \to e^+e^+e^-) < 1.0 \times 10^{-12}$, although a huge improvement is expected to obtain by the Mu3e experiment [163]. This

Table 2.1: Present upper bounds and future expected sensitivities for cLFV transitions.

LFV Obs.	Present Bound (90%CL)		Future Sensitivity	
BR$(\mu \to e\gamma)$	4.2×10^{-13}	MEG (2016)[61]	6×10^{-14}	MEG-II [161]
BR$(\tau \to e\gamma)$	3.3×10^{-8}	BABAR (2010) [64]	10^{-9}	BELLE-II [65]
BR$(\tau \to \mu\gamma)$	4.4×10^{-8}	BABAR (2010) [64]	10^{-9}	BELLE-II [65]
BR$(\mu \to eee)$	1.0×10^{-12}	SINDRUM (1988) [162]	10^{-16}	Mu3E (PSI) [163]
BR$(\tau \to eee)$	2.7×10^{-8}	BELLE (2010) [164]	$10^{-9,-10}$	BELLE-II [65]
BR$(\tau \to \mu\mu\mu)$	2.1×10^{-8}	BELLE (2010) [164]	$10^{-9,-10}$	BELLE-II [65]
BR$(\tau \to \mu\eta)$	2.3×10^{-8}	BELLE (2010) [165]	$10^{-9,-10}$	BELLE-II [65]
CR$(\mu - e, \text{Ti})$	4.3×10^{-12}	SINDRUM II (2004)[166]	10^{-18}	PRISM (J-PARC) [167]
CR$(\mu - e, \text{Au})$	7.0×10^{-13}	SINDRUM II (2006)[62]		
CR$(\mu - e, \text{Al})$			3.1×10^{-15}	COMET-I (J-PARC)[63]
			2.6×10^{-17}	COMET-II (J-PARC)[63]
			2.5×10^{-17}	Mu2E (Fermilab) [168]

experiment has been proposed at PSI, with the aim of reaching decay rates up to $\mathcal{O}(10^{-15})$ with the current muon beamline and $\mathcal{O}(10^{-16})$ if an upgrade to a High Intensity Muon Beam (HiMB) is achieved at PSI.

Alternatively to muon decays, LFV between muons and electrons has been extensively searched for in $\mu \to e$ conversion experiments. Here, muons are stopped in a thin layer and form muonic atoms, in which a muon can be converted into an electron,

$$\mu^- + N \to e^- + N \,. \tag{2.1}$$

Such a conversion in the field of the nucleus has as clear signal the emission of a monochromatic electron of $E \simeq 100$ MeV, where the precise value depends on the nucleus [169]. Current upper bound comes from the SINDRUM II Collaboration, which is set to 7.0×10^{-13} using gold atoms [62]. Nevertheless, a strong experimental effort is planned in this direction, implying extraordinary expected sensitivities of $\mathcal{O}(10^{-17})$ for the next generation of μ-e conversion experiments, as COMET [63] at J-PARC or Mu2E at Fermilab [168]. Interestingly, these μ-e conversion experiments can be also used to look for a muon conversion into a positron

$$\mu^- + N(A, Z) \to e^+ + N(A, Z - 2) \,, \tag{2.2}$$

in a process that violates, besides lepton flavor, total lepton number in two units. These searches are complementary to other experiments, like $0\nu\beta\beta$, looking for LN violation and, therefore, they are very interesting for testing the Majorana character of the neutrinos. Despite the experimental signal is not as clear as in the μ^--e^- conversions, the SINDRUM II

Figure 2.2: Summary on present LFV τ decays upper limits by the HFLAV group [170].

collaboration was able to set a very compelling upper bound on the $\mu^- + \text{Ti} \rightarrow e^+ + \text{Ca(g.s.)}$ transition of 4.3×10^{-12} at the 90% CL [166]. Furthermore, additional cLFV evidences are been looking for, like $\mu^+ e^- \rightarrow \mu^- e^+$ transitions of muonium atoms. We refer to Ref. [159] for a complete review of cLFV in muon transitions.

In order to study LFV processes in the tau sector, we need to look at B factories. The BABAR collaboration put the most constraining upper bounds of LFV radiative tau decays, setting $\text{BR}(\tau^\pm \rightarrow \mu^\pm \gamma) < 4.4 \times 10^{-8}$ and $\text{BR}(\tau^\pm \rightarrow e^\pm \gamma) < 3.3 \times 10^{-8}$ [64]. On the other hand, BELLE was able to constraint LFV three body decays [164], setting $\text{BR}(\tau^- \rightarrow \mu^- \mu^+ \mu^-) < 2.1 \times 10^{-8}$, $\text{BR}(\tau^- \rightarrow e^- e^+ e^-) < 2.7 \times 10^{-8}$, and similar bounds for mixed combinations of muons and electrons in the final state. The LHCb collaboration has also performed searches for $\tau^- \rightarrow \mu^- \mu^+ \mu^-$ decays, finding an upper bound of 4.6×10^{-8} [171]. This analysis, done with 1fb^{-1} of proton-proton collision at $\sqrt{s} = 7$ TeV and 2fb^{-1} at 8 TeV, already has a sensitivity close to the best current bounds, so we could expect that LHCb can tell us something new about this decay channel in a near future. Moreover, in 2018, the BELLE-II experiment [65] will start its operation with the aim of improving the sensitivities to both type of LFV τ decays in up to two orders or magnitudes. We summarize these current upper bounds, as well as future expected sensitivities, on cLFV transitions in Table 2.1.

Table 2.2: Present upper bounds for some LFV/LNV meson decays. Notice that some of these processes also violate total lepton number.

LFV/LNV Obs.	Present Bound (90%CL)	
$\mathrm{BR}(\pi^0 \to \mu e)$	3.59×10^{-10}	KTeV (2008) [172]
$\mathrm{BR}(K_L \to \mu e)$	4.7×10^{-12}	BNL E871 (1998) [173]
$\mathrm{BR}(K_L \to \pi^0 \mu e)$	7.56×10^{-11}	KTeV (2008) [172]
$\mathrm{BR}(K_L \to \pi^0 \pi^0 \mu e)$	1.64×10^{-10}	KTeV (2008) [172]
$\mathrm{BR}(K^+ \to \pi^+ \mu^+ e^-)$	1.3×10^{-11}	BNL E777/865 (2005) [174]
$\mathrm{BR}(K^+ \to \pi^+ \mu^- e^+)$	5.2×10^{-10}	BNL E865 (2000) [175]
$\mathrm{BR}(K^+ \to \pi^- \mu^+ e^+)$	5.0×10^{-10}	BNL E865 (2000) [175]
$\mathrm{BR}(K^+ \to \pi^- e^+ e^+)$	6.4×10^{-10}	BNL E865 (2000) [175]
$\mathrm{BR}(K^+ \to \pi^- \mu^+ \mu^+)$	1.1×10^{-9}	NA48/2 (2010) [176]
$\mathrm{BR}(B^+ \to K^- \mu^+ \mu^+)$	5.4×10^{-8}	LHCb (2012) [177]
$\mathrm{BR}(B^+ \to \pi^- \mu^+ \mu^+)$	5.8×10^{-8}	LHCb (2012) [177]

An interesting feature about τ leptons is that their mass is large enough to decay into hadrons. This fact opens a new experimental window looking for semileptonic LFV tau decays. We summarize current upper bounds on the LFV τ decays in Fig. 2.2, taken from the Heavy Flavor Average (HFLAV) group [170], which are around 10^{-8}-10^{-7}. Nevertheless, we can expect that BELLE-II will improve these sensitivities in about two orders of magnitude.

Experimental searches of meson decays are also extremely interesting for looking for both LFV and LNV processes. LFV neutral kaon decay, $K_L \to \mu e$, has been extensively searched at experiments (see Ref. [160] for a review) and currently the most stringent bound by the BNL collaboration sets $\mathrm{BR}(K_L \to \mu^\pm e^\mp) < 4.7 \times 10^{-12}$ [173]. Other LFV or LNV K_L or π^0 decays, as well as charged kaon $K^+ \to \pi^\pm \ell_1^+ \ell_2^\mp$ decays, have been searched at several experiments, although no positive signal has been found. We summarize in Table 2.2 some of these upper bounds.

We conclude this overview about cLFV experimental searches by commenting on possible Z and Higgs boson LFV decays. LEP, as a Z factory, searched for LFV $Z \to \ell \ell'$ decays with no luck. Thus, they established upper limits to these processes, as we summarize in Table 2.3, which are still the most constraining ones when a tau lepton is involved. At present, these processes are being searched at LHC and ATLAS is already at the level of LEP results for the LFV Z decay rates, and even better for $Z \to \mu e$ [70]. Thus, we can expect that new LHC runs would help testing these channels. Moreover, the sensitivity to LFV Z decay rates are expected to highly improve at the next generation of colliders In particular, following the discussion in Ref. [49], the future linear colliders are expected to reach sensitivities of 10^{-9} [73, 74], and at a Future Circular e^+e^- Collider (such as FCC-ee (TLEP)[75]), where it

Table 2.3: Present upper bounds at 95% CL on LFV decays of Z and H bosons.

LFV Obs.	Present Bounds (95%CL)			
BR$(Z \to \mu e)$	1.7×10^{-6}	LEP (1995) [71]	7.50×10^{-7}	ATLAS (2014) [70]
BR$(Z \to \tau e)$	9.8×10^{-6}	LEP (1995) [71]		
BR$(Z \to \tau \mu)$	1.2×10^{-5}	LEP (1995) [72]	1.69×10^{-5}	ATLAS (2014) [68]
BR$(H \to \mu e)$	3.5×10^{-4}	CMS (2016) [66]		
BR$(H \to \tau e)$	6.1×10^{-3}	CMS (2017) [67]	1.04×10^{-2}	ATLAS (2016) [68]
BR$(H \to \tau \mu)$	2.5×10^{-3}	CMS (2017) [67]	1.43×10^{-2}	ATLAS (2016) [68]

is estimated that up to 10^{13} Z bosons would be produced, the sensitivities to LFVZD rates could be improved up to 10^{-13}. More recently, the discovery of the Higgs boson has opened new channels for looking for LFV in the charged sector, with LFV H decays $H \to \ell\ell'$. The first search of this kind was done by CMS for the $H \to \tau\mu$ at $\sqrt{s} = 7$ TeV and, interestingly, a 2.4σ excess was found with a best fit value of [69]

$$\mathrm{BR}(H \to \tau\mu) = 8.4^{+3.9}_{-3.7} \times 10^{-3}\,, \tag{2.3}$$

which coincided with a smaller excess of around 1σ at ATLAS. Unfortunately, this excess has not been confirmed with more data at $\sqrt{s} = 8$ TeV neither with the LHC run II. Therefore, both ATLAS and CMS have constraint these ratios at the $\mathcal{O}(10^{-3,-4})$, as summarized in Table 2.3. All these bounds have been obtained using the run-I data at $\sqrt{s} = 7$ and 8 TeV, with the exception of the very recent result by CMS [67], where the upper bounds $\mathrm{BR}(H \to \tau e) < 0.61\%$ and $\mathrm{BR}(H \to \tau\mu) < 0.25\%$ have been set after analyzing 35.9 fb^{-1} of data at $\sqrt{s} = 13$ TeV. These upper bounds improve previous constraints from indirect measurements at LHC [178] by roughly one order of magnitude (see also [179]), and it is close to the previous estimates in [180] that predicted sensitivities of 4.5×10^{-3} (see also, [181]). The future perspectives for LFVHD searches are encouraging due to the expected high statistics of Higgs events at future hadronic and leptonic colliders. Although, to our knowledge, there is no realistic study, including background estimates, of the expected future experimental sensitivities for these kinds of rare LFVHD events, a naive extrapolation from the present situation can be done. For instance, the future LHC runs with $\sqrt{s} = 14$ TeV and total integrated luminosity of first 300 fb^{-1} and later 3000 fb^{-1} expect the production of about 25 and 250 million Higgs events, respectively, to be compared with 1 million Higgs events that the LHC produced after the first runs [182–184]. These large numbers suggest an improvement in the long-term sensitivities to $\mathrm{BR}(H \to \ell_k \bar{\ell}_m)$ of at least two orders of magnitude with respect to the present sensitivity. Similarly, at the planned lepton colliders, like the international linear collider (ILC) with[1] $\sqrt{s} = 1$ TeV and 2.5 ab^{-1}[185], and the

---

[1]We thank J. Fuster for private communication with the updated ILC perspectives.

future electron-positron circular collider (FCC-ee) as the TLEP with $\sqrt{s} = 350$ GeV and 10 ab^{-1}[186], the expectations are of about 1 and 2 million Higgs events, respectively, with much lower backgrounds due to the cleaner environment, which will also allow for a large improvement in LFV Higgs searches with respect to the current sensitivities.

Overall, we see that an incredible experimental effort is being made in searching for charged lepton flavor violating processes. As we said, any positive signal will automatically imply the existence of new physics even beyond the SM model with a minimal ad-hoc addition of neutrino masses. Nowadays, the lack of such a signal has allowed to several experiments to establish upper bounds on this kind of processes, specially in μ-e transitions, where the bounds are in general several orders of magnitude stronger than the equivalent ones for τ-e or τ-μ sectors. Nevertheless, we hope that the expected improved sensitivities for next generation of experiments will find evidences for new physics in the form of charged lepton flavor violation.

2.2 Study of $\ell_m \to \ell_k \gamma$ and $\ell_m \to \ell_k \ell_k \ell_k$ in the ISS

In order to better understand the implications on cLFV phenomenology of the TeV scale right-handed neutrinos, we first explore in this section the LFV lepton decays that, as we see in Table 2.1, are one of the most constrained cLFV observables. Concretely, we will consider the ISS model as a specific realization of low scale seesaw models and study in this section the LFV radiative decays $\ell_m \to \ell_k \gamma$ and the LFV three body decays $\ell_m \to \ell_k \ell_k \ell_k$ with $k \neq m$. The numerical estimations will be done using the full one-loop formulas given in Refs. [90, 187], which we collect in App. A for completeness.

In all the forthcoming study, we will always impose agreement with light neutrino data[2] in Eq. (1.6). For that purpose, we will make use of one of the two parametrizations described in Section 1.3, i.e, the Casas-Ibarra parametrization given in Eq. (1.44) or the μ_X parametrization in Eq. (1.46). By comparing the results when using these two parametrizations we will learn about the advantages and disadvantages of using one parametrization or the other for exploring the parameter space of the model.

We focus first on the LFV radiative decays, since their analytical expressions are simpler and therefore very useful to gain intuition about cLFV processes in this kind of models. All the numerical estimates and plots are made using the full formulas in App. A. Nevertheless, for the purpose of the discussion, we have derived the following simple but useful approximated expression:

$$\text{BR}(\ell_m \to \ell_k \gamma) \approx \frac{\alpha_W^3 s_W^2}{1024\pi^2 m_W^4} \frac{m_{\ell_m}^5}{\Gamma_{\ell_m}} \frac{v^4}{M_R^4} \left| \left(Y_\nu Y_\nu^\dagger \right)_{km} \right|^2 , \tag{2.4}$$

___

[2]We will show our results for the case of a Normal Hierarchy, although similar results have been obtained for an Inverted Hierarchy.
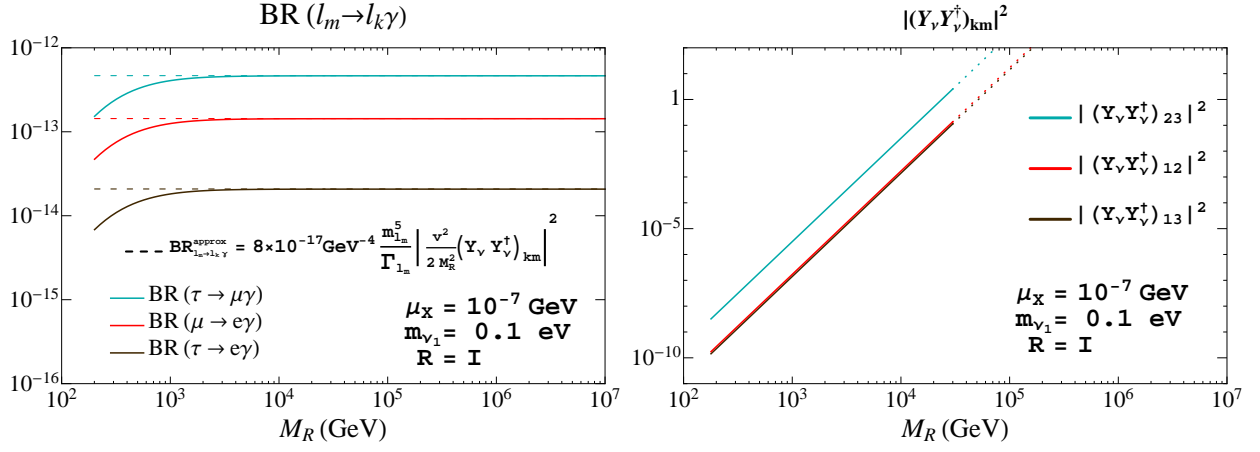
47

Figure 2.3: Comparison of the full one-loop (solid lines) and approximate (dashed lines) rates for the radiative decays $\ell_m \to \ell_k \gamma$ as functions of M_R and their relation with the $(Y_\nu Y_\nu^\dagger)_{km}$ non-diagonal matrix elements in the Casas-Ibarra parametrization. Dotted lines in the right panel indicate non-perturbative Yukawa coupling according to $|Y_\nu^{ij}|^2/4\pi > 1.5$. The other input parameters are set to $\mu_X = 10^{-7}\,\mathrm{GeV}$, $m_{\nu_1} = 0.1\,\mathrm{eV}$, and $R = \mathbb{1}$.

which works quite well for a single heavy mass scale, $M_R = M_R \mathbb{1}$, and in the seesaw limit, $v Y_\nu \ll M_R$, as we will see.

We display in Fig. 2.3 the numerical results for the LFV $\ell_m \to \ell_k \gamma$ decay rates when using the Casas-Ibarra parametrization to accommodate neutrino oscillation data. As explained before, this parametrization builds the Yukawa coupling matrix taking M_R, μ_X, m_ν and the orthogonal matrix R as input parameters in Eq. (1.44). In this first plot, we consider a simplified scenario where both M_R and μ_X matrices are diagonal and degenerate, i.e. $M_R \equiv M_R \mathbb{1}$ and $\mu_X \equiv \mu_X \mathbb{1}$. Concretely, we set $\mu_X = 10^{-7}$ GeV, $m_{\nu_1} = 0.1$ eV and $R = \mathbb{1}$, while we vary M_R from 200 to 10^7 GeV. The left panel of Fig. 2.3 illustrates the numerical predictions of BR($\ell_m \to \ell_k \gamma$) rates in this scenario, using both full analytical expression in Eq. (A.5) (solid lines) and approximated expression in Eq. (2.4) (dashed lines). This plot already shows that the approximated expression works very well for large enough values of M_R, as we anticipated. Therefore, we can make use of Eq. (2.4) in order to understand the analytical dependence of these ratios with de heavy neutrino mass M_R.

In the left panel of Fig. 2.3 we clearly see that these rates saturate to a constant value for increasing M_R, leading to an apparent non-decoupling behavior with the mass of the heavy neutrinos. Nevertheless, this non-decoupling effect is an artifact of the Casas-Ibarra parametrization, since it induces a M_R dependence in the Yukawa coupling matrix, which in principle are independent parameters. More precisely, looking at Eq. (1.44) we can see that the elements of the relevant combination in Eq. (2.4), $(Y_\nu Y_\nu^\dagger)$, grow with M_R approximately

48

as M_R^2, as can be seen in the right panel of Fig. 2.3, and therefore, the final prediction for $\mathrm{BR}(\ell_m \to \ell_k \gamma)$ is constant with M_R.

We will deal with this kind of apparent non-decoupling effects every time we use the Casas-Ibarra parametrization. The growing of the Y_ν coupling with M_R will compensate the suppression coming from the heavy mass scale running in the loops, leading to a fake violation of the decoupling theorem [188]. Nevertheless, we have checked that for constant value of the Yukawa coupling the predictions for the different one-loop processes considered in this thesis decrease with M_R, as can be seen for the LFV radiative decay rates in Eq. (2.4). This expected decoupling behavior will become manifest when using the μ_X parametrization, since it works with Y_ν and M_R as independent input parameters.

Finally, we can compare the results for the LFV radiative decay rates in Fig. 2.3 with the present experimental upper bounds in Table 2.1. We see that, for this choice of parameters, $\mu \to e\gamma$ is the closest one to its upper bound of 4.2×10^{-13} [61]. Being this bound much stronger that the ones on LFV radiative τ decays, we found that $\mu \to e\gamma$ is the most constraining radiative decay for most of the parameter space of the model. Moreover, looking at Table 2.1, we see that in general strongest cLFV bounds will come from processes involving a μ-e transition, not only from the mentioned $\mu \to e\gamma$, but also from $\mu \to eee$ or μ-e transitions in nuclei.

2.2.1 Proposal of scenarios with suppressed μ-e transitions

Motivated by the fact that experimental searches in Table 2.1 show much more constrained cLFV processes in the μ-e sector than in the other τ-μ and τ-e sectors, we look for phenomenological scenarios where μ-e transitions are suppressed. In order to do this, we find more useful to consider the μ_X parametrization instead of the Casas-Ibarra one, since it allow us to consider the Yukawa coupling directly as an input parameter. Looking again at Eq. (2.4), we learn that, for diagonal and degenerate M_R matrix, the relevant Yukawa combination for cLFV processes is $Y_\nu Y_\nu^\dagger$, which is simplified to $Y_\nu Y_\nu^T$ in the case of real matrices[3]. Then, it will be very useful and instructive to consider a geometrical interpretation of the Yukawa matrix, where its entries are interpreted as the components of three generic neutrino vectors in flavor space $(\boldsymbol{n}_e, \boldsymbol{n}_\mu, \boldsymbol{n}_\tau)$,

$$Y_\nu = \begin{pmatrix} Y_{\nu_{11}} & Y_{\nu_{12}} & Y_{\nu_{13}} \\ Y_{\nu_{21}} & Y_{\nu_{22}} & Y_{\nu_{23}} \\ Y_{\nu_{31}} & Y_{\nu_{32}} & Y_{\nu_{33}} \end{pmatrix} \equiv f \begin{pmatrix} \boldsymbol{n}_e \\ \boldsymbol{n}_\mu \\ \boldsymbol{n}_\tau \end{pmatrix}, \tag{2.5}$$

---

[3]In the following derivation μ-e suppressed scenarios, we will assume the situation of having real matrices in order to avoid potential constraints from lepton electric dipole moments.
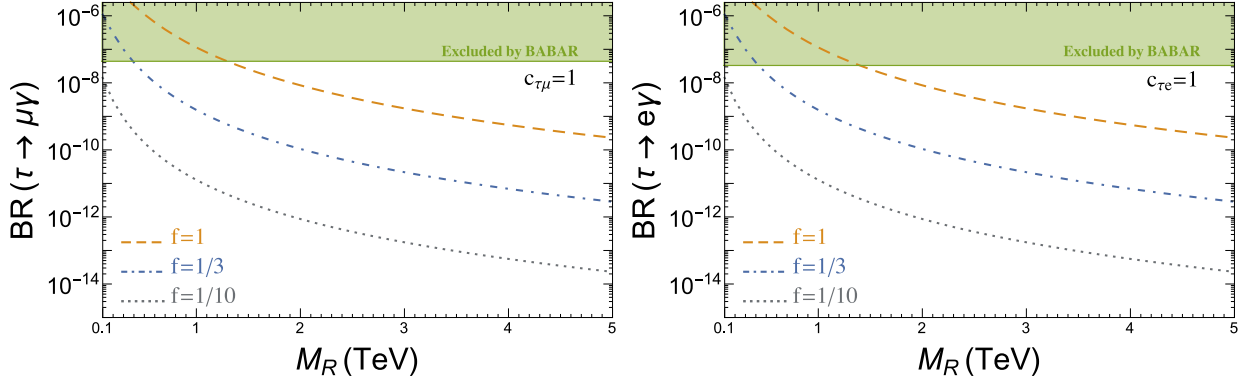
Figure 2.4: Predictions for the BR($\tau\mu\gamma$) and BR($\tau \to e\gamma$) as functions of M_R in the μ_X parametrization. The input Y_ν matrix is written as explained in the text, with different values of the strength parameter f. In the left (right) panel τ-μ (τ-e) transitions are maximized by setting $c_{\tau\mu}(c_{\tau e}) = 1$. The other cosines are set to zero, the modulus $|\boldsymbol{n}_{e,\mu,\tau}| = 1$ and $\mathcal{O} = \mathbb{1}$.

which for the relevant combination in cLFV processes give:

$$Y_\nu Y_\nu^T = f^2 \begin{pmatrix} |\boldsymbol{n}_e|^2 & \boldsymbol{n}_e \cdot \boldsymbol{n}_\mu & \boldsymbol{n}_e \cdot \boldsymbol{n}_\tau \\ \boldsymbol{n}_e \cdot \boldsymbol{n}_\mu & |\boldsymbol{n}_\mu|^2 & \boldsymbol{n}_\mu \cdot \boldsymbol{n}_\tau \\ \boldsymbol{n}_e \cdot \boldsymbol{n}_\tau & \boldsymbol{n}_\mu \cdot \boldsymbol{n}_\tau & |\boldsymbol{n}_\tau|^2 \end{pmatrix}. \tag{2.6}$$

This means that the 9 input parameters determining the Y_ν matrix can be seen as the 3 modulus of these three vectors $(|\boldsymbol{n}_e|, |\boldsymbol{n}_\mu|, |\boldsymbol{n}_\tau|)$, the 3 relative *flavor* angles between them $(\theta_{\mu e}, \theta_{\tau e}, \theta_{\tau\mu})$, with $\theta_{ij} \equiv \widehat{\boldsymbol{n}_i \boldsymbol{n}_j}$, and 3 extra angles $(\theta_1, \theta_2, \theta_3)$ that parametrize a global rotation $\mathcal{O}$ of these 3 vectors that does not change their relative angles. In addition, we have introduced an extra parameter f that characterizes the global Yukawa coupling strength and that will be useful in forthcoming analysis. Since the combination $Y_\nu Y_\nu^T / f^2$ is symmetric, it only depends on 6 parameters that we take to be the 3 modulus $(|\boldsymbol{n}_e|, |\boldsymbol{n}_\mu|, |\boldsymbol{n}_\tau|)$ and the cosine of the three flavor angles $(c_{\mu e}, c_{\tau e}, c_{\tau\mu})$, with $c_{ij} \equiv \cos\theta_{ij}$. The names of the angles are motivated by the fact that the cosine of the angle θ_{ij} controls the LFV transitions in the ℓ_i-ℓ_j sector, which we write in short as LFV$_{\ell_i \ell_j}$. It is interesting to notice that the global rotation $\mathcal{O}$ does not enter in the $Y_\nu Y_\nu^T$ combination and, therefore, it will not affect any of the cLFV processes studied in this work.

Before going to the scenarios with suppressed μ-e transitions, we study in Fig. 2.4 the predictions for the LFV radiative decay rates in terms of the most relevant parameters in this parametrization. In the left panel, we show BR($\tau \to \mu\gamma$) in a scenario where τ-μ transitions are maximized by setting[4] $c_{\tau\mu} = 1$, while they are suppressed in the τ-e and μ-e sectors,

---

[4]We actually set $c_{\tau\mu} = 0.99$ for this plot, since the μ_X parametrization in Eq. (1.46) requests a non-singular Y_ν. Nevertheless, the results for cLFV processes are basically the same as setting $c_{\tau\mu} = 1$.

$c_{\tau e} = c_{\mu e} = 0$. Equivalently, the right panel displays $\mathrm{BR}(\tau \to e\gamma)$ in a scenario where τ-e transitions are favored. Both plots show the dependence of these observables on the heavy neutrino mass scale M_R for several values of the Yukawa coupling strength factor f.

First of all, we see that both observables show the expected decoupling behavior with M_R. This is in contrast with the apparent non-decoupling effects we saw in Fig. 2.3 when using the Casas-Ibarra parametrization. As we explained before, the difference is that now the Yukawa coupling is treated as an independent parameter and, therefore, the dominant dependence on the M_R comes from the mass in the propagators of the right-handed neutrinos running in the loops, whose effects decrease as M_R becomes heavier. On the other hand, the rates are bigger the larger the Yukawa coupling strength f is. Moreover, although not shown here, we have checked that the rates for $\tau \to \mu\gamma$ ($\tau \to e\gamma$) grow with $c_{\tau\mu}$ ($c_{\tau e}$), $|\boldsymbol{n}_\tau|$ and $|\boldsymbol{n}_\mu|$ ($|\boldsymbol{n}_e|$), while being independent of the other parameters, in particular the rotation matrix $\mathcal{O}$. In summary, the full radiative decays rates follow the behavior of the approximate formula in Eq. (2.4).

Second, we learn that the predictions for $\tau \to \mu\gamma$ in the left panel are the same than those for $\tau \to e\gamma$ in the right panel. The reason for this similarity is that they are related by the interchange $\boldsymbol{n}_\mu \leftrightarrow \boldsymbol{n}_e$ in Eq. (2.5) and, therefore, we expect to have basically the same results in both scenarios. Based on this relation, we will show most of our results only for the τ-μ sector, knowing that the conclusions for the τ-e sector can be obtained by just exchanging $\boldsymbol{n}_\mu$ with $\boldsymbol{n}_e$.

Third, we observe that the predictions can reach the present experimental upper bounds from BABAR (see Table 2.1) and, therefore, they will constrain our parameter space when exploring other observables. In particular, for scenarios with favored τ-μ or τ-e transitions, maximum allowed values of $f \sim \mathcal{O}(1\text{-}0.5)$ for $M_R = 1$ TeV and the minimum allowed values for M_R are $\sim \mathcal{O}(1\text{-}2)$ TeV for $f = 1$. In the future, searches at BELLE-II are expected to improve the sensitivity up to 10^{-9} for these channels, so they will be able to prove values of $f \gtrsim 0.3$ for 1 TeV neutrinos.

As we have seen, using this geometrical interpretation of the Yukawa matrix the μ-e suppression can be easily realized by just assuming that $\boldsymbol{n}_e$ and $\boldsymbol{n}_\mu$ are orthogonal vectors, i.e, $c_{\mu e} = 0$. Such a condition defines a family of ISS scenarios that can be parametrized using the following Yukawa matrix:

$$Y_\nu = A \cdot \mathcal{O} \quad \text{with} \quad A \equiv f \begin{pmatrix} |\boldsymbol{n}_e| & 0 & 0 \\ 0 & |\boldsymbol{n}_\mu| & 0 \\ |\boldsymbol{n}_\tau|c_{\tau e} & |\boldsymbol{n}_\tau|c_{\tau\mu} & |\boldsymbol{n}_\tau|\sqrt{1 - c_{\tau e}^2 - c_{\tau\mu}^2} \end{pmatrix}, \qquad (2.7)$$

where $\mathcal{O}$ is the above commented orthogonal rotation matrix, which does not enter in the product $Y_\nu Y_\nu^T$, and f is again the parameter controlling the global strength of the Yukawa coupling matrix. The fact that we are assuming real and non-singular Y_ν imposes the condition $c_{\tau e}^2 + c_{\tau\mu}^2 < 1$. Notice that the Y_ν matrix in Eq. (2.7) is the most general one that
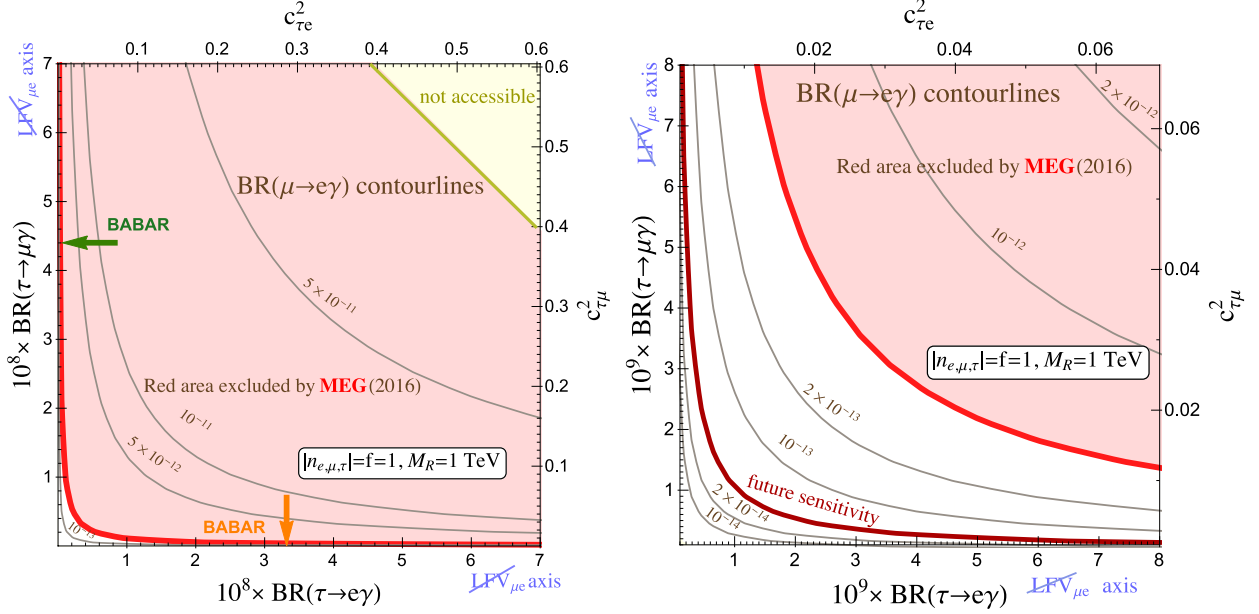
Figure 2.5: Left panel: Contour lines for $\mathrm{BR}(\mu \to e\gamma)$ as a function of $\mathrm{BR}(\tau \to e\gamma)$ and $\mathrm{BR}(\tau \to \mu\gamma)$ rates, for fixed $M_R = 1$ TeV, $|\boldsymbol{n}_{e,\mu,\tau}| = f = 1$ values and varying $c_{\tau e}^2$ and $c_{\tau \mu}^2$ from 0 to 0.6, as shown in the right and top axes. The yellow area represents the region that cannot be accessed with real Yukawa matrices. The red area is excluded by the upper bound on $\mu \to e\gamma$ from MEG, while the orange (green) arrow marks the present upper bound on $\tau \to e\gamma$ ($\tau \to \mu\gamma$) from BABAR, see Table 2.1. Right panel: Zoom on the lower left corner of the plot in the left panel which allows for a better reading of the region allowed by present experimental data. The extra darker red line represents the future expected sensitivity of 4×10^{-14} by MEG-II [161].

satisfies the condition $\left(Y_\nu Y_\nu^T\right)_{\mu e} = 0$.

We can now explore the predictions for $\mathrm{BR}(\ell_m \to \ell_k \gamma)$ when this kind of scenarios is considered. Looking at Eq. (2.4), we can easily see that the LFV radiative decays of the τ lepton depend on the most relevant parameters, f, M_R and $c_{\tau \ell}$ as follows:

$$\mathrm{BR}(\tau \to \ell\gamma) \sim \frac{f^4}{M_R^4} \, c_{\tau \ell}^2 \quad \text{with } \ell = e, \mu. \tag{2.8}$$

The case of $\mu \to e\gamma$ is different, since the assumption $c_{\mu e} = 0$ cancels the leading order contribution given by the approximate formula in Eq. (2.4), and therefore the first relevant contribution in this observable is of higher order in the expansion series in powers of the Yukawa coupling over M_R. Specifically it is of the type $(Y_\nu Y_\nu^T Y_\nu Y_\nu^T)/M_R^8$. Consequently, it

is suppressed with respect to Eq. (2.8) and the predicted rates for this observable turn out to depend on the product of both $c_{\tau e}$ and $c_{\tau \mu}$:

$$\mathrm{BR}(\mu \to e\gamma) \sim \frac{f^8}{M_R^8}\, c_{\tau e}^2 c_{\tau \mu}^2. \tag{2.9}$$

Therefore, in order to define a scenario where all μ-e transitions are completely suppressed, i.e., $\left(Y_\nu Y_\nu^T\right)_{\mu e} = \left(Y_\nu Y_\nu^T Y_\nu Y_\nu^T\right)_{\mu e} = \cdots = 0$, we see that the condition $c_{\mu e} = 0$ is not enough and that we also need $c_{\tau e} = 0$ or $c_{\tau \mu} = 0$.

These behaviors of the $\mathrm{BR}(\ell_m \to \ell_k \gamma)$ rates are numerically illustrated in Fig. 2.5, where the full one-loop formulas in App. A have been used. These plots show contourlines for $\mathrm{BR}(\mu \to e\gamma)$ in terms of the other radiative decay rates. It also displays the above commented correlations between the $\mathrm{BR}(\tau \to \mu\gamma)$ and $\mathrm{BR}(\tau \to e\gamma)$ rates and the parameters $c_{\tau \mu}$ and $c_{\tau e}$, respectively. The contour lines for $\mathrm{BR}(\mu \to e\gamma)$ are obtained by varying $c_{\tau \mu}^2$ and $c_{\tau e}^2$ within the interval $(0, 0.6)$, which in turn provide predictions for $\mathrm{BR}(\tau \to \mu\gamma)$ and $\mathrm{BR}(\tau \to e\gamma)$ that are represented in the vertical and horizontal axes respectively. This is for the simple case with $|\boldsymbol{n}_{e,\mu,\tau}| = f = 1$, $M_R = 1$ TeV and $\mathcal{O} = \mathbb{1}$ (although we checked again that the rates do not depend on $\mathcal{O}$), but similar qualitative conclusions can be obtained for other choices of these parameters. Notice that the above mentioned condition of $c_{\tau e}^2 + c_{\tau \mu}^2 < 1$ from the Yukawa matrix in Eq. (2.7) makes the yellow area, where $c_{\tau e}^2 + c_{\tau \mu}^2 \geq 1$, not accesible in our analysis. We also find that the rates for $\tau \to \mu\gamma$ ($\tau \to e\gamma$) can in general be large, for the values of the parameters selected in this plot, of the order of the present upper bound from BaBar [64], marked here with a green (orange) arrow, and that they depend just on $c_{\tau \mu}^2$ ($c_{\tau e}^2$), in agreement with the approximate expression in Eq. (2.8).

We also learn that the predictions for $\mathrm{BR}(\mu \to e\gamma)$ are between 3 and 4 orders of magnitude smaller than the τ radiative decay rates, as expected from Eq. (2.9). Nevertheless, they are still above the upper bound from the MEG experiment for most of the parameter space. In fact, the MEG bound excludes everything but the area close to the axes, since the $\mathrm{BR}(\mu \to e\gamma)$ goes asymptotically to zero when approaching the axes, as can be seen in the zoom over the lower left corner shown in the right panel of Fig. 2.5. When lying just on top of these axes, the predictions for $\mathrm{BR}(\mu \to e\gamma)$ completely vanish, as seen in Eq. (2.9), implying that $\mathrm{BR}(\tau \to e\gamma)$ must be small in order to allow for large $\mathrm{BR}(\tau \to \mu\gamma)$, and viceversa.

Therefore, we can identify our phenomenological scenarios with suppressed μ-e transitions, which we will refer to as ISS-$\mathrm{LFV}_{\mu e}$, with the two axes in Fig. 2.5. We then consider two classes of scenarios: the TM scenarios along the $\mathrm{LFV}_{\tau \mu}$ axis ($c_{\tau e} = 0$) that may give sizable rates for τ-μ transitions, but always give negligible contributions to $\mathrm{LFV}_{\mu e}$ and $\mathrm{LFV}_{\tau e}$; and the TE scenarios along the $\mathrm{LFV}_{\tau e}$ axis ($c_{\tau \mu} = 0$) that may lead to large rates only for the τ-e transitions. In table 2.4 we list some specific examples that we will use along this Thesis for the numerical estimates of our selected TM scenarios. Equivalent examples for the

Table 2.4: TM scenarios for numerical estimates of large τ-μ transitions. Notation '$\simeq$' means $c_{\tau\mu} = 0.99$ instead of 1 in order to have non-singular Y_ν matrices, see Eq. (1.46). The notation $Y_{\tau\mu}^{(1-3)}$ corresponds to the original one introduced in Ref. [97]. Equivalent TE scenarios are easily obtained by exchanging μ and e in these TM ones.

Scenario Name	$c_{\tau\mu}$	$|\boldsymbol{n}_e|$	$|\boldsymbol{n}_\mu|$	$|\boldsymbol{n}_\tau|$	Example
TM-1	$1/\sqrt{2}$	1	1	1	$Y_\nu = f \begin{pmatrix} 1 & 0 & 0 \\ 0 & 1 & 0 \\ 0 & 1/\sqrt{2} & 1/\sqrt{2} \end{pmatrix}$
TM-2	1	1	1	1	$Y_\nu \simeq f \begin{pmatrix} 1 & 0 & 0 \\ 0 & 1 & 0 \\ 0 & 1 & 0 \end{pmatrix}$
TM-3	$1/\sqrt{2}$	0.1	1	1	$Y_\nu = f \begin{pmatrix} 0.1 & 0 & 0 \\ 0 & 1 & 0 \\ 0 & 1/\sqrt{2} & 1/\sqrt{2} \end{pmatrix}$
TM-4	1	0.1	1	1	$Y_\nu \simeq f \begin{pmatrix} 0.1 & 0 & 0 \\ 0 & 1 & 0 \\ 0 & 1 & 0 \end{pmatrix}$
TM-5	1	$\sqrt{2}$	1.7	$\sqrt{3}$	$Y_\nu \equiv Y_{\tau\mu}^{(1)} = f \begin{pmatrix} 0 & 1 & -1 \\ 0.9 & 1 & 1 \\ 1 & 1 & 1 \end{pmatrix}$
TM-6	1/3	$\sqrt{2}$	$\sqrt{3}$	$\sqrt{3}$	$Y_\nu \equiv Y_{\tau\mu}^{(2)} = f \begin{pmatrix} 0 & 1 & 1 \\ 1 & 1 & -1 \\ -1 & 1 & -1 \end{pmatrix}$
TM-7	0.1	$\sqrt{2}$	$\sqrt{3}$	1.1	$Y_\nu \equiv Y_{\tau\mu}^{(3)} = f \begin{pmatrix} 0 & -1 & 1 \\ -1 & 1 & 1 \\ 0.8 & 0.5 & 0.5 \end{pmatrix}$
TM-8	1	1/2	1/3	1/4	$Y_\nu \simeq f \begin{pmatrix} 1 & 0 & 0 \\ 0 & 0.5 & 0 \\ 0 & 0.08 & 0.32 \end{pmatrix}$
TM-9	0.77	0.1	0.46	$\sqrt{2}$	$Y_\nu = f \begin{pmatrix} 0.1 & 0 & 0 \\ 0 & 0.46 & 0.04 \\ 0 & 1 & 1 \end{pmatrix}$
TM-10	0.64	0.1	0.94	$\sqrt{2}$	$Y_\nu = f \begin{pmatrix} 0 & 0.1 & 0 \\ 0.94 & 0 & 0.08 \\ 1 & 0 & -1 \end{pmatrix}$
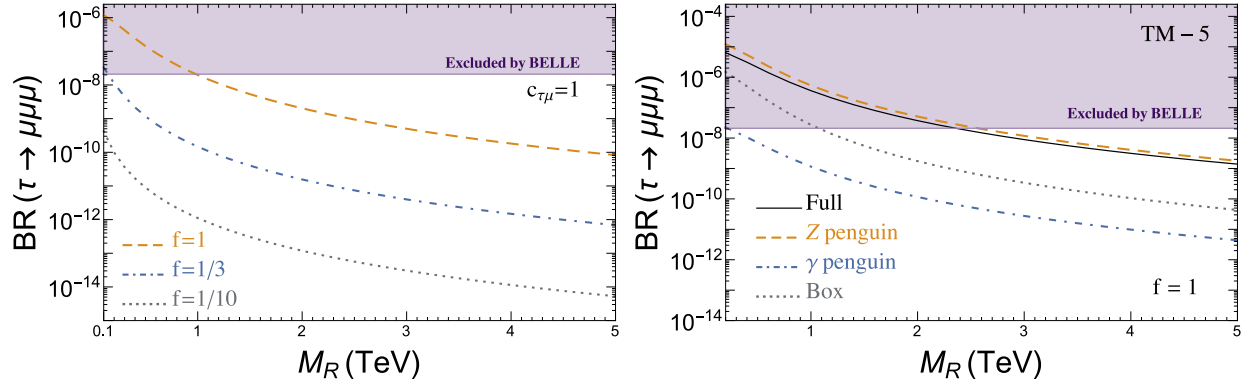
Figure 2.6: BR($\tau \to \mu\mu\mu$) as a function of M_R in two TM-like scenarios with $c_{\tau\mu} = 1$ and $c_{\tau e} = 0$. Left panel: Full predictions for $|\boldsymbol{n}_{e,\mu,\tau}| = 1$ and three values of f. Right panel: Full prediction (solid line) in the TM-5 scenario with $f = 1$, decomposed in its contributions from γ penguin (blue dot-dashed), boxes (gray dotted) and Z penguin (yellow dashed), the dominant one. Purple shadowed area is excluded by BELLE.

TE scenarios are obtained by exchanging μ and e everywhere in the previous TM scenarios. Notice that we introduced the notation $Y_{\tau\mu}^{(1)}$, $Y_{\tau\mu}^{(2)}$ and $Y_{\tau\mu}^{(3)}$ for the Yukawa matrices in the scenarios TM-5, TM-6 and TM-7, respectively, which corresponds to the original notation in Ref. [97]. We will indistinguishably use both notations along this Thesis.

We can next study the predictions for the LFV three body decays $\ell_m \to \ell_k\ell_k\ell_k$ in this kind of scenarios. Fig. 2.6 shows the BR($\tau \to \mu\mu\mu$) rates in a TM-like scenario of maximized τ-μ transitions, i.e, $c_{\tau\mu} = 1$ and $c_{\tau e} = c_{\mu e} = 0$, although the general conclusions are the same for BR($\tau \to eee$) in a TE scenario. In the left panel, the dependence of the full decay rate is displayed as a function of M_R for different values of f. We clearly see that the rates are again large, within present and future experimental sensitivities, specially for large f values and low M_R. For example, in this particular case of $c_{\tau\mu} = 1$, present bound from BELLE of BR($\tau \to \mu\mu\mu$) $< 2.1 \times 10^{-8}$ excludes large couplings of $f \gtrsim 1$ for heavy neutrinos below 1 TeV. Future expected sensitivities at BELLE-II may be able to probe values of M_R up to 2-3 TeV for $f = 1$.

As in the case of the radiative decay $\tau \to \mu\gamma$, we see again that the rates decrease with increasing M_R, manifesting the decoupling behavior expected when using the μ_X parametrization. Although we do not show all the plots here, we have explored how the rates for $\tau \to \mu\mu\mu$ depend on the most relevant parameters finding that they grow with f, $c_{\tau\mu}$, $|\boldsymbol{n}_\tau|$ and $|\boldsymbol{n}_\mu|$, whereas they are independent of $c_{\tau e}$, $c_{\mu e}$, $|\boldsymbol{n}_e|$ and the rotation $\mathcal{O}$.

Nevertheless, the dependence of $\tau \to \mu\mu\mu$ on these parameters is not exactly equal to that of $\tau \to \mu\gamma$, since the former receives contributions from different type of diagrams,

namely, the γ-penguin, Z-penguin and box diagrams. In order to better understand this, we display separately the contributions from each type of diagram to the total decay rate in the right panel of Fig. 2.6. We choose the TM-5 scenario from Table 2.4, although similar qualitative results are found for other TM scenarios. The dependences on f, M_R and $c_{\tau\mu}$ are slightly different for each of the contributions, leading to a more complicated dependence for the total decay rate. Moreover, we see that, for this value of f, the dominant contribution is mostly coming from the Z-penguin. This fact will be important when studying the LFV Z decay rates $Z \to \ell_k \bar{\ell}_m$ in Chapter 4.

In the rest of this Thesis we will consider the two parametrizations described in Chapter 1. We will consider more generic searches using the Casas-Ibarra parametrization for scanning the ISS parameter space, although in that case it will be difficult to access to these particular directions and, therefore, to conclude on maximum allowed rates. Therefore, we will focus on the scenarios in Table 2.4 for studying maximum allowed LFV rates involving τ leptons making sure that we are not generating potentially constrained μ-e transitions.

2.3 Other implications from low scale seesaw neutrinos

Generically, the addition of heavy Majorana neutrinos to the particle content of the SM has a phenomenological impact on several low energy observables, via their mixing with the active neutrinos. These observables can be related to lepton flavor violation, as the ones above studied, lepton number violation, lepton universality or others. Therefore, we want to ensure that our forthcoming analysis in Chapters 3, 4 and 5 comply with the relevant theoretical and experimental constraints, in all the regimes of the considered right handed neutrino masses. We briefly discuss in the following the constraints that we have found to be the most relevant ones for the present thesis and which we consequently include in our analysis. For this study we have used our own *Mathematica* code which includes all the relevant formulas for the constraining observables that are taken from the literature and that we include in App. B for completeness.

2.3.1 Lepton flavor universality

Leptonic and semileptonic decays of pseudoscalar mesons (K, D, D_s, B) could put important constraints on the mixing between the active and the sterile neutrinos in the ISS model, as it has been shown in Refs. [26, 27]. In particular, the most severe bounds arise from the violation of lepton universality in leptonic kaon decays[5]. Following these references, we

---

[5]We do not consider other lepton universality tests in view of the fact that they give similar bounds, as in the case of Δr_π, or they are less constraining, like the ones involving τ leptons [27].
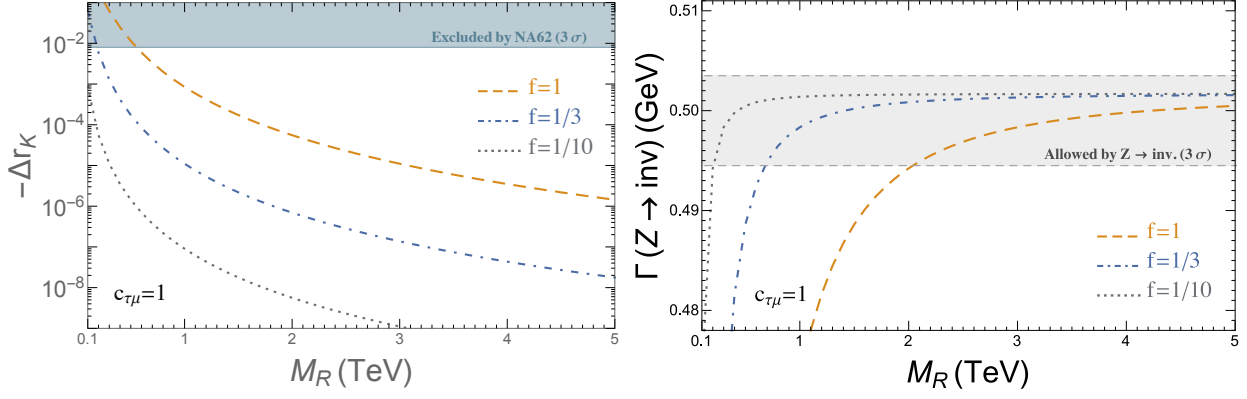
Figure 2.7: Predictions for Δr_k and $\Gamma(Z \to \text{inv.})$ as functions of M_R. In both plots we set $|\boldsymbol{n}_{e,\mu,\tau}| = 1$, $c_{\tau\mu} = 1$, $c_{\mu e} = c_{\tau e} = 0$, $\mathcal{O} = \mathbb{1}$ and consider three values of f. The shadowed band in the left (right) plot is the present excluded (allowed) region at 3σ.

consider the contributions of the sterile neutrinos to the Δr_k parameter, defined as:

$$\Delta r_k = \frac{R_K}{R_K^{\text{SM}}} - 1 \quad \text{with} \quad R_K = \frac{\Gamma(K^+ \to e^+\nu)}{\Gamma(K^+ \to \mu^+\nu)}. \tag{2.10}$$

The comparison of the theoretical calculation in the SM [189, 190] with the recent measurements from the NA62 collaboration [191, 192] shows that the experimental measurements agree with the SM prediction within 1σ:

$$\Delta r_k = (4 \pm 4) \times 10^{-3}. \tag{2.11}$$

We compute the new physics contributions to Δr_k using the formulas listed in App. B that we take from [26] and compare the results with the bound in Eq. (2.11) at the 3σ level.

We display in Fig. 2.7 our numerical findings using the μ_X parametrization. In particular, we choose for this plot a maximized τ-μ scenario with $c_{\tau\mu} = 1$, $c_{\tau e} = c_{\mu e} = 0$, $|\boldsymbol{n}_{e,\mu,\tau}| = 1$, $\mathcal{O} = \mathbb{1}$ and three different values of f. We see that Δr_k is always negative, meaning that $R_K < R_K^{SM}$. Nevertheless, R_K tends to R_K^{SM} for large values of M_R, as the new physics effects decouple with the heavy scale. We also see that the deviations from the SM values are larger for larger values of f, implying that the bound from NA62 can exclude the parameter space region of low M_R and large f. Furthermore, we have found that this observable is also independent of the rotation matrix $\mathcal{O}$ and very sensitive to the modulus $|\boldsymbol{n}_e|$ and $|\boldsymbol{n}_\mu|$, as expected. Actually, the bound from this observable becomes an important constraint at low values of M_R when the ratio between $|\boldsymbol{n}_e|$ and $|\boldsymbol{n}_\mu|$ is different from one.

2.3.2   The invisible decay width of the Z boson

The invisible decay width of the Z boson puts very strong constraints on how many neutrinos with masses below m_Z are present. The Z invisible decay width was measured in LEP to be [193]:

$$\Gamma(Z \to \text{inv.})_{\text{Exp}} = 499 \pm 1.5 \text{ MeV}, \tag{2.12}$$

which is about 2σ below the SM prediction:

$$\Gamma(Z \to \text{inv.})_{\text{SM}} = \sum_\nu \Gamma(Z \to \nu\bar{\nu})_{\text{SM}} = 501.69 \pm 0.06 \text{ MeV}. \tag{2.13}$$

Although we are not considering the possibility of having $m_N < m_Z$ here, the presence of sterile neutrinos affects the tree level predictions of the Z invisible width even if they are above the kinematical threshold, since they modify the couplings of the active neutrinos to the Z boson. We compute the tree level predictions using the formulas provided in Ref. [27], which we collect in App. B for completeness, and we further include the ρ parameter that accounts for the part of the radiative corrections coming from SM loops, *i.e.*,

$$\Gamma(Z \to \text{inv.})_{\text{ISS}} = \sum_{\substack{i,j=1 \\ i \leq j}}^{3} \Gamma(Z \to n_i n_j)_{\text{ISS}} = \rho\,\Gamma(Z \to \text{inv.})_{\text{ISS}}^{\text{tree}}, \tag{2.14}$$

where n_i runs over all kinematically allowed neutrinos and ρ is evaluated as:

$$\rho = \frac{\Gamma(Z \to \text{inv.})_{\text{SM}}}{\Gamma(Z \to \text{inv.})_{\text{SM}}^{\text{tree}}}. \tag{2.15}$$

We have also estimated the size of the extra loop corrections induced by the new heavy neutrino states using the formulas of Ref. [194] and found out that they are numerically very small compared with the SM loop corrections, in agreement with Ref. [194], and therefore we will neglect them in the following.

We show our numerical results as a function of M_R in Fig. 2.7, for $c_{\tau\mu} = 1$ and three values of f. We see again that the deviations from the SM value decrease with M_R while they grow with f. Moreover, we found that the Z invisible width only depends on M_R, f and the modulus $|\boldsymbol{n}_{e,\mu,\tau}|$, while it is not dependent on $\mathcal{O}$ and on the flavor angles $(c_{\tau\mu}, c_{\tau e})$, as it was expected, since when adding all the possible neutrino final states in Eq. (2.14) the dependence on $\mathcal{O}$ and on the flavor angles appearing in each channel disappears in the sum. When comparing with data we require our predictions to be within the 3σ experimental band (Eq. (2.12)). As we can see in Fig. 2.7, the Z invisible width provides in general quite strong constraints, indeed comparable or even tighter in some cases than the previous constraints from the LFV lepton decays. For instance, for this scenario with $c_{\tau\mu} = 1$ and $f = 1$, this observable also excludes M_R values lower than around 1-2 TeV, similar to the constraints from $\tau \to \mu\gamma$ and $\tau \to \mu\mu\mu$.
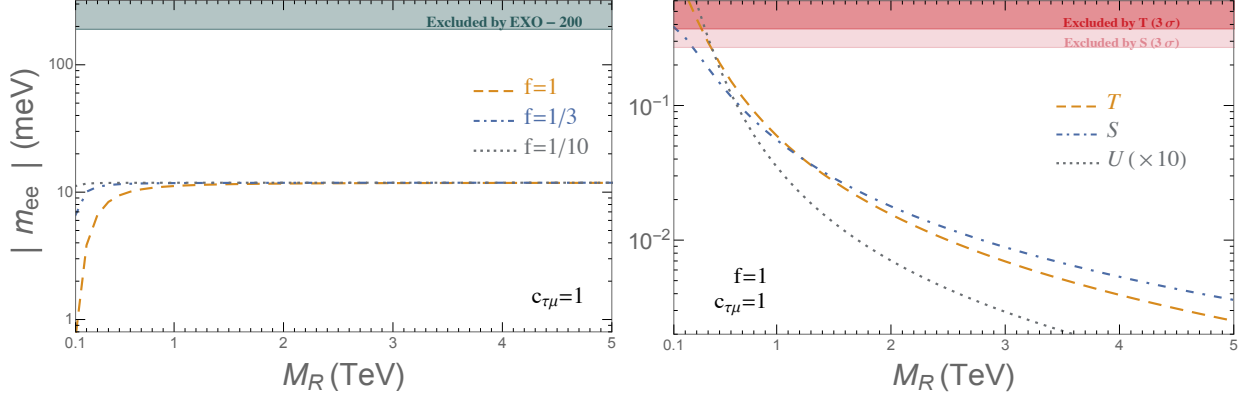
Figure 2.8: Predictions for $|m_{ee}|$ and the Electroweak Precision Parameters S, T, U (the latter enhanced by a factor of 10 to see it more clearly) as functions of M_R. In both plots we set $|\boldsymbol{n}_{e,\mu,\tau}| = 1$, $c_{\tau\mu} = 1$, $c_{\mu e} = c_{\tau e} = 0$, $\mathcal{O} = \mathbb{1}$ and for three different values of f. The shadowed bands are the present excluded regions at 3σ.

2.3.3 Neutrinoless double beta decay

Models that introduce single neutrinos with Majorana mass terms allow for lepton number violating processes, such as neutrinoless double beta decay[195]. Within the ISS framework with 6 sterile fermions added to the SM particle content, the effective neutrino mass m_{ee} is given by [30, 151, 196]

$$m_{ee} \simeq \sum_{i=1}^{9}(B_{en_i})^2 \, p^2 \frac{m_{n_i}}{p^2 - m_{n_i}^2} \simeq \left(\sum_{i=1}^{3}(B_{en_i})^2 \, m_{n_i}\right) + p^2 \left(\sum_{i=4}^{9}(B_{en_i})^2 \, \frac{m_{n_i}}{p^2 - m_{n_i}^2}\right), \quad (2.16)$$

where $p^2 \simeq -(125 \text{ MeV})^2$ is an average estimate over different values from different decaying nucleus of the virtual momentum of the neutrino exchanged in the process.

Despite current experiments are searching for neutrinoless double beta decay, it has not been observed yet. This lack of signal has allowed to the experiments with highest sensitivity such as GERDA [197], EXO-200 [198, 199] and KamLAND-ZEN [200] to set strong bounds on the neutrino effective mass. These bounds on the effective neutrino Majorana mass in Eq. (2.16) lie in the range

$$|m_{ee}| \lesssim 140 \text{ meV} - 700 \text{ meV}. \quad (2.17)$$

In our analysis, we will apply the most recent constraint of $|m_{ee}| \lesssim 190$ meV from Ref. [199].

Fig. 2.8 displays the behavior of m_{ee} with M_R for different values of the Yukawa strength f. As can be seen in this plot, a maximum value of $|m_{ee}| \sim 10$ meV is reached at large $M_R \gtrsim 1$ TeV and for all studied values of f. We have checked that this asymptotic value

depends linearly on the mass of the light active neutrinos, i.e.:

$$m_{\nu_1} \sim 0.01(0.1)\text{eV} \rightarrow |\text{m}_{\text{ee}}| \sim 0.01(0.1)\text{eV}\,. \tag{2.18}$$

As a conclusion, we learn that the prediction for this observable will be below the current experimental bound and, therefore, it will not impose an important constraint to our parameter space.

2.3.4 Electroweak precision observables

The addition of new physics in the neutrino sector will, in general, modify the prediction of Electroweak Precision Observables (EWPO), which are well determined by experiments. We take into account the constraints to the ISS model from EWPO by computing the S, T and U parameters [201] and comparing our predictions to the experimental results [193]:

$$S = -0.03 \pm 0.10\,, \qquad T = 0.01 \pm 0.12\,, \qquad U = 0.05 \pm 0.10\,. \tag{2.19}$$

We use the formulas from Ref. [202] (which we report in App. B) and compare them with the 3σ experimental bands.

We show in Fig. 2.8 the prediction for S, T and U versus M_R, choosing again a scenario with maximized τ-μ transitions. As can be seen, the predictions rapidly decrease with M_R and, in consequence, the constraints from these observables are in general weaker than from the LFV lepton decays and from the Z invisible width. In this an most of the studied scenarios, we have found that the most constraining EWPO is the T parameter and next, although quite close, the S parameter. For instance, for $f = 1$ and $c_{\tau\mu} = 1$ we find that M_R below around 300 GeV are excluded by T.

2.3.5 Heavy neutrino decay widths

In this Thesis, we are considering sizable neutrino Yukawa couplings, so we should check that they are still within the perturbative regime. In order to impose perturbativity we will either choose a direct constraint on the maximum allowed size of the Yukawa matrix entries like, for instance, $|Y_\nu^{ij}|^2/(4\pi) < 1$ or, alternatively, we will apply a constraint on an observable that grows with this Yukawa coupling, like it is the case of the total width of the heavy neutrinos. When choosing the second method, we will require that the total decay width of each heavy neutrino is always somehow smaller than the corresponding heavy neutrino mass.

The computation of the total decay width, in the limit $M_R \gg m_D$ that we work with, is reduced to a few possible decay channels. In this limit, the masses of all the heavy neutrinos are almost degenerate, close to M_R with small differences of $\mathcal{O}(m_D^2 M_R^{-1})$
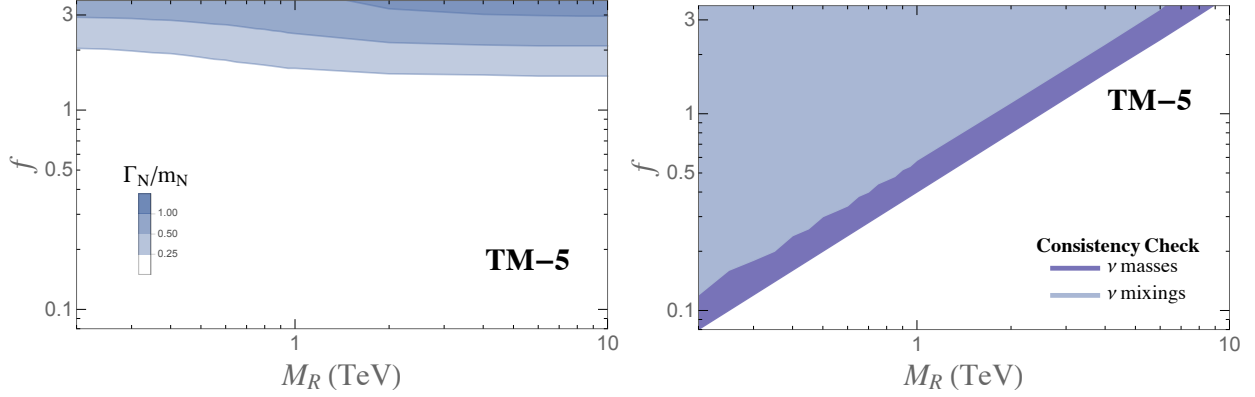
Figure 2.9: Theoretical constraints from the requirement of perturbativity (three plots on the left) and from the consistency of the μ_X parametrization (three plots on the right), for the scenario TM-5. The regions excluded by the constraints are the shadowed areas.

between the different pseudo-Dirac pairs and, therefore, their potential decays into other heavy neutrinos are suppressed. In consequence, the dominant decay channels are simply $N_j \to Z\nu_i, H\nu_i$ and $W^\pm \ell_i^\mp$, and the total neutrino width can be then easily computed by adding the corresponding partial widths of these four decays. The partial decay width of these decay channels are given by:

$$\Gamma_{N_j \to W\ell_i} = \frac{\sqrt{\left(m_{N_j}^2 - m_{\ell_i}^2 - m_W^2\right)^2 - 4m_{\ell_i}^2 m_W^2}}{16\pi m_{N_j}^3} \left|\overline{F_W}\right|^2, \tag{2.20}$$

with similarly expressions for the other channels and with the following form factors, correspondingly:

$$\left|\overline{F_H}\right|^2 = \frac{g^2 m_{N_j}^4}{4m_W^2}\left\{(1 - x_i)^2\left[(1 - x_i)^2 - x_H\right]\left|C_{ij}\right|^2 + 4\sqrt{x_i}\left(2 + 2x_i - x_H\right)\left(\mathrm{Re}C_{ij}\right)^2\right\}$$

$$\left|\overline{F_Z}\right|^2 = \frac{g^2 m_{N_j}^4}{4m_W^2}\left\{\left[(1 - x_i)^2 + x_Z\left(1 + x_i - 6\sqrt{x_i}\right) - x_Z^2\right]\left|C_{ij}\right|^2 + 12x_Z\sqrt{x_i}\left(\mathrm{Re}C_{ij}\right)^2\right\}$$

$$\left|\overline{F_W}\right|^2 = \frac{g^2 m_{N_j}^4}{4m_W^2}\left|B_{\ell_i N_j}\right|^2\left\{(1 - x_i)^2 + x_W(1 + x_i) - 2x_W^2\right\}, \tag{2.21}$$

where $x_i \equiv m_{\ell_i}^2/m_{N_j}^2$, $x_H \equiv m_H^2/m_{N_j}^2$, $x_Z \equiv m_Z^2/m_{N_j}^2$ and $x_W \equiv m_W^2/m_{N_j}^2$. The total width is then computed as

$$\Gamma_{N_j} = \sum_{i=1}^{3}\left(\Gamma_{N_j \to h\nu_i} + \Gamma_{N_j \to Z\nu_i} + 2\,\Gamma_{N_j \to W^+ l_i^-}\right) \tag{2.22}$$

When summing over all flavors, $i = 1, 2, 3$, in the final state the four ratios turn out to be approximately equal [96]:

$$\text{BR}(N_j \to H\nu) = \text{BR}(N_j \to Z\nu) = \text{BR}(N_j \to W^+\ell^-) = \text{BR}(N_j \to W^-\ell^+) = 25\% \,. \quad (2.23)$$

We have explored three different assumptions to comply with the perturbative unitary condition. In particular we have taken:

$$\frac{\Gamma_{N_i}}{m_{N_i}} < 1, \frac{1}{2}, \frac{1}{4} \quad \text{for } i = 1, \ldots, 6. \quad (2.24)$$

The results for the TM-5 scenario from Table 2.4 are displayed in Fig. 2.9, although similar qualitative results are found for other scenarios. Here, we show the areas in the (M_R, f) plane that are excluded by the different assumptions in Eq. (2.24). We find that this perturbativity requirement is not much sensitive to M_R, giving an excluded area in the (M_R, f) plane that is a band nearly horizontal and located at the top, which constrains basically just the size of the global Yukawa coupling f, in the most restricted scenarios, to be below order 2-3.

For the rest of this Thesis, we will take the second choice, $1/2$, in Eq. (2.24) when we decide to use heavy neutrino widths as perturbativity criteria.

2.3.6   Validity range of the μ_X parametrization

As explained in Chapter , one of the novelties of this Thesis is the introduction and use of the μ_X parametrization as tool for exploring the model parameter space being always in agreement with oscillation data. In order to check the validity range of this parametrization, we require that both the predicted light neutrino mass squared differences and the neutrino mixing angles that we obtain from the diagonalization of the full neutrino mass matrix in Eq. (1.35), lie within the 3σ experimental bands [131, 203–206].

More specifically, we demand that the corresponding entries of the U_ν matrix that refer to the light neutrinos sub-block agree with the 3σ range given in Ref. [131]:

$$|U_{\text{PMNS}}^{3\sigma}| = \begin{pmatrix} 0.801 \to 0.845 & 0.514 \to 0.580 & 0.137 \to 0.158 \\ 0.225 \to 0.517 & 0.441 \to 0.699 & 0.614 \to 0.793 \\ 0.246 \to 0.529 & 0.464 \to 0.713 & 0.590 \to 0.776 \end{pmatrix} \,. \quad (2.25)$$

We show in Fig. 2.9 the predictions for the constraints found in the (M_R, f) plane for the TM-5 scenario. As can be seen in this figure, the bounds obtained from the constraints on the active neutrinos squared mass differences are in this scenario stronger than the ones from the light neutrino mixing matrix entries. For other scenarios, like TM-8, we have checked that this can be reversed, *i.e.* the constraints from the neutrino mixings can be stronger than from the neutrino masses. Additionally, we have also compared the range of validity

of this parametrization for two values of the input lightest neutrino mass, 0.1eV and 0.01eV (the chosen value for Fig. 2.9) and we have concluded that the μ_X-parametrization works better for the case with a smaller value of the light neutrino mass.

In general, we found that the area in the (M_R, f) parameter space that is allowed by all the experimental bounds above studied is also allowed by the consistency checks of the μ_X parametrization, meaning that the parametrization works well for the parameter space allowed by data. Nevertheless, the validity of this parametrization can be improved by considering next order contributions to M_{light} in Eq. (1.40), as it was done in Ref. [207].

Summarizing, in this Chapter we have learnt that the presence of right-handed neutrinos at the TeV scale can have a large impact in many low energy observables if their couplings are sizable. Since the aim of this Thesis is to study LFV consequences of these ν_R fields, we focused mostly in LFV radiative and three-body decays of the leptons, i.e, $\ell_m \to \ell_k \gamma$ and $\ell_m \to \ell_k \ell_k \ell_k$ with $k \neq m$. This study allowed us to acquire some general ideas about LFV processes in this kind of models, to discuss the advantages and disadvantages of using the two parametrizations described in Chapter 1, as well as to introduce the phenomenological TM and TE scenarios in Table 2.4, where the experimentally most constrained μ-e transitions are *ad-hoc* suppressed. Additionally, we also reviewed the effects of the TeV neutrinos in other observables, including processes with lepton number violation, lepton flavor universality violation, precision physics or theoretical implications, as perturbativity of the new Yukawa coupling. All these observables will be important in the following Chapters, as they will constrain the allowed parameter space for our study of maximum LFV H and Z decays in presence of TeV right-handed neutrinos.

Chapter 3

LFV Higgs decays from low scale seesaw neutrinos

The recent discovery of the Higgs boson has opened a new experimental area to search for new physics beyond the SM, in particular with new LFV Higgs decay (LFVHD) channels. As we discussed before, LFV transitions are forbidden in the SM, therefore any observation of a LFV Higgs decay would automatically imply the existence of new physics.

The ATLAS and CMS collaborations are actively searching for these LFV Higgs boson decay processes. Interestingly, the CMS collaboration saw an excess on the $H \to \tau\mu$ channel after the run-I, with a significance of 2.4σ and a value of $\mathrm{BR}(H \to \tau\mu) = (0.84^{+0.39}_{-0.37})\%$. Unfortunately, neither this excess, nor other positive LFVHD signal, have been observed at the present run-II, so ATLAS and CMS have set bounds on these processes, as summarized in Table 2.3. At present, ATLAS has released their results after analyzing 20.3 fb^{-1} of data at a center of mass energy of $\sqrt{s} = 8$ TeV, reaching sensitivities of the order of 10^{-2} for $H \to \tau\mu$ and $H \to \tau e$ channels [68]. On the other hand, CMS has also search for the $H \to \mu e$ channel after the run-I [66] and has further improved the sensitivities of the $H \to \tau\mu$ and $H \to \tau e$ channels with new run-II data [67], setting the most stringent upper bounds for the LFV Higgs decays, which at the 95% CL are given by:

$$\mathrm{BR}(H \to \mu e) < 3.5 \times 10^{-4}\,, \tag{3.1}$$

$$\mathrm{BR}(H \to \tau e) < 6.1 \times 10^{-3}\,, \tag{3.2}$$

$$\mathrm{BR}(H \to \tau\mu) < 2.5 \times 10^{-3}\,. \tag{3.3}$$

Additional indirect constraints on LFVHD rates have been also derived using other LFV transitions [178, 179]. For instance, the upper bounds on $\mu \to e\gamma$ transitions can be translated into a very strong upper bound of $\mathrm{BR}(H \to \mu e) < \mathcal{O}(10^{-9})$. On the contrary, much weaker indirect upper bounds, of order $\mathcal{O}(10\%)$, are derived for the other two channels. This fact further motivates the kind of phenomenological scenarios that we introduced in

Section 2.2.1, where μ-e transitions are *ad-hoc* suppressed.

From the theoretical point of view, there are many extensions of the SM that naturally predict large ratios for these LFV Higgs decays. For instance, they have been studied in the context of supersymmetric models [208–225], in composite Higgs models [226], two Higgs doublet models [227–231], the Zee model [232], minimal flavor violation [233–236], Randall-Sundrum models [237, 238], using effective Lagrangians [92, 239–241] and many others [242–252]. Likewise, the addition of new right-handed neutrinos to the SM can induce large LFVHD rates, specially if they are allowed to have large Yukawa interactions, which is precisely the interaction to the Higgs boson. As we saw in Chapter 1, this is precisely the case in the low scale seesaw models, as the ISS or the SUSY-ISS models, where neutrinos can have large Yukawa couplings and moderately heavy neutrino masses. Consequently, we consider extremely timely to study the LFV Higgs boson decays in these low scale seesaw models.

The LFV Higgs decays were analyzed in the context of the SM enlarged with three heavy Majorana neutrinos for the first time in Ref. [76, 77]. Later, they were computed in the context of the type-I seesaw model in Ref. [82], and they were found to lead to extremely small rates due to the strong suppression from the extremely heavy right-handed neutrino masses, at 10^{14-15} GeV, in that case. This motivates our study of the LFV Higgs decays in the case where the right-handed neutrino masses lie in contrast at the $\mathcal{O}(\text{TeV})$ energy scale and, at the same time, can have large Yukawa couplings. As we saw in Chapter 1, the ISS model contemplates this possibility and, therefore, the rates are expected to be larger than in the type-I seesaw model case.

In this Chapter we perform a detailed study of lepton flavor violating Higgs boson decays $H \to \ell_k \bar{\ell}_m$. We consider the inverse seesaw model as an explicit realization of a low scale seesaw model and analyze, both analytically and numerically, the one-loop induced LFV H decays. Furthermore, we make use of the mass insertion approximation as to compute a simple effective LFV $H\ell_k\ell_m$ vertex that allows to rapidly estimate these rates in models with right-handed neutrinos. Additionally, we also explore a supersymmetric realization of the ISS model and study the new one-loop contributions to the LFV H decays coming from the sneutrinos with TeV masses. The results presented in this Chapter have been published in Refs. [97, 98, 101].

3.1   LFV H decays in the ISS model

LFV Higgs decay rates within the SM with new heavy Majorana neutrinos were first studied in Refs. [76, 82]. In this section, we analyze these rates in the context of the ISS model with three pairs of fermionic singlets added to the SM, and fully study their one-loop contributions to the LFVHD rates. As we did for the LFV radiative decays in the previous Chapter,
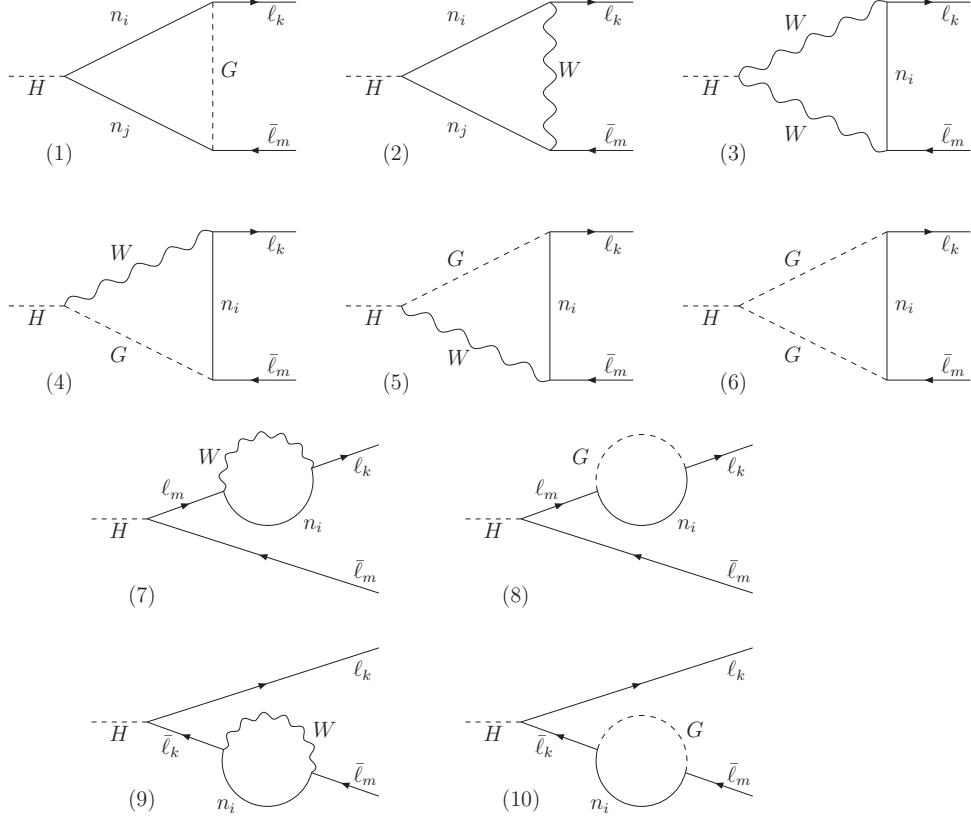
Figure 3.1: One-loop diagrams contributing to the full computation of $H \to \ell_k \bar{\ell}_m$ decays in the physical neutrino mass eigenstate basis and in the Feynman-'t Hooft gauge.

we use the two parametrizations introduced in Section 1.3, the Casas-Ibarra and the μ_X parametrization, to explore these LFVHD rates and discuss the main differences of using one parametrization versus the other.

The decay amplitude of the process $H(p_1) \to \ell_k(-p_2)\bar{\ell}_m(p_3)$ can be generically decomposed in terms of two form factors $F_{L,R}$ by:

$$i\mathcal{M} = -ig\bar{u}_{\ell_k}(-p_2)(F_L P_L + F_R P_R)v_{\ell_m}(p_3)\,, \tag{3.4}$$

and the partial decay width is then written as follows:

$$\Gamma(H \to \ell_k \bar{\ell}_m) = \frac{g^2}{16\pi m_H}\sqrt{\left(1 - \left(\frac{m_{\ell_k} + m_{\ell_m}}{m_H}\right)^2\right)\left(1 - \left(\frac{m_{\ell_k} - m_{\ell_m}}{m_H}\right)^2\right)}$$
$$\times \left((m_H^2 - m_{\ell_k}^2 - m_{\ell_m}^2)\left(|F_L|^2 + |F_R|^2\right) - 4m_{\ell_k}m_{\ell_m}\text{Re}(F_L F_R^*)\right). \tag{3.5}$$

Here, p_1, $-p_2$ and p_3 are the momenta of the ingoing Higgs boson, the outgoing lepton ℓ_k and the outgoing antilepton $\bar{\ell}_m$, respectively, and the conservation of momentum has been implemented as $p_1 = p_3 - p_2$. Moreover, m_H stands for the Higgs mass and $m_\ell = v\, Y_\ell$ for lepton masses (with $v = 174$ GeV). The widths of the CP-conjugate channels $H \to \ell_m \bar{\ell}_k$ are trivially related to the previous ones and their numerical values will coincide for the case of real mass matrices, as will be the case for most of this Thesis.

In the calculation of the LFV Higgs decay rates, we will first work in the physical basis for the neutrinos and consider the full set of contributing one-loop diagrams in the Feynman-'t Hooft gauge, drawn in Fig. 3.1. The form factors can be written in this case as the sum of the different contributions:

$$F_L = \sum_{i=1}^{10} F_L^{(i)}, \qquad F_R = \sum_{i=1}^{10} F_R^{(i)}. \tag{3.6}$$

These form factors were computed in the context of the type-I seesaw in Ref. [82] and we have adapted them to to our present ISS case. The complete results are given in the App. C.

The process $H \to \ell_k \bar{\ell}_m$ with $k \neq m$ does not exist at the tree level, neither in the SM nor in the context of the ISS model we study here, therefore the full one-loop process must be finite. We have explicitly checked that the diagrams (2)-(6) are finite and that the divergent terms from diagrams (7) and (9) are cancelled when adding to all the neutrinos running in the loop. Hence, the only divergent contributions to the LFV Higgs decays arise from the diagrams (1), (8), and (10), and we have checked that they cancel among each other, giving rise to a total finite result. This cancellation is in agreement with the results for the type-I seesaw [82].

The numerical estimates of these LFV Higgs form factors and the LFV Higgs partial decay widths have been done by our private `Mathematica` code. In order to get numerical predictions for the $\mathrm{BR}(H \to \ell_k \bar{\ell}_m)$ rates we use $m_H = 125$ GeV and its corresponding SM total width is computed with `FeynHiggs` [253–255] including two-loop corrections.

In order to be in agreement with present neutrino oscillation data in Eq. (1.6), we will make use of the two parametrizations presented in Chapter 1. We will start this study by taking the matrices M_R and μ_X as input parameters and reconstructing the Yukawa coupling by means of the Casas-Ibarra parametrization in Eq. (1.44). Next, we will follow the idea behind the μ_X parametrization of choosing the M_R and Y_ν matrices as input parameters and then building the proper μ_X matrix that leads to the right light neutrino masses and mixing angles.

In order to compare the predictions of the LFVHD rates with other LFV observables, we also present here the predictions for the related radiative decay rates, $\mathrm{BR}(\mu \to e\gamma)$, $\mathrm{BR}(\tau \to e\gamma)$, and $\mathrm{BR}(\tau \to \mu\gamma)$. We will considere a more complete set of constraining observables and the corresponding updated bounds when looking for the maximum allowed LFV H decay rates at the end of this Chapter.

3.1.1 LFVHD with the Casas-Ibarra parametrization

We present first our numerical results for the LFV Higgs decay rates, $\mathrm{BR}(H \to \mu\bar{\tau})$, $\mathrm{BR}(H \to e\bar{\tau})$ and $\mathrm{BR}(H \to e\bar{\mu})$, when using the Casas-Ibarra parametrization to accommodate light neutrino data. We start by considering the simplest scenario where both M_R and μ_X matrices are diagonal at the same time, $M_R \equiv \mathrm{diag}(M_{R_1}, M_{R_2}, M_{R_3})$ and $\mu_X \equiv \mathrm{diag}(\mu_{X_1}, \mu_{X_2}, \mu_{X_3})$. Although this is not the most general case, it will be very illustrative to learn how these observables depend on the parameters of the model and to find an optimal strategy to study a most general scenario afterwards.

We study the LFV rates as functions of the input ISS parameters in this case, namely, M_{R_i}, μ_{X_i}, the lightest neutrino mass[1] m_{ν_1} and the angles θ_i of the R matrix, trying to localize the areas of the parameter space where the LFV Higgs decays can be both large and respect the constraints on the radiative decays. For a given set of these input parameters, we will build the Yukawa coupling by using Eq. (1.44). Nevertheless, since this procedure can generate arbitrarily large Yukawa couplings, we will enforce their perturbativity in this study by setting an upper limit on the entries of the neutrino Yukawa coupling matrix, given by

$$\frac{\left|Y_{ij}\right|^2}{4\pi} < 1.5\,, \quad \text{for } i,j = 1,2,3\,. \tag{3.7}$$

The results of this first case will be presented in two generically different scenarios for the heavy neutrinos: the case of (nearly) degenerate heavy neutrinos, and the case of hierarchical heavy neutrinos.

The case of (nearly) degenerate heavy neutrinos is implemented by choosing degenerate entries in M_R and in μ_X, i.e., by setting $M_{R_i} \equiv M_R$ and $\mu_{X_i} \equiv \mu_X$ for $i = 1,2,3$. First we show in Fig. 3.2 the results for all the LFV rates as functions of the common right-handed neutrino mass parameter M_R. The left panel shows the LFV Higgs decay channels, while the right panel displays de LFV radiative decays. Here we have fixed the other input parameters to $\mu_X = 10^{-7}$ GeV, $m_{\nu_1} = 0.05$ eV, and $R = \mathbb{1}$. We find that the largest LFV Higgs decay rates are for $\mathrm{BR}(H \to \mu\bar{\tau})$ and the largest radiative decay rates are for $\mathrm{BR}(\tau \to \mu\gamma)$. We also see that, for this particular choice of input parameters, all the predictions for the LFV Higgs decays are allowed by the present experimental upper bounds on the three radiative decays (dashed horizontal lines in the plots for the radiative decays) for all explored values of M_R in this interval of $(200, 10^7)\,\mathrm{GeV}$. Nevertheless, it shows clearly that the most constraining radiative decay at present is by far the $\mu \to e\gamma$ radiative decay.

Regarding the M_R dependence shown in Fig. 3.2, we clearly see that the LFVHD rates grow faster with M_R than the radiative decays, which tend, as we already saw in Chapter 2,

---

[1]We will show again our results for a normal ordering, varying the value of the lightest neutrino mass m_{ν_1} and setting the other two masses using the mass differences in Eq. (1.6). Although not shown here, we found similar results for the inverted hierarchy.
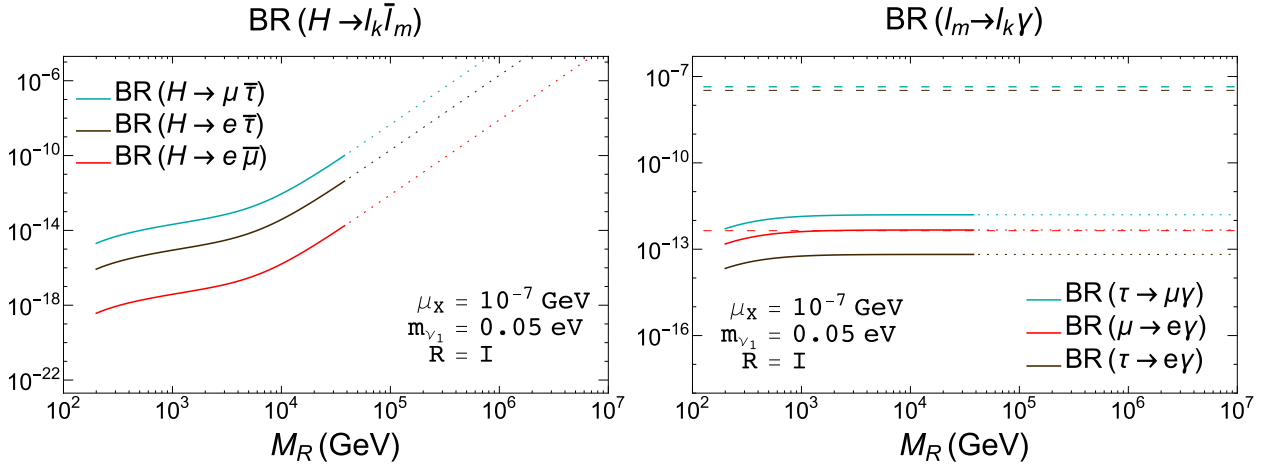
Figure 3.2: Predictions for the LFV decay rates as functions of M_R in the degenerate heavy neutrinos case with the Casas-Ibarra parametrization. Left panel: $\mathrm{BR}(H \to \mu\bar{\tau})$ (upper blue line), $\mathrm{BR}(H \to e\bar{\tau})$ (middle dark brown line), $\mathrm{BR}(H \to e\bar{\mu})$ (lower red line). Right panel: $\mathrm{BR}(\tau \to \mu\gamma)$ (upper blue line), $\mathrm{BR}(\mu \to e\gamma)$ (middle red line), $\mathrm{BR}(\tau \to e\gamma)$ (lower dark brown line). The other input parameters are set to $\mu_X = 10^{-7}\,\mathrm{GeV}$, $m_{\nu_1} = 0.05\,\mathrm{eV}$, $R = \mathbb{1}$. Dotted lines indicate non-perturbative Y_ν, meaning that Eq. (3.7) is not fulfill. Horizontal dashed lines in the right panel are the (90% C.L.) upper bounds: $\mathrm{BR}(\tau \to \mu\gamma) < 4.4 \times 10^{-8}$ [64] (blue line), $\mathrm{BR}(\tau \to e\gamma) < 3.3 \times 10^{-8}$ [64] (dark brown line), $\mathrm{BR}(\mu \to e\gamma) < 4.2 \times 10^{-13}$ [61] (red line).

to a constant value for M_R above $\sim 10^3$ GeV. In fact, the LFVHD rates can reach quite sizable values at the large M_R region of these plots, yet allowed by the constraints on the radiative decays. For example, we obtain $\mathrm{BR}(H \to \mu\bar{\tau}) \sim 10^{-6}$ for $M_R \sim 10^6$ GeV. However, our requirement of perturbativity for the neutrino Yukawa coupling entries in Eq. (3.7) does not allow for such large M_R values leading to too-large Y_ν values in the framework of the Casas-Ibarra parametrization of Eq. (1.44). This non-perturbative region is illustrated using dotted lines in these plots.

The qualitatively different functional behavior with M_R of the LFVHD and the radiative rates shown by Fig. 3.2 is an interesting feature that we wish to explore further. The results for the radiative decay rates can be understood with the approximated formula in Eq. (2.4), valid for large values of M_R. As already explained in Chapter 2, the $(Y_\nu Y_\nu^\dagger)_{km}$ elements grow with M_R as M_R^2 when using the Casas-Ibarra parametrization in Eq. (1.44), and therefore the radiative decay rates saturate to a constant value at large values of M_R, as can be seen in the plot on the right in Fig. 3.2. This simple behavior with M_R is certainly not the case of the LFVHD rates, and we conclude that these do not follow this same behavior with $|(Y_\nu Y_\nu^\dagger)_{km}|^2$. This different functional behavior of $\mathrm{BR}(H \to \ell_k\bar{\ell}_m)$ with M_R will be further

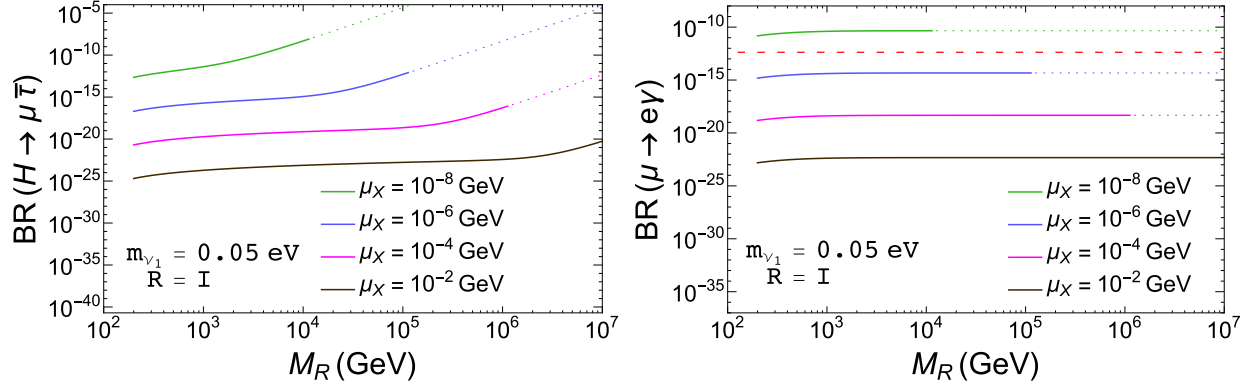Figure 3.3: BR($H \to \mu\bar{\tau}$) (left panel) and BR($\mu \to e\gamma$) (right panel) as functions of M_R for different values of $\mu_X = (10^{-8}, 10^{-6}, 10^{-4}, 10^{-2})$ GeV from top to bottom. In both panels, $m_{\nu_1} = 0.05$ eV and $R = \mathbb{1}$. The horizontal red dashed line denotes the current experimental upper bound on $\mu \to e\gamma$ and dotted lines nonperturbative Y_ν as in Eq. (3.7).

explored and clarified later by mans of our study using the mass insertion approximation. However, we want to emphasize again that the apparent non-decoupling behavior of the LFV rates with the heavy mass scale M_R is again an artifact of the Casas-Ibarra parametrization. As we already said in Chapter 2, the expected decoupling behavior with M_R will become manifest when using the μ_X parametrization, as will be seen in the next subsection.

Next we study the sensitivity in the LFV rates to other choices of μ_X. For this study we focus on the largest LFVHD rates, BR($H \to \mu\bar{\tau}$), and on the most constraining BR($\mu \to e\gamma$) rates, although similar qualitative results are found for the other channels. In Fig. 3.3 we show the predictions for the LFV rates for different values of $\mu_X = (10^{-8}, 10^{-6}, 10^{-4}, 10^{-2})$ GeV. The other input parameters have been fixed here to $m_{\nu_1} = 0.05$ eV and $R = \mathbb{1}$. On the left panel of Fig. 3.3 we see again the increase of BR($H \to \mu\bar{\tau}$) as M_R grows, which is more pronounced in the region where M_R is large and μ_X is low, i.e, where the Yukawa couplings are large (see Eq. (1.44)). We have checked that, in that region, the dominant diagrams are by far the divergent diagrams (1), (8) and (10), and that the BR($H \to \mu\bar{\tau}$) rates grow as M_R^4. Diagrams (2)-(6) have relevant contributions to BR($H \to \mu\bar{\tau}$) only for low values of the Yukawa couplings, while diagrams (7) and (9) are subleading. This will be further explored using the Mass Insertion Approximation in Section 3.3. We also observe that the LFV Higgs rates grow as μ_X decreases from 10^{-2} GeV to 10^{-8} GeV. However, not all the values of M_R and μ_X are allowed, because they may generate nonperturbative Yukawa entries, as we have already said, expressed again in this figure by dotted lines. Therefore, the largest LFV Higgs rates that are permitted by our perturbativity requirements in Eq. (3.7) are approximately of BR($H \to \mu\bar{\tau}$) $\sim 10^{-9}$, obtained for $\mu_X = 10^{-8}$ GeV and $M_R \simeq 10^4$ GeV. Larger values of
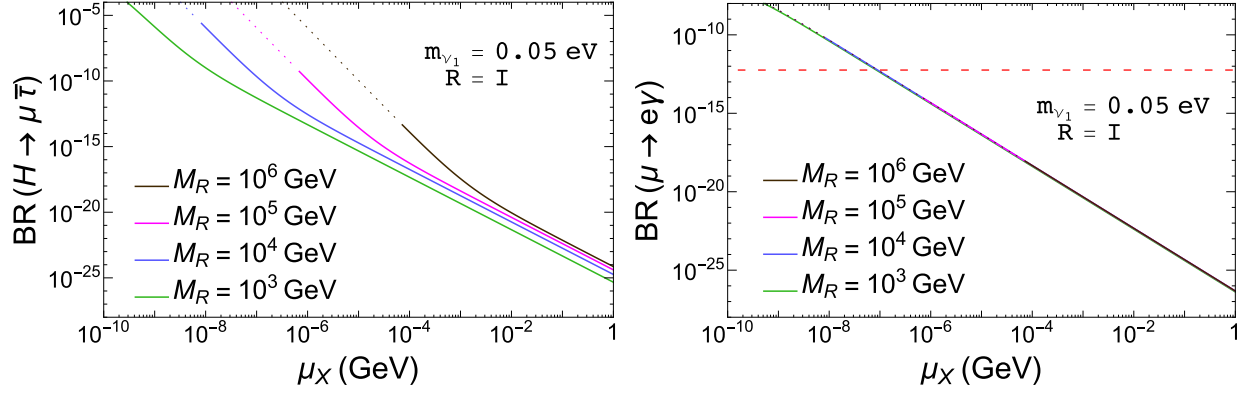
Figure 3.4: Branching ratios of $H \to \mu\bar{\tau}$ (left) and $\mu \to e\gamma$ (right) as functions of μ_X for different values of $M_R = (10^6, 10^5, 10^4, 10^3)$ GeV from top to bottom. In both panels, $m_{\nu_1} = 0.05$ eV and $R = \mathbb{1}$. The horizontal red dashed line denotes the current experimental upper bound on $\mu \to e\gamma$ and dotted lines nonperturbative Y_ν as in Eq. (3.7).

M_R, for this choice of μ_X, would produce Yukawa couplings that are not perturbative.

On the other hand, we must also pay attention to the predictions of $\mathrm{BR}(\mu \to e\gamma)$ for this choice of parameters, because the present experimental upper bound on this ratio is quite constraining. We explore this observable in the right panel of Fig. 3.3, where the dependence of $\mathrm{BR}(\mu \to e\gamma)$ on M_R is depicted, for the same parameter choice as in the left panel. The horizontal red dashed line denotes again its present bound of $\mathrm{BR}(\mu \to e\gamma) < 4.2 \times 10^{-13}$ [61]. In addition to what we have already learned about the constant behavior of $\mathrm{BR}(\mu \to e\gamma)$ with M_R, we also learn from this figure about the generic behavior with μ_X, which leads to increasing LFV rates for decreasing μ_X values. This latter behavior is actually true for both LFV observables. In particular, we see that two small values of $\mu_X \leq \mathcal{O}(10^{-8}$ GeV) lead to $\mathrm{BR}(\mu \to e\gamma)$ rates that are excluded by the experimental upper bound. Taking this into account, the largest value of $\mathrm{BR}(H \to \mu\bar{\tau})$, for this choice of parameters, that is allowed by the $\mathrm{BR}(\mu \to e\gamma)$ upper bound is around 10^{-12}, which is obtained for $M_R \sim 10^5$ GeV and $\mu_X \sim 10^{-6}$ GeV.

The predictions of $\mathrm{BR}(H \to \mu\bar{\tau})$ and $\mathrm{BR}(\mu \to e\gamma)$ as functions of μ_X, for several values of M_R, $m_{\nu_1} = 0.05$ eV, and $R = \mathbb{1}$, are displayed in Fig. 3.4. As already seen in Fig. 3.3, both LFV rates decrease as μ_X grows; however, the functional dependence is not the same. The LFV radiative decay rates decrease approximately as μ_X^{-2}, in agreement with the approximate expression in Eq. (2.4), while the LFVHD rates go as μ_X^{-4} in the regime of large Yukawa couplings. For a fixed value of μ_X, the larger M_R is, the larger $\mathrm{BR}(H \to \mu\bar{\tau})$ can be, while the prediction for $\mathrm{BR}(\mu \to e\gamma)$ is the same for all tested values of M_R. We have already learned this independence of the LFV radiative decays on M_R from the previous
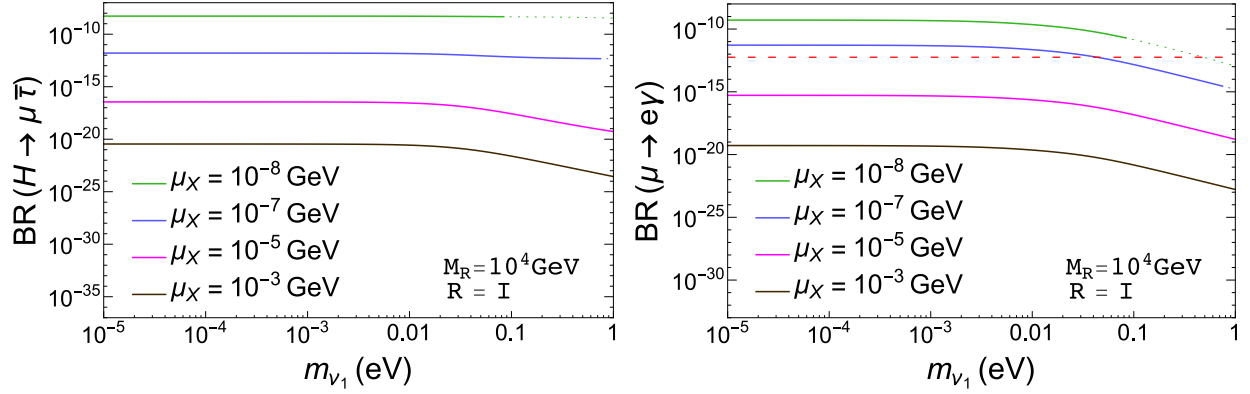
Figure 3.5: Branching ratios of $H \to \mu\bar{\tau}$ (left panel) and $\mu \to e\gamma$ (right panel) as functions of m_{ν_1} for $M_R = 10^4$ GeV, $R = \mathbb{1}$ and different values of $\mu_X = (10^{-8}, 10^{-7}, 10^{-5}, 10^{-3})$ GeV from top to bottom. The horizontal red dashed line denotes the current experimental upper bound on $\mu \to e\gamma$) and dotted lines nonperturbative Y_ν as in Eq. (3.7).

figure, which can be easily confirmed on the right panel of Fig. 3.4, where all the lines for different values of M_R are overplaced. We also see in this figure that the smallest value of μ_X that is allowed by the BR($\mu \to e\gamma$) upper bound is $\mu_X \sim 10^{-7}$ GeV, which is directly translated to a maximum allowed value of BR($H \to \mu\bar{\tau}$) $\sim 10^{-9}$, for $M_R \sim 10^4$ GeV.

The dependence of BR($H \to \mu\bar{\tau}$) and BR($\mu \to e\gamma$) on the lightest neutrino mass m_{ν_1} is studied in Fig. 3.5, for different values of μ_X with $M_R = 10^4$ GeV and $R = \mathbb{1}$. For the chosen parameters, a similar dependence on m_{ν_1} is observed in both observables, in which there is a nearly flat behavior with m_{ν_1} until $m_{\nu_1} \gtrsim 0.01$ eV, where the LFV rates start to decrease. The behavior of BR($\ell_m \to \ell_k\gamma$) with m_{ν_1} can be understood again from Eq. (2.4). In this simplified case of real R and U_{PMNS} matrices and degenerate M_R and μ_X, we find the following simple expression for the nondiagonal $\left(Y_\nu Y_\nu^\dagger\right)_{km}$ elements after Eq. (1.44):

$$\frac{v^2 \left(Y_\nu Y_\nu^\dagger\right)_{km}}{M_R^2} \approx \begin{cases} \dfrac{1}{\mu_X} \left(U_{\text{PMNS}} \sqrt{\Delta m^2}\, U_{\text{PMNS}}^T\right)_{km} & , \text{ for } m_{\nu_1}^2 \ll |\Delta m_{ij}^2| \,, \\[2ex] \dfrac{1}{\mu_X} \dfrac{\left(U_{\text{PMNS}} \Delta m^2\, U_{\text{PMNS}}^T\right)_{km}}{2 m_{\nu_1}} & , \text{ for } m_{\nu_1}^2 \gg |\Delta m_{ij}^2| \,, \end{cases} \tag{3.8}$$

where we have defined:

$$\Delta m^2 \equiv \text{diag}(0, \Delta m_{21}^2, \Delta m_{31}^2) \,, \tag{3.9}$$

and we have expanded properly m_{ν_2} and m_{ν_3} in terms of m_{ν_1} and Δm_{ij}^2. Using these equations, we conclude that the BR($\mu \to e\gamma$) rates have a flat behavior with m_{ν_1} for low
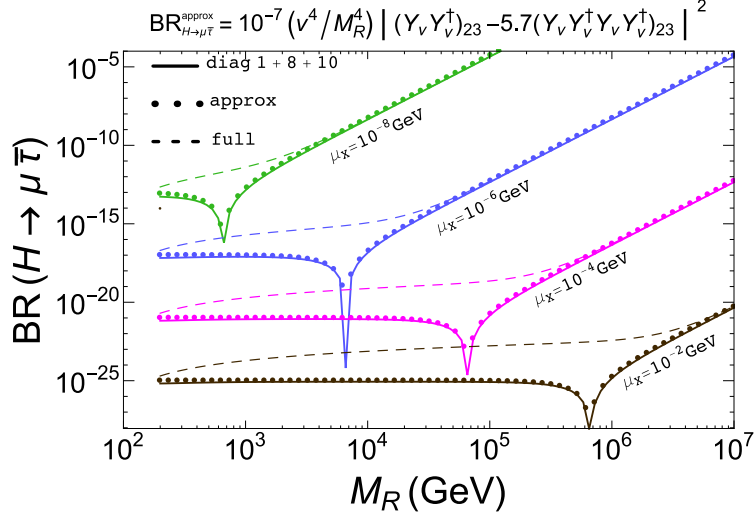
Figure 3.6: Comparison between the predicted rates for $\mathrm{BR}(H \to \mu\bar\tau)$ computed with the full one-loop formulas (dashed lines), just the contributions from diagrams (1), (8), and (10) of Fig. 3.1 (solid lines); and the approximate formula of Eq. (3.10) (dotted lines). In both plot we set $m_{\nu_1} = 0.05$ eV and $R = \mathbb{1}$.

values of $m_{\nu_1} \lesssim 0.01$ eV, but they decrease with m_{ν_1} for larger values, explaining the observed behavior in Fig. 3.5. Again, the predictions for the $\mathrm{BR}(H \to \mu\bar\tau)$ rates do not follow exactly the same pattern as for the $\mathrm{BR}(\mu \to e\gamma)$.

By taking into account all the behaviors learned above, we have tried to find an approximate simple formula that could explain the main features of the $\mathrm{BR}(H \to \mu\bar\tau)$ rates. As we have already said, in contrast to what we have seen for the LFV radiative decays in Eq. (2.4), a simple functional dependence being proportional to $|(Y_\nu Y_\nu^\dagger)_{23}|^2$ is not enough to describe our results for the $\mathrm{BR}(H \to \mu\bar\tau)$ rates. Considering that, in the interesting region where the Yukawa couplings are large, the LFVHD rates are dominated by diagrams (1), (8), and (10), we have looked for a simple expression that could properly fit the contributions from these dominant diagrams. From this numerical fit we have found the following approximate formula:

$$\mathrm{BR}_{H \to \mu\bar\tau}^{\mathrm{approx}} = 10^{-7} \frac{v^4}{M_R^4} \left| (Y_\nu Y_\nu^\dagger)_{23} - 5.7 (Y_\nu Y_\nu^\dagger Y_\nu Y_\nu^\dagger)_{23} \right|^2, \tag{3.10}$$

which turns out to work reasonably well. This particular analytical form in Eq. (3.10) will be justified later in Section 3.3.

In Fig. 3.6 we show the predicted rates of $\mathrm{BR}(H \to \mu\bar\tau)$ computed with the full one-loop formulas (dashed lines); taking just the contributions from diagrams (1), (8), and (10)
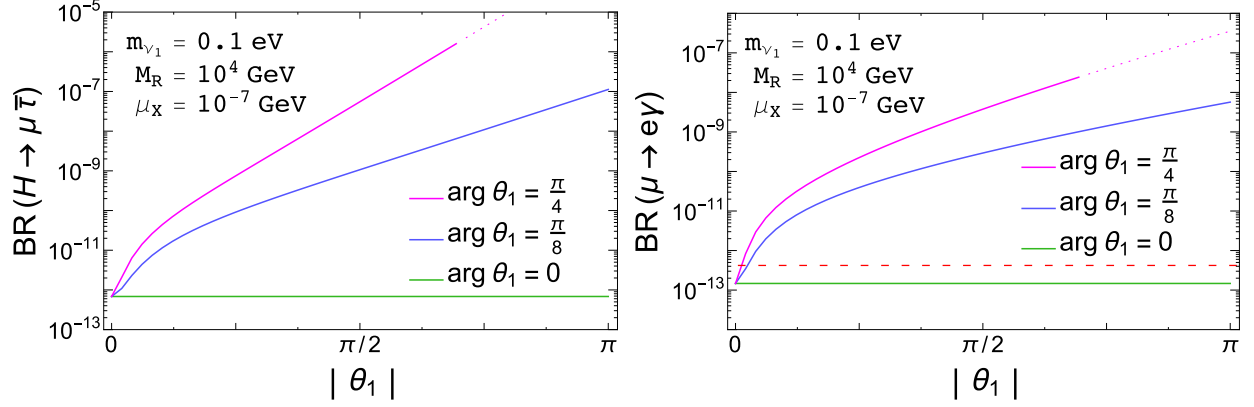
74

Figure 3.7: Branching ratios of $H \to \mu\bar{\tau}$ (left panel) and $\mu \to e\gamma$ (right panel) as functions of $|\theta_1|$ for $M_R = 10^4$ GeV, $\mu_X = 10^{-7}$ GeV, $m_{\nu_1} = 0.1$ eV and different values of $\arg\theta_1$. The horizontal red dashed line denotes the current experimental upper bound on $\mathrm{BR}(\mu \to e\gamma)$ and dotted lines represent nonperturbative Y_ν as in Eq. (3.7).

of Fig. 3.1 (solid lines); and using Eq. (3.10) (dotted lines). We see clearly that Eq. (3.10) reproduces extremely well the contributions from diagrams (1), (8), and (10) and approximates reasonably well the full rates, particularly in the fast growing as M_R^4 in the large M_R region.

This approximate expression in Eq. (3.10) contains an extra contribution in the amplitude of $\mathcal{O}(Y_\nu^4)$ with respect to the one for radiative decays in Eq. (2.4). By using again the parametrization in Eq. (1.44), we obtain

$$\frac{v^2 (Y_\nu Y_\nu^\dagger Y_\nu Y_\nu^\dagger)_{km}}{M_R^2} = \frac{M_R^2}{v^2 \mu_X^2} \left(U_{\mathrm{PMNS}} \Delta m^2 \, U_{\mathrm{PMNS}}^T \right)_{km}. \tag{3.11}$$

Thus, we can clearly see from the above result that the second contribution in Eq. (3.10) is the one that dominates the LFVHD rates at large M_R and low μ_X, i.e., at large Yukawa couplings, and, indeed, it reproduces properly the behavior of $\mathrm{BR}(H \to \mu\bar{\tau}) \propto M_R^4/\mu_X^4$ in this limit. It is also independent of m_{ν_1}, explaining the flat behavior in Fig. 3.5 for low values of μ_X. Moreover, since the two contributions in Eq. (3.10) have opposite signs, they interfere destructively, leading to dips in the contribution from these diagrams to the full decay rates, as seen in Fig. 3.6. The particular choice for the fitting functions will become clear from our posterior analysis in Section 3.3, where we will study in full analytical detail this observable by applying the Mass Insertion Approximation.

Next, we study the effects of taking $R \neq \mathbb{1}$. We display in Fig. 3.7 the dependence of the $H \to \mu\bar{\tau}$ and $\mu \to e\gamma$ decay rates on $|\theta_1|$ for different values of $\arg\theta_1 = 0, \pi/8, \pi/4$, with $M_R = 10^4$ GeV, $\mu_X = 10^{-7}$ GeV, and $m_{\nu_1} = 0.1$ eV. First, we highlight the flat behavior of

both LFV rates with $|\theta_1|$ for real R matrix ($\arg\theta_1 = 0$). This is a direct consequence of the degeneracy of M_R and μ_X, since the LFV rates for the degenerate heavy neutrinos case are independent of R if it is real. Once we abandon the real case and consider values of $\arg\theta_1$ different from zero, a strong dependence on $|\theta_1|$ appears. The larger $|\theta_1|$ and/or $\arg\theta_1$ are, the larger the LFV rates. However, only values of $|\theta_1|$ lower than $\pi/32$ with $\arg\theta_1 = \pi/8$ in this figure are allowed by the BR($\mu \to e\gamma$) constraint, which allows us to reach values of BR($H \to \mu\bar{\tau}$) $\sim 10^{-12}$ at the most. We have also explored the dependence on complex θ_2 and θ_3 and we have reached similar conclusions as for θ_1. Therefore, we conclude that, in the case of degenerate M_R and μ_X matrices, choosing complex $\theta_{1,2,3}$ does not increase the allowed LFVHD rates respect to te previous $R = \mathbb{1}$ case.

Once we have studied the behavior of all the LFV observables considered here with the most relevant parameters, we next present the concluding results for the maximum allowed LFV Higgs decay rates in the case of heavy degenerate neutrinos. The left panel in Fig. 3.8 shows the contour lines of BR($H \to \mu\bar{\tau}$) in the (M_R, μ_X) plane for $R = \mathbb{1}$ and $m_{\nu_1} = 0.05\,\text{eV}$. The horizontal area in pink is excluded by the upper bound on BR($\mu \to e\gamma$). The oblique area in blue is excluded by not respecting the perturbativity requirement of the neutrino Yukawa couplings, according to Eq. (3.7). These contour lines summarize the previously learned behavior with M_R and μ_X, which lead to our findings for the largest values for the LFVHD rates that we localized at large M_R and low μ_X, i.e, in the bottom right-hand corner of the plot. As a conclusion from this contour plot in the left panel of Fig. 3.8, we learn that a maximum allowed LFVHD rates of approximately BR($H \to \mu\bar{\tau}$) $\sim 10^{-10}$ are found for degenerate $M_R \sim 2 \times 10^4\,\text{GeV}$ and $\mu_X \sim 10^{-7}\,\text{GeV}$. We have found similar conclusions for BR($H \to e\bar{\tau}$).

We can now move to the case of hierarchical heavy neutrinos. This case refers here to the assumption of hierarchical masses among the heavy neutrino generations and it is implemented, still assuming diagonal M_R and μ_X matrices, but choosing instead hierarchical entries in the $M_R = \text{diag}(M_{R_1}, M_{R_2}, M_{R_3})$ matrix. As for the $\mu_X = \text{diag}(\mu_{X_1}, \mu_{X_2}, \mu_{X_3})$ matrix that introduces the tiny splitting among the heavy masses in the same generation we choose them here to be degenerate, $\mu_{X_{1,2,3}} = \mu_X$. We focus here on the normal hierarchy case $M_{R_1} < M_{R_2} < M_{R_3}$, since we have found similar conclusions for other hierarchies.

The results of the LFV rates for both Higgs (left panel) and radiative (right panel) decays in this $M_{R_1} < M_{R_2} < M_{R_3}$ hierarchical case are shown in Fig. 3.9. This figure shows that the behavior of these rates in the hierarchical case with respect to the heaviest neutrino mass M_{R_3} is similar to the previously found one for the degenerate case with respect to the common M_R. As before, the BR($H \to \ell_k\bar{\ell}_m$) rates grow fast with M_{R_3} at large $M_{R_3} > 3000\,\text{GeV}$, whereas the BR($\ell_m \to \ell_k\gamma$) rates stay flat with M_{R_3}. We also see in this plot that, for the chosen parameters, the hierarchical scenario leads to larger BR($H \to \ell_k\bar{\ell}_m$) rates than the previous degenerate case. For instance, BR($H \to \mu\bar{\tau}$) reaches 10^{-9} at $M_{R_3} = 3 \times 10^4\,\text{GeV}$, to be compared with 10^{-11} at $M_R = 3 \times 10^4\,\text{GeV}$ that we got in
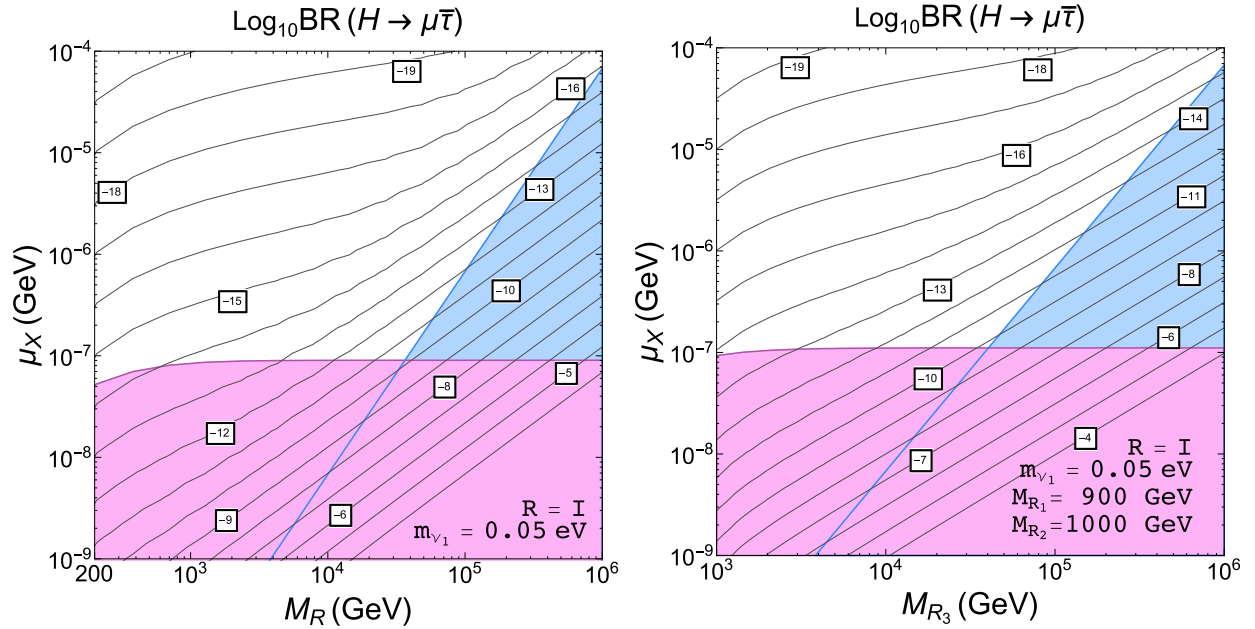
Figure 3.8: Left panel: Contour lines of BR($H \to \mu\bar{\tau}$) in the (M_R, μ_X) plane in the case of degenerate heavy neutrinos. Right panel: Contour lines of BR($H \to \mu\bar{\tau}$) in the (M_{R_3}, μ_X) plane in the case of hierarchical heavy neutrinos with $M_{R_1} = 900$ GeV and $M_{R_2} = 1000$ GeV. In both panels $R = \mathbb{1}$ and $m_{\nu_1} = 0.05$ eV. Horizontal area in pink is excluded by the upper current bound on $\mu \to e\gamma$ and the oblique area in blue is excluded by the perturbativity requiremen for Y_ν in Eq. (3.7).

Fig. 3.2 for the degenerate case. We have found this same behavior of enhanced LFVHD rates by approximately one or two orders of magnitude in the hierarchical case as compared to the degenerate case in most of the explored parameter space regions. This same enhancement can also be seen in the contour plot in the right panel of Fig. 3.8, where the maximum allowed BR($H \to \mu\bar{\tau}$) rates reach larger values up to about 10^{-9} for $M_{R_1} = 900$ GeV, $M_{R_2} = 1000$ GeV, $M_{R_3} = 3 \times 10^4$ GeV, $\mu_X = 10^{-7}$ GeV, and $R = \mathbb{1}$.

Finally, we study the effects of the R matrix for this case of hierarchical heavy neutrinos. In contrast to the degenerate case, there is a dependence on the R matrix even if it is real. Thus, we explore the behavior with the real $\theta_{1,2}$ angles. We have found that for this particular hierarchy of $M_{R_1} < M_{R_2} < M_{R_3}$, there is near independence with θ_3 but there is a clear dependence with θ_1 and θ_2, as it is illustrated in Fig. 3.10. These plots also show that the BR($H \to \ell_k \bar{\ell}_m$) rates with $\theta_{1,2} \neq 0$ can indeed increase or decrease with respect to the reference $R = \mathbb{1}$ case. In particular, for $0 < \theta_1 < \pi$ we find that BR($H \to \mu\bar{\tau}$) is always lower than for $R = \mathbb{1}$, whereas BR($H \to e\bar{\tau}$) can be one order of magnitude larger if θ_1 is
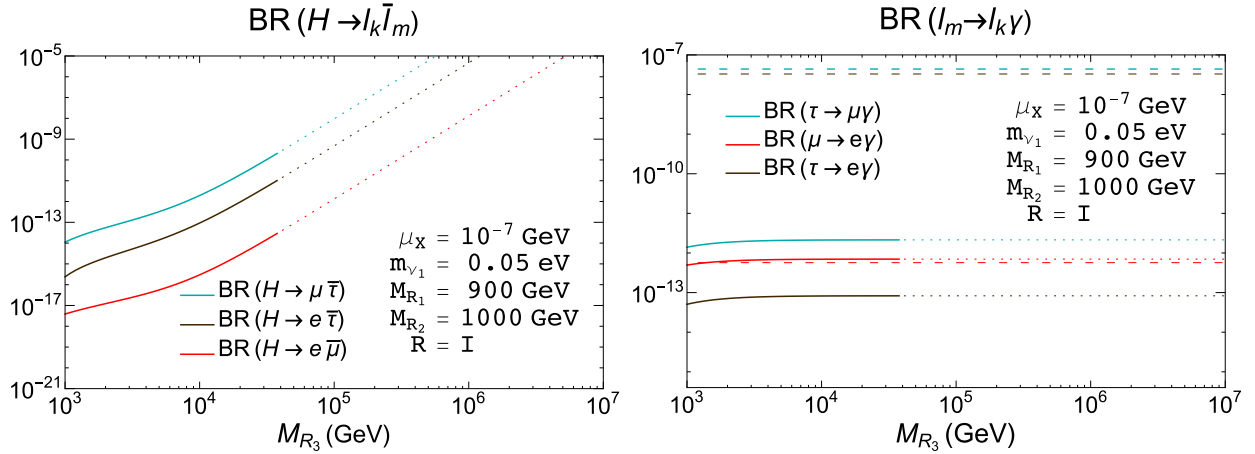
Figure 3.9: Predictions for the LFV Higgs (left panel) and radiative (right panel) decay rates as functions of M_{R_3} in the hierarchical heavy neutrinos case with $M_{R_1} < M_{R_2} < M_{R_3}$. The other input parameters are set to $M_{R_1} = 900$ GeV, $M_{R_2} = 1000$ GeV, $\mu_X = 10^{-7}$ GeV, $m_{\nu_1} = 0.05$ eV, $R = \mathbb{1}$. The color code is as in Fig. 3.2.

near $\pi/2$. For the case of $0 < \theta_2 < \pi$, we find again that $\mathrm{BR}(H \to \mu\bar{\tau})$ is always lower than for $R = \mathbb{1}$, and $\mathrm{BR}(H \to e\bar{\tau})$ can be one order of magnitude larger than for $R = \mathbb{1}$ if θ_2 is near $\pi/4$. In this latter case, it is interesting to notice that in the region of θ_2 close to $\pi/4$ $\mathrm{BR}(H \to e\bar{\tau})$ reaches the maximum value close to 10^{-9} and it is allowed by the constraints on the radiative decays and by the perturbativity condition. The results for the other decay channel $\mathrm{BR}(H \to e\bar{\mu})$ are not shown here because they again give much smaller rates, as in the degenerate case. We have also tried other choices for the hierarchies among the three heavy masses $M_{R_{1,2,3}}$, finding similar conclusions.

3.1.2 LFVHD with the μ_X parametrization

Next, we explore the implications on LFV Higgs decays of going beyond the simplest previous hypothesis of diagonal μ_X and M_R mass matrices in the ISS model. Here, we will focus on the case of degenerate M_R and will explore only the LFV Higgs decay channels with the largest rates, namely, $H \to \mu\bar{\tau}$ and $H \to e\bar{\tau}$, looking for the largest rates allowed by the radiative decays.

In order to get an idea of how large the LFVHD rates could be, we first make a rough estimate of the expected maximal rates for the $H \to \mu\bar{\tau}$ channel by using our approximate formula of Eq. (3.10), which is given just in terms of the neutrino Yukawa coupling matrix Y_ν and M_R. On the other hand, in order to keep the predictions for the radiative decays below their corresponding experimental upper bounds, we need to require a maximum value
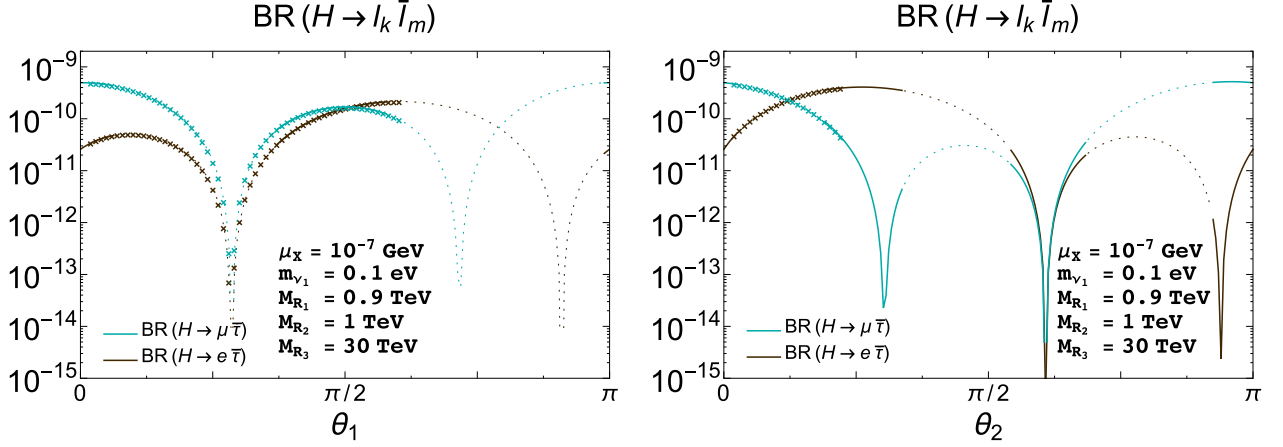
Figure 3.10: Predictions for $\mathrm{BR}(H \to \mu\bar{\tau})$ (blue lines) and $\mathrm{BR}(H \to e\bar{\tau})$ (dark brown lines) rates as a function of real θ_1 (left panel) and θ_2 (right panel). The other input parameters are set to $\mu_X = 10^{-7}$ GeV, $m_{\nu_1} = 0.1$ eV, $M_{R_1} = 0.9$ TeV, $M_{R_2} = 1$ TeV, $M_{R_3} = 30$ TeV, $\theta_2 = \theta_3 = 0$ in the left panel and $\theta_1 = \theta_3 = 0$ in the right panel. The dotted lines indicate nonperturbative neutrino Yukawa couplings and the crossed lines are excluded by the present upper bound on $\mathrm{BR}(\mu \to e\gamma)$. The solid lines are allowed by all the constraints.

for the non-diagonal $(Y_\nu Y_\nu^\dagger)_{ij}$ entries. By using our approximate formula of Eq. (2.4) and the present bounds in Table 2.1, we obtain:

$$v^2 (Y_\nu Y_\nu^\dagger)_{12}^{\max}/M_R^2 \quad \sim \quad 2.5 \times 10^{-5}, \tag{3.12}$$
$$v^2 (Y_\nu Y_\nu^\dagger)_{13}^{\max}/M_R^2 \quad \sim \quad 0.015, \tag{3.13}$$
$$v^2 (Y_\nu Y_\nu^\dagger)_{23}^{\max}/M_R^2 \quad \sim \quad 0.017. \tag{3.14}$$

Then, in order to simplify our search, and given the above relative strong suppression of the 12 element, it seems reasonable to neglect it against the other off-diagonal elements. In that case, by assuming $(Y_\nu Y_\nu^\dagger)_{12} \simeq 0$ we have

$$(Y_\nu Y_\nu^\dagger Y_\nu Y_\nu^\dagger)_{23} \simeq (Y_\nu Y_\nu^\dagger)_{22}(Y_\nu Y_\nu^\dagger)_{23} + (Y_\nu Y_\nu^\dagger)_{23}(Y_\nu Y_\nu^\dagger)_{33}, \tag{3.15}$$

and the approximate formula of Eq. (3.10) can then be rewritten as follows:

$$\mathrm{BR}_{H \to \mu\bar{\tau}}^{\mathrm{approx}} = 10^{-7} \left| \frac{v^2}{M_R^2}(Y_\nu Y_\nu^\dagger)_{23} \right|^2 \left| 1 - 5.7\Big((Y_\nu Y_\nu^\dagger)_{22} + (Y_\nu Y_\nu^\dagger)_{33}\Big) \right|^2. \tag{3.16}$$

This equation clearly shows that the maximal $\mathrm{BR}(H \to \mu\bar{\tau})$ rates are obtained for the maximum allowed values of $(Y_\nu Y_\nu^\dagger)_{23}$, $(Y_\nu Y_\nu^\dagger)_{22}$, and $(Y_\nu Y_\nu^\dagger)_{33}$. Thus, before going to any
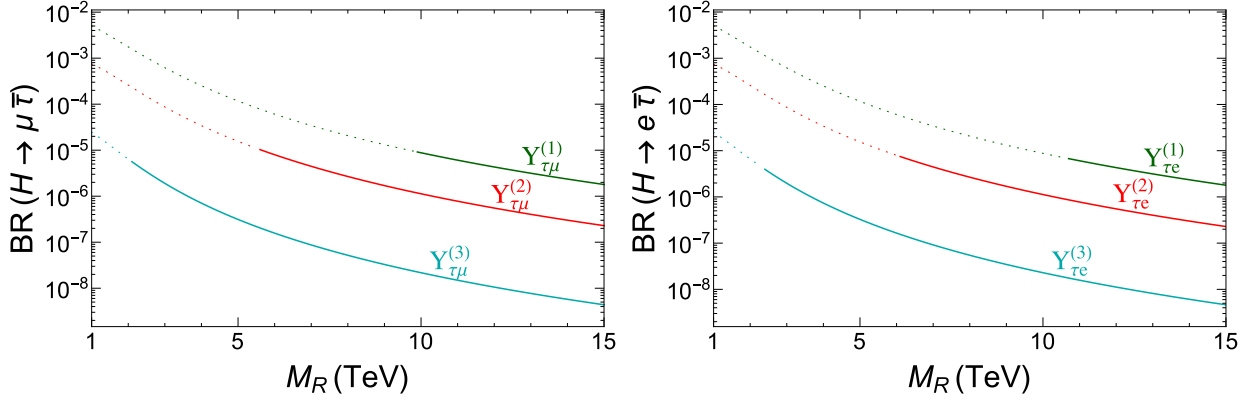
Figure 3.11: Predictions for the LFVHD rates versus M_R obtained when using the μ_X parametrization. Left panel: BR$(H \to \mu\bar{\tau})$ for $Y_{\tau\mu}^{(1)}$ (upper green line), $Y_{\tau\mu}^{(2)}$ (middle red line) and $Y_{\tau\mu}^{(3)}$ (lower blue line) given in Table 2.4 with $f = \sqrt{6\pi}$. Right panel: BR$(H \to e\bar{\tau})$ for the equivalent TE scenarios. Solid (dotted) lines indicate input values allowed (disallowed) by upper bounds on radiative decays.

specific assumption for the Y_ν texture we can already conclude on these maximal rates, by setting the maximum allowed value for $v^2(Y_\nu Y_\nu^\dagger)_{23}^{\text{max}}/M_R^2$ to that given in eq. (3.14) and fixing the values of $(Y_\nu Y_\nu^\dagger)_{22}$ and $(Y_\nu Y_\nu^\dagger)_{33}$ to their maximum allowed values that are implied by our perturbativity condition in Eq. (3.7). This leads to our approximate prediction for the maximal rates:

$$\text{BR}_{H \to \mu\bar{\tau}}^{\text{max}} \simeq 10^{-5} \,. \tag{3.17}$$

We found similar conclusions for the $H \to e\bar{\tau}$ channel.

For the purpose of reaching these large rates, we find more useful and effective to use the μ_X parametrization instead of the Casas-Ibarra one. As explained in Chapter 2, the main advantage when using this parametrization is that it allows us to consider M_R and Y_ν, the relevant parameters for the LFV processes, as the independent input parameters. Furthermore, it makes very easy to focus our analysis directly in the TM and TE scenarios introduced in Table 2.4, which are designed to explore the parameter space directions where τ-μ or τ-e transitions are maximized, respectively, whereas the μ-e transitions are extremely suppressed.

We present in Fig. 3.11 our predictions for the LFVHD as a function of the degenerate right-handed neutrino mass M_R when using the μ_X parametrization for accommodating neutrino oscillation data. Here, we show the results in the scenarios TM-5 $\left(Y_{\tau\mu}^{(1)}\right)$, TM-6 $\left(Y_{\tau\mu}^{(2)}\right)$ and TM-7 $\left(Y_{\tau\mu}^{(3)}\right)$ in Table 2.4 and for $f = \sqrt{6\pi}$, although similar results are found in other scenarios. As before, we have used the full one-loop formulas, even though we have also checked that the approximate formula in Eq. (3.10), and the equivalent one for $H \to e\bar{\tau}$

obtained by choosing the 13 entries instead of the 23 ones, gives a quite good estimate in the large M_R region. Notice again that the μ_X parametrization makes explicit the expected decoupling behavior with M_R, in contrast with the previous plots done with the Casas-Ibarra parametrization.

The main numerical conclusion from these plots is that in these scenarios one can indeed reach large LFVHD rates of the order of 10^{-5} and still be compatible with all the bounds from radiative decays, mainly $\tau \to \mu\gamma$ ($\tau \to e\gamma$) in the left (right) panel. The scenario with input $Y_{\tau\mu}$ ($Y_{\tau e}$) corresponding to lower $c_{\tau\mu}$ ($c_{\tau e}$) allows for lower M_R values and vice versa. Thus, $Y_{\tau\mu}^{(1)}$ ($Y_{\tau e}^{(1)}$) leads to the maximum allowed BR($H \to \mu\bar{\tau}$) (BR($H \to e\bar{\tau}$)) rates for M_R around 10 TeV, $Y_{\tau\mu}^{(2)}$ ($Y_{\tau e}^{(2)}$) 6 TeV and $Y_{\tau\mu}^{(3)}$ ($Y_{\tau e}^{(3)}$) around 2 TeV.

Summarizing, in this section we have studied the LFV Higgs and radiative decays, by considering two different parametrizations to accommodate light neutrino data: the Casas-Ibarra and the μ_X parmaterization. We have showed the advantages of using the latter for looking for large allowed LFVHD rates. By doing this, we found larger rates for BR($H \to \mu\bar{\tau}$) and BR($H \to e\bar{\tau}$) of about 10^{-5} in the TM and TE scenarios, respectively. Of course, in order to properly conclude on maximum allowed LFVHD rates, one must take into account a more complete set of constraining observables. We will do this in Section 3.4. Furthermore, we have also learnt that LFVHD rates do not behave with the heavy M_R mass as the LFV radiative decays, as can be seen from the plots presented in this section and by comparing the respective approximated expressions in Eqs. (3.10) and (2.4). We will study this particular behavior un more detail using the MIA in Section 3.3.

Nevertheless, before going to the full analysis of the right-handed neutrino contribution to the LFVHD rates, we want to explore these rates also in a different model, where the ISS is embedded in a Supersymetric context. In such a case, new important contributions could arise from diagrams with SUSY particles running in the loops and, as we will present next, they increase the LFVHD rates considerably.

3.2 LFVHD in the SUSY-ISS model

We have seen in Chapter 1 that the ISS model can be easily embedded into a Supersymmetric context, leading to a new model that we refer to as the SUSY-ISS model. Interestingly, previous studies have demonstrated that Supersymmetric contributions usually enhance the LFV rates (see, for instance, Refs. [42, 46, 50, 82]). In particular, in the present SUSY-ISS model, we expect that a lower value of the heavy neutrino mass scale M_R in the ISS, compared with the type-I seesaw, will enhance the flavor slepton mixing due to the RGE-induced radiative effects by the large neutrino Yukawa couplings, and this mixing will in turn generate via the slepton loops an enhancement in the LFVHD rates. On the other hand, new relevant couplings appear, like the neutrino trilinear coupling A_ν, which for sneutrinos,
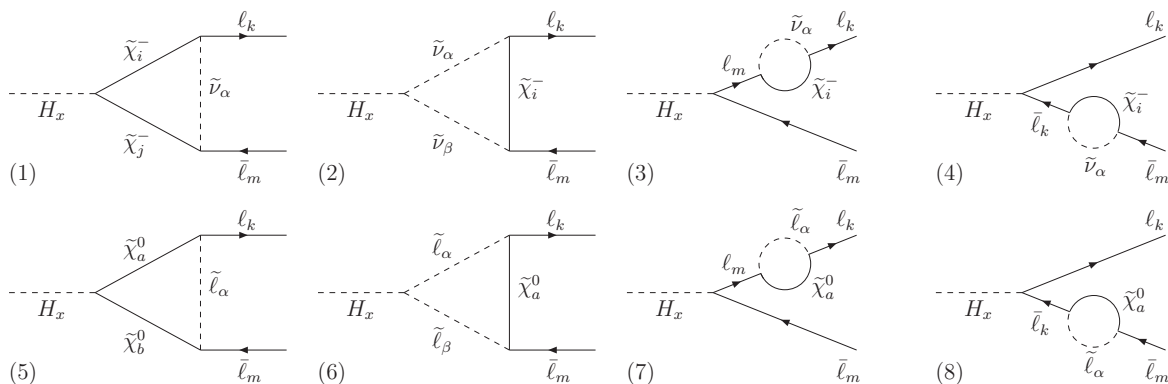
Figure 3.12: One-loop supersymmetric diagrams contributing to the process $H_x \to \ell_k \bar{\ell}_m$.

that are the SUSY partners of the heavy ν_R, with $\mathcal{O}(1\,\text{TeV})$ masses may lead to new loop contributions to LFVHD that could even dominate [46]. This calls up for a new evaluation of the LFVHD rates in the SUSY-ISS model.

Additionally, the CMS experiment saw an interesting excess in the $H \to \mu\tau$ channel after the LHC run-I [69] with a value of $\text{BR}(H \to \mu\tau) = 8.4^{+3.9}_{-3.7} \times 10^{-3}$ and a significance of 2.4σ. Motivated by the fact that the ISS model could not explain such a large ratio, we started by exploring the size of the new SUSY particle contribution to these LFVHD rates. Of course, a more detailed analysis considering the full set of contributions in the SUSY-ISS model is needed and will come in a future work. Nonetheless, we expect that the dominant contributions will come from the new SUSY particles and, therefore, we will study first their impact on LFVHD rates.

In this Section, then, we consider a full one-loop diagrammatic computation of all the supersymmetric loops within the SUSY-ISS model for $\text{BR}(H_x \to \ell_k \bar{\ell}_m)$, where H_x refers in this section to the three neutral MSSM Higgs bosons, $H_x = (h, H, A)$. This is in contrast to the previous estimate in Ref. [46], where an effective Lagrangian description of the Higgs mediated contributions to LFV processes was used, which was valid to capture just the relevant contributions at large $\tan\beta$, and where the mass insertion approach was used to incorporate, working in the electroweak basis, the flavor slepton mixing $(\Delta m_{\tilde{L}}^2)_{ij}$. However, an expansion up to the first order in the mass insertion approximation may not be enough for the type of scenarios studied here, due to the large value of the flavor-non-diagonal matrix entries. On the other hand, we are interested also in small and moderate $\tan\beta$ values and we also wish to explore more generic soft masses for the SUSY particles and scan over the relevant neutrino/sneutrino parameters, mainly M_R, A_ν and $m_{\tilde{\nu}_R}$, not focusing only on scenarios with universal or partially universal soft parameters nor fixing the relevant

parameters to one particular value as in Ref. [46]. Therefore, we perform the calculation instead in the more convenient mass basis for all the SUSY particles involved in the loops, i.e, the charged sleptons, sneutrinos, charginos, and neutralinos.

The decay amplitude for $H_x \to \ell_k \bar{\ell}_m$ can be written, similarly to Eq. (3.4), as

$$\imath F_x = -\imath g \bar{u}_{\ell_k}(-p_2)(F_{L,x}P_L + F_{R,x}P_R)v_{\ell_m}(p_3)\,, \tag{3.18}$$

with again $H_x = (h, H, A)$ and $p_1 = p_3 - p_2$ is the ingoing Higgs boson momentum. The full LFVHD widths can be then obtained from Eq. (3.5), with the proper substitution of $m_H \to m_{H_x}$ for the Higgs masses and $F_{L/R} \to F_{L/R,x}$ in the form factors.

Since we work in the mass basis, the set of diagrams contributing to the LFV Higgs decays is the same as in the SUSY type-I seesaw model which was previously considered in Ref. [82]. We display this set of 8 diagrams, four diagrams with charginos and sneutrinos in the loops, and four more with neutralinos and charged sleptons, in Fig. 3.12. The contributions of the SUSY diagrams are summed in $F_{L,x}$ and $F_{R,x}$ according to

$$F_{L,x} = \sum_{i=1}^{8} F_{L,x}^{(i)}, \quad F_{R,x} = \sum_{i=1}^{8} F_{R,x}^{(i)}\,. \tag{3.19}$$

We take the analytical expressions from Ref. [82] and properly adapt them to the SUSY-ISS model. The resulting formulas are collected in App. D

As in the non-SUSY case, this observable does not exist at the tree level and, therefore, the full one loop contributions must give a finite result. In the type-I seesaw SUSY model, we have checked that each diagram in Fig. 3.12 gives a finite contribution to the $H_x \to \ell_k \bar{\ell}_m$ process when summing over all internal indexes, in agreement with Refs. [82, 221]. This is not the case in the SUSY-ISS model, where we have found that the new terms in the coupling factor $A_{R_{\alpha j}}^{(\ell)}$, see Eq. (D.1), give rise to divergent terms in diagrams (3) and (4). Nevertheless, these divergences cancel out when adding both diagrams, such that the full result is finite, as expected. Notice that the contributions from the sneutrino-chargino sector, adding diagrams (1)-(4), and the ones from the slepton-neutralino sector, adding diagrams (5)-(8), are finite separately and, therefore, it is legit to study both contributions separately, as we will do below.

Next, we show the numerical results of the LFV decay rates of the lightest neutral Higgs boson, BR($h \to \tau\bar{\mu}$), as a function of the most relevant parameters for the full SUSY contribution to LFVHD, namely, M_R, A_ν and $m_{\tilde{\nu}_R}$. We will assume that the lightest CP-even Higgs boson, h, is the particle found by the LHC with a mass of 125 GeV, and explore, consequently, the process $h \to \mu\bar{\tau}$. In order to ensure a Higgs boson mass in agreement with the experimental value, we will adjust the squark parameters, since they are irrelevant for the LFVHD studied here, and make sure that they lead to a supersymmetric spectrum allowed by ATLAS and CMS searches. As in the non-SUSY case, we restrict ourselves to the case

of heavy neutrinos and sneutrinos above the Higgs boson mass, with $M_R > m_h$, avoiding constraints from the invisible Higgs decay widths, and consider only real U_{PMNS} and mass matrices, making constraints from lepton electric dipole moments irrelevant. Furthermore, this absence of CP violation makes $\text{BR}(h \to \tau\bar{\mu})=\text{BR}(h \to \mu\bar{\tau})$ and, therefore, a factor of two should be added to our results in comparing with experimental data for $\text{BR}(h \to \tau\mu)\equiv \text{BR}(h \to \tau\bar{\mu})+\text{BR}(h \to \mu\bar{\tau})$.

As in the previous section, we will also compute here, using the expressions in Ref. [156], the LFV radiative decays as a good reference of the most relevant experimental constraints on LFV, whose current upper limits at the 90% C.L. are

$$\text{BR}(\mu \to e\gamma) \leq 4.2 \times 10^{-13}[61]\,, \tag{3.20}$$

$$\text{BR}(\tau \to e\gamma) \leq 3.3 \times 10^{-8}\ [64]\,, \tag{3.21}$$

$$\text{BR}(\tau \to \mu\gamma) \leq 4.4 \times 10^{-8}\ [64]\,. \tag{3.22}$$

In the following plots, the points excluded by LFV radiative decays will be denoted by crosses, while triangles will represent the allowed ones. We present here the predictions of $\text{BR}(h \to \tau\bar{\mu})$ for three examples of the TM scenarios exposed in the Table 2.4 that maximize τ-μ transitions ensuring, at the same time, practically vanishing LFV in the μ-e sector, in particular, leading to $\text{BR}(\mu \to e\gamma) \sim 0$ and $\text{BR}(h \to e\bar{\mu}) \sim 0$. It should be noticed that in these TM scenarios LFV transitions in the τ-e sector are also substantially suppressed and, therefore, the most stringent radiative decay is that of the related LFV radiative decay $\tau \to \mu\gamma$. Although not shown here, we want to emphasize again that equivalent results are obtained for $\text{BR}(h \to e\bar{\tau})$ in the TE scenarios.

In Fig. 3.13, we show the behavior of $\text{BR}(h \to \tau\bar{\mu})$ as a function of M_R in the above commented scenarios, $Y_{\tau\mu}^{(1)}$ from TM-5 (upper left panel), $Y_{\tau\mu}^{(2)}$ from TM-6 (upper right panel), and $Y_{\tau\mu}^{(3)}$ from TM-7 (lower left panel), for different values of the scaling factor f. First of all, we clearly see that, as expected, the larger the value of f is, the larger the LFV rates are. We also observe qualitatively different behaviors of the LFV rates between small ($f < 1$) and large ($f > 1$) neutrino Yukawa couplings. This difference comes from the different behavior with the parameters of the two participating types of loops, the ones with charged sleptons where the LFV is generated exclusively by the mixing $(\Delta m_{\tilde{L}}^2)_{ij}$ and the ones with sneutrinos where the LFV is generated by both $(\Delta m_{\tilde{L}}^2)_{ij}$ and $(Y_\nu)_{ij}$. For small values of f, the dominant contributions come from the slepton-neutralino loops, which only depend logarithmically on M_R, as can be seen from Eq. (1.63), leading to the apparent flat behavior. Nevertheless, we checked that this flat behavior disappears when both M_R and M_0, and consequently all slepton and sneutrino masses, increase simultaneously. On the other hand, when the scale factor f becomes larger, contributions from sneutrino-chargino loops become sizable and even dominate at low M_R. These contributions decrease with M_R, due to the increase in the singlet sneutrino masses, which explains the decrease in $\text{BR}(h \to \tau\bar{\mu})$ observed in the plots in Fig. 3.13 for large $f > 1$. In this latter situation, the appearance
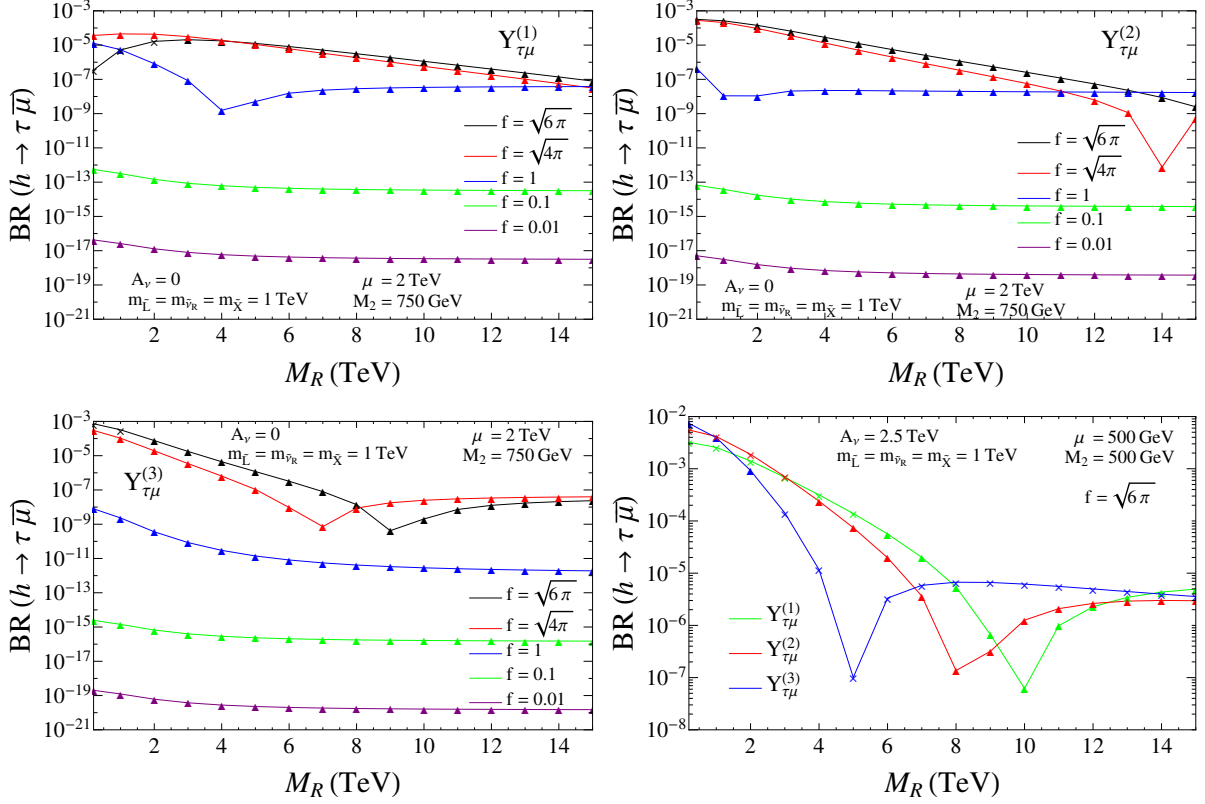
Figure 3.13: BR($h \to \tau\bar{\mu}$) as a function of M_R for $Y_{\tau\mu}^{(1)}$ (upper left panel), $Y_{\tau\mu}^{(2)}$ (upper right panel), and $Y_{\tau\mu}^{(3)}$ (lower left panel) with $M_2 = 750$ GeV, $\mu = 2$ TeV, $A_\nu = 0$, $\tan\beta = 5$ and different values of the scaling factor $f = 0.01, 0.1, 1, \sqrt{4\pi}, \sqrt{6\pi}$. The lower right panel shows the results in these three scenarios with $M_2 = \mu = 500$ GeV, $A_\nu = 2.5$ TeV, $\tan\beta = 10$ and $f = \sqrt{6\pi}$. In all panels, $m_{\tilde{L}} = m_{\tilde{e}} = m_{\tilde{\nu}_R} = m_{\tilde{X}} = 1$ TeV, $m_A = 800$ GeV and $M_0 = 1$ TeV. We set, in these and all the figures of this section, $A_0 = A_e = B_X = B_R = 0$, $M = 10^{18}$ GeV and the GUT inspired relation $M_1 = 5/3\ M_2 \tan^2\theta_W$. Crosses (triangles) represent points in the SUSY-ISS parameter space excluded (allowed) by the upper bound BR($\tau \to \mu\gamma$) $< 4.4 \times 10^{-8}$ [64].

of dips due to negative interferences between the two types of loops marks the transition between the two regimes, with the main contribution coming from sneutrino-chargino loops at low M_R and from slepton-neutralino loops at large M_R.

Regarding the numerical predictions, we find that, for these parameters, the largest BR($h \to \tau\bar{\mu}$) allowed by the $\tau \to \mu\gamma$ upper limit are obtained for $f = \sqrt{4\pi}$ or $\sqrt{6\pi}$ and $M_R < 2$ TeV, with a value of around 10^{-4} for the three shown scenarios, which could be probed in
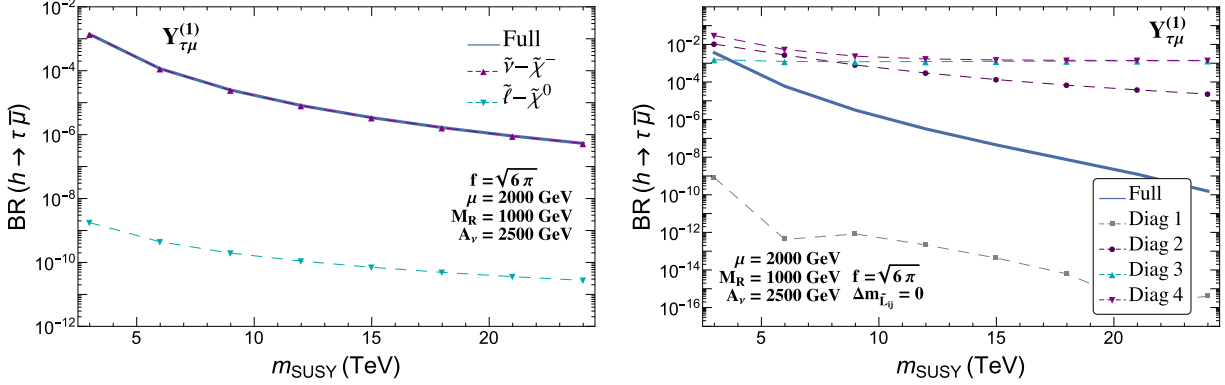
Figure 3.14: $\mathrm{BR}(h \to \tau\bar{\mu})$ as a function of the common SUSY mass parameter m_{SUSY} in Eq. (3.23) for the TM-5 scenario $\left(Y_{\tau\mu}^{(1)}\right)$ with $M_R = 1$ TeV, $f = \sqrt{6\pi}$, $m_A = 800$ GeV, $\mu = 2$ TeV, $\tan\beta = 10$ and $A_\nu = 2.5$ TeV. Left panel: Contributions from sneutrino-chargino loops, denoted by $\widetilde{\nu}$-$\widetilde{\chi}^-$, slepton-neutralino loops, denoted by $\widetilde{\ell}$-$\widetilde{\chi}^0$, and full results for $\mathrm{BR}(h \to \tau\bar{\mu})$. Right panel: Individual contributions from each $\widetilde{\nu}$-$\widetilde{\chi}^-$, diagrams (1)-(4) in Fig. 3.12, and full result in the case of $\Delta m_{\tilde{L}_{ij}} = 0$, where the $\widetilde{\ell}$-$\widetilde{\chi}^0$ contributions vanish.

future runs of the LHC. Nonetheless, these predictions can have strong dependencies on the SUSY parameters, as we want to further study next. In particular, we study the effects on these LFV observables of the trilinear coupling A_ν, which had been set to zero up to now. On the lower right panel of Fig. 3.13 we have chosen $A_\nu = 2.5$ TeV and show the behavior of $\mathrm{BR}(h \to \tau\bar{\mu})$ with M_R for the three textures with a scaling factor $f = \sqrt{6\pi}$. This value of A_ν leads to an enhancement of the $\mathrm{BR}(h \to \tau\bar{\mu})$ while simultaneously suppressing the $\tau \to \mu\gamma$ rates. As a consequence, very large LFVHD branching ratios can be obtained for $Y_{\tau\mu}^{(3)}$ with low M_R close to 1 TeV, allowed by $\tau \to \mu\gamma$, achieving values up to 7×10^{-3}. These large rates are very close to the percent level and within the sensitivity of the present experiments.

We next study the behavior of the $h \to \tau\bar{\mu}$ rates as a function of the SUSY mass scales in a simplified scenario where all the SUSY masses are equal to a common parameter m_{SUSY}, namely,

$$m_{\mathrm{SUSY}} = m_{\tilde{L}} = m_{\tilde{e}} = m_{\tilde{\nu}_R} = m_{\tilde{X}} = M_0 = M_1 = M_2. \tag{3.23}$$

The left panel of Fig. 3.14 shows the expected decoupling with m_{SUSY} behavior where $\mathrm{BR}(h \to \tau\bar{\mu})$ decreases when increasing all the heavy sparticle masses. This plot is for the particular case of the TM-5 scenario $\left(Y_{\tau\mu}^{(1)}\right)$, but similar behaviors (not shown) are obtained for the other scenarios. In this figure we have included the full predictions for $\mathrm{BR}(h \to \tau\bar{\mu})$, as well as the separated contributions coming only from sneutrino-chargino loops, diagrams (1)-(4) in Fig. 3.12, and from slepton-neutralino loops, diagrams (5)-(8) in Fig. 3.12. We see
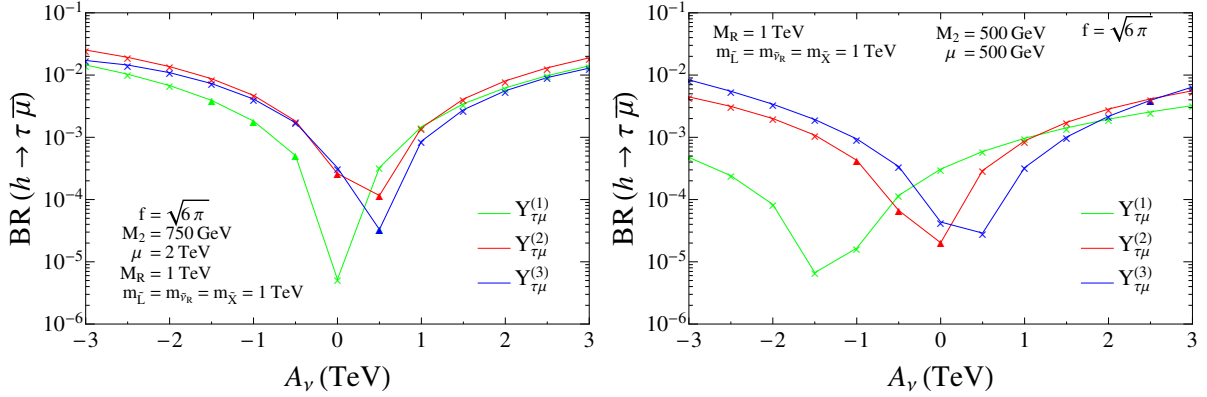
Figure 3.15: Dependence of $\mathrm{BR}(h \to \tau\bar{\mu})$ on A_ν for scenarios TM-5 $\left(Y_{\tau\mu}^{(1)}\right)$, TM-6 $\left(Y_{\tau\mu}^{(2)}\right)$, and TM-7 $\left(Y_{\tau\mu}^{(3)}\right)$, with $M_2 = 750$ GeV, $\tan\beta = 5$ and $\mu = 2$ TeV (left panel) or with $\tan\beta = 10$ and $M_2 = \mu = 500$ GeV (right panel). On both panels, $m_A = 800$ GeV, $M_0 = 1$ TeV, $M_R = m_{\tilde{L}} = m_{\tilde{e}} = m_{\tilde{\nu}_R} = m_{\tilde{X}} = 1$ TeV, and the scaling factor $f = \sqrt{6\pi}$. Crosses (triangles) represent points in the SUSY-ISS parameter space excluded (allowed) by the $\tau \to \mu\gamma$ upper limit, $\mathrm{BR}(\tau \to \mu\gamma) < 4.4 \times 10^{-8}$ [64].

that not only the full prediction but also the separated contributions from these two subsets decrease with m_{SUSY}, showing that the decoupling occurs in both, the charginos-sneutrinos and the neutralinos-sleptons sectors, as expected from the decoupling theorem.

In this heavy sparticle scenario, the full predictions are dominated by the contributions from the sneutrino-chargino sector, which is the one containing new sparticles with respect to the MSSM. In order to better understand the contributions from this sector, we study the simple case of $\Delta m_{\tilde{L}_{ij}} = 0$, where the contributions from the slepton-neutralino sector vanish. We show in the right panel of Fig. 3.14 the full result in this situation, as well as the individual contributions from diagrams (1) to (4) in Fig. 3.12. We see that the vertex correction, diagram (2), and the self-energies, diagrams (3) and (4), clearly compete in size and that their interference is destructive, manifesting a strong cancellation among self-energies and vertex corrections. The contributions from diagram (1), on the other hand, are subleading by several orders of magnitude. Notice also that the contributions from diagrams (3) and (4) do not decouple individually with m_{SUSY}, but their addition does, as expected.

As mentioned before, we have found that the LFVHD rates are indeed very sensitive to the particular value of the trilinear coupling A_ν. Thus, we study in Fig. 3.15 the behavior of $\mathrm{BR}(h \to \tau\bar{\mu})$ with A_ν for the two SUSY scenarios considered in Fig. 3.13, with $M_R = 1$ TeV and $f = \sqrt{6\pi}$. The strong dependence on A_ν is manifest in both panels, presenting deep dips in different positions that depend mainly on the values of Y_ν, μ, m_A and $\tan\beta$.
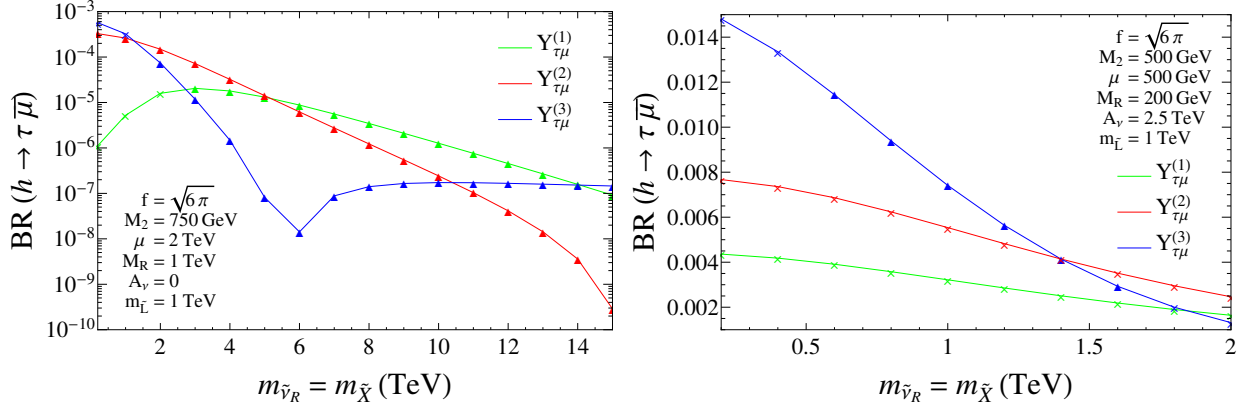
Figure 3.16: Dependence of $\mathrm{BR}(h \to \tau\bar{\mu})$ on $m_{\tilde{\nu}_R} = m_{\tilde{X}}$ for scenarios TM-5 $\left(Y_{\tau\mu}^{(1)}\right)$, TM-6 $\left(Y_{\tau\mu}^{(2)}\right)$, and TM-7 $\left(Y_{\tau\mu}^{(3)}\right)$, with $M_R = m_{\tilde{L}} = m_{\tilde{e}} = 1$ TeV, $M_2 = 750$ GeV, $\mu = 2$ TeV, $\tan\beta = 5$ and $A_\nu = 0$ (left panel) or with $M_R = 200$ GeV, $m_{\tilde{L}} = m_{\tilde{e}} = 1$ TeV, $M_2 = \mu = 500$ GeV, $\tan\beta = 10$ and $A_\nu = 2.5$ TeV (right panel). On both panels, $m_A = 800$ GeV, $M_0 = 1$ TeV, and $f = \sqrt{6\pi}$. Crosses (triangles) represent points in the SUSY-ISS parameter space excluded (allowed) by the $\tau \to \mu\gamma$ upper limit, $\mathrm{BR}(\tau \to \mu\gamma) < 4.4 \times 10^{-8}$ [64].

These parameters control, in particular, the h^0-$\tilde{\nu}_L$-$\tilde{\nu}_R$ coupling and the $\tilde{\nu}_L$-$\tilde{\nu}_R$ mixing, which would lead to the appearance of dips in the regime where contributions from sneutrino-chargino loops dominate, as it is the case of Fig. 3.15. It is interesting to note that, for this choice of parameters, practically all the parameter space is excluded by $\tau \to \mu\gamma$ except the points within the dips and surrounding them, where the LFV radiative decay $\tau \to \mu\gamma$ suffers also a strong reduction. An interesting feature we found is that the location of the dips in $\mathrm{BR}(h \to \tau\bar{\mu})$ and $\mathrm{BR}(\tau \to \mu\gamma)$ usually do not coincide, therefore allowing for large LFV Higgs decays rates, above 10^{-3} and within the reach of the LHC experiments, that are not excluded by $\tau \to \mu\gamma$.

Finally, the dependence of the LFVHD rates on the new sneutrino soft SUSY breaking scalar masses, $m_{\tilde{\nu}_R}$ and $m_{\tilde{X}}$, is depicted in Fig. 3.16, where we vary these parameters independently from the SUSY scale. As when modifying M_R, increasing $m_{\tilde{\nu}_R}$ and $m_{\tilde{X}}$ makes the singlet sneutrinos heavier and decreases the size of the chargino contribution. In the case of $Y_{\tau\mu}^{(1)}$ and $Y_{\tau\mu}^{(2)}$ which are dominated by this contribution, the $\mathrm{BR}(h \to \tau\bar{\mu})$ exhibits a strong decrease in the range explored in Fig. 3.16, by more than five orders of magnitude in the case of $Y_{\tau\mu}^{(2)}$. For $Y_{\tau\mu}^{(3)}$ a dip can be observed, due again to cancellations between the chargino and neutralino contributions, with the latter dominating at large $m_{\tilde{\nu}_R}$. For the benchmark point in the left panel, the largest $h \to \tau\bar{\mu}$ rates allowed by the $\tau \to \mu\gamma$ upper limit are obtained for $Y_{\tau\mu}^{(2)}$ with $m_{\tilde{\nu}_R} = 200$ GeV, with a maximum value of $\sim 3 \times 10^{-4}$, just

one order of magnitude below the present LHC sensitivity. In the second benchmark point in the right panel of Fig. 3.16, we found large LFVHD rates with $M_R = 200$ GeV, $A_\nu = 2.5$ TeV and low values of $m_{\tilde{\nu}_R}$. We observe a huge increase in $\text{BR}(h \to \tau\bar{\mu})$ for the three Yukawa couplings $Y_{\tau\mu}^{(1)}$, $Y_{\tau\mu}^{(2)}$, and $Y_{\tau\mu}^{(3)}$, with maximum values of approximately 4×10^{-3}, 8×10^{-3} and 1.5×10^{-2}, respectively, due mainly to the low values of $m_{\tilde{\nu}_R}$ and M_R. Unfortunately, the $\tau \to \mu\gamma$ upper limit excludes all the parameter space for $Y_{\tau\mu}^{(1)}$ and $Y_{\tau\mu}^{(2)}$ cases. In contrast, most of the points for the $Y_{\tau\mu}^{(3)}$ texture are in agreement with this upper bound, since they are located in a region where the $\tau \to \mu\gamma$ rates suffer a strong suppression as a consequence of the value set for A_ν in this case, $A_\nu = 2.5$ TeV. This fact allows us to obtain a maximum value of $\text{BR}(h \to \tau\bar{\mu}) \sim 1.1\%$, completely within the reach of the current LHC experiments and large enough to explain the CMS excess if confirmed by other experiments and/or future data.

Summarizing, in this section we have studied the LFVHD rates in presence of the SUSY particles in the SUSY-ISS model. We saw that much larger contributions from the SUSY loops are obtained with respect to the predicted rates in the type-I seesaw due to large $Y_\nu^2/(4\pi) \sim \mathcal{O}(1)$, the presence of right-handed sneutrinos at the TeV scale and an increased RGE-induced slepton mixing from the GUT scale down to the M_R scale, We also demonstrated that in the SUSY-ISS model new contributions coming from the SUSY particle loops can considerably enhance the LFVHD rates with respect to the non-SUSY ISS model. We found particularly interesting the new contributions from the trilinear coupling A_ν, since, in addition to enhance the LFVHD rates, it can lead to suppressions in the corresponding LFV radiative decay rates. We find these results very promising and therefore it calls up for a more complete analysis. We will therefore present in a future work a complete study including both the SUSY and non-SUSY contributions in the SUSY-ISS model, exploring also the heavy Higgs bosons LFV decays and considering a detailed analysis of experimental constraints beyond radiative LFV decays.

3.3 The effective LFV $H\ell_k\ell_m$ vertex from heavy ν_R within the Mass Insertion Approximation

As we have seen in Section 3.1, LFV H decays in the ISS model do not behave as other LFV processes like the radiative decays. By comparing the approximated expressions for the LFV radiative decays in Eq. (2.4) and for the H decays in Eq. (3.10), it is clear that the latter contains, in addition to the usual $\mathcal{O}(Y_\nu^2)$ contribution, an extra contribution of $\mathcal{O}(Y_\nu^4)$ that is not present in the former.

In order to understand these results, we will perform a completely different and independent analysis of the LFVHD rates within the ISS model. Instead of using the physical neutrino basis, we will perform our computation of the LFVHD widths directly in the chiral

electroweak interaction basis with left- and right-handed neutrinos being the fields propagating in the loops. This will allow us to express the results explicitly in terms of the most relevant model parameters, namely, the neutrino Yukawa coupling matrix Y_ν and the right-handed mass matrix M_R.

We will do this new one-loop computation by using the Mass Insertion Approximation (MIA), which turns out to be a very powerful tool in presence of heavy right-handed neutrinos. In this context, the MIA provides the results in terms of a well defined expansion in powers of Y_ν, which is the unique relevant coupling originating lepton flavor violation in this model, and therefore it is a very useful and convenient method for an easier and clearer interpretation of the related phenomenology.

For the present study of the $H \to \ell_k \bar{\ell}_m$ decay amplitude we will calculate this MIA expansion first to the leading order, $\mathcal{O}((Y_\nu Y_\nu^\dagger)_{km})$, and second to the next to leading order $\mathcal{O}((Y_\nu Y_\nu^\dagger Y_\nu Y_\nu^\dagger)_{km})$. In addition, we will also use the MIA to compute the one-loop effective vertex $H\ell_k\ell_m$, that is the relevant one for these decays. For this purpose, we will explore the proper large M_R mass expansion, which in the present case we must apply for the assumed mass hierarchy,

$$m_{\ell_{i,j}} \ll vY_\nu, m_W, m_H \ll M_R \,, \tag{3.24}$$

with $m_{\ell_{i,j}}$ the lepton masses, v the Higgs vacuum expectation value, and m_W and m_H, the W boson and Higgs particle masses, respectively. As we will see, the most appealing feature of our computation is that it provides very simple formulas, which turn out to work very well, for both the one-loop effective $H\ell_k\ell_m$ LFV vertex and the partial width $\Gamma(H \to \ell_k \bar{\ell}_m)$ in terms of the most relevant parameters Y_ν and M_R. These simple formulas could be easily used by other authors to rapidly estimate, without the need of a heavy numerical computation, the LFVHD rates with their own inputs for Y_ν and M_R. Moreover, since these results are based only in the mass hierarchy in Eq. (3.24) and the fact that Y_ν is the main source of LFV, they could presumably be used in alternative neutrino models that share these properties. In order to make this statement clearer, we explain in more detail the hypothesis behind our calculation in the next section.

3.3.1 The proper basis and Feynman rules for a MIA computation

In order to use the MIA for the computation of the one-loop generated effective $H\ell_k\ell_m$ vertex from right-handed neutrinos, it is important first to choose the proper EW interaction basis and to set up the necessary Feynman rules in terms of these fields. The main point of the MIA is precisely based on the use of the EW basis instead of the mass basis which is the one usually used in the literature for the one-loop generated LFV observables in models with massive Majorana neutrinos. Nevertheless, these computations can be even further simplified by choosing the proper EW basis for each model, as we will discuss in the following.

In the case of the ISS model, the 9×9 mass matrix in Eq. (1.35) provides all the relevant masses and mass insertions for the EW eigenstates that are needed for our computation. These mass insertions connect two different neutrino states, they are in general flavor non-diagonal, and can be expressed in terms of the three 3×3 matrices m_D, μ_X and M_R. Specifically, the mass insertion given by m_D connects ν_L and ν_R fields, M_R connects ν_R and X, and μ_X connects two X. To simplify the computation, we will use again the freedom of redefining the new fields (ν_R, X) in such a way that the M_R matrix is flavor diagonal. Thus, all the flavor violation is contained in the matrices μ_X and m_D. Nevertheless, since we are working with μ_X being extremely small as to accommodate the light neutrino masses, this mass matrix will be irrelevant for the LFV physics that we will study in this Thesis. Therefore, the only relevant flavor violating insertion will be provided by the m_D matrix and, in consequence, by the Yukawa coupling matrix Y_ν.

On the other hand, it should be noticed that the flavor preserving mass insertions given by M_R can be very large if M_R is taken to be heavy, as it will be our case with M_R being at the TeV scale. Since we are finally interested in a perturbative MIA computation of the one-loop LFV Higgs form factors and effective vertices that are valid for heavy M_R masses, we find convenient to use a different chiral basis where 'the big insertions' given by M_R are resumed in such a way that the 'large mass' M_R appears effectively in the denominator of the propagators of the new states. The key point in choosing this proper chiral basis is provided by the fact that for the quantities of our interest here, having H, ℓ_k and ℓ_m in the external particles, the only neutrino states that interact with them are ν_L and ν_R. The singlet fields X interact exclusively with the ν_R fields via the M_R mass insertions and, therefore, they will only appear in the computation of the loop diagrams for LFV as internal intermediate states inside internal lines that start and end with ν_R's. This motivates clearly our choice of modified propagators for the ν_R fields which are built on purpose to include inside all the effects of the sequential insertions of the X fields, given each of these insertions by M_R. More concretely, we sum all the M_R insertions and define two types of modified propagators: one with the same initial and final particle, corresponding to an even number of M_R mass insertions which we call *fat propagators*, and one with different initial and final particles, corresponding to an odd number of insertions. The *fat propagator*, which propagates a ν_R into a ν_R and contains the sum of all the infinite series of even number of M_R insertions due to the interactions with X, is the one we need for the present computation. The details of the procedure to reach this proper chiral basis and the derivation of the modified propagators are explained in App. E.1. Similar results are obtained within the context of the Flavor Expansion Theorem[2] [256, 257].

In order to complete the set-up for our computations, we summarize the relevant Feynman rules in our previously chosen proper chiral basis in Fig. 3.17. These include the relevant

---

[2]We warmly thank Michael Paraskevas for his kind comment about the similarities between our *fat propagators* and the results in the Flavor Expansion Theorem.
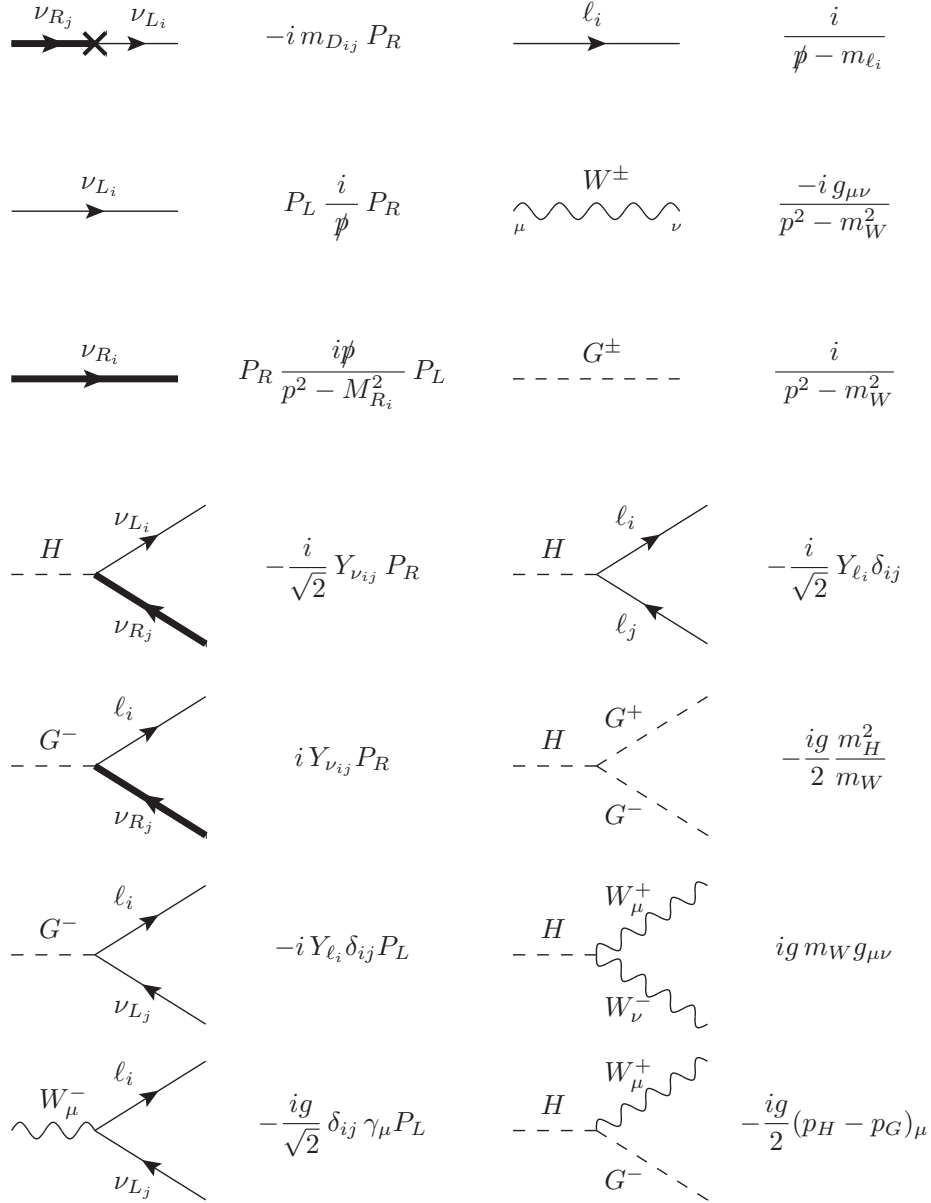
Figure 3.17: Relevant Feynman Rules for the present MIA computation of $\mathrm{BR}(H \to \ell_k \bar{\ell}_m)$ in the Feynman-'t Hooft gauge. The rules involving neutrinos are written in terms of the proper EW chiral basis for ν_R and ν_L, as defined in the text. For completeness, some additional SM Feynman rules that are needed are also included. The momenta p_H and p_G are incoming. The thick solid line represents the *fat propagator* of ν_R introduced in the text.

flavor changing mass insertions, given by m_D, the relevant propagators, both the usual SM EW propagators and the new *fat propagators* of the ν_R's, as well as the relevant interaction vertices needed for our computation, both the SM EW vertices and the new ones involving the ν_R's.

Finally, we want to stress that, although we have considered the ISS model to make our computations, our results could be applied in practice to any low scale seesaw model that leads to the same Feynman rules as in Fig. 3.17. These are indeed quite generic Feynman rules in models with right-handed heavy neutrinos. The few specific requirements are that the only relevant LFV source is the Yukawa neutrino coupling matrix and that the heavy right-handed neutrino propagator is like our *fat propagator* introduced above.

3.3.2 $\Gamma(H \to \ell_k \bar{\ell}_m)$ to one-loop within the MIA

Once we have introduced the set-up for our MIA calculation, we are ready to compute the LFVHD rates. We perform a diagrammatic MIA calculation of $\Gamma(H \to \ell_k \bar{\ell}_m)$ considering the following points:

1. We use the EW chiral neutrino basis.
2. We treat the external particles H, ℓ_k and $\bar{\ell}_m$ in their physical mass basis.
3. We use the *fat propagator* for the heavy right-handed neutrinos and the Feynman rules as described in Section 3.3.1.
4. The LFVHD amplitude is evaluated at the one-loop order in the Feynman-'t Hooft gauge. In the App. E.4 we show that the same result is obtained in the Unitary gauge.
5. All the loops must contain one right-handed neutrino at least since they are the only particles transmitting LFV through the flavor off-diagonal neutrino Yukawa matrix entries.
6. According to the Feynman rules in Fig. 3.17, these flavor changing Yukawa couplings, appear just in two places, the mass insertions given by m_D and the interactions of H with ν_L and ν_R, being proportional to Y_ν.
7. All the one-loop diagrams will get an even number of powers of Y_ν, since Y_ν appears twice for each ν_R in an internal line, and because of the absence of interactions containing two right-handed neutrinos.
8. We further simplify our computation by considering that the diagonal matrix M_R has degenerate entries, i.e, $M_{R_i} \equiv M_R$. The generalization to the non-degenerate case will be commented in App. E.

In summary, taking into account all the points exposed above, the one-loop contributions to the LFV Higgs decay amplitude, as computed with the MIA, will then be given by an expansion in even powers of Y_ν, concretely as $Y_\nu Y_\nu^\dagger$. Therefore, the form factors defined

in Eq. (3.4), which we recall here for completeness:

$$i\mathcal{M} = -ig\bar{u}_{\ell_k}(-p_2)(F_L P_L + F_R P_R)v_{\ell_m}(p_3)\,, \tag{3.25}$$

can be written as follows:

$$F_{L,R}^{\mathrm{MIA}\ (Y^2+Y^4)} = \left(Y_\nu Y_\nu^\dagger\right)^{km} f_{L,R}^{(Y^2)} + \left(Y_\nu Y_\nu^\dagger Y_\nu Y_\nu^\dagger\right)^{km} f_{L,R}^{(Y^4)}\,, \tag{3.26}$$

where $\mathcal{O}(Y_\nu Y_\nu^\dagger)$ are the Leading Order (LO) terms and $\mathcal{O}(Y_\nu Y_\nu^\dagger Y_\nu Y_\nu^\dagger)$ the Next to Leading Order (NLO) terms in our expansion. We expect that, in the perturbativity regime of the neutrino Yukawa couplings, the next terms in this expansion, *i.e.* those of $\mathcal{O}(Y_\nu^6)$ and higher, will be very tiny and can be safely neglected. Furthermore, as will be explained in more detail below, considering this expansion in powers of Y_ν and working with the hypothesis of M_R being the heaviest scale, also lead to an implicit ordering of the various contributions in powers of v/M_R. In fact, we will demonstrate, by an explicit analytical expansion of the form factors in the large $M_R \gg v$ limit, that the dominant terms of the two contributions in Eq. (3.26), the LO $f_{L,R}^{(Y^2)}$ and the NLO $f_{L,R}^{(Y^4)}$, indeed scale both as $(v/M_R)^2$. In contrast, the next order contributions, *i.e* those of $\mathcal{O}(Y_\nu^6)$, scale as $(v/M_R)^4$, and therefore they will be negligible for heavy right-handed neutrinos, even when the Yukawa couplings are sizable. Thus, considering just these two first terms in Eq. (3.26) of the MIA expansion will be sufficient to approach quite satisfactorily the full one-loop calculation of the neutrino mass basis in the case of $\mu_X \ll m_D \ll M_R$ that we are interested in.

In order to estimate the validity of the MIA results for the present study of the LFV Higgs decays we include a numerical comparison of these MIA results with those of the full one-loop computation in the physical neutrino basis presented in Section 3.1. For an easy comparison, we adopt in the MIA the same notation (i) (i=1,...,10) for the ten types of generic diagrams as in the full computation shown in Fig. 3.1. They can be classified into diagrams with vertex corrections, i=1,..,6, and diagrams with external leg corrections, i=7,..,10.

For the one-loop computation in the MIA, we also follow a diagrammatic procedure that consists of the systematic insertion of right-handed neutrino *fat-propagators* in all possible places inside the loops which are built with the interaction vertices and propagators of Fig. 3.17. Generically, diagrams with one right-handed neutrino propagator will contribute to the form factors of $\mathcal{O}(Y_\nu^2)$, whereas diagrams with two right-handed neutrino propagators will contribute to the form factors of $\mathcal{O}(Y_\nu^4)$. We show in Figs. 3.18, 3.19, 3.20 and 3.21 the relevant one-loop diagrams in the MIA corresponding to the dominant contributions of the LO and the NLO, respectively, in Eq. (3.26). These are also classified into those of vertex corrections and those of leg corrections type. The MIA form factors are then obtained accordingly as the sum of all these contributions that can be summarized as follows:

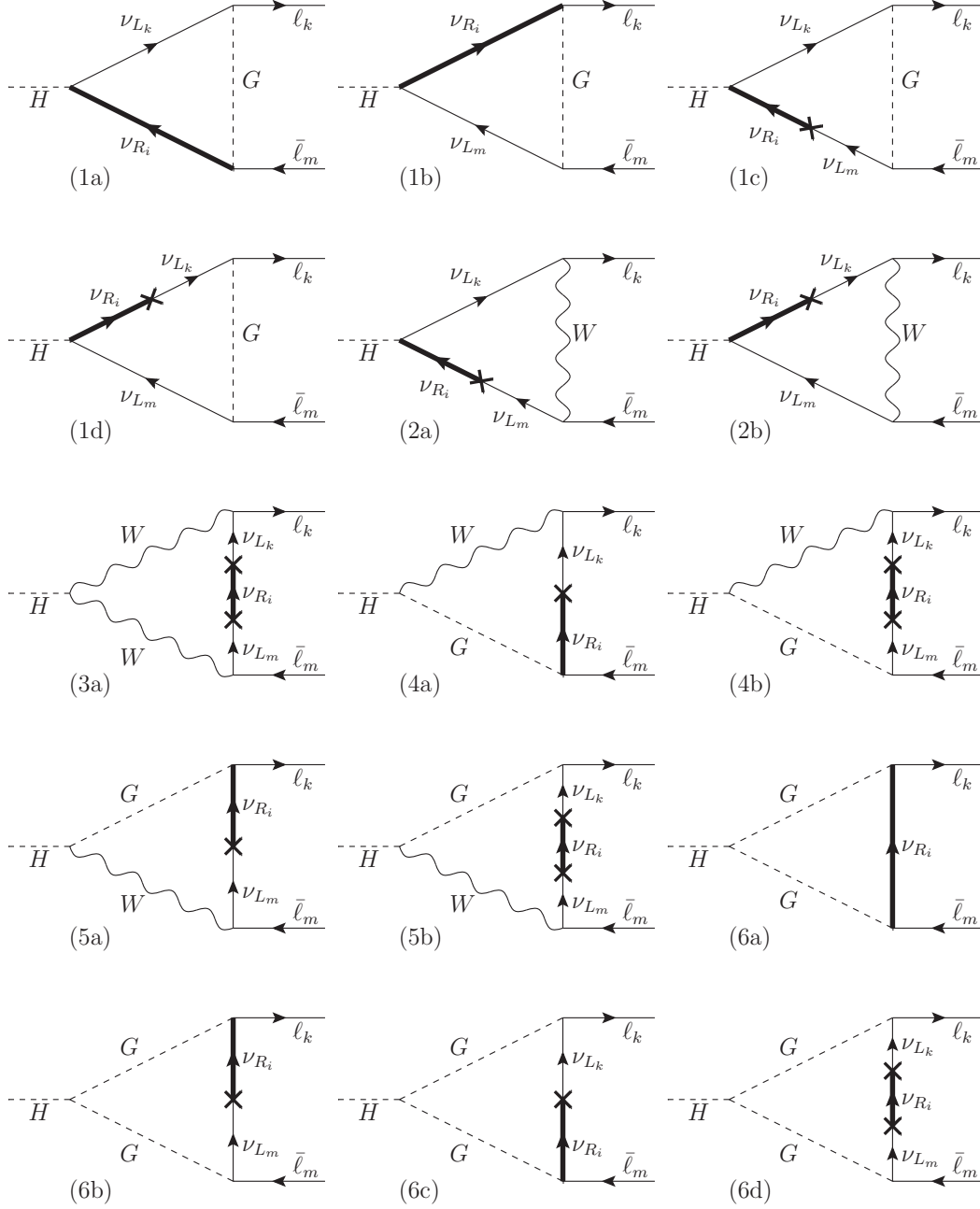$$F_{L,R}^{\mathrm{MIA}} = \sum_{i=1}^{10} F_{L,R}^{\mathrm{MIA(i)}}\,. \tag{3.27}$$

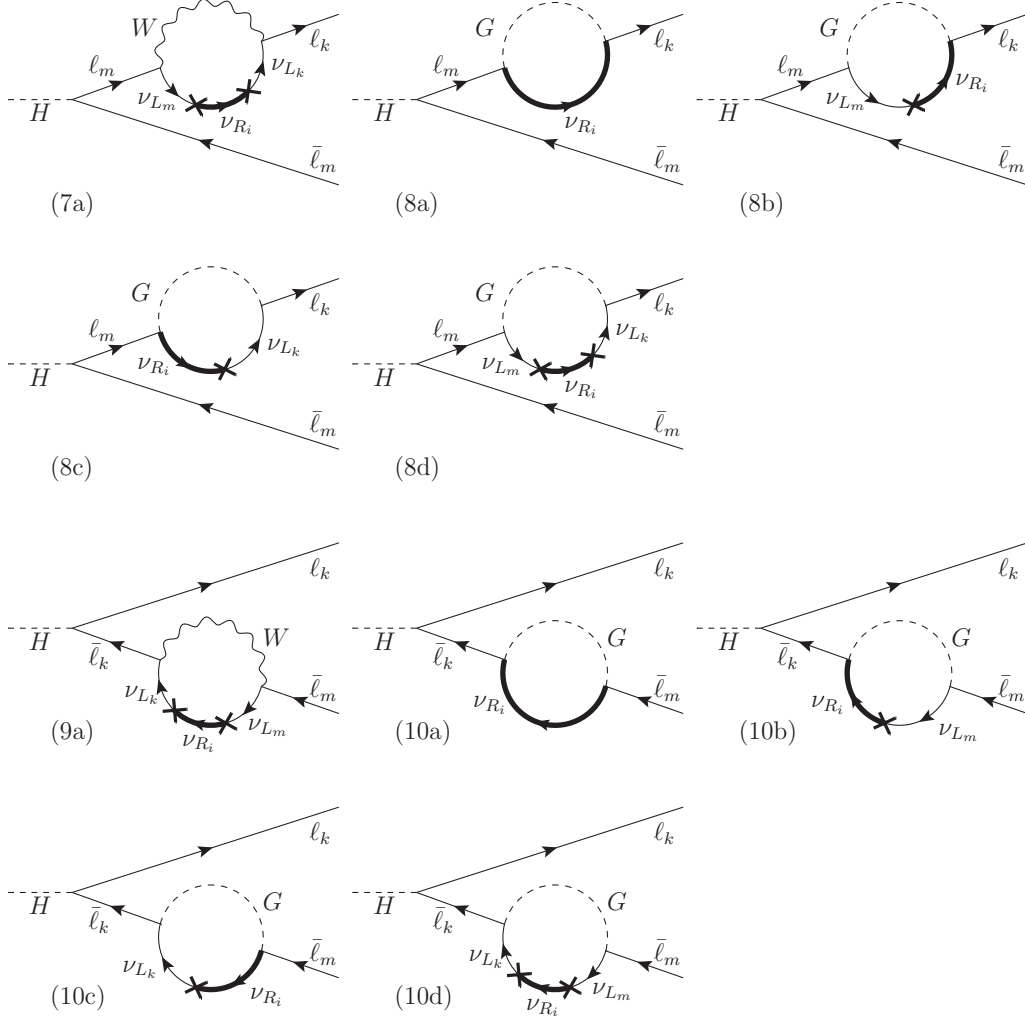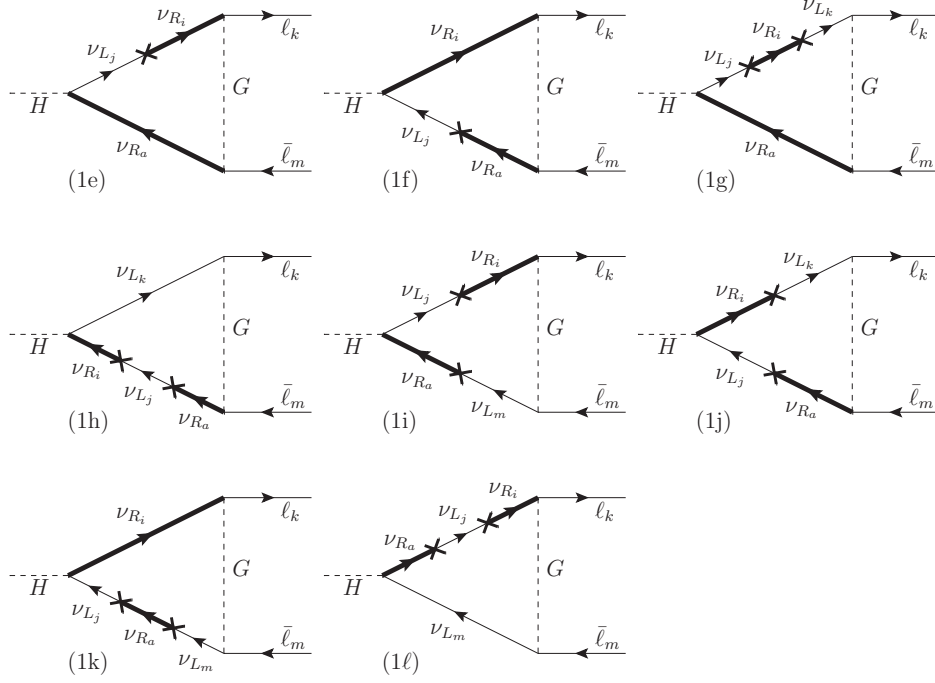Figure 3.18: Relevant vertex diagrams for the MIA form factors of LFVHD to $\mathcal{O}(Y_\nu^2)$.

Figure 3.19: Relevant external leg diagrams for the MIA form factors of LFVHD to $\mathcal{O}(Y_\nu^2)$.

At LO, i.e, $\mathcal{O}(Y_\nu^2)$, each $F_{L,R}^{\text{MIA(i)}}$ receives contributions from diagrams all containing 1 right-handed neutrino propagator and one of these three combinations: i) 1 vertex with ν_R and 1 m_D insertion, ii) 0 vertices with ν_R and 2 m_D insertions, iii) 2 vertices with ν_R and 0 m_D insertions. This leads to the relevant diagrams in Figs. 3.18 and 3.19 whose contributions are given, in an obvious correlated notation, by:

$$F_{L,R}^{\text{MIA(1) } (Y^2)} = F_{L,R}^{(1a)} + F_{L,R}^{(1b)} + F_{L,R}^{(1c)} + F_{L,R}^{(1d)} \,,$$
$$F_{L,R}^{\text{MIA(2) } (Y^2)} = F_{L,R}^{(2a)} + F_{L,R}^{(2b)} \,,$$

Figure 3.20: Relevant vertex diagrams for the MIA form factors of LFVHD to $\mathcal{O}(Y_\nu^4)$.

$$
\begin{aligned}
F_{L,R}^{\text{MIA}(3)\ (Y^2)} &= F_{L,R}^{(3a)} , \\
F_{L,R}^{\text{MIA}(4)\ (Y^2)} &= F_{L,R}^{(4a)} + F_{L,R}^{(4b)} , \\
F_{L,R}^{\text{MIA}(5)\ (Y^2)} &= F_{L,R}^{(5a)} + F_{L,R}^{(5b)} , \\
F_{L,R}^{\text{MIA}(6)\ (Y^2)} &= F_{L,R}^{(6a)} + F_{L,R}^{(6b)} + F_{L,R}^{(6c)} + F_{L,R}^{(6d)} , \\
F_{L,R}^{\text{MIA}(7)\ (Y^2)} &= F_{L,R}^{(7a)} , \\
F_{L,R}^{\text{MIA}(8)\ (Y^2)} &= F_{L,R}^{(8a)} + F_{L,R}^{(8b)} + F_{L,R}^{(8c)} + F_{L,R}^{(8d)} , \\
F_{L,R}^{\text{MIA}(9)\ (Y^2)} &= F_{L,R}^{(9a)} , \\
F_{L,R}^{\text{MIA}(10)\ (Y^2)} &= F_{L,R}^{(10a)} + F_{L,R}^{(10b)} + F_{L,R}^{(10c)} + F_{L,R}^{(10d)}.
\end{aligned}
\tag{3.28}
$$

The explicit analytical results for all these form factors are given in Eqs. (E.8)-(E.11) of the App. E.2. These results are expressed in terms of the usual one-loop Veltman-Passarino functions of two points (B_0 and B_1), three points (C_0, C_{11}, C_{12} and $\tilde{C}_0$) and four points (D_{12}, D_{13} and $\tilde{D}_0$) whose definitions are given in Eqs. (E.5)-(E.7).

At NLO, i.e $\mathcal{O}(Y_\nu^4)$, each $F_{L,R}^{\text{MIA}(i)}$ receives contributions from diagrams all containing 2
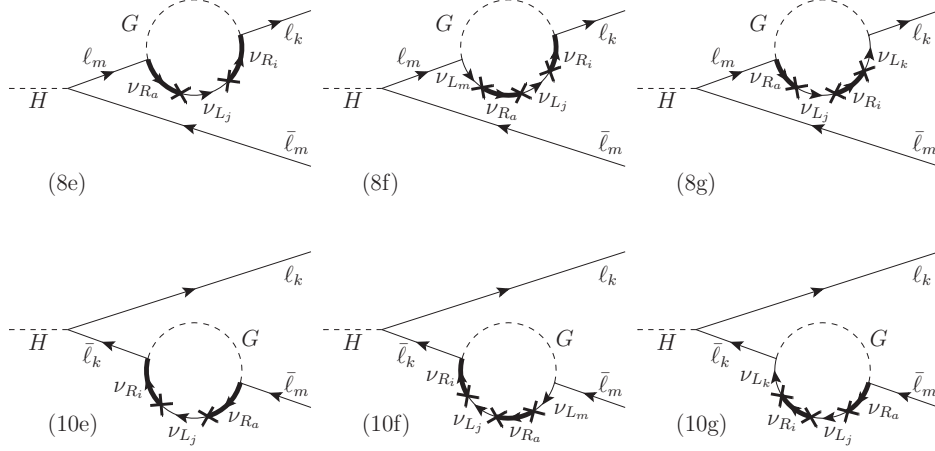
Figure 3.21: Relevant external leg diagrams for the MIA form factors of LFVHD to $\mathcal{O}(Y_\nu^4)$.

right-handed neutrino propagators and one of these three combinations: i) 2 vertices with ν_R and 2 m_D insertions, ii) 3 vertices with ν_R and 1 m_D insertion, iii) 1 vertex with ν_R and 3 m_D insertions. Other possible combinations will provide subleading corrections in the heavy M_R case of our interest, since they will come with extra powers of M_R in the denominator. Thus, we find that the most relevant diagrams are those of type (1), (8) and (10) summarized in Figs. 3.20 and 3.21, whose respective contributions are given by:

$$
\begin{aligned}
F_{L,R}^{\mathrm{MIA}(1)\ (Y^4)} &= F_{L,R}^{(1e)} + F_{L,R}^{(1f)} + F_{L,R}^{(1g)} + F_{L,R}^{(1h)} + F_{L,R}^{(1i)} + F_{L,R}^{(1j)} + F_{L,R}^{(1k)} + F_{L,R}^{(1\ell)} \,, \\
F_{L,R}^{\mathrm{MIA}(8)\ (Y^4)} &= F_{L,R}^{(8e)} + F_{L,R}^{(8f)} + F_{L,R}^{(8g)} \,, \\
F_{L,R}^{\mathrm{MIA}(10)\ (Y^4)} &= F_{L,R}^{(10e)} + F_{L,R}^{(10f)} + F_{L,R}^{(10g)} .
\end{aligned}
\tag{3.29}
$$

Their explicit analytical results are collected in Eqs. (E.8)-(E.11) of the App. E.2.

Some comments about the analytical properties of the previous MIA results are in order. First, we analyze their ultraviolet behavior. From the results presented in Section 3.1, we know that in the full one-loop computation of the mass basis only the contributions to the amplitude from diagrams (1), (8) and (10) of Fig. 3.1 are ultraviolet divergent separately, and that the total sum from these diagrams (1)+(8)+(10) is finite, therefore providing a total one-loop amplitude that is ultraviolet finite as it must be. We have explored the divergences of the MIA diagrams and find the same results. Our calculation in the MIA also shows that diagrams of type (2), (3), (4), (5), (6), (7) and (9) are convergent separately, while each contribution of $\mathcal{O}(Y_\nu^2)$ from diagrams (1), (8) and (10) are divergent, although their divergences cancel out again in their sum. For this reason, in the next numerical analysis,

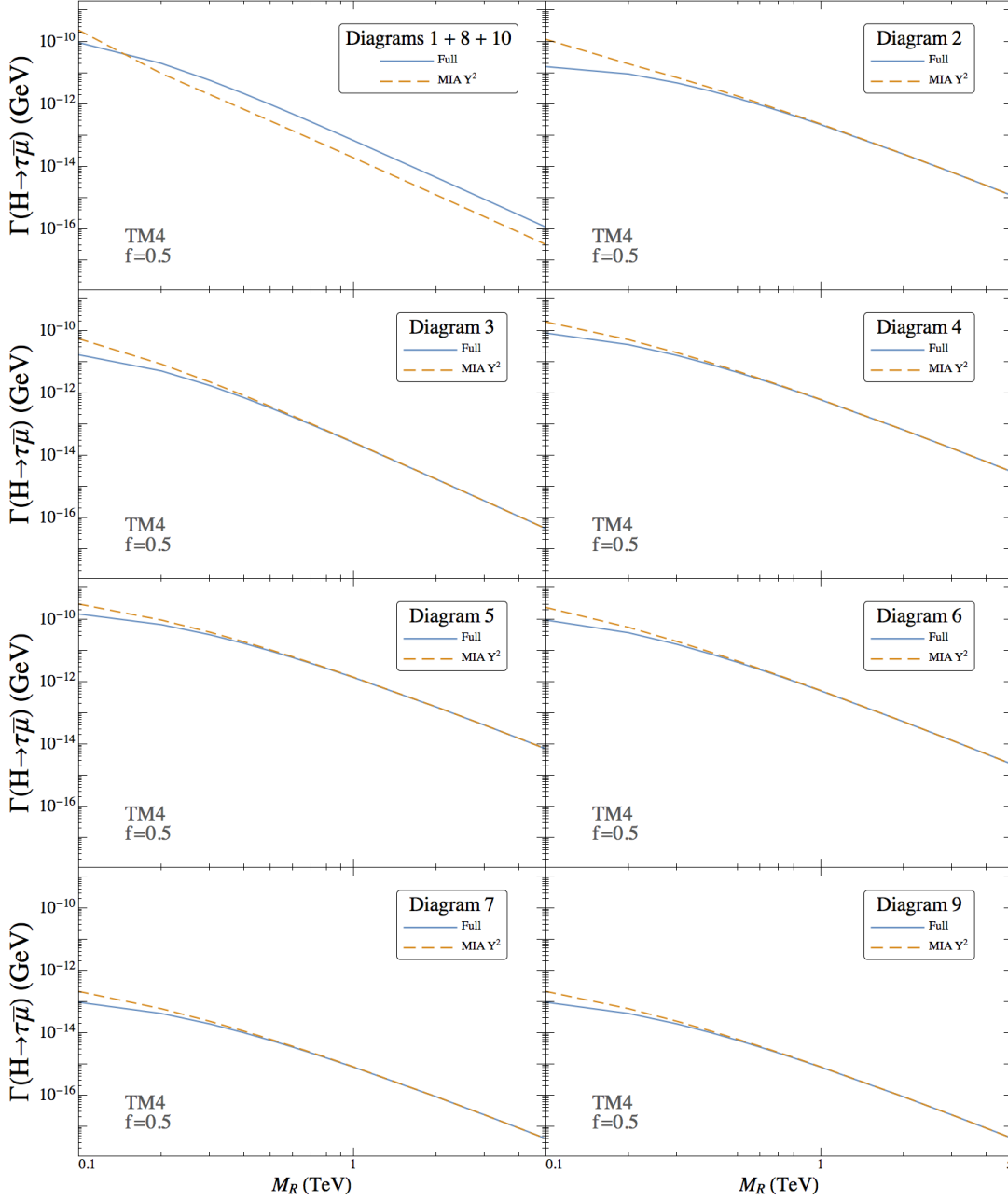Figure 3.22: Contributions from the various diagrams to $\Gamma(H \to \tau\bar{\mu})$ as a function of M_R in the TM-4 scenario from Table 2.4 for $f = 0.5$. Dashed lines are the predictions from the MIA to $\mathcal{O}(Y_\nu^2)$, while solid lines are from the full one loop computation in the mass basis.
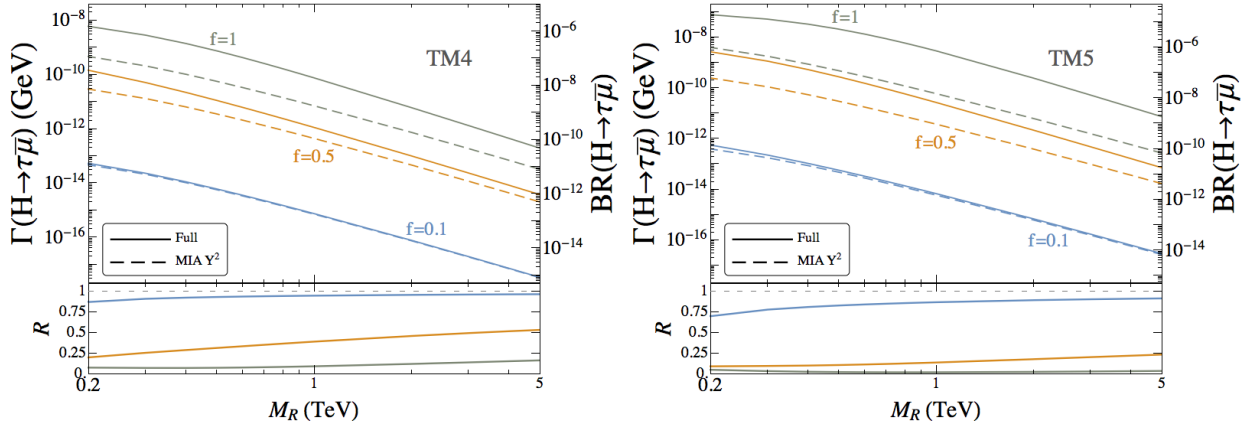
Figure 3.23: Predictions for the partial width $\Gamma(H \to \tau\bar{\mu})$ and branching ratio $\mathrm{BR}(H \to \tau\bar{\mu})$ as a function of M_R. The dashed lines are the predictions from the MIA to $\mathcal{O}(Y_\nu^2)$. The solid lines are the predictions from the full-one loop computation of the mass basis. Here the examples TM4 (left panel) and TM5 (right panel) with f=0.1,0.5,1, as explained in the text, are chosen. In the bottom of these plots the ratio $R = \Gamma_{\mathrm{MIA}}/\Gamma_{\mathrm{full}}$ is also shown.

whenever we present results for each diagram we will consider the sum (1)+(8)+(10), which is convergent and therefore meaningful, instead of the contributions from each of these diagrams separately.

Second, it is also worth to comment on the gauge invariance of our previous MIA results for the decay amplitude, computed in the Feynman-'t Hooft gauge. In order to prove the gauge invariance of our results, we have computed the amplitude also in other gauges and checked that we get the same result. Specifically, we have computed the form factors $F_{L,R}$ in the Unitary gauge and in an arbitrary R_ξ gauge. The details of the Unitary gauge computation are collected in App. E.4.

Next, we show our numerical results of these LO results in the MIA, together with the outcome from the full computation in the physical basis. We display our results only for scenarios TM-4 and TM-5 in Table 2.4, although we have found similar conclusions for other scenarios and input values of Y_ν.

We first display in Fig. 3.22 the partial decay width of the full calculation together with our predictions from the MIA to $\mathcal{O}(Y_\nu^2)$, separating the contributions from the various diagrams. We observe here that the contribution from each diagram (or group of diagrams in the case of (1)+(8)+(10)) to the form factor and in consequence to the width decreases with M_R. This behavior will be very well understood with our simple formulas of the large M_R expansions in Eq. (E.14). In particular, when adding the three contributions (1)+(8)+(10) in the MIA we will see explicitly the cancellation of the divergent contributions from Δ terms
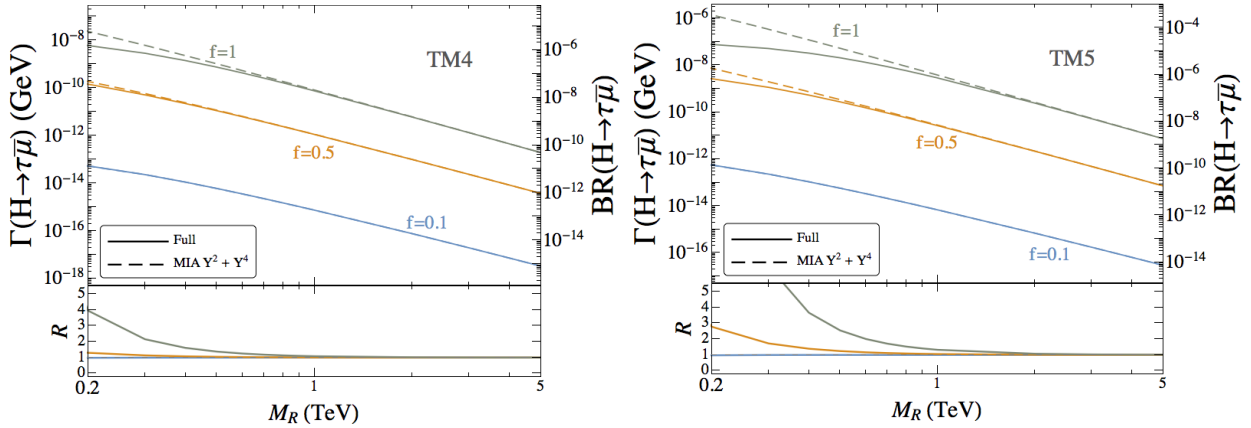
100

Figure 3.24: Predictions for the partial width $\Gamma(H \to \tau\bar{\mu})$ and branching ratio $BR(H \to \tau\bar{\mu})$ as a function of M_R. The dashed lines are the predictions from the MIA to $\mathcal{O}(Y_\nu^2 + Y_\nu^4)$. The solid lines are the predictions from the full-one loop computation of the mass basis. Here the examples TM4 (left panel) and TM5 (right panel) with f=0.1,0.5,1, as explained in the text, are chosen. In the bottom of these plots the ratio $R = \Gamma_{\text{MIA}}/\Gamma_{\text{full}}$ is also shown.

and the corresponding cancellation of the regularization μ scale dependent terms. The final behavior of the remaining finite terms in each form factor will go generically as $\sim (v^2/M_R^2)$, and in addition there are also logarithmic terms going as $\sim (v^2/M_R^2)(\text{Log}(v^2/M_R^2))$.

We see in Fig. 3.22 a consistent agreement between the MIA and full results for diagrams (2), (3), (4), (5), (6), (7) and (9). For the sum (1)+(8)+(10), the MIA reproduces the behavior of the full calculation very well but there is a mismatch in the partial decay width, that depends on the value of f. The larger f, the worse the discrepancy between them. This disagreement is then translated to the total partial width, as can be seen in Fig. 3.23. In order to give a quantitative statement on this observation, we define the ratio $R = \Gamma_{\text{MIA}}/\Gamma_{\text{full}}$. From the bottom of Fig. 3.23, we have R close to 1 for low values of f ($f = 0.1$) and large M_R above 1 TeV. If we increase f up to 1, poor values of R far from 1 are obtained in the full M_R interval studied, so the MIA results to $\mathcal{O}(Y_\nu^2)$ do not reproduce satisfactorily the results of the full calculation. We conclude that for large values of f, which are the interesting ones from a phenomenological point of view, the MIA only reproduces the functional behavior but not the numerical values. Thus, it is necessary to include in the MIA computation the next order contributions, i.e. $\mathcal{O}(Y_\nu^4)$.

The results after including all the relevant $\mathcal{O}(Y_\nu^2 + Y_\nu^4)$ contributions are shown in Fig. 3.24. We can clearly see that the sum of MIA diagrams is in very good agreement with the full results for different values of f. Therefore, we can conclude that our MIA calculation with the inclusion of the most relevant $\mathcal{O}(Y_\nu^4)$ terms, corrects the $\mathcal{O}(Y_\nu^2)$ contributions and
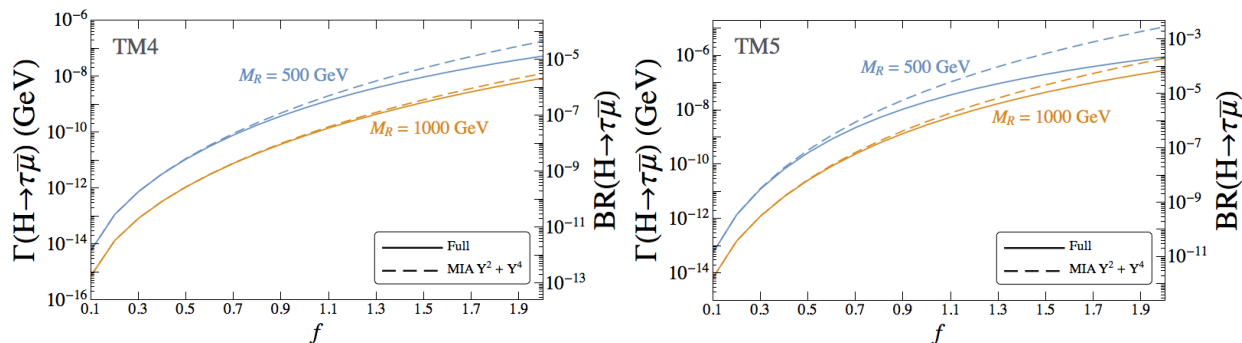
Figure 3.25: Predictions for the partial width $\Gamma(H \to \tau\bar{\mu})$ and branching ratio $\mathrm{BR}(H \to \tau\bar{\mu})$ as a function of the global Yukawa coupling strength f. The dashed lines are the predictions from the MIA to $\mathcal{O}(Y_\nu^2 + Y_\nu^4)$. The solid lines are the predictions from the full-one loop computation of the mass basis. Here the examples TM4 (left panel) and TM5 (right panel) with $M_R = 500, 1000$ GeV, as explained in the text, are chosen.

achieves a better fit to the full numerical results for this process in the large $M_R \gg vY_\nu$ mass range. In particular, we see this improvement with respect to $\mathcal{O}(Y_\nu^2)$ contributions from the closeness of R to 1 for different values of f. How large M_R should be in order to get a good numerical prediction of the LFVHD rates depends obviously on the size of the Yukawa coupling. For small Yukawa coupling, i.e. for small $f \lesssim 0.5$ the MIA works quite well for M_R above 400 GeV, whereas for larger couplings, say f above 0.5, the MIA also provides a good result but requires heavier M_R, above 1000 GeV.

Before going to the derivation of the effective vertex in the large M_R limit, we concentrate on the dependence of the branching ratios with f. In Fig. 3.25, we show the partial width and branching ratio as a function of f for the scenarios TM4 and TM5 with two different values of M_R. In the perturbativity range of Yukawa couplings (implying approximately $f \lesssim 3.5$) we find a significant increase in the branching ratios up to $\mathcal{O}(10^{-4})$ for large $f \sim \mathcal{O}(2)$. However, for such large f values the MIA provides an accurate prediction only for large M_R values, say above 1000 GeV, as can be seen in Fig. 3.25. Overall, we can conclude that the results for the MIA form factors to $\mathcal{O}(Y_\nu^2 + Y_\nu^4)$ work reasonably well for heavy M_R enough, say above 1 TeV and f values not too large, such that Y_ν is within the perturbativity region, given by $Y_\nu^2/4\pi < 1$.

3.3.3 Computation of the one-loop effective vertex for LFVHD

In this section we present our results in the large M_R limit of the form factors involved in our computation of the LFVHD rates. In order to reach this simple expression for the effective vertex, valid in the large $M_R \gg v$ regime, we perform a systematic expansion in powers

of (v/M_R) of the one-loop MIA amplitude that we have computed in the previous section. Generically, the first order in this expansion is $\mathcal{O}(v^2/M_R^2)$, the next order is $\mathcal{O}(v^4/M_R^4)$, etc. There is also a logarithmic dependence with M_R, which is not expanded but left explicit in this calculation. In the final result for the effective vertex we will be interested just in the leading terms of $\mathcal{O}(v^2/M_R^2)$ which are by far the dominant ones for sufficiently heavy M_R.

We start with the formulas found in the previous section and in App. E.2 for the one-loop LFVHD form factors in the MIA. Assuming the hierarchy $m_\ell \ll m_W, m_H \ll M_R$, we may first ignore the tiny contributions that come from terms in the sum with factors of the lepton masses in our analytical results of Eqs. (E.8)-(E.11). This leads to the following compact formula for the total one-loop MIA form factors to $\mathcal{O}(Y_\nu^2 + Y_\nu^4)$,

$$
\begin{aligned}
F_L^{\text{MIA}} = {} & \frac{1}{32\pi^2} \frac{m_{\ell_k}}{m_W} \left(Y_\nu Y_\nu^\dagger\right)^{km} \Big(\tilde{C}_0(p_2, p_1, m_W, 0, M_R) - B_0(0, M_R, m_W) \\
& - 2m_W^2 \big((C_0 + C_{11} - C_{12})(p_2, p_1, m_W, 0, M_R) + (C_{11} - C_{12})(p_2, p_1, m_W, M_R, 0)\big) \\
& + 4m_W^4 (D_{12} - D_{13})(0, p_2, p_1, 0, M_R, m_W, m_W) \\
& - 2m_W^2 m_H^2 D_{13}(0, p_2, p_1, 0, M_R, m_W, m_W) + 2m_W^2 \big(C_0 + C_{11} - C_{12}\big)(p_2, p_1, M_R, m_W, m_W) \\
& + m_H^2 \big(C_0 + C_{11} - C_{12}\big)(p_2, p_1, M_R, m_W, m_W)\Big) \\
& + \frac{1}{32\pi^2} \frac{m_{\ell_k}}{m_W} \left(Y_\nu Y_\nu^\dagger Y_\nu Y_\nu^\dagger\right)^{km} v^2 \Big(-2(C_{11} - C_{12})(p_2, p_1, m_W, M_R, M_R) \\
& + \tilde{D}_0(p_2, 0, p_1, m_W, 0, M_R, M_R) + \tilde{D}_0(p_2, p_1, 0, m_W, 0, M_R, M_R) - C_0(0, 0, M_R, M_R, m_W)\Big).
\end{aligned}
\tag{3.30}
$$

Here, we have ordered the various contributions as follows: the first line is from diagrams (1)+(8)+(10), the second line from (2), the third line from (3), the fourth line from (4)+(5), the fifth line from (6) and the last two lines containing the $\mathcal{O}(Y_\nu^4)$ contribution are from (1)+(8)+(10). Notice that there are not final contributions from (7)+(9), since they cancel each other. Similarly, for the right-handed form factor we get:

$$
\begin{aligned}
F_R^{\text{MIA}} = {} & \frac{1}{32\pi^2} \frac{m_{\ell_m}}{m_W} \left(Y_\nu Y_\nu^\dagger\right)^{km} \Big(\tilde{C}_0(p_2, p_1, m_W, M_R, 0) - B_0(0, M_R, m_W) \\
& - 2m_W^2 (C_{12}(p_2, p_1, m_W, 0, M_R) + (C_0 + C_{12})(p_2, p_1, m_W, M_R, 0)) \\
& + 4m_W^4 D_{13}(0, p_2, p_1, 0, M_R, m_W, m_W) \\
& - 2m_W^2 m_H^2 (D_{12} - D_{13})(0, p_2, p_1, 0, M_R, m_W, m_W) + 2m_W^2 \big(C_0 + C_{12}\big)(p_2, p_1, M_R, m_W, m_W) \\
& + m_H^2 \big(C_0 + C_{12}\big)(p_2, p_1, M_R, m_W, m_W)\Big) \\
& + \frac{1}{32\pi^2} \frac{m_{\ell_m}}{m_W} \left(Y_\nu Y_\nu^\dagger Y_\nu Y_\nu^\dagger\right)^{km} v^2 \Big(-2C_{12}(p_2, p_1, m_W, M_R, M_R) \\
& + \tilde{D}_0(p_2, p_1, 0, m_W, M_R, M_R, 0) + \tilde{D}_0(p_2, 0, p_1, m_W, M_R, M_R, 0) - C_0(0, 0, M_R, M_R, m_W)\Big),
\end{aligned}
$$

$$(3.31)$$

where the explanation for the various contributions in each line is as specified for F_L. Note also that the right-handed form factor can be obtained from the left-handed one by exchanging p_2 and m_{ℓ_k} with p_3 and m_{ℓ_m}, respectively. From the previous compact formulas, assuming the hierarchy $m_{\ell_k} \gg m_{\ell_m}$, it is also clear that the left-handed form factor is the dominant one for the decay mode $H \to \ell_k \bar{\ell}_m$. Conversely, the right-handed form factor will be the dominant one in the opposite case $m_{\ell_m} \gg m_{\ell_k}$. For the rest of this section, we will assume $m_{\ell_k} \gg m_{\ell_m}$ and, therefore, we will focus on the dominant F_L.

The next step is to perform the large M_R expansion of the loop integrals appearing in the MIA form factor. The details of how we perform these expansions are explained in App. E.3, where we also collect the results for both the loop integrals and the separate contributions to the form factors from all type of diagrams, i=1..10. Finally, by plugging these large M_R expansions into Eq. (3.30) we get the one-loop effective vertex, $F_L \simeq V^{\text{eff}}_{H\ell_k\ell_m}$, which parametrizes the one-loop amplitude of $H \to \ell_k \bar{\ell}_m$ as

$$i\mathcal{M} \simeq -ig\bar{u}_{\ell_k} V^{\text{eff}}_{H\ell_k\ell_m} P_L v_{\ell_m} \,, \tag{3.32}$$

with the corresponding partial decay width:

$$\Gamma(H \to \ell_k \bar{\ell}_m) \simeq \frac{g^2}{16\pi} m_H \big| V^{\text{eff}}_{H\ell_k\ell_m} \big|^2 \,. \tag{3.33}$$

At the end, we find the following simple result for the on-shell Higgs boson effective LFV vertex:

$$V^{\text{eff}}_{H\ell_k\ell_m} = \frac{1}{64\pi^2} \frac{m_{\ell_k}}{m_W} \left[\frac{m_H^2}{M_R^2} \left(r\left(\frac{m_W^2}{m_H^2}\right) + \log\left(\frac{m_W^2}{M_R^2}\right) \right) \left(Y_\nu Y_\nu^\dagger\right)^{km} - \frac{3v^2}{M_R^2} \left(Y_\nu Y_\nu^\dagger Y_\nu Y_\nu^\dagger\right)^{km} \right], \tag{3.34}$$

where,

$$r(\lambda) = -\frac{1}{2} - \lambda - 8\lambda^2 + 2(1 - 2\lambda + 8\lambda^2)\sqrt{4\lambda - 1}\arctan\left(\frac{1}{\sqrt{4\lambda - 1}}\right)$$
$$+ 16\lambda^2(1 - 2\lambda)\arctan^2\left(\frac{1}{\sqrt{4\lambda - 1}}\right). \tag{3.35}$$

Notice that this solution is valid for $m_H < 2m_W$ and that for the physical values of $m_H = 125$ GeV and $m_W = 80.4$ GeV we obtain numerically $r(m_W^2/m_H^2) \sim 0.31$. The partial width is then simplified correspondingly to:

$$\Gamma(H \to \ell_k \bar{\ell}_m)^{\text{MIA}} = \frac{g^2 m_{\ell_k}^2 m_H}{2^{16}\pi^5 m_W^2} \left| \frac{m_H^2}{M_R^2} \left(r\left(\frac{m_W^2}{m_H^2}\right) + \log\left(\frac{m_W^2}{M_R^2}\right) \right) \left(Y_\nu Y_\nu^\dagger\right)^{km} - \frac{3v^2}{M_R^2} \left(Y_\nu Y_\nu^\dagger Y_\nu Y_\nu^\dagger\right)^{km} \right|^2. \tag{3.36}$$

Some comments are in order. First we notice that the dominant behavior with M_R of $V_{H\ell_k\ell_m}^{\text{eff}}$ for large M_R goes as $\log(M_R^2)/M_R^2$ and the next dominant one goes as $1/M_R^2$. Second, the terms of $\mathcal{O}(Y_\nu^2)$ depend on m_H, whereas the terms of $\mathcal{O}(Y_\nu^4)$ do not. Notice also that the two contributions of $\mathcal{O}(Y_\nu^2)$ and $\mathcal{O}(Y_\nu^4)$ get M_R^2 in the denominator and not M_R^4 as one could naively expect for the $\mathcal{O}(Y_\nu^4)$ term. Third, we have also checked that we recover the simple phenomenological formula in Eq. (3.10), which we obtained by a naive numerical fit of the dominant contributions at large M_R from diagrams (1)+(8)+(10) in the physical mass basis. Specifically, if we extract the contributions exclusively from diagrams (1), (8) and (10) in our MIA results in Eq. (3.36), we get:

$$\text{BR}(H \to \ell_k\bar{\ell}_m)_{(1)+(8)+(10)}^{\text{MIA}} = \frac{g^2 m_{\ell_k}^2 m_H}{2^{16}\pi^5 m_W^2 \Gamma_H} \left| \frac{m_H^2}{M_R^2} \left(Y_\nu Y_\nu^\dagger\right)^{km} - \frac{3v^2}{M_R^2} \left(Y_\nu Y_\nu^\dagger Y_\nu Y_\nu^\dagger\right)^{km} \right|^2$$

$$\simeq 10^{-7} \frac{v^4}{M_R^4} \left| \left(Y_\nu Y_\nu^\dagger\right)^{km} - 5.7 \left(Y_\nu Y_\nu^\dagger Y_\nu Y_\nu^\dagger\right)^{km} \right|^2, \tag{3.37}$$

where in the last line we have used the numerical values of the physical parameters with $m_H = 125$ GeV and Γ_H given by the predicted value in the SM. As announced, we reach the previous result in Eq. (3.10).

It is also illustrative to compare our previous MIA result in Eq. (3.36) for the partial width in the large M_R regime with the analytical approximate formula that was found in Ref. [76] after expanding the full one-loop computation in the physical neutrino mass basis in inverse powers of the physical heavy neutrino mass m_N. Concretely we compare our result in Eq. (3.36) with those in Eqs. (26), (31)-(34) of Ref. [76], which were obtained assuming $m_H^2/m_W^2 \ll 4$ and $m_H^2/m_N^2 \ll 1$. By doing some algebra to express the physical neutrino couplings $B_{\ell_i j}$ and C_{ij} appearing in those equations in terms of the Yukawa couplings, and by extracting just the m_H independent terms, we obtain a coincidence with our result in Eq. (3.36) in the $m_H \to 0$ limit. Specifically, by using

$$\sum_{i\in\text{Heavy}} B_{\ell_k i} B_{\ell_m i}^* \simeq \frac{v^2}{m_N^2} \left(Y_\nu Y_\nu^\dagger\right)^{km}, \tag{3.38}$$

$$\sum_{i,j\in\text{Heavy}} B_{\ell_k i} C_{ij} B_{\ell_m j}^* \simeq \frac{v^4}{m_N^4} \left(Y_\nu Y_\nu^\dagger Y_\nu Y_\nu^\dagger\right)^{km}, \tag{3.39}$$

and neglecting $\mathcal{O}(1/m_N^4)$ and higher order terms, we get from Ref. [76],

$$\Gamma(H \to \ell_k\bar{\ell}_m)^{\text{full}} \simeq \frac{g^2 m_{\ell_k}^2 m_H}{2^{16}\pi^5 m_W^2} \left| -\frac{3m_W^2}{m_N^2} \left(Y_\nu Y_\nu^\dagger\right)^{km} - \frac{3v^2}{m_N^2} \left(Y_\nu Y_\nu^\dagger Y_\nu Y_\nu^\dagger\right)^{km} \right|^2, \tag{3.40}$$

which matches with our result in Eq. (3.36) after the substitution
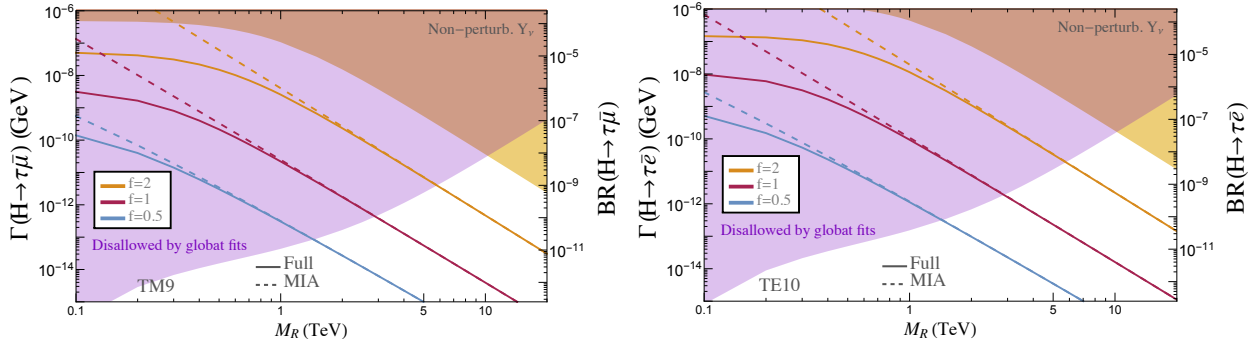
$$(m_H^2/m_W^2)r(m_W^2/m_H^2) \to -3, \tag{3.41}$$

Figure 3.26: Left panel: Predictions for $H \to \tau\bar{\mu}$ with the effective vertex computed with the MIA (dashed lines) for Y_ν^{TM9}. Right panel: Predictions for $H \to \tau\bar{e}$ with the effective vertex computed with the MIA (dashed lines) for Y_ν^{TE10}. The chosen examples TM9 and TE10 are explained in the text. Solid lines are the corresponding predictions from the full one-loop computation in the mass basis. Shadowed areas to the left part of these plots (in purple) are disallowed by global fits. Shadowed areas to the right part of these plots (in yellow) give a non-perturbative Yukawa coupling.

corresponding to the limit $m_H \to 0$. In this sense, although a complete comparison is out of the scope of this work, we conclude that our MIA effective vertex and the effective vertex of the mass basis in Ref. [76] agree analytically in the limit $m_H \to 0$. Nevertheless, we have checked by a numerical estimate of the LFVHD widths that the approximation of neglecting the Higgs boson mass in the effective vertex does not provide in general an accurate result and, therefore, in order to obtain a realistic estimate of these branching ratios, our final formula for the effective vertex in Eq. (3.34) should be used, which is specific for on-shell Higgs decays and accounts properly for the Higgs boson mass effects.

Finally, we wish to illustrate numerically the accuracy of our simple results of the effective vertex and the partial width in Eqs. (3.34) and (3.36), respectively. For that purpose, we compare again our numerical predictions from these simple formulas with the predictions from the full one-loop results of the mass basis in Fig. 3.26. Here, we display the results for the most interesting channels $H \to \tau\bar{\mu}$ and $H \to \tau\bar{e}$ and for two scenarios, Y_ν^{TM9} and Y_ν^{TE10} in Table 2.4. Nonetheless, we have checked that the effective vertex in Eqs. (3.34) also works for other choices of scenarios.

The plots in Fig. 3.26 show the predictions of both the LFVHD partial widths and branching ratios, as functions of M_R and three different values of $f = 2, 1, 0.5$, with the colored areas being disallowed by global fit constraints (purple) or by non-perturbative Yukawa couplings (yellow). Concretely, we have imposed the constraints on all the entries of the η matrix (see Eq. (3.42)) that we have taken from the global analysis in Ref. [258] at the three sigma level. For the perturbativity bound, we impose the condition $|Y_\nu^{ij}|^2/(4\pi) < 1$ for every

entry of the Y_ν coupling matrix. The areas in white are in consequence the regions that are allowed by the Global Fits and by perturbativity.

From these plots we learn that the agreement between the full prediction and the MIA result obtained from the effective vertices computed in this section is quite good for values of M_R above 1 TeV and for all the explored Yukawa coupling examples. In fact, the MIA works extremely well for the whole region of interest where both the global fits constraints and the perturbativity of the Yukawa coupling are respected. Consequently, we conclude that the simple expression for the effective vertex in Eq. (3.34) is quite accurate and provides a good approximation for the partial width in Eq. (3.36), in agreement with the full LFVHD rates. Therefore, it is a very useful formula for making fast numerical estimations of these rates in terms of the relevant model parameters Y_ν and M_R.

3.4 Maximum allowed $\mathrm{BR}(H \to \ell_k \bar{\ell}_m)$

We conclude this Chapter by combining everything we have learnt about LFV H decays and by trying to conclude on the maximum rates allowed by a more complete set of present constraints, including both LFV and lepton flavor preserving observables. For this purpose, we consider the constraints obtained by the global fit analysis done in Ref. [258], where upper bounds on the η matrix were derived. More concretely, these constraints define a maximum allowed by data η matrix given by:

$$\eta_{3\sigma}^{\mathrm{max}} = \begin{pmatrix} 1.62 \times 10^{-3} & 1.51 \times 10^{-5} & 1.57 \times 10^{-3} \\ 1.51 \times 10^{-5} & 3.92 \times 10^{-4} & 9.24 \times 10^{-4} \\ 1.57 \times 10^{-4} & 9.24 \times 10^{-4} & 3.67 \times 10^{-3} \end{pmatrix}, \tag{3.42}$$

We can easily apply these bounds by means of the μ_X parametrization introduced in Eq. (1.46). As we said, this parametrization allows us to choose the Y_ν and M_R matrices as input parameters of the model. In our situation of degenerate M_R matrix, the η matrix is related to the Yukawa matrix approximately by,

$$\eta = \frac{v^2}{2M_R^2} Y_\nu Y_\nu^\dagger. \tag{3.43}$$

Therefore, we can combine Eq. (3.42) and (3.43) in order to find a Yukawa matrix that saturates the $\eta_{3\sigma}^{\mathrm{max}}$ bounds. Then, the Eq. (1.46) will ensure the agreement with oscillation data by building the proper μ_X matrix.

A possible solution to this problem is given by our choice:

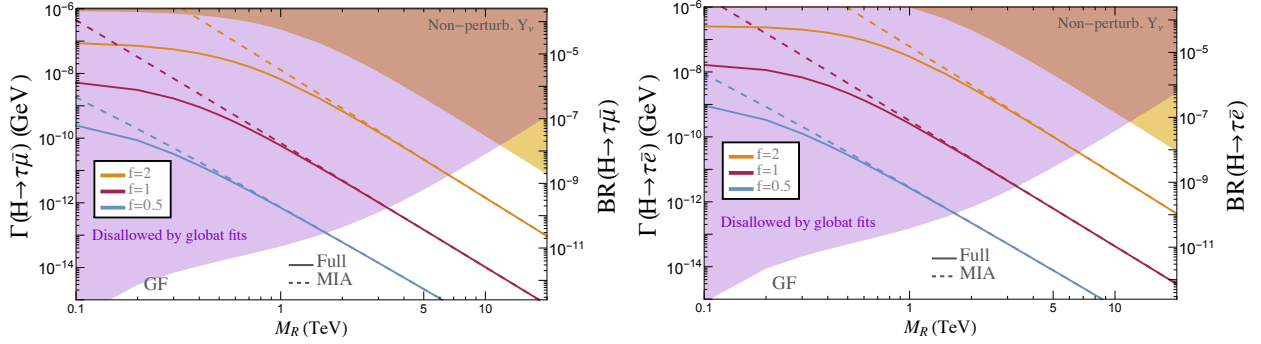$$Y_\nu^{\mathrm{GF}} = f \begin{pmatrix} 0.33 & 0.83 & 0.6 \\ -0.5 & 0.13 & 0.1 \\ -0.87 & 1 & 1 \end{pmatrix}, \tag{3.44}$$

Figure 3.27: Predictions for $H \to \tau\bar{\mu}$ (left panel) and $H \to \tau\bar{e}$ (right panel) with the effective vertex computed with the MIA (dashed lines) for Y_ν^{GF}. The chosen example GF is explained in the text. Solid lines are the corresponding predictions from the full one-loop computation in the mass basis. Shadowed areas to the left part of these plots (in purple) are disallowed by global fits. Shadowed areas to the right part of these plots (in yellow) give a non-perturbative Yukawa coupling.

which saturates the $\eta_{3\sigma}^{\max}$ bounds in a parameter space line given by the ratio $f/M_R = (3/10)\,\mathrm{TeV}^{-1}$, i.e. for $(f, M_R) = (3, 10\,\mathrm{TeV})$, $(1, 3.3\,\mathrm{TeV})$, $(0.3, 1\,\mathrm{TeV})$, ..., etc. The Yukawa coupling matrix in Eq. (3.44) defines our last scenario, that we refer to as GF.

We show the numerical results in Fig. 3.27 for the most promising channels $H \to \tau\bar{\mu}$ and $H \to \tau\bar{e}$ in the GF scenario. We also computed the $H \to \mu\bar{e}$ channel, but we do not show the results for this case here, since the rates are extremely small due to strong bounds on $\eta_{\mu e}$. As before, the purple area covers the parameter space region where the η matrix is above the 3σ bound in Eq. (3.42), at least in one entry. The yellow area represents violation of the perturbativity bound

$$\frac{\left|Y_{ij}\right|^2}{4\pi} < 1\,, \quad \text{for } i, j = 1, 2, 3\,. \tag{3.45}$$

Our predictions are done with both full expressions in the mass basis, derived in Section 3.1, and the effective vertex obtained in Section 3.3. We see again that the agreement of the simple formula in Eq. (3.34) is excellent in all the region allowed by both the global fit and the perturbativity constrains. Finally, we can conclude on the maximum LFVHD rates allowed by the complete set of present constraints as extracted from the approach of a global fit analysis. From Fig. 3.27 we learn that the maximum allowed branching ratios values are, respectively:

$$\mathrm{BR}(H \to \tau\bar{\mu})_{\max} \sim 10^{-8}\,, \tag{3.46}$$
$$\mathrm{BR}(H \to \tau\bar{e})_{\max} \sim 10^{-7}\,. \tag{3.47}$$

Finally, we summarize shortly our findings in this Chapter, where we have explored in full detail the LFV H decays induced from right-handed neutrinos from the ISS model. We found that, having these neutrinos TeV scale masses and large Yukawa couplings at the same time, the LFVHD rates are manifestly enhanced with respect to the standard type-I seesaw, where rates of $\mathcal{O}(10^{-30})$ were obtained [82]. After applying present bounds from a global fit analysis, we found maximum allowed rates of 10^{-7} and 10^{-8} for $H \to \tau \bar{e}$ and $H \to \tau \bar{\mu}$, respectively, which unfortunately are far from present LHC experimental sensitivities. However, in our aim of fully understanding the predictions for this observable, we have derived a one-loop effective vertex for the LFV interaction of our interest here, namely, the interaction of a Higgs boson with two leptons of different flavor $H\ell_k\ell_m$ with $k \neq m$. With such a simple expression for the involved effective vertex, one may perform a fast estimate of the LFV Higgs decay rates, for many different input parameter values, mainly for Y_ν and M_R, without the need of a diagonalization process to reach the physical neutrino basis, and thus avoiding the computation of the full one-loops in this basis, which is by far more computer time consuming. Moreover, the explicit dependence on the relevant parameters Y_ν and M_R facilitates the interpretation of the numerical results. We find this simple formula useful also for other models that shares the desired basic properties with the ISS model, since they can be easily used by other authors to obtain a fast estimate of the LFVHD rates, which are ready for an easy test with experimental data.

Finally, we have also explored these rates in the SUSY-ISS model, finding that new loops involving SUSY particles, sleptons and sneutrinos, could enhance the predictions for the allowed LFVHD rates close to the present or near future experimental sensitivities.

Chapter 4

LFV Z decays from low scale seesaw neutrinos

As we previously discussed, the LHC is providing new data on lepton flavor violating Z boson decays, $Z \to \ell_k \bar{\ell}_m$. After LHC run-I, the ATLAS experiment has improved previous bounds for $Z \to \mu e$ [70] and it is already at the level of the LEP results for the $Z \to \tau \mu$ channel. These searches will continue in the next LHC runs with more luminosity and higher energies and, thus, the LHC will provide new data on these LFV observables. Furthermore, the sensitivity to LFVZD rates are expected to highly improve at future linear colliders, with an expected sensitivity of 10^{-9} [73, 74], or at a Future Circular $e^+ e^-$ Collider (such as FCC-ee (TLEP)[75]), where it is estimated that up to 10^{13} Z bosons would be produced and the sensitivities to LFVZD rates could be improved up to 10^{-13}. Therefore, we consider extremely timely to explore the predictions for these LFVZD rates in any new physics scenario that could be related to neutrino physics, as has been previously done in Beyond the Standard Model frameworks like those with massive (Majorana and/or Dirac) neutrinos [24, 78–81, 187, 259, 260], or those using an Effective Field Theory approach [261–264].

In this Chapter, we consider again the Inverse Seesaw model with three pairs of right-handed neutrinos as a specific realization of the low scale seesaw models, which as we saw in previous Chapters it is an appealing model with a very rich phenomenology, in particular for the charged LFV processes. Nevertheless, as we discussed before, the present experimental upper bounds in Table 2.1 for cLFV processes involving μ-e transitions, here called LFV$_{\mu e}$ in short, are much stronger that the ones in the other sectors, i.e, cLFV processes involving τ-μ and τ-e transitions, named here in short LFV$_{\tau \mu}$ and LFV$_{\tau e}$, respectively. These very stringent constraints in the μ-e sector motivate the directions in the parameter space considered here, which incorporate automatically this suppression in their input. Specifically, we will implement this μ-e suppression requirement within the context of the ISS, by working with the TM and TE scenarios we introduced in Table 2.4. These particular ISS settings

with suppressed $\mathrm{LFV}_{\mu e}$ rates provide very interesting scenarios for exploring the relevant ISS parameter space directions that may lead to large cLFV rates in the other sectors, τ-μ and/or τ-e.

Motivated by all the peculiarities exposed above, in this Chapter we perform a dedicated study of the LFVZD rates, in particular $\mathrm{BR}(Z \to \tau\mu)$ and $\mathrm{BR}(Z \to \tau e)$, in the context of these ISS scenarios with an *ad-hoc* suppression of $\mathrm{LFV}_{\mu e}$ rates, which will be called from now on ISS-$\overline{\mathrm{LFV}}_{\mu e}$ in short. LFVZD processes in the presence of low-scale heavy neutrinos have recently been studied considering the full one-loop contributions [49] or computing the relevant Wilson coefficients [265]. In these works, maximum allowed LFVZD rates in the reach of future linear colliders were found when considering a minimal "3+1" toy model, with $\mathrm{BR}(Z \to \tau\mu)$ up to $\mathcal{O}(10^{-8})$ for a neutrino mass in the few TeV range. For more realistic models, like the (2,3) or (3,3) realizations of the ISS model, and after imposing all the relevant theoretical and experimental bounds, smaller LFVZD rates were achieved, $\mathrm{BR}(Z \to \tau\mu) \lesssim \mathcal{O}(10^{-9})$, which would be below the reach of future linear colliders sensitivities and might be accessible only at future circular e^+e^- colliders. The main difference of our study with the ones previously done relies on the different settings of the ISS parameters, as we will focus on some specific directions that are more difficult to access with a random scan of the ISS parameter space. We have learnt about this issue when studying the LFV Higgs boson decays in Chapter 3. In the following, we will perform a complementary analysis to the one in Ref. [49] and we will show that larger maximum allowed rates for $\mathrm{BR}(Z \to \tau\mu)$ and $\mathrm{BR}(Z \to \tau e)$ can be obtained by considering the particular TM and TE scenarios in Table 2.4, such that for some specific directions of the parameter space they could be reached at future linear colliders. The results presented in this Chapter have been published in Ref. [100].

4.1 LFV Z decays in the ISS model

LFV Z decays (LFVZD) in the context of right-handed neutrinos were first studied in Refs. [80, 81, 187]. More recently, LFVZD processes in the presence of low-scale heavy neutrinos have been studied [49, 265], considering a simplified $3 + 1$ model as well as different realizations of the ISS model. In this section, we revisit these decay rates in the ISS model with three pairs of fermionic singlets, focusing on the μ_X parametrization and the scenarios in Table 2.4, which have been proven to be useful for finding large rates in the case of LFV Higgs decays, as discussed in Chapter 3.

Following Refs. [49, 80], we can write the partial decay width for the LFV process $Z \to \ell_k \bar{\ell}_m$ process as

$$\Gamma(Z \to \ell_k \bar{\ell}_m) = \frac{\alpha_W^3}{192\pi^2 c_W^2} \, m_Z \left| \mathcal{F}_Z \right|^2, \tag{4.1}$$
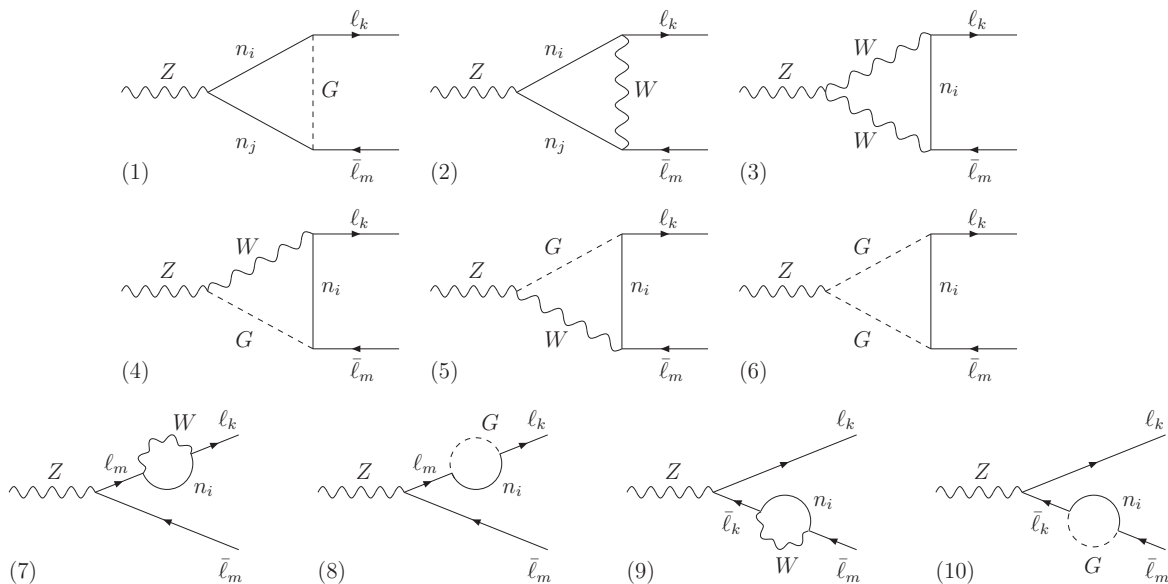
Figure 4.1: One-loop diagrams in the Feynman-'t Hooft gauge for LFV Z decays with massive neutrinos.

after neglecting final state lepton masses. In the Feynman-'t Hooft gauge, the one-loop form factor $\mathcal{F}_Z$ receives contributions from the ten diagrams shown in Fig. 4.1. Then, we can write it as

$$\mathcal{F}_Z = \sum_{a=1}^{10} \mathcal{F}_Z^{(a)}. \tag{4.2}$$

We have taken the full one-loop formulas from Ref. [80] and we have adapted them to the ISS model we consider, rewriting them in terms of the proper physical neutrino masses and couplings introduced in Section 1.3. We include these formulas, for completeness, in App. F where we have also adapted the loop functions to the usual notation in the literature.

For the numerical analysis of the $\mathrm{BR}(Z \to \ell_k\ell_m) = \mathrm{BR}(Z \to \ell_k\bar{\ell}_m) + \mathrm{BR}(Z \to \ell_m\bar{\ell}_k)$ rates, we will evaluate these expressions with our code and with the help of the *LoopTools* [266] package for *Mathematica*. As for the LFV H decays analysis, we will always demand a good agreement with experimental data coming from neutrino oscillations. This can be easily done by using any of the two parametrizations explained in Chapter 1, i.e, the Casas-Ibarra parametrization in Eq. (1.44) or the μ_X-parametrization in Eq. (1.46). As explained before, the choice of parametrization cannot change the physics, however it can help to study the parameter space more efficiently, or to design scenarios with phenomenologically appealing

features.

The LFVZD in the context of the ISS model with three pairs of fermionic singlets were first studied in Ref. [49]. In this work, the Authors used the Casas-Ibarra parametrization to accommodate the neutrino oscillation data and they scanned over a large range of the parameter space. Concretely, the modulus of the entries of the input M_R and μ_X matrices are randomly taken between $(0.1\,\mathrm{MeV}, 10^6\,\mathrm{GeV})$ and $(0.01\,\mathrm{eV}, 1\,\mathrm{MeV})$, respectively, with complex entries for μ_X and varying also the complex angles of the R matrix in Eq. (1.45) between 0 and 2π. After applying all the constraints, the Authors concluded from the scatter plots in Figs. 8-10 that maximum allowed rates of $\mathrm{BR}(Z \to \tau\mu) \sim 10^{-9}$ can be obtained in our same realization of the ISS model.

As we saw in the context of LFV Higgs decays in Chapter 3, random scans with the Casas-Ibarra parametrization allow one to explore a large region of the parameter space and to study the general features of the model, however, they are not always optimal to reach specific directions along the parameter space that are still allowed by experimental constraints and that can give indeed large predictions for some LFV observables. In the case of LFVHD, for instance, we found maximum allowed rates for $H \to \tau\mu$ and $H \to \tau e$ when using the μ_X parametrization and the scenarios in Table 2.4 that were two orders of magnitud larger than when using the Casas-Ibarra parametrization. In this sense, the study of this *ad-hoc* scenarios looking for maximum allowed rates is complementary to the general scan over the full parameter space. Therefore, in the following we focus on the LFV Z decays along these particular directions in the parameters space, with the aim of complementing the study in Ref. [49] covering points that a generic random scan could have missed.

Looking again at the present experimental upper bounds, summarized in Section 2.1, we see that the constraints on cLFV processes involving μ-e transitions, $\mathrm{LFV}_{\mu e}$ in short, are much stronger that the ones in the other sectors, i.e, cLFV processes involving τ-μ and τ-e transitions, $\mathrm{LFV}_{\tau\mu}$ and $\mathrm{LFV}_{\tau e}$ respectively. These very stringent constraints in the μ-e sector motivated the class of scenarios introduced in Table 2.4, which incorporate automatically this suppression in their input. We showed that these directions were not usually reached by the scans using the Casas-Ibarra parametrization, however they were easily implemented by using our μ_X parametrization and the geometrical interpretation of the Yukawa matrix introduced in Eq. (2.5). On the other hand, these particular ISS settings with suppressed $\mathrm{LFV}_{\mu e}$ rates provide very interesting scenarios for exploring the relevant ISS parameter space directions that may lead to large cLFV rates in the other sectors, τ-μ and/or τ-e, as we saw in the context of LFV Higgs decays in Chapter 3. Thus, we will analyze the LFV Z decay rates $Z \to \tau\mu$ and $Z \to \tau e$ within these directions.

Before going to the analysis os maximum allowed LFV Z decay rates in these directions, we study how this observable depends on the most relevance parameters. We show here our results for the particular case of $\mathrm{BR}(Z \to \tau\mu) = \mathrm{BR}(Z \to \tau\bar{\mu}) + \mathrm{BR}(Z \to \mu\bar{\tau})$ within the TM scenarios, which are defined by taking $c_{\tau e} = 0$ in Eq. (2.7), although similar results are
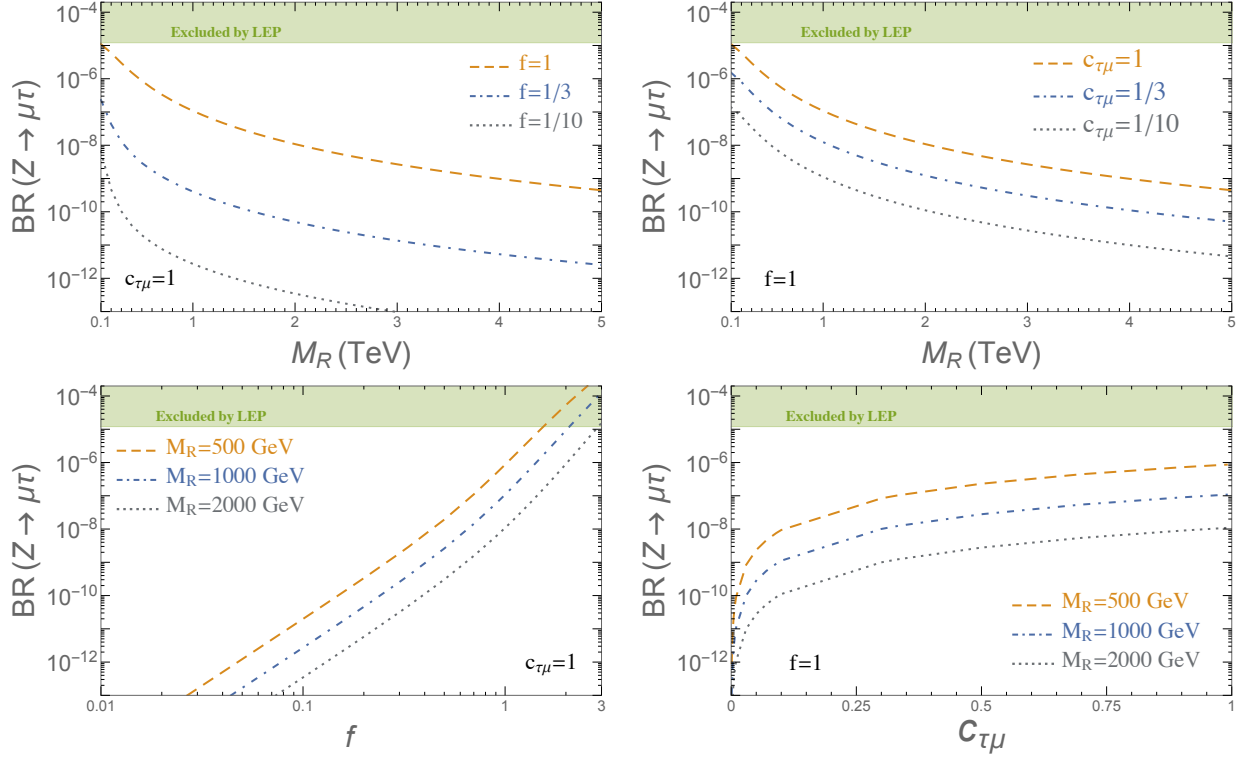
Figure 4.2: Predictions for BR($Z \to \tau\mu$) within the ISS model as a function of the heavy neutrino mass parameter M_R (two upper panels), the neutrino Yukawa coupling strength f (lower left panel) and $c_{\tau\mu}$ (lower right panel) for various choices of the relevant parameters. In all plots we have fixed, $c_{\tau e} = 0$ and $|\boldsymbol{n}_{e,\mu,\tau}| = 1$. The upper shadowed areas (in green) are excluded by LEP [72]. Similar results for BR($Z \to \tau e$) by exchanging $c_{\tau e}$ and $c_{\tau\mu}$.

found for BR($Z \to \tau e$) within the TE scenarios. Along these directions, only the $Z \to \tau\mu$ channel gives relevant ratios and their predictions depend mainly on M_R, f, $|\boldsymbol{n}_\tau|$, $|\boldsymbol{n}_\mu|$ and $c_{\tau\mu}$.

We display in Fig. 4.2 the behavior of the BR($Z \to \tau\mu$) rates with the M_R, f and $c_{\tau\mu}$ parameters for fixed values of $|\boldsymbol{n}_e| = |\boldsymbol{n}_\mu| = |\boldsymbol{n}_\tau| = 1$, $c_{\tau e} = 0$ and $\mathcal{O} = \mathbb{1}$. As can be seen in this figure, these ISS directions give in general large rates for the LFV $Z \to \tau\mu$ decay, indeed close to the upper bound from LEP (and also close to the present LHC sensitivity) in the upper left corner of the two upper plots and in the upper right corner of the two lower plots. We also see that the rates decrease with the heavy scale M_R and grow with the Yukawa coupling strength f, as expected. We found this growth to be approximately as f^4 in the low f region and as f^8 in the high f region of the studied interval of this parameter. This suggests that, in contrast to the radiative decays, the two kinds of contributions $Y_\nu Y_\nu^\dagger$ and

$Y_\nu Y_\nu^\dagger Y_\nu Y_\nu^\dagger$ participate in this observable, similar to what we obtained for the LFV H decays (see Eq. (3.34)). These dependencies will be further studied by means of the Mass Insertion Approximation in a forthcoming work.

In the lower right panel, we observe that the rates also grow with $c_{\tau\mu}$, albeit the dependence is milder, approximately as $c_{\tau\mu}^2$. Although not shown here, we have also studied the dependence of the decay rates with the modulus of the vectors, $|\mathbf{n}_i|$, finding that the predictions for BR$(Z \to \tau\mu)$ grow with both $|\boldsymbol{n}_\mu|$ and $|\boldsymbol{n}_\tau|$, while they are constant with $|\boldsymbol{n}_e|$, as expected. Finally, we checked that the results do not depend on the global rotation $\mathcal{O}$, as argued when the parametrization for the Y_ν coupling matrix was motivated.

In order to conclude on the maximum allowed LFV Z decay rates, we need to consider all the relevant constraints. Nevertheless, prior to the full study, we find interesting first to compare the predictions of these LFV Z decays with the predictions of the three body LFV lepton decays in our particular ISS scenarios with suppressed μ-e transitions. Looking back to the right panel of Fig. 2.6, we notice again that in these ISS directions the $\tau \to \mu\mu\mu$ decay is mostly dominated by the Z penguin. This fact implies a strong correlation between $\tau \to \mu\mu\mu$ and $Z \to \tau\mu$, as already found in Ref. [49]. We have also checked in some examples of the ISS parameter space that our numerical predictions of these two observables are in agreement with that reference.

We study this correlation in more detail Fig. 4.3, where we consider three of the scenarios given in Table 2.4, TM-5, TM-6 and TM-7, varying the values of the parameters within the ranges of $f \in (0.1, 2)$ and $M_R \in (0.2, 10)$ TeV. Both observables grow with f and decrease with M_R in approximately the same way, due to the already mentioned Z penguin dominance in the three body decays. Although the predicted rates in each scenario are obviously different, see for instance the positions of the reference points with $f = 1$ and $M_R = 3$ TeV, we clearly see that there is a strong correlation between the two observables in these ISS directions. We can also conclude from this plot that by considering just the constraints from the three body decays, *i.e.* the present upper bound on $\tau \to \mu\mu\mu$ from BELLE, already suggests a maximum allowed rate of BR$(Z \to \tau\mu) \sim 2 \times 10^{-7}$, which is clearly within the reach of future linear colliders (10^{-9} in the most conservative option). Interestingly, comparing the future expected sensitivities for both observables, we find some parameter space points where the LFVZD rates are in the reach of future linear colliders while the cLFV three body decay rates would not be accessible in other facilities, like BELLE-II. This fact suggests that experiments looking for LFVZD would be able to provide additional information about the model that complements the results of other searches, like the ones in Table 2.1. We found a similar correlation between BR$(\tau \to eee)$ and BR$(Z \to \tau e)$ in the TE scenarios.
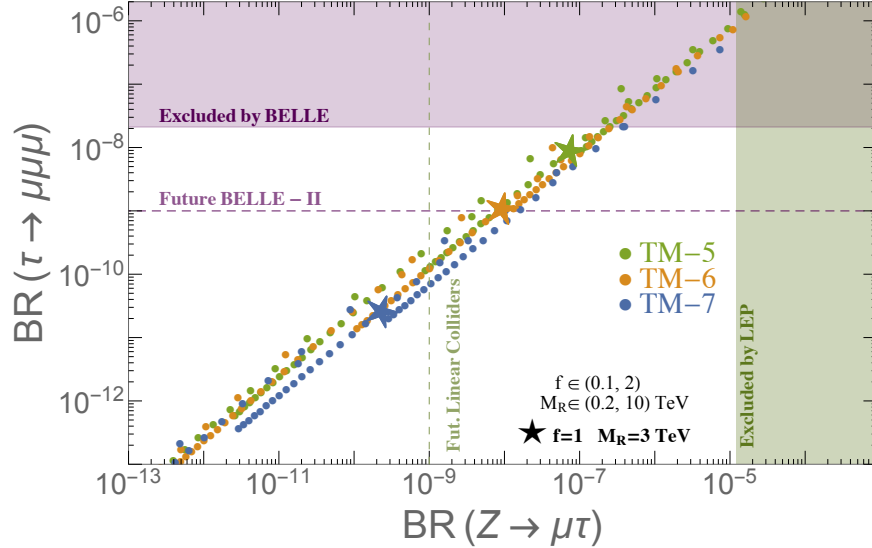
Figure 4.3: Correlation plot for $\mathrm{BR}(Z \to \mu\tau)$ and $\mathrm{BR}(\tau \to \mu\mu\mu)$ for scenarios TM-5 (green), TM-6 (yellow) and TM-7 (blue) defined in Table 2.4. The dots are obtained by varying $f \in (0.1, 2)$ and $M_R \in (0.2, 10)$ TeV, while the stars are for the reference point $f = 1$ and $M_R = 3$ TeV. Purple (green) shadowed area is excluded by BELLE [164] (LEP [72]), while the dashed line denotes expected future sensitivity from Belle-II (future linear colliders).

4.2 Maximum allowed $\mathrm{BR}(Z \to \ell_k \bar{\ell}_m)$

In the following we present our full analysis of the LFVZD rates in the ISS scenarios with suppressed μ-e transitions introduced in Section 2.2.1, including all the most relevant constraints. For this analysis we have explored the (M_R, f) plane for the eight TM scenarios given in Table 2.4 and provide numerical predictions for the $\mathrm{BR}(Z \to \ell_k \ell_m)$ rates together with the predictions of the most constraining observables and their present bounds, which we reviewed in Chapter 2. Alternative checks of the allowed ISS parameter space can be made by using global fits results [258, 267–271], but we prefer to make the explicit computations of the selected observables here and to compare them directly to their experimental bounds.

We show in Fig. 4.4 the results for $\mathrm{BR}(Z \to \tau\mu)$ together with the constraints from: $\tau \to \mu\mu\mu$, $\tau \to \mu\gamma$, $Z \to$ inv., Δr_K and the EWPO (S, T and U). As in the previous section, we show our results only for the LFV$_{\tau\mu}$ sector in the TM scenarios, although the conclusions are very similar for LFV$_{\tau e}$ in the TE scenarios. We use different colors in the shadowed areas to represent the exclusion regions from each of the constraints listed above. Specifically, the purple area is excluded by the upper bound on $\mathrm{BR}(\tau \to \mu\mu\mu)$, the green area by $\mathrm{BR}(\tau \to \mu\gamma)$, the yellow area by the Z invisible width, the cyan area by Δr_k and the

area above the pink solid line is excluded by the S, T, U parameters. Although we are not explicitly showing them here, we have also checked that the total parameter space allowed by all these constraints are also permitted by our requirements on perturbativity and on the validity of the μ_X parametrization explored in Section 2.3.6. Notice that in some scenarios some of the colored areas are hidden below the excluded regions corresponding to the more constraining observables.

On top of all the bounds, we display in Fig. 4.4 the predicted contour lines for BR($Z \to \tau\mu$) as dashed lines. As expected from the correlation studied in Fig. 4.3, we see that these contour lines have approximately the same slope as the border of the exclusion region from BR($\tau \to \mu\mu\mu$), and in particular the line corresponding to BR($Z \to \tau\mu$) $= 2 \times 10^{-7}$, is very close to the upper bound line of the three body decay in all the TM scenarios (*i.e.*, the border of the purple line). Furthermore, in the large M_R - large f region of these plots we see that for several TM scenarios, concretely TM-2, TM-3, TM-4 and TM-5, the BR($\tau \to \mu\mu\mu$) is indeed the most constraining observable.

In contrast, in the low M_R and low f region, the most constraining cLFV observable is the radiative decay $\tau \to \mu\gamma$. On the other hand, regarding the flavor preserving observables, it is clear that the EWPO do not play a relevant role here, but both Δr_K and the invisible Z width put relevant constraints in some scenarios. In particular, Δr_K is the most constraining observable in the case of TM-8, and the Z invisible width is so in the scenarios TM-1, TM-6 and TM-7. We also learn that, typically, the Z invisible width is the most constraining observable in the region of low M_R values, whereas BR($\tau \to \mu\mu\mu$) is the most constraining observable in the region of high M_R values. Thus, generically, it is the crossing of these two excluded areas in the (M_R, f) plane that gives the focus area of the maximum allowed LFV Z decay rates, BR($Z \to \tau\mu$) $\sim 2 \times 10^{-7}$, and this crossing occurs at different values of M_R and f in each scenario. For example, in the TM-4 and TM-5 scenarios it happens at $M_R \sim 2 - 4$ TeV and for $f \sim \mathcal{O}(1)$, while in the TM-6 M_R is around 10 TeV and $f \sim \mathcal{O}(2)$. On the other hand, if we focus our attention on the mass range of interest for present direct neutrino production searches at LHC, say masses around 1 TeV and below, we observe that the allowed BR($Z \to \tau\mu$) rates are smaller than this maximum value 2×10^{-7}; nevertheless they are still in the reach of future linear colliders (10^{-9}) for some scenarios, like TM-4 or TM-5.

Summarizing, in this Chapter we have studied in full detail the LFV Z decays in scenarios with suppressed μ-e transitions that are designed to find large rates for processes including a τ lepton, and we have investigated those that are allowed by all the present constraints. We have therefore fully explored in parallel also the most relevant constraints within these scenarios of the ISS model. Important constraints come from experimental upper bounds on the LFV three body lepton decays, since they are strongly correlated to the LFVZD in these scenarios. Taking into account all the relevant bounds, we found that
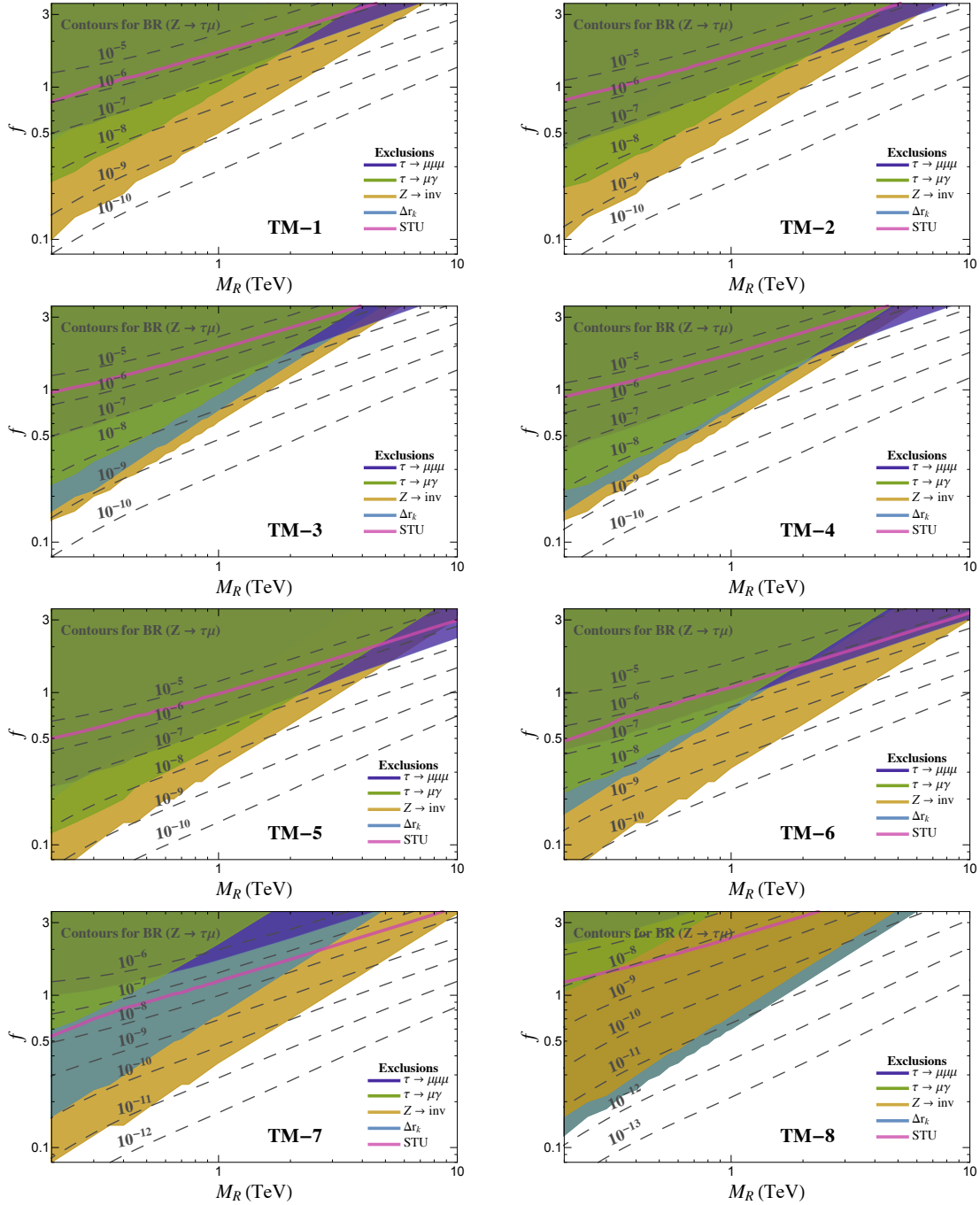
Figure 4.4: Contour lines for BR($Z \rightarrow \tau\mu$) (dashed lines) in the (M_R, f) plane of the ISS model for the eight TM scenarios in Table 2.4. Shadowed areas are the excluded regions by $\tau \rightarrow \mu\mu\mu$ (purple), $\tau \rightarrow \mu\gamma$ (green), Z invisible width (yellow) and Δr_k (cyan). The region above the pink solid line is excluded by the S, T, U parameters. We obtain similar results for BR($Z \rightarrow \tau e$) in the TE scenarios by exchanging μ and e in these plots of the TM scenarios.

heavy ISS neutrinos with masses in the few TeV range can induce maximal rates of $\mathrm{BR}(Z \to \tau\mu) \sim 2 \times 10^{-7}$ and $\mathrm{BR}(Z \to \tau e) \sim 2 \times 10^{-7}$ in the TM and TE scenarios, respectively, larger than what was found in previous studies. These rates are potentially measurable at future linear colliders and FCC-ee. Therefore, we have shown that searches for LFVZD at future colliders may be a powerful tool to probe cLFV in low scale seesaw models, in complementarity with low-energy (high-intensity) facilities searching for cLFV processes. Another appealing feature of our results is that the here presented improved sensitivity to LFVZD rates could come together with the possibility that the heavy neutrinos could be directly produced at LHC, as we will explore in the next Chapter.

Chapter 5

Exotic LFV signals from low scale seesaw neutrinos at the LHC

One of the most interesting phenomenological implications of the existence of low scale seesaw neutrinos, with masses in the energy range from the hundreds of GeV up to few TeV, is that they can be directly searched for at the CERN LHC and that, if their couplings to the SM particle are large, the probability of producing them can be sizable. The most frequently studied signatures of heavy neutrinos are those related to their Majorana nature [93–96] and, in particular, the most characteristic signal is the same-sign dilepton plus two jets events which is being searched for at the LHC.

In the low scale seesaw models we are interested in, as long as they assume an approximated Lepton Number conservation to fit the observed light neutrino masses, the heavy neutrinos form pseudo-Dirac pairs, with a small Majorana character proportional precisely to the small LN breaking scale. Therefore, the rates of the smoking-gun signal of Majorana neutrinos are suppressed in these models. Alternative searches for this pseudo-Dirac character of the heavy neutrinos have also been explored in the literature in connection with the appearance of other interesting multilepton signals [272] at the LHC, like the trilepton final state [31–38].

In this Chapter, we propose a new exotic signal of the right-handed neutrinos at the LHC that is based on another interesting feature of the low scale seesaw models, the fact that they incorporate large lepton flavor violation for specific choices of the model parameters, as we have extensively studied in the previous Chapters of this Thesis. We focus again on the inverse seesaw model as a specific realization of these low scale seesaw models and study the LFV effects coming from the neutrino Yukawa couplings Y_ν. Our specific proposal here is to look at rare LHC events of the type of $\ell_k^\pm \ell_m^\mp jj$, and more specifically with one muon, one tau lepton and two jets in the final state that are produced in these ISS scenarios with large LFV, and that presumably will have a very small SM background. This Chapter then summarizes
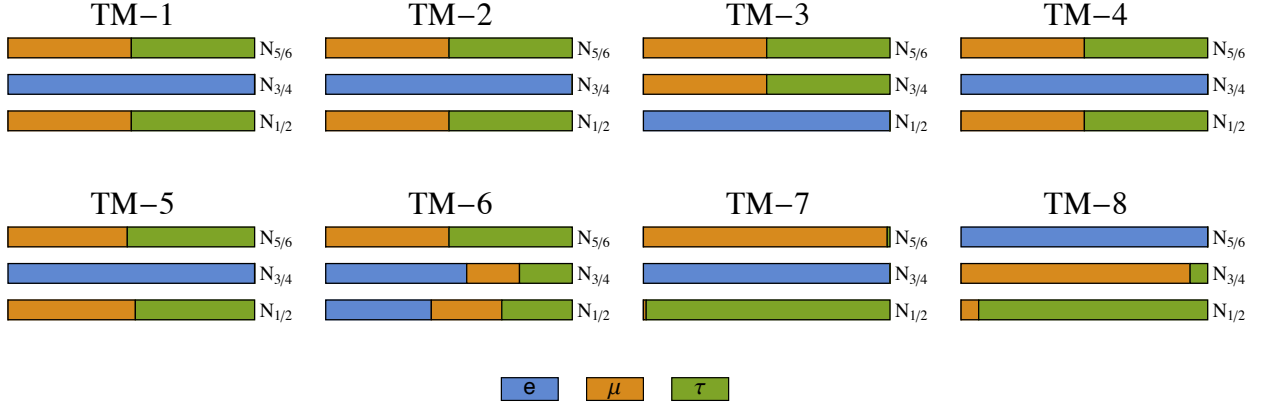
Figure 5.1: Heavy neutrino flavor mixings, as defined in Eq. (5.1), within some of the ISS scenarios of Table 2.4. Blue, orange and green colors represent the relative mixing with the electron, muon and tau flavor, respectively.

our computation of the rates for these exotic $\mu\tau jj$ events due to the production and decays of the heavy quasi-Dirac neutrinos at the LHC within the ISS. The results presented in this Chapter have been published in Ref. [99].

5.1 The flavor of the heavy neutrinos

As we have seen in previous Chapters, radiatively induced LFV processes are sensitive to a particular combination of the Yukawa coupling matrix, i.e., to $|Y_\nu Y_\nu^\dagger|$. Therefore, in terms of the heavy neutrino flavor mixing, $B_{\ell N}$ introduced in Eq. (1.52), they constrain the combination $|B_{\ell N} B_{\ell N}^*|$, but not the $B_{\ell N}$ itself, which is the relevant element that controls the flavor pattern of each of the heavy neutrinos.

In Fig. 5.1 we show the flavor content of each heavy neutrino for some of the TM scenarios in Table 2.4 in the same language of the flavor structure in Fig. 1.1 for the light neutrinos. Concretely we chose as examples the scenarios from TM-1 to TM-8, and define the length of the colored bars as

$$S_{\ell N_i} = \frac{|B_{\ell N_i}|^2}{\displaystyle\sum_{\ell=e,\mu,\tau} |B_{\ell N_i}|^2} \tag{5.1}$$

and, therefore, it represents the relative mixing of the heavy neutrino N_i with a given flavor ℓ. It should be further noticed, that the values of these $B_{\ell N}$ mixing parameters are determined within the ISS model in terms of the input m_D and M_R mass matrices and, therefore, in the

range where $m_D \ll M_R$ they are suppressed as $B_{\ell N} \sim \mathcal{O}(m_D M_R^{-1})$. This fact implies that, for our assumptions of degenerate entries of the diagonal M_R matrix, the relative mixings defined as in Eq. (5.1) are independent of M_R in this situation.

We learn from Fig. 5.1 that, although these TM scenarios share the property of suppressing the LFV μ-e and τ-e rates while maximizing the τ-μ ones, the heavy neutrino flavor mixing pattern is not always the same in each scenario. We also see that some heavy neutrinos carry an interesting amount of both μ and τ flavors, specially in the first six scenarios, pointing towards signals with both μ and τ leptons simultaneously. Therefore, in the following we will explore the possibility of producing this kind of events at the LHC, concretelly $\tau^{\pm}\mu^{\mp}jj$ events, which can be considered as naively background free in the SM, and are therefore interesting exotic events to search for. Moreover, we notice that similar results can be obtained for τejj events if the TE scenarios are considered.

5.2 Predictions of exotic $\tau\mu jj$ event rates from heavy neutrinos

Heavy neutrinos with masses of the TeV order and bellow can be produced at present and future colliders, in particular in this second run of the LHC. The dominant production mechanism in this case is the Drell-Yan (DY) process, Fig. 5.2 left, where the heavy neutrino is produced in association with a charged lepton. The γW fusion, Fig. 5.2 right, also produces the same signal with two extra jets and, in fact, can be also relevant especially for large neutrino masses in the $\mathcal{O}(1 \text{ TeV})$ energy range [273, 274].

In order to estimate the heavy neutrino production at the LHC, we have used Feynrules [275] to implemente the model in MadGraph 5 [276]. Following Ref. [273], we have used a K-factor of 1.2 for the DY-process and split the γW process in three regimes characterized by the virtuality of the photon[1]: elastic, inelastic and deep inelastic scattering (DIS) regimes. In particular, we have set the boundaries between these three regimes to $\Lambda_\gamma^{\text{Elas}} = 1.22$ GeV and $\Lambda_\gamma^{\text{DIS}} = 15$ GeV. In order to regularize possible collinear singularities, we have also imposed the following cuts to the transverse momentum and pseudorapidity of the outgoing leptons:

$$p_T^\ell > 10 \text{ GeV}, \quad |\eta^\ell| < 2.4 . \tag{5.2}$$

The results for the scenarios TM-5, TM-6 and TM-7 from Table 2.4 are shown in Fig. 5.3, where the dominant DY production cross sections normalized by f^2 are plotted as functions of the heavy mass parameter M_R. We see that the production cross sections can be of the fb order, reachable at the LHC, for masses $M_R \lesssim 600$ GeV. Notice that the

---

[1]We warmly thank Richard Ruiz, Tao Han and Daniel Alva for their generous help and clarifications in the implementation of the γW process.
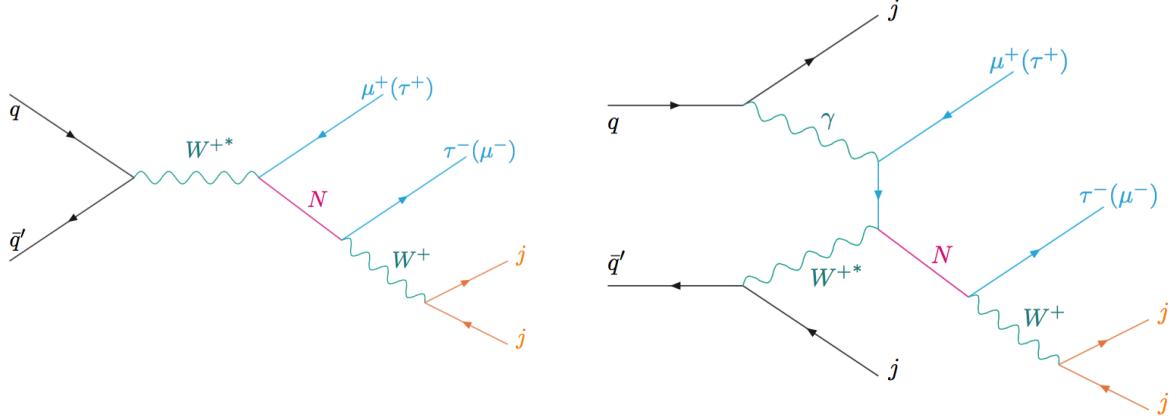
Figure 5.2: The two main processes, Drell-Yan and γW fusion, producing exotic $\tau \mu j j$ events via heavy neutrino production and decay at the LHC.

results are always equal for the pseudo-Dirac pairs, since their Majorana character plays a subleading role in their production.

We can also learn that the flavor of the associated charged lepton is different depending on the heavy neutrino produced and the scenario considered, and that this pattern can be understood looking at the mixing in Fig. 5.1. For example, $N_{3/4}$ are mainly electronic neutrinos in the TM-1,2,4,5, 7 scenarios and, therefore, they are basically produced exclusively with electrons. $N_{1/2}$ are equally produced with muons and taus in the TM-1,2,4,5 scenarios, dominantly produced with electrons in the TM-3 scenario, and mainly produced with taus in the TM-7 and 8 scenarios. On the other hand, $N_{5/6}$ are equally produced with muons and taus in TM-1,2,3,4,5,6 scenarios, mainly produced with muons in the TM-7 scenario and mostly produced with electrons in the TM-8 scenario.

Once the heavy neutrinos are produced, they will decay inside the detector. As mentioned in Section 2.3.5, in the limit $M_R \gg m_D$ the heavy neutrino masses are close to M_R, with small differences of $\mathcal{O}(m_D^2 M_R^{-1})$ between the different pseudo-Dirac pairs and, therefore, assuming that they are practically degenerate, their decay into each other should be suppressed, with the dominant channels, then, being $N_j \to Z\nu_i, H\nu_i, W^{\pm}l_i^{\mp}$. The expressions for these relevant channels are given in Eqs. (2.20) and (2.21).

It is interesting to study the rich flavor structure of the decay products, which depends on the decaying heavy neutrino and the scenario we are considering. Like in the production, the flavor preference of the decays to $W^{\pm}l^{\mp}$, which are the ones relevant to this study and are given in Fig. 5.2, also follows the same pattern as in Fig. 5.1. Therefore, we can expect the production and decay of the heavy neutrinos to lead to exotic $\mu \tau j j$ events with no missing energy and $M_{jj} \sim M_W$, with M_{jj} the invariant mass of the two jets.

124
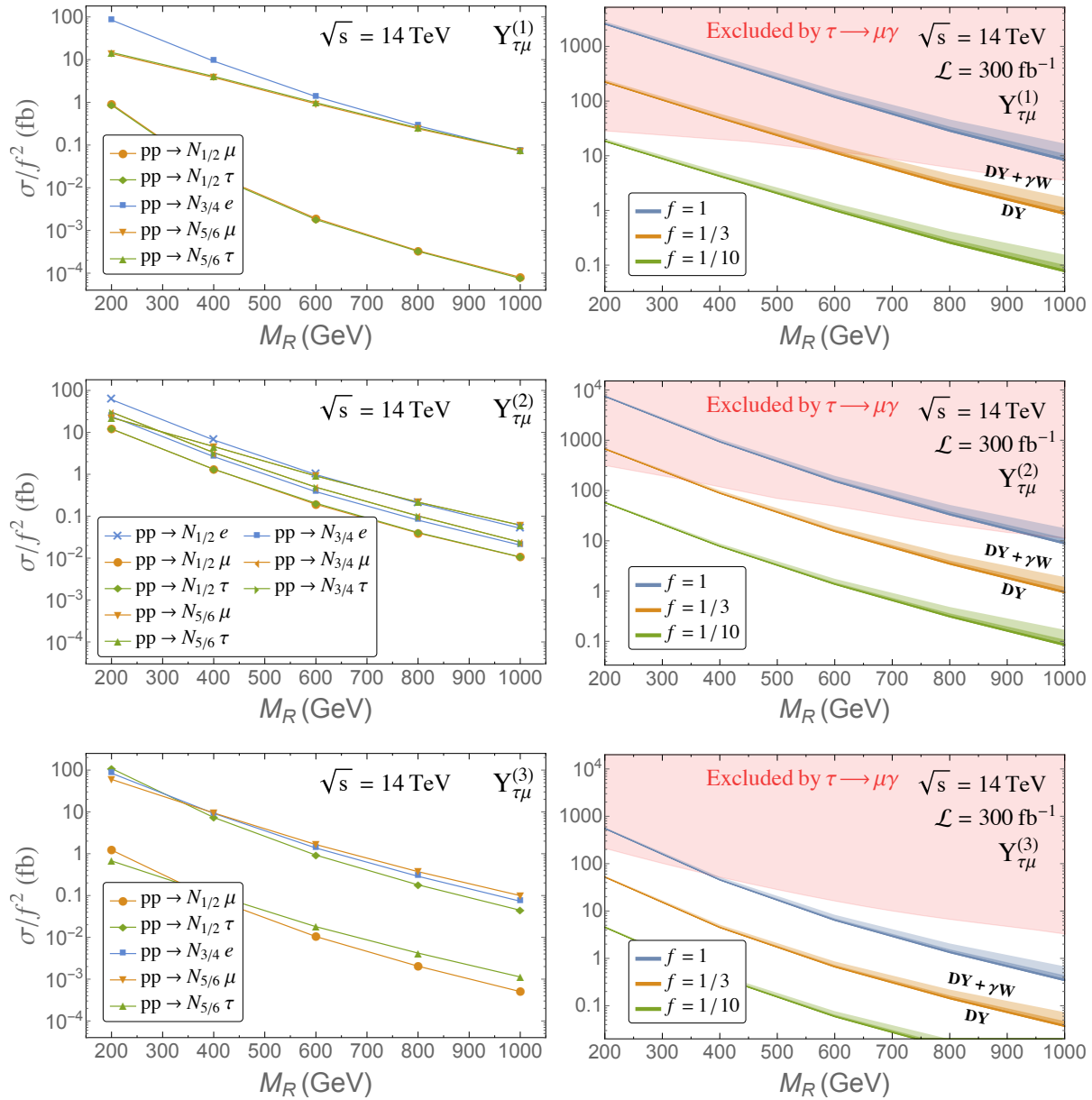
Figure 5.3: Left panels: Heavy neutrino DY-production, normalized by f^2, at the LHC for scenarios TM-5 ($Y_{\tau\mu}^{(1)}$), TM-6 ($Y_{\tau\mu}^{(2)}$), TM-7 ($Y_{\tau\mu}^{(3)}$) from Table 2.4. Processes not shown are negligible. Right panels: Number of exotic $\mu\tau jj$ events at the LHC for the same scenarios and for three values of f. For each f, the bottom solid line is the prediction of $\mu\tau jj$ events from DY and the upper lines on top of each of the three shadowed regions are the predictions after adding the $\mu\tau jj$ events from γW, for $p_T^{\max} = 10, 20, 40$ GeV from bottom to top, to the two extra jets. The upper red shadowed areas are excluded by $\tau \to \mu\gamma$.

125

Using the narrow width approximation, the total cross section of the exotic events we are interested in is given by:

$$\sigma(pp \to \mu\tau jj) = \sum_{i=1}^{6} \left\{ \sigma(pp \to N_i\mu^{\pm})\text{BR}(N_i \to W^{\pm}\tau^{\mp}) + \sigma(pp \to N_i\tau^{\pm})\text{BR}(N_i \to W^{\pm}\mu^{\mp}) \right\}$$
$$\times \text{BR}(W^{\pm} \to jj). \tag{5.3}$$

Fig. 5.3 shows the expected number of exotic events $\mu\tau jj$ at the LHC for an integrated luminosity of $\mathcal{L} = 300$ fb^{-1} at $\sqrt{s} = 14$ TeV. The lower solid lines for each choice of f are the number of events considering only the DY-production.

Moreover, γW fusion processes can also contribute to this kind of exotic events if the p_T of the extra jets are below a maximum value $p_T^{\max}$ and, therefore, they can be considered as soft or collinear jets which can escape detection. In this case the predicted total number of exotic events are the sum of the events produced by DY and γW channels. These total contributions for different values of $p_T^{\max} = 10, 20$ and 40 GeV are shown as the border lines on top of the shadowed areas with gradual decreasing intensity above each solid line. In addition we have included in the plots red shadowed areas that represent the regions excluded by the experimental upper bound on BR($\tau \to \mu\gamma$), which as we saw in the previous Chapters is the most constraining LFV observable at this range of masses. We can see that, after considering all the LFV constraints, the three scenarios lead to an interesting number of $\mathcal{O}(10-100)$ total $\mu\tau jj$ exotic events for the range of M_R studied here of [200 GeV, 1 TeV]. Applying constraints from other observables beyond the LFV ones, like the ones studied in Section 2.3, could change this final conclusion. For example, looking at Fig. 4.4, we see that in the TM-5 scenario for M_R values in the (200, 1000) GeV interval, the Z invisible width sets a maximum value for f of about 1.5 times stronger, meaning that the maximum allowed number of events would be about 2-3 times smaller. Similarly, considering the global fit constraints as in Section 3.4 would increase the excluded red area, reducing the maximum number of events predicted in the allowed parameter space. A more complete analysis deserves further study and will be done in a forthcoming work, where we will also explore the larger luminosity options for future LHC phases.

The SM backgrounds for events with two leptons of different flavor have been studied in Ref. [277]. However, a high efficiency in the τ-tagging and a good reconstruction of the W boson invariant mass from the two leading jets would help in reducing the background. In that case, the main background would come from processes with photons or jets misidentified as leptons, mainly from $W/Z+\gamma^*$, $W/Z+$ jets and multijet events with at least four jets with one of them misidentified as a muon and another as a tau; and from $Z/\gamma^* +$ jets $\to \mu^+\mu^-$ $+$ jets if one of the muons is misidentified as a τ candidate. Nevertheless, a dedicated background study for these particular $\mu\tau jj$ exotic events is needed and will be done in a future work.

Summarizing, in this Chapter we have proposed a new interesting way to study the production and decay of the heavy neutrinos of the ISS in connection with LFV. We have presented the computation of the predicted number of exotic $\mu\tau jj$ events which can be produced in these ISS scenarios with large LFV by the production of heavy pseudo-Dirac neutrinos together with a lepton of flavor ℓ, both via DY and γW fusion processes, and their subsequent decay into W plus a lepton of different flavor. We have concluded that, for the three TM-like scenarios studied here, a number of $\mathcal{O}(10-100)$ total $\mu\tau jj$ exotic events without missing energy can be produced at the next run of the LHC when $300\,\mathrm{fb}^{-1}$ are collected, for values of M_R from 200 GeV to 1 TeV. Similarly, rare $\tau e jj$ processes could be produced within the equivalent TE ISS scenarios. Although in other scenarios with large LFV $\mu e jj$ events could also be produced, which would be interesting since they could provide in addition observable CP asymmetries [278], the number of events would be strongly limited by the $\mu \to e\gamma$ upper bound. This idea of looking for $\tau\mu jj$ exotic events has been recently explored in the context of a 100 TeV pp collider in Ref. [279], finding promising results for a luminosity of $L = 10\mathrm{ab}^{-1}$. Of course, a more realistic study of these exotic events, including detector simulation, together with a full background study should be done in order to reach a definitive conclusion, but this will be addressed in a future work.

Conclusions

Flavor violating processes have been, are and will be crucial for the construction and developments of Particle Physics theory. In the last years, the observation of lepton flavor violation in the neutral sector via neutrino oscillations has established that neutrinos do have masses, which is at present the most clear experimental evidence telling us that the SM must be extended. In the same manner, any evidence of LFV transitions in the charged sector would automatically imply the presence of new physics, even beyond the SM with neutrino masses minimally added. This fact makes charged LFV processes an optimal place to look for new physics. Unfortunately, no such cLFV processes have been observed yet, although a strong experimental effort is being made in this direction, and future experiments are planning to improve the sensitivities up to really impressive levels.

In general, any modification of the neutral lepton sector in order to account for neutrino masses will affect directly or indirectly, mainly via quantum corrections, to the charged lepton sector, leaving a trail of phenomenological implications that experiments could potentially observe. Among the many different extensions for addressing neutrino mass generation, we have focused in low scale seesaw models, in particular in the ISS and SUSY-ISS models, which share the appealing feature of adding new right-handed neutrinos with masses at the TeV range, i.e, at the energy scale that present colliders as the LHC are exploring. Therefore, in this Thesis we have explored the connection between the presence of right-handed neutrinos at the TeV mass scale and the potential existence of processes with charged LFV.

As we discussed when introducing the ISS model in Chapter 1, one of the most important features of this ISS model is that it introduces three different mass scales with three different purposes: a small lepton number violating scale, μ_X, responsible of explaining the smallness of the light neutrino masses, a large M_R scale that governs the masses of the heavy pseudo-Dirac neutrino pairs, and a Dirac mass at the electroweak scale, $m_D = v Y_\nu$, which controls the interaction between the (mainly left-handed) light and (mainly right-handed) heavy neutrinos with the Higgs boson. Along this Thesis, we have clearly seen that the most relevant parameters for the cLFV processes that we are interested in are M_R and Y_ν. Consequently, we have introduced a new parametrization for accommodating neutrino oscillation data, the μ_X parametrization, alternative to the often used Casas-Ibarra parametrization and that allows to chose precisely M_R and Y_ν as independent input parameters of the model.

In order to gain intuition on the general properties of cLFV processes in the ISS model, we have first revisited in Chapter 2 the LFV lepton decays, meaning the radiative decays $\ell_m \to \ell_k \gamma$ and the three body decays $\ell_m \to \ell_k \ell_k \ell_k$ with $k \neq m$. This study have allowed us to establish the basic ideas of our analysis, as well as to understand the main differences of using the Casas-Ibarra parametrization or the μ_X parametrization. We have seen that, although physics must not depend on the parametrization one chooses, the efficiency of an analysis in reaching some particular but interesting directions in the parameter space may radically change. As a particular example of this idea, we have studied the LFV radiative decays when using the μ_X parametrization, where the Yukawa coupling matrix is one of the independent input parameters. Using this freedom, and the geometrical interpretation of the Yukawa matrix discussed in Section 2.2.1, we were able to define directions in the parameter space where the cLFV transitions are favored between two particular flavors, while keeping μ-e transitions always highly suppressed. This is particularly interesting in the light of present experimental bounds on cLFV processes, since there are very strong bounds in the μ-e sector, while they are weaker in the τ-e and τ-μ sectors and, therefore, there is more room for larger allowed LFV predictions in these two sectors.

In Chapter 3 we have studied in full details the LFV Higgs decays $H \to \ell_k \bar{\ell}_m$ induced at the one-loop level from the ISS right-handed neutrinos. We have presented a full one-loop computation of the $\mathrm{BR}(H \to \ell_k \bar{\ell}_m)$ rates for the three possible channels, $\ell_k \bar{\ell}_m = \mu \bar{\tau}, e\bar{\tau}, e\bar{\mu}$, and have also analyzed in full detail the predictions as functions of the various relevant ISS parameters. We found, as in the LFV lepton decays, that the most relevant parameters are M_R and Y_ν. Nevertheless, we have seen that, interestingly, the dependence of the LFVHD rates on these parameters is not the same of that of the LFV radiative decays.

In order to better understand these differences, we have performed a new and independent computation using a very different approach which turns out to provide simpler and more useful analytical results. Instead of applying the usual diagrammatic method of the full one-loop computation, we have used the MIA which works with the chiral EW neutrino basis, including the left- and right-handed states ν_L, and ν_R and the extra singlets, X of the ISS, instead of dealing with the nine physical neutrino states, $n_{1\ldots 9}$ of the mass basis.

To simplify further this MIA computation we have first prepared the chiral basis in a convenient way, such that all the effects of the singlet X states are collected into a redefinition of the ν_R propagator, which we have called here *fat propagator*, and then we have derived the set of Feynman rules for these proper chiral states that summarizes the relevant interactions involved in the one-loop computation of the LFVHD rates. The peculiarity of using this particular chiral basis is that it leads to a quite generic set of Feynman rules for the subset of interactions involving the neutrino sector, mainly ν_L and ν_R, which are the relevant ones for the LFV observables of our interest here, and therefore our results could be valid for other low scale seesaw models sharing these same Feynman rules. With the MIA we have then organized the one-loop computation of the LFVHD rates in terms of a perturbative

130

expansion in powers of the neutrino Yukawa coupling Y_ν matrix. It is worth recalling that in the ISS model, the Y_ν matrix is the unique relevant origin of LFV and, thus, it is the proper expansion parameter in the MIA computation.

We have presented here the analytical results using the MIA for the form factors that define the one-loop LFVHD amplitude, and we have done this computation first to leading order, $\mathcal{O}((Y_\nu Y_\nu^\dagger)_{km})$, and later to the next to leading order, i.e. including terms up to $\mathcal{O}((Y_\nu Y_\nu^\dagger Y_\nu Y_\nu^\dagger)_{km})$. Moreover, we have demonstrated that our analytical results are gauge invariant, obtaining the same result in the Feynman-'t Hooft gauge and the unitary gauge. This is certainly a good check of our analytical results. Numerically, we have found that in order to get a good numerical convergence of the MIA with the full results, it is absolutely necessary to include both $\mathcal{O}(Y_\nu^2)$ and $\mathcal{O}(Y_\nu^4)$ terms. Indeed, the presence of the $\mathcal{O}(Y_\nu^4)$ terms is what explains the different funcional behavior with the parameters that we observed for the LFVHD rates with respect to the radiative decays, which are well described with only the $\mathcal{O}(Y_\nu^2)$ terms. We have then checked numerically that the MIA works pretty well in a big range of the relevant model parameters Y_ν and M_R. For a small Yukawa coupling, given in our notation by a small global factor say $f < 0.5$ we have obtained an extremely good convergence of the MIA and full results even for moderate M_R of a few hundred GeV and above. For larger Yukawa couplings, say with $0.5 < f < 2$ we have also found a good convergence, but for heavier M_R, say above $\mathcal{O}(1\mathrm{TeV})$.

In addition to the form factors, we have also derived in Section 3.3.3 an analytical expression of the LFV effective vertex describing the $H\ell_k\ell_m$ coupling that is radiatively generated to one-loop from the heavy right-handed neutrinos. For that computation we have presented our systematic expansion of the form factors in inverse powers of M_R, which is valid in the mass range of our interest, $m_\ell \ll m_D, m_W, m_H \ll M_R$, and we have found the most relevant terms of $\mathcal{O}(v^2/M_R^2)$ in this series. In doing this expansion, we have taken care of the contributions from the external Higgs boson momentum which are relevant since in this observable the Higgs particle is on-shell, and we have also followed the track of all the EW masses involved like m_W and m_H which are both of order v and therefore contribute to the wanted $\mathcal{O}(v^2/M_R^2)$ terms. The lepton masses (except for the global factor from the heaviest lepton $m_{\ell_k} \gg m_{\ell_m}$) do not provide relevant corrections and have been neglected in this computation of the effective vertex. We have shown with several examples that this simple MIA formula works extremely well for the interesting window in the (Y_ν, M_R) parameter space which is allowed by the present experimental constraints. Therefore, we believe that our final analytical formula for the LFV effective $H\ell_k\ell_m$ vertex given in Eq. (3.34) is very simple and can be useful for other authors who wish to perform a fast estimate of the LFVHD rates in terms of their own preferred input parameter values, Y_ν and M_R.

For the numerical estimates of the full one-loop results of the LFVHD rates, we have explored the ISS parameter space considering again the two discussed parametrization for accommodating light neutrino masses and mixings. First, we have considered the Casas-

Ibarra parametrization and explored the LFVHD rates from the simplest case of diagonal μ_X and M_R matrices with degenerate entries for M_{R_i}, to a more general case with hierarchical neutrinos. In this case, we conclude that the largest maximum LFV Higgs decay rates within the ISS that are allowed by the constraints on the LFV radiative decays are for $\mathrm{BR}(H \to e\bar{\tau})$ and $\mathrm{BR}(H \to \mu\bar{\tau})$ and reach at most 10^{-10} for the degenerate heavy neutrino case and 10^{-9} for the hierarchical case. Second, we have considered the μ_X parametrization and explored the well phenomenologically motivated scenarios that are more promising for LFVHD searches in the τ-e and τ-μ sectors. We have demonstrated that in this kind of ISS scenarios there are solutions with much larger allowed LFVHD rates than in the previous cases, leading to maximal rates allowed by the bounds on the radiative decays of around 10^{-5} for either $\mathrm{BR}(H \to \mu\bar{\tau})$ or $\mathrm{BR}(H \to e\bar{\tau})$.

Finally, we have considered the effects of other kind of constraints to the ISS parameter space by making use of the global fits analysis to present data and the perturbativity requirements on the Yukawa couplings. These constraints result in allowed $\mathrm{BR}(H \to e\bar{\tau})$ and $\mathrm{BR}(H \to \mu\bar{\tau})$ ratios being at most at about 10^{-7}, which are unfortunately far below the present experimental sensitivities and, therefore, future experiments would be needed for testing these predictions.

In Section 3.2, we have also addressed the question of whether the SUSY realization of the ISS model can lead to enhanced predictions for the LFV Higgs decay rates. We have considered the MSSM model with the lightest CP-even Higgs boson h identified as the SM-like Higgs boson, and extended with three pairs of ISS neutrinos and their corresponding SUSY partners, the sneutrinos. We have then presented the results of an updated and full one-loop calculation of the SUSY contributions to lepton flavor violating Higgs decays in the SUSY-ISS model. These contributions come from chargino-sneutrino loops with sneutrino couplings off-diagonal in flavor, and from neutralino-slepton loops, due to the misalignment in flavor between the slepton and lepton sectors caused by running effects. We found much larger contributions than in the type-I seesaw model coming from the lower values of $M_R \sim \mathcal{O}(1 \text{ TeV})$, an increased RGE-induced slepton mixing, and the presence of new right-handed sneutrinos at the TeV scale. Then, the couplings of both sleptons and sneutrinos can transmit sizable LFV due to the large $Y_\nu^2/(4\pi) \sim \mathcal{O}(1)$ we considered. We showed that the branching ratio of $h \to \tau\bar{\mu}$ exhibits different behaviors as a function of the seesaw and SUSY scale if it is dominated by chargino or neutralino loops. Moreover, a non-zero trilinear coupling A_ν leads to increased LFVHD rates. Choosing different benchmark points, we found that $\mathrm{BR}(h \to \tau\mu)$ of the order of 10^{-2} can be reached while agreeing with the experimental limits on radiative decays, which can be tested at the present runs of the LHC. This calls up for a complete study including non-supersymmetric contributions in the SUSY-ISS model, like those from the extended Higgs sector, and a detailed analysis of experimental constraints beyond radiative LFV decays, which will be addressed in a future work.

In Chapter 4 we have revisited the LFV Z decays in presence of right-handed neutri-

nos with TeV range masses, which are very interesting observables that are currently being searched for in the LHC and will be further explored by the next generation of experiments. A first study of these observables within the ISS context with three pairs of fermionic singlets was done in Ref. [49], finding maximum allowed ratios of about 10^{-9}. Here, we have alternatively studied in full detail the LFVZD rates in our selected TM and TE scenarios, which as we said are designed to find large rates for processes including a τ lepton, and we have investigated those that are allowed by all the present constraints. In addition to the radiative decays, important constraints come from experimental upper bounds on the LFV three body lepton decays, since they are strongly correlated to the LFVZD in these scenarios. Taking into account all the relevant bounds, we found that heavy ISS neutrinos with masses in the few TeV range can induce maximal rates of $\mathrm{BR}(Z \to \tau\mu) \sim 2 \times 10^{-7}$ and $\mathrm{BR}(Z \to \tau e) \sim 2 \times 10^{-7}$ in the TM and TE scenarios, respectively. These rates are considerably larger than what was found in previous studies and potentially measurable at future linear colliders and FCC-ee. Therefore, we have seen that searches for LFVZD at future colliders may be a powerful tool to probe cLFV in low scale seesaw models, in complementarity with low-energy (high-intensity) facilities searching for cLFV processes.

Another appealing feature of our results is that the predictions for the cLFV processes come together with the possibility that the heavy neutrinos could be directly produced at the LHC. Being the ISS neutrinos pseudo-Dirac fermions, the standard same-sign dilepton searches for heavy Majorana neutrinos are not effective, implying that new search strategies need to be explored. In Chapter 5 we have proposed a new interesting way of studying the production and decay of the heavy neutrinos of the ISS in connection with LFV. We have presented the computation of the predicted number of exotic $\mu\tau jj$ events, which can be produced in the TM scenarios with large LFV, where the heavy pseudo-Dirac neutrinos are produced together with a lepton of a given flavor, both via Drell-Yan and γW fusion processes, and then decay into W plus a lepton of different flavor. We have concluded that, for the studied benchmark scenarios, a number of $\mathcal{O}(10-100)$ total $\mu\tau jj$ exotic events without missing energy can be produced at the next run of the LHC when 300 fb^{-1} of integrated luminosity is reached, and for values of M_R from 200 GeV to 1 TeV respecting the constraints from LFV violating observables. Similarly, other rare processes like $\tau e jj$ or $\mu e jj$ could be produced within other ISS scenarios with large LFV, although for the latter ones the number of events would be strongly limited by the $\mu \to e\gamma$ upper bound. These promising results deserve a more realistic study of these exotic events, including detector simulation, together with a full background study, which should be done in order to reach a definitive conclusion and it will be addressed in a future work.

As an overall conclusion of this Thesis, we can state that searching for charged lepton flavor violating processes is a very powerful strategy for testing the presence of low scale seesaw neutrinos with masses of a few TeV or below, which on the other hand are common in many models for explaining the observed neutrino masses. As we have seen along this

Thesis, the addition to the SM of these new states, not much heavier that the EW scale and with a potentially complex flavor structure, has an important impact in the phenomenology of the charged leptons, which could be seen at lepton flavor violating processes. Flavor physics has been crucial in the history of the SM and it will play a major role in the discovery of new physics.

Conclusiones

Los procesos con violación de sabor han sido, son y serán cruciales para la construcción y desarrollo teórico de la Física de Partículas. En los últimos años, la observación de violación de sabor leptónico en las oscilaciones de neutrinos ha demostrado que los neutrinos tienen masas, hecho que supone la evidencia experimental actual más clara de que el SM debe ser extendido. De la misma manera, cualquier evidencia de transiciones con LFV en el sector cargado supondría automáticamente la existencia de nueva física, más allá incluso del SM con las masas de los neutrinos añadidas de manera mínima. Este hecho hace de los procesos con LFV en el sector cargado un lugar óptimo para buscar nueva física. Por desgracia, no se ha observado ningún proceso con cLFV todavía, aunque se está realizando un gran esfuerzo experimental en esta línea y los futuros experimentos prevén mejorar las sensibilidades a este tipo de procesos hasta niveles realmente impresionantes.

En general, cualquier modificación en el sector de leptones neutros tratando de explicar la masa de los neutrinos afectará directa o indirectamente, a través de correcciones cuánticas, al sector de leptones cargados, dejando así una traza de implicaciones fenomenológicas que los experimentos podrían llegar a observar. Entre las muchas y diferentes extensiones posibles para explicar la generación de masas de los neutrinos, nos hemos centrado en los modelos seesaw de baja escala, en particular en los modelos ISS y SUSY-ISS, que comparten la interesante cualidad de añadir nuevos neutrinos dextrógiros con masas en el rango del TeV, i.e, a la escala de energía que los colisionadores actuales como el LHC están explorando. Por tanto, en esta Tesis hemos explorado la conexión entre la presencia de neutrinos dextrógiros en la escala de masas del TeV y la posible existencia de procesos con LFV en el sector cargado.

Como hemos discutido al introducir el modelo ISS en el Capítulo 1, una de las cualidades más interesantes de este modelo es que introduce tres escalas diferentes con tres propósitos muy diferentes: una escala ligera que viola el número leptónico, μ_X, la responsable de explicar la ligereza de la masa de los neutrinos que observamos, una escala pesada M_R que gobierna las masas de los pares de neutrinos pesados pseudo-Dirac, y una masa de Dirac en la escala electrodébil, $m_D = v Y_\nu$, que controla la interacción entre los neutrinos ligeros (mayormente levógiros) y los pesados (mayormente dextrógiros) con el bosón de Higgs. A lo largo de esta Tesis, hemos visto claramente que los parámetros más relevantes

para los procesos con cLFV en los que estamos interesados son M_R y Y_ν. Por tanto, hemos introducido una nueva parametrización para ajustar los datos de las oscilaciones de neutrinos, la parametrización μ_X, alternativa a la frecuentemente utilizada parametrización de Casas-Ibarra, y que permite elegir como parámetros libres del modelo precisamente M_R y Y_ν.

Con el objetivo de obtener intuición sobre las propiedades generales de los procesos con cLFV en el modelo ISS, en el Capítulo 2 hemos empezado por repasar las desintegraciones con LFV de los leptones, centrándonos en las radiativas $\ell_m \to \ell_k \gamma$ y las de tres cuerpos $\ell_m \to \ell_k \ell_k \ell_k$ con $k \neq m$. Este estudio nos ha permitido establecer las ideas básicas de nuestro análisis, así como de entender las principales diferencias a la hora de utilizar la parametrización de Casas-Ibarra o la de μ_X. Hemos visto que, aunque la física no puede depender de la parametrización que uno utilice, esta decisión sí que puede afectar a la eficiencia de un análisis a la hora de alcanzar ciertas direcciones particulares pero interesantes del espacio de parámetros. Como ejemplo ilustrativo de esta idea, hemos estudiado las desintegraciones radiativas con LFV utilizando la parametrización μ_X, lo que nos ha permitido trabajar con la matriz de acoplamiento de Yukawa como parámetro libre. Utilizando esta libertad, junto con la interpretación geométrica de la matriz de Yukawa discutida en la Sección 2.2.1, hemos podido definir direcciones en el espacio de parámetros donde las transiciones con cLFV están favorecidas entre dos sabores particulares, a la vez que están muy suprimidas en el sector μ-e. Esta situación es especialmente interesante a la luz de las cotas actuales sobre procesos cLFV, dado que las cotas son muy fuertes en el sector μ-e, pero más débiles en los sectores τ-e y τ-μ y, por tanto, existe más espacio para procesos con LFV con tasas de desintegración más altas en estos dos sectores.

En el Capítulo 3 hemos estudiado detalladamente las desintegraciones con LFV del bosón de Higgs, $H \to \ell_k \bar{\ell}_m$, inducidas por los neutrinos dextrógiros del modelo ISS a nivel de un *loop*. Hemos presentado el cálculo completo de $\mathrm{BR}(H \to \ell_k \bar{\ell}_m)$ a un *loop* para los tres posibles canales, $\ell_k \bar{\ell}_m = \mu\bar{\tau}, e\bar{\tau}, e\bar{\mu}$, y hemos analizado en detalle la predición de este observable en función de los diferentes parámetros del modelo ISS. Hemos encontrado que, al igual que en el caso de las desintegraciones radiativas con LFV, los parámetros más relevantes son M_R y Y_ν. Sin embargo, hemos visto que, interesantemente, la dependencia de los LFVHD con estos parámetros no es la misma que la de las desintegraciones radiativas con LFV.

Con el objetivo de entender mejor estas diferencias, hemos realizado un cálculo nuevo e independiente, abordando el problema de una manera diferente y que proporciona resultados analíticos más simples y útiles. En vez de realizar el cálculo completo a nivel de un *loop* siguiendo el proceso diagramático habitual, hemos usado la técnica de la MIA, que trabaja con la base electrodébil de los neutrinos, incluyendo los estados levógiros ν_L, dextrógiros ν_R y los singletes extra X del ISS, en vez de lidiar con los nueve neutrinos físicos, $n_{1\ldots9}$, de la base de masas.

De cara a simplificar aún más nuestro cálculo en la MIA, primero hemos preparado

la base quiral en una forma conveniente, de modo que todos los efectos de los singletes X estén contenidos en la redefinición de los propagadores de ν_R, a los que hemos llamado *propagadores gordos*, y después hemos derivado el conjunto de reglas de Feynman de las interacciones necesarias para realizar el cálculo a un *loop* de los LFVHD en esta base quiral. La peculiaridad de usar esta base quiral es que lleva a una serie de reglas de Feynman bastante genéricas para este conjunto de interacciones que involucran el sector de los neutrinos, ν_L y ν_R mayormente, que son los relevantes para los observables con LFV en los que estamos interesados, y por tanto los resultados obtenidos podrían ser válidos para cualquier otro modelo de seesaw de baja escala que comparta las mismas reglas de Feynman. Usando la técnica de la MIA hemos organizado el cálculo de los LFVHD a un *loop* como una expansión perturbativa en potencias de la matriz de acoplamiento Yukawa Y_ν de los neutrinos. Merece la pena remarcar que en el modelo ISS, la matriz Y_ν es el único origen relevante de LFV y, por tanto, es el parámetro adecuado en el que realizar la expansión MIA.

Hemos presentado los resultados analíticos de nuestro cálculo con la MIA de los factores de forma que definen la amplitud del LFVHD, cálculo que hemos realizado al orden dominante $\mathcal{O}((Y_\nu Y_\nu^\dagger)_{km})$ primero, y al siguiente orden después, i.e. incluyendo los términos de hasta $\mathcal{O}((Y_\nu Y_\nu^\dagger Y_\nu Y_\nu^\dagger)_{km})$. Asímismo, hemos demostrado la invariancia gauge de nuestros resultados obteniéndolos tanto en el gauge de Feynman-'t Hooft y como en el unitario. Este es sin duda un buen test de nuestros resultados. Numéricamente, hemos visto que para obtener una buena convergencia entre los resultados de la MIA y los completos es necesario incluir tanto los términos $\mathcal{O}(Y_\nu^2)$ como los $\mathcal{O}(Y_\nu^4)$. De hecho, son justo estos términos $\mathcal{O}(Y_\nu^4)$ los que explican las diferencias con respecto a las desintegraciones radiativas, las cuales son bien descritas sólo con los términos $\mathcal{O}(Y_\nu^2)$. Hemos comprobado que estas fórmulas dan un resultado muy parecido al del cálculo completo en un gran rango de los parámetros relevantes Y_ν y M_R. En el caso de acoplamientos Yukawa pequeños, que en nuestra notación viene definido por un valor pequeño de f, digamos $f < 0.5$, hemos obtenido una convergencia muy buena entre los resultados de la MIA y los completos incluso para valores de M_R moderados, de unos pocos cientos de GeV, y mayores. Para acoplamientos Yukawa más grandes, digamos $0.5 < f < 2$, también hemos visto que los resultados convergen, pero esto ocurre a valores más altos de M_R, digamos que por encima de $\mathcal{O}(1\,\mathrm{TeV})$.

Además de los factores de forma, en la Sección 3.3.3 hemos derivado una expresión analítica para el vértice efectivo con LFV que describe el acoplamiento $H\ell_k\ell_m$ que se genera radiativamente a nivel de un *loop* con neutrinos dextrógiros pesados. Para este cálculo hemos realizado una expansión sistemática de los factores de forma en potencias inversas de M_R, válida en el rango de masas en el que estamos interesados $m_\ell \ll m_D, m_W, m_H \ll M_R$, y hemos obtenido los términos más relevantes a $\mathcal{O}(v^2/M_R^2)$. En esta expansión hemos tenido en cuenta la contribuciones del momento de la pata externa del bosón de Higgs, que son necesarias al tratarse de un observable con el Higgs en su capa de masas, y también hemos seguido la pista a todas las masas EW involucradas, m_W y m_H, ambas de orden v y por

tanto importantes para los terminos $\mathcal{O}(v^2/M_R^2)$. Las masas de los leptones, sin embargo, no contribuyen de manera relevante (salvo en el factor global con una masa del leptón más pesado, $m_{\ell_k} \gg m_{\ell_m}$ en nuestro caso) y las hemos por tanto despreciado al calcular el vértice efectivo. Hemos demostrado con varios ejemplos que esta simple fórmula de la MIA funciona muy bien en la ventana de interés del espacio de parámetros (Y_ν, M_R) permitido por las cotas experimentales actuales. Por tanto, consideramos que nuestra fórmula analítica final para el vértice efectivo LFV $H\ell_k\ell_m$, dado en la Ec. (3.34), es simple y puede ser útil para otros autores que deseen estimar de forma rápida las tasas de LFVHD para sus valores preferidos de Y_ν y M_R.

A la hora de realizar las estimaciones numéricas de los resultados a un *loop* completos de las tasas LFVHD, hemos explorado el espacio de parámetros del modelo ISS considerando de nuevo las dos parametrizaciones mencionadas anteriormente, que resultan útiles para ajustar los datos de las oscilaciones de neutrinos. En primer lugar, hemos considerado la parametrización de Casas-Ibarra y explorado las LFVHD desde el caso más simple en el que las matrices μ_X y M_R son diagonales y con entradas degeneradas para M_{R_i}, hasta un caso más genérico donde los neutrinos pesados son jerárquicos. En este caso, hemos concluído que las mayores tasas de desintegración con LFV del Higgs permitidas por las cotas sobre las desintegraciones radiativas con LFV son para los canales $\mathrm{BR}(H \to e\bar{\tau})$ y $\mathrm{BR}(H \to \mu\bar{\tau})$ y alcanzan como mucho 10^{-10} en el caso con neutrinos pesados degenerados y 10^{-9} en el caso jerárquico. En segundo lugar, hemos considerado la parametrización μ_X y explorado los previamente introducidos y motivados escenarios fenomenológicamente, que son más prometedores de cara a las LFVHD en los sectores τ-e y τ-μ. Hemos demostrado que en este tipo de escenarios del ISS existen soluciones, permitidas por las desintegraciones radiativas, con tasas de LFVHD mayores que en el caso anterior, de hasta 10^{-5} para $\mathrm{BR}(H \to \mu\bar{\tau})$ o $\mathrm{BR}(H \to e\bar{\tau})$.

Por último, hemos estudiado los efectos de otro tipo de restricciones al espacio de parámetros del ISS considerando los resultados de los análisis globales a los datos actuales, y exigiendo también que los acoplamientos Yukawa sean perturbativos. Estas cotas resultan en un máximo para $\mathrm{BR}(H \to e\bar{\tau})$ y $\mathrm{BR}(H \to \mu\bar{\tau})$ del orden de 10^{-7}, aproximadamente, las cuales, por desgracia, se encuentran lejos de las sensibilidades experimentales actuales y, por ende, se necesitarán experimentos futuros para falsar estas predicciones.

En la Sección 3.2, nos hemos planteado la pregunta de si la realización SUSY del ISS podría llevar a mayores predicciones de las tasas de desintegración LFV del Higgs. Hemos considerado para ello el modelo MSSM con el bosón de Higgs con CP par más ligero actuándo como el bosón de Higgs del SM, y extendido con tres pares de neutrinos del ISS y sus correspondientes compañeros SUSY, los sneutrinos. Hemos presentado los resultados del cálculo completo y actualizado de las contribuciones SUSY a un *loop* a las desintegraciones con violación de sabor leptónico en el modelo SUSY-ISS. Estas contribuciones vienen de los *loops* de charginos-sneutrinos, siendo los acoplamientos de los sneutrinos no diagonales en sabor,

y *loops* de neutralinos-sleptones, debido a la no alineación entre los sectores de sleptones y los leptones inducida por los efectos de las ecuaciones del grupo de renormalización. Hemos encontrado que estas contribuciones son mucho mayores que en el modelo de seesaw de tipo-I debido al valor más bajo de $M_R \sim \mathcal{O}(1 \text{ TeV})$, al crecimiento de la mezcla entre sleptones inducida via RGE, y a la presencia de sneutrinos dextrógiros a la escala del TeV. En esta situación los acoplamientos de tanto los sleptones como los sneutrinos pueden transmitir una LFV grande, dado que estamos considerando valores altos para $Y_\nu^2/(4\pi) \sim \mathcal{O}(1)$. Hemos demostrado que las anchuras de desintegración de $h \to \tau\mu$ se comportan diferente al variar la escala seesaw o la SUSY, dependiendo de si están dominadas por los loops de charginos o neutralinos. Además, la presencia de un acoplamiento trilineal A_ν tiende a aumentar aún más las tasas LFVHD. Eligiendo diferentes escenarios, hemos encontrado que pueden alcanzarse $\text{BR}(h \to \tau\mu)$ del orden de 10^{-2} en puntos permitidos por las cotas a las desintegraciones radiativas, valores que podrían ser observados actualmente por el LHC. Este hecho motiva un estudio más completo, incluyendo las contribuciones no supersimétricas del modelo SUSY-ISS, como las del sector extendido de Higgs, y un análisis más detallado de las cotas experimentales más allá de las desintegraciones radiativas con LFV. Todo ello será abordado en un futuro trabajo.

En el Capítulo 4 hemos revisado las desintegraciones con LFV del Z en presencia de neutrinos dextrógiros en el rango de masas del TeV, unos observables muy interesantes ya que están siendo actualmente buscados por el LHC, y que la siguiente generación de experimentos planea hacerlo con gran precisión. Un primer estudio de estos observables en el contexto del ISS con tres pares de singletes fermiónicos fue llevado a cabo en la Ref. [49], donde encontraron tasas de desintegración máximas de 10^{-9}. En este Capítulo, en cambio, hemos estudiado en todo detalle las LFVZD en nuestros escenarios TM y TE, que como decíamos han sido diseñados para encontrar tasas altas en los procesos que involucran un leptón τ, y hemos investigado el espacio de parámetros que está permitido por todas las cotas experimentales actuales. Junto con las desintegraciones radiativas, hemos encontrado cotas importantes provenientes de las desintegraciones a tres cuerpos con LFV, dado que están fuertemente correlacionadas con las LFVZD en estos escenarios. Teniendo en cuenta todas las cotas relevantes, hemos encontrado que neutrinos del ISS con masas de unos pocos TeV pueden inducir tasas de $\text{BR}(Z \to \tau\mu) \sim 2 \times 10^{-7}$ y $\text{BR}(Z \to \tau e) \sim 2 \times 10^{-7}$ en los escenarios TM y TE, respectivamente. Estos valores son considerablemente más altos que los obtenidos en estudios previos y alcanzables por los colisionadores lineales futuros y los FCC-ee. Por lo tanto, hemos visto que las búsquedas de LFVZD en los colisionadores futuros pueden ser una herramienta útil a la hora de testar la cLFV en los modelos de seesaw de bajas energías, complementariamente a otros experimentos en busca de cLFV de baja energía.

Otra de las cualidades interesantes de nuestros resultados es que las predicciones para los procesos cLFV vienen acompañados de la posibilidad de que los neutrinos pesados sean producidos directamente en el LHC. Siendo estos neutrinos fermiones pseudo-Dirac, las

búsquedas estándares de neutrinos de Majorana, basadas en leptones con la misma carga, no son efectivas, por lo que nuevas estrategias son necesarias. En el Capítulo 5 hemos propuesto una nueva forma interesante de estudiar la producción y desintegración de los neutrinos pesados del ISS en conexión con la LFV. Hemos presentado una predicción del número de eventos exóticos $\mu\tau jj$, que podrían ocurrir en los escenarios TM con gran LFV, donde los neutrinos pesados pseudo-Dirac se producen junto con un leptón de un sabor, mediante Drell-Yan o fusión γW, y se desintegran dando un W y otro leptón de un sabor distinto. Hemos concluido que, para los escenarios estudiados, se podrían producir del orden de $\mathcal{O}(10-100)$ eventos exóticos del tipo $\mu\tau jj$ sin energía transversa perdida en la próxima etapa del LHC cuando se alcance la luminosidad integrada de 300 fb^{-1}, para valores de M_R entre los 200 GeV y 1 TeV y respetando las cotas actuales sobre procesos con LFV. De manera parecida, otros procesos exóticos del tipo τejj or μejj podrían producirse en escenarios equivalentes del ISS, aunque en estos últimos el número total de eventos estaría muy suprimido debido a las fuertes cotas sobre $\mu \to e\gamma$. Los resultados obtenidos son prometedores y merecen un estudio más realista de estos eventos exóticos, incluyendo la simulación del detector, junto con un estudio completo del ruido, el cual es necesario para poder concluir de manera definitiva y será llevado a cabo en un trabajo futuro.

Como conclusión final de esta Tesis, podemos afirmar que las búsquedas de procesos con violación de sabor leptónico en el sector cargado son una estrategia muy potente a la hora de testar la presencia de neutrinos de modelos seesaw a baja energía, con masas en el entorno del TeV o debajo, que por otro lado son comunes en muchos modelos que explican las masas observadas de los neutrinos. Tal y como hemos visto a lo largo de esta Tesis, el hecho de añadir nuevos estados al SM, no mucho más pesados que la escala EW y con una estructura de sabor compleja, tiene un impacto importante en la fenomenología de los leptones cargados, algo que podría ser observado en procesos con violación de sabor leptónico. La física del sabor ha sido crucial en la historia del SM y jugará un papel esencial en el descubrimiento de nueva física.

Appendix A

Formulas for LFV lepton decays

In this Appendix we collect, for completeness, the needed formulas for the full one-loop computation of the LFV lepton decays in the particle mass basis, both the three body $\ell_m \to \ell_k \ell_k \ell_k$ and the radiative $\ell_m \to \ell_k \gamma$ decays, with $k \neq m$. We have taken these expressions from Refs. [90, 187] and implemented them in our code.

In the case of the three body decays, the branching ratio $\text{BR}(\ell_m \to \ell_k \ell_k \ell_k)$ can be expressed as [90, 187]:

$$
\begin{aligned}
\text{BR}(\ell_m \to \ell_k \ell_k \ell_k) = &\frac{\alpha_W^4}{24576\pi^3} \frac{m_{\ell_m}^4}{m_W^4} \frac{m_{\ell_m}}{\Gamma_{\ell_m}} \times \Bigg\{ 2 \left| \frac{1}{2} F_{\text{Box}}^{\ell_m \ell_k \ell_k \ell_k} + F_Z^{\ell_m \ell_k} - 2s_W^2 \left(F_Z^{\ell_m \ell_k} - F_\gamma^{\ell_m \ell_k} \right) \right|^2 \\
&+ 16 s_W^2 \text{Re} \left[\left(F_Z^{\ell_m \ell_k} + \frac{1}{2} F_{\text{Box}}^{\ell_m \ell_k \ell_k \ell_k} \right) G_\gamma^{\ell_m \ell_k *} \right] - 48 s_W^4 \text{Re} \left[\left(F_Z^{\ell_m \ell_k} - F_\gamma^{\ell_m \ell_k} \right) G_\gamma^{\ell_m \ell_k *} \right] \\
&+ 4 s_W^4 \left| F_Z^{\ell_m \ell_k} - F_\gamma^{\ell_m \ell_k} \right|^2 + 32 s_W^4 \left| G_\gamma^{\ell_m \ell_k} \right|^2 \left[\ln \frac{m_{\ell_m}^2}{m_{\ell_k}^2} - \frac{11}{4} \right] \Bigg\} .
\end{aligned}
\tag{A.1}
$$

The $\text{BR}(\ell_m \to \ell_k \ell_k \ell_k)$ contains several form factors, corresponding to the dipole, penguin (photon and Z) and box diagrams. The expressions for these form factors are given by:

$$
G_\gamma^{\ell_m \ell_k} = \sum_{i=1}^9 B_{\ell_k n_i} B_{\ell_m n_i}^* G_\gamma(x_i) ,
$$

$$
F_\gamma^{\ell_m \ell_k} = \sum_{i=1}^9 B_{\ell_k n_i} B_{\ell_m n_i}^* F_\gamma(x_i) ,
$$

$$
F_Z^{\ell_m \ell_k} = \sum_{i,j=1}^9 B_{\ell_k n_i} B_{\ell_m n_j}^* \left(\delta_{ij} F_Z(x_i) + C_{n_i n_j} G_Z(x_i, x_j) + C_{n_i n_j}^* H_Z(x_i, x_j) \right) ,
$$

$$F_{\text{Box}}^{\ell_m \ell_k \ell_k \ell_k} = \sum_{i,j=1}^{9} B_{\ell_k n_i} B_{\ell_m n_j}^* \left(B_{\ell_k n_i} B_{\ell_k n_j}^* G_{\text{Box}}(x_i, x_j) + 2\, B_{\ell_k n_i}^* B_{\ell_k n_j} F_{\text{Box}}(x_i, x_j) \right) . \tag{A.2}$$

where x_i stands for the dimensionless ratio of masses ($x_i = m_{n_i}^2/m_W^2$). Moreover, the following loop functions enter in the previous form factors [90, 187]:

$$F_Z(x) = -\frac{5x}{2(1-x)} - \frac{5x^2}{2(1-x)^2} \ln x\,,$$

$$G_Z(x,y) = -\frac{1}{2(x-y)} \left[\frac{x^2(1-y)}{1-x} \ln x - \frac{y^2(1-x)}{1-y} \ln y \right]\,,$$

$$H_Z(x,y) = \frac{\sqrt{xy}}{4(x-y)} \left[\frac{x^2-4x}{1-x} \ln x - \frac{y^2-4y}{1-y} \ln y \right]\,,$$

$$F_\gamma(x) = \frac{x(7x^2-x-12)}{12(1-x)^3} - \frac{x^2(x^2-10x+12)}{6(1-x)^4} \ln x\,,$$

$$G_\gamma(x) = -\frac{x(2x^2+5x-1)}{4(1-x)^3} - \frac{3x^3}{2(1-x)^4} \ln x$$

$$F_{\text{Box}}(x,y) = \frac{1}{x-y} \left\{ \left(1+\frac{xy}{4}\right) \left[\frac{1}{1-x} + \frac{x^2}{(1-x)^2} \ln x \right] - 2xy \left[\frac{1}{1-x} + \frac{x}{(1-x)^2} \ln x \right] - (x \to y) \right\},$$

$$G_{\text{Box}}(x,y) = -\frac{\sqrt{xy}}{x-y} \left\{ (4+xy) \left(\frac{1}{1-x} + x\frac{\ln x}{(1-x)^2} \right) - 2 \left(\frac{1}{1-x} + x^2\frac{\ln x}{(1-x)^2} \right) - (x \to y) \right\}. \tag{A.3}$$

In the limit of degenerate neutrino masses ($x=y$), we get the following expressions:

$$G_Z(x,x) = \left[x(-1+x-2\ln x)/(2(1-x)) \right]\,,$$

$$H_Z(x,x) = -\left[x(4-5x+x^2+(4-2x+x^2)\ln x)/(4(1-x)^2) \right]\,,$$

$$F_{\text{Box}}(x,x) = \left[(4-19x^2+16x^3-x^4-2x(-4+4x+3x^2)\ln x)/(4(1-x)^3) \right]\,,$$

$$G_{\text{Box}}(x,x) = x \left[\left(6-8x+4x^2-2x^3+(4+x^2+x^3)\ln x \right)/(-1+x)^3 \right]\,. \tag{A.4}$$

For the LFV radiative decay rates, we use the analytical formulas appearing in [42, 90, 187] that have also been implemented in our code:

$$\text{BR}(\ell_m \to \ell_k \gamma) = \frac{\alpha_W^3 s_W^2}{256\pi^2} \left(\frac{m_{\ell_m}}{m_W} \right)^4 \frac{m_{\ell_m}}{\Gamma_{\ell_m}} \left| G_{mk} \right|^2, \tag{A.5}$$

where Γ_{l_m} is total decay width of the lepton l_m, and

$$G_{mk} = \sum_{i=1}^{9} B_{ki} B_{mi}^* G_\gamma(x_i)\,, \tag{A.6}$$

with $G_\gamma(x)$ defined in Eq. (A.3) and, again, $x_i \equiv m_{n_i}^2/m_W^2$.

Appendix B

Formulas for low energy flavor conserving observables

In this Appendix we collect the expressions needed for computing the low energy observables described in Section 2.3. These formulas are taken from the literature and summarized here for completeness.

Lepton Universality: Δr_k

We collect here the formulas to calculate the quantity Δr_K (see Eq. (2.10)), which parametrizes the deviation from the SM prediction arising from the sterile neutrinos contribution, as a test of lepton flavor universality. The expression for Δr_K in generic SM extension with sterile neutrinos has been given in [26]:

$$\Delta r_K \; = \; \frac{m_\mu^2(m_K^2 - m_\mu^2)^2}{m_e^2(m_K^2 - m_e^2)^2} \; \frac{\sum_{i=1}^{N_{\max}^{(e)}} |B_{en_i}|^2 \left[m_K^2(m_{n_i}^2 + m_e^2) - (m_{n_i}^2 - m_e^2)^2\right] \lambda^{1/2}(m_K, m_{n_i}, m_e)}{\sum_{j=1}^{N_{\max}^{(\mu)}} |B_{\mu n_j}|^2 \left[m_K^2(m_{n_j}^2 + m_\mu^2) - (m_{n_j}^2 - m_\mu^2)^2\right] \lambda^{1/2}(m_K, m_{n_j}, m_\mu)} - 1 \,,$$

(B.1)

where $N_{\max}^{e,\mu}$ is the heaviest neutrino mass eigenstate kinematically allowed in association with e or μ respectively, and the kinematical function $\lambda(m_K, m_{n_i}, m_\ell)$ reads [26]:

$$\lambda(a, b, c) \; = \; (a^2 - b^2 - c^2)^2 - 4\, b^2\, c^2 \,.$$

(B.2)

The Z invisible decay width

The Z invisible decay width in presence of massive Majorana neutrinos, like it is the case of the present ISS model, reads [27]:

$$
\begin{aligned}
\Gamma(Z \to \text{inv.})_{\text{ISS}} &= \sum_n \Gamma(Z \to nn)_{\text{ISS}} \\
&= \sum_{i \leq j=1}^{N_{\max}} (1 - \tfrac{1}{2}\delta_{ij}) \frac{\sqrt{2}G_F}{48\,\pi\,m_Z} \times \lambda^{1/2}(m_Z, m_{n_i}, m_{n_j}) \\
&\quad \times \left[2|C_{n_i n_j}|^2 \left(2m_Z^2 - m_{n_i}^2 - m_{n_j}^2 - \frac{(m_{n_i}^2 - m_{n_j}^2)^2}{m_Z^2} \right) - 12 m_{n_i} m_{n_j} \operatorname{Re}\left[\left(C_{n_i n_j} \right)^2 \right] \right] .
\end{aligned}
\tag{B.3}
$$

where $N_{\max}$ is the heaviest neutrino mass which is kinematically allowed and λ is given in Eq. (B.2).

Oblique parameters: S, T, U

The Majorana neutrino contributions to the S, T, U parameters have been computed in Ref. [202]. We apply those formulas to compute the sterile neutrinos contributions to the oblique parameters in the ISS model.

The equation for the T parameter reads:

$$
\begin{aligned}
T_{\text{tot}} = T_{\text{ISS}} + T_{\text{SM}} = \frac{-1}{8\pi s_W^2 m_W^2} &\left\{ \sum_{\alpha=1}^{3} m_{\ell_\alpha}^2 B_0(0, m_{\ell_\alpha}^2, m_{\ell_\alpha}^2) - 2 \sum_{i=1}^{9} \sum_{\alpha=1}^{3} \left| B_{\ell_\alpha n_i} \right|^2 Q(0, m_{n_i}^2, m_{\ell_\alpha}^2) \right. \\
&\left. + \sum_{i,j=1}^{9} \left(C_{n_i n_j} C_{n_j n_i} Q(0, m_{n_i}^2, m_{n_j}^2) + (C_{n_i n_j})^2 m_{n_i} m_{n_j} B_0(0, m_{n_i}^2, m_{n_j}^2) \right) \right\} ,
\end{aligned}
\tag{B.4}
$$

where the index α refers to the charged leptons and

$$
Q(q^2, m_1^2, m_2^2) \equiv (D-2)B_{00}(q^2, m_1^2, m_2^2) + q^2 \left[B_1(q^2, m_1^2, m_2^2) + B_{11}(q^2, m_1^2, m_2^2) \right] ,
\tag{B.5}
$$

with $D \equiv 4 - 2\epsilon$ ($\epsilon \to 0$) and B_0, B_1, B_{11} and B_{00} are the Passarino-Veltman functions [280] in the *LoopTools* [266] notation.

The SM contribution can be cast as:

$$
T_{\text{SM}} = -\frac{1}{8\pi s_W^2 m_W^2} \left\{ 3Q(0,0,0) - 2\sum_{\alpha=1}^{3} Q(0,0,m_{\ell_\alpha}^2) + \sum_{\alpha=1}^{3} m_{\ell_\alpha}^2 B_0(0, m_{\ell_\alpha}^2, m_{\ell_\alpha}^2) \right\} ,
\tag{B.6}
$$

where it has been used that the active neutrino masses are zero and the leptonic mixing matrix U is unitary in the SM.

The equation for the S parameter is:

$$S_{\text{tot}} = S_{\text{ISS}} + S_{\text{SM}} = -\frac{1}{2\pi m_Z^2} \left\{ \sum_{i,j=1}^{9} C_{n_i n_j} C_{n_j n_i} \Delta Q(m_Z^2, m_{n_i}^2, m_{n_j}^2) \right.$$
$$+ \sum_{i,j=1}^{9} (C_{n_i n_j})^2 m_{n_i} m_{n_j} \left(B_0(0, m_{n_i}^2, m_{n_j}^2) - B_0(m_Z^2, m_{n_i}^2, m_{n_j}^2) \right)$$
$$\left. + \sum_{\alpha=1}^{3} m_{\ell_\alpha}^2 \left(B_0(0, m_{\ell_\alpha}^2, m_{\ell_\alpha}^2) - 2B_0(m_Z^2, m_{\ell_\alpha}^2, m_{\ell_\alpha}^2) \right) + Q(m_Z^2, m_{\ell_\alpha}^2, m_{\ell_\alpha}^2) \right\},$$

(B.7)

where $\Delta Q(q^2, m_1^2, m_2^2) \equiv Q(0, m_1^2, m_2^2) - Q(q^2, m_1^2, m_2^2)$ and

$$S_{\text{SM}} = -\frac{1}{2\pi m_Z^2} \left\{ 3\Delta Q(m_Z^2, 0, 0) \right.$$
$$\left. + \sum_{\alpha=1}^{3} m_{\ell_\alpha}^2 \left(B_0(0, m_{\ell_\alpha}^2, m_{\ell_\alpha}^2) - 2B_0(m_Z^2, m_{\ell_\alpha}^2, m_{\ell_\alpha}^2) \right) + Q(m_Z^2, m_{\ell_\alpha}^2, m_{\ell_\alpha}^2) \right\}.$$

(B.8)

Finally, the U parameter is given by:

$$U_{\text{tot}} = U_{\text{ISS}} + U_{\text{SM}} = \frac{1}{2\pi m_Z^2} \left\{ \sum_{i,j=1}^{9} C_{n_i n_j} C_{n_j n_i} \Delta Q(m_Z^2, m_{n_i}^2, m_{n_j}^2) \right.$$
$$+ \sum_{i,j=1}^{9} (C_{n_i n_j})^2 m_{n_i} m_{n_j} \left(B_0(0, m_{n_i}^2, m_{n_j}^2) - B_0(m_Z^2, m_{n_i}^2, m_{n_j}^2) \right)$$
$$- \sum_{i=1}^{9} \sum_{\alpha=1}^{3} 2 \frac{m_Z^2}{m_W^2} |B_{\ell_\alpha n_i}|^2 \Delta Q(m_W^2, m_{n_i}^2, m_{\ell_\alpha}^2)$$
$$\left. + \sum_{\alpha=1}^{3} m_{\ell_\alpha}^2 \left(B_0(0, m_{\ell_\alpha}^2, m_{\ell_\alpha}^2) - 2B_0(m_Z^2, m_{\ell_\alpha}^2, m_{\ell_\alpha}^2) \right) - Q(m_Z^2, m_{\ell_\alpha}^2, m_{\ell_\alpha}^2) \right\},$$

(B.9)

and its SM contribution reads:

$$U_{\text{SM}} = \frac{1}{2\pi m_Z^2} \left\{ 3\Delta Q(m_Z^2, 0, 0) + \sum_{\alpha=1}^{3} \left(m_{\ell_\alpha}^2 \left(B_0(0, m_{\ell_\alpha}^2, m_{\ell_\alpha}^2) - 2B_0(m_Z^2, m_{\ell_\alpha}^2, m_{\ell_\alpha}^2) \right) \right. \right.$$
$$\left. \left. - Q(m_Z^2, m_{\ell_\alpha}^2, m_{\ell_\alpha}^2) - 2 \frac{m_Z^2}{m_W^2} \Delta Q(m_W^2, 0, m_{\ell_\alpha}^2) \right) \right\}.$$

(B.10)

Appendix C

Form factors for LFVHD in the ISS model

In this Appendix we collect the analytical results for the form factors contributing to the LFV Higgs decay $H \to \ell_k \bar{\ell}_m$, as defined in Eq. (3.4). They are computed in the Feynman-'t Hooft gauge and expressed in the physical basis. The numbers (1)-(10) correspond to the diagrams in Fig. 3.1. These formulas are taken from Ref. [82] and adapted for the case of the ISS model with three pairs of fermionic singlets. Notice that we have corrected the global signs of $F_L^{(1)}$, $F_{L,R}^{(4)}$ and $F_{L,R}^{(5)}$, which were typos in the original expressions given in [82].

In all these formulas, summation over neutrino indices is understood, which run as $i, j = 1, ..., 9$. The loop functions are the Passarino-Veltman functions [280] in the *LoopTools* [266] notation, and they are defined in Eqs. (E.5) and (E.6).

$$
\begin{aligned}
F_L^{(1)} &= \frac{g^2}{4m_W^3} \frac{1}{16\pi^2} B_{\ell_k n_i} B_{\ell_m n_j}^* \Bigg\{ m_{\ell_k} m_{n_j} \Big[(m_{n_i} + m_{n_j}) \text{Re}\left(C_{n_i n_j}\right) + i(m_{n_j} - m_{n_i}) \text{Im}\left(C_{n_i n_j}\right) \Big] \tilde{C}_0 \\
&\quad + (C_{12} - C_{11}) \Big[(m_{n_i} + m_{n_j}) \text{Re}\left(C_{n_i n_j}\right) \left(-m_{\ell_k}^3 m_{n_j} - m_{n_i} m_{\ell_k} m_{\ell_m}^2 + m_{n_i} m_{n_j}^2 m_{\ell_k} + m_{n_i}^2 m_{n_j} m_{\ell_k} \right) \\
&\quad + i(m_{n_j} - m_{n_i}) \text{Im}\left(C_{n_i n_j}\right) \left(-m_{\ell_k}^3 m_{n_j} + m_{n_i} m_{\ell_k} m_{\ell_m}^2 - m_{n_i} m_{n_j}^2 m_{\ell_k} + m_{n_i}^2 m_{n_j} m_{\ell_k} \right) \Big] \Bigg\}, \\
F_R^{(1)} &= \frac{g^2}{4m_W^3} \frac{1}{16\pi^2} B_{\ell_k n_i} B_{\ell_m n_j}^* \Bigg\{ m_{n_i} m_{\ell_m} \Big[(m_{n_i} + m_{n_j}) \text{Re}\left(C_{n_i n_j}\right) - i(m_{n_j} - m_{n_i}) \text{Im}\left(C_{n_i n_j}\right) \Big] \tilde{C}_0 \\
&\quad + C_{12} \Big[(m_{n_i} + m_{n_j}) \text{Re}\left(C_{n_i n_j}\right) \left(m_{\ell_m}^3 m_{n_i} - m_{n_i} m_{n_j}^2 m_{\ell_m} - m_{n_i}^2 m_{n_j} m_{\ell_m} + m_{n_j} m_{\ell_k}^2 m_{\ell_m} \right) \\
&\quad + i(m_{n_j} - m_{n_i}) \text{Im}\left(C_{n_i n_j}\right) \left(-m_{\ell_m}^3 m_{n_i} + m_{n_i} m_{n_j}^2 m_{\ell_m} - m_{n_i}^2 m_{n_j} m_{\ell_m} + m_{n_j} m_{\ell_k}^2 m_{\ell_m} \right) \Big] \Bigg\},
\end{aligned}
$$

where $C_{11,12} = C_{11,12}(m_{\ell_k}^2, m_H^2, m_W^2, m_{n_i}^2, m_{n_j}^2)$ and $\tilde{C}_0 = \tilde{C}_0(m_{\ell_k}^2, m_H^2, m_W^2, m_{n_i}^2, m_{n_j}^2)$.

$$F_L^{(2)} = \frac{g^2}{2m_W}\frac{1}{16\pi^2}B_{\ell_k n_i}B_{\ell_m n_j}^* m_{\ell_k}\Big\{-m_{n_j}\Big[(m_{n_i}+m_{n_j})\mathrm{Re}\left(C_{n_i n_j}\right)+i(m_{n_j}-m_{n_i})\mathrm{Im}\left(C_{n_i n_j}\right)\Big]C_0$$

$$+(C_{12}-C_{11})\Big[(m_{n_i}+m_{n_j})^2\,\mathrm{Re}\left(C_{n_i n_j}\right)+i(m_{n_j}-m_{n_i})^2\,\mathrm{Im}\left(C_{n_i n_j}\right)\Big]\Big\},$$

$$F_R^{(2)} = -\frac{g^2}{2m_W}\frac{1}{16\pi^2}B_{\ell_k n_i}B_{\ell_m n_j}^* m_{\ell_m}\Big\{m_{n_i}\Big[(m_{n_i}+m_{n_j})\mathrm{Re}\left(C_{n_i n_j}\right)-i(m_{n_j}-m_{n_i})\mathrm{Im}\left(C_{n_i n_j}\right)\Big]C_0$$

$$+C_{12}\Big[(m_{n_i}+m_{n_j})^2\,\mathrm{Re}\left(C_{n_i n_j}\right)+i(m_{n_j}-m_{n_i})^2\,\mathrm{Im}\left(C_{n_i n_j}\right)\Big]\Big\},$$

where $C_{0,11,12}=C_{0,11,12}(m_{\ell_k}^2,m_H^2,m_W^2,m_{n_i}^2,m_{n_j}^2)$.

$$F_L^{(3)} = \frac{g^2}{16\pi^2}B_{\ell_k n_i}B_{\ell_m n_i}^* m_{\ell_k}m_W\left(C_{11}-C_{12}\right),$$

$$F_R^{(3)} = \frac{g^2}{16\pi^2}B_{\ell_k n_i}B_{\ell_m n_i}^* m_{\ell_m}m_W C_{12},$$

where $C_{11,12}=C_{11,12}(m_{\ell_k}^2,m_H^2,m_{n_i}^2,m_W^2,m_W^2)$.

$$F_L^{(4)} = \frac{g^2}{4m_W}\frac{1}{16\pi^2}B_{\ell_k n_i}B_{\ell_m n_i}^* m_{\ell_k}\Big\{m_{\ell_m}^2(C_{12}-2C_{11})+m_{n_i}^2(C_{11}-C_{12})-m_{n_i}^2 C_0\Big\},$$

$$F_R^{(4)} = \frac{g^2}{4m_W}\frac{1}{16\pi^2}B_{\ell_k n_i}B_{\ell_m n_i}^* m_{\ell_m}\Big\{\tilde{C}_0+2m_{\ell_m}^2 C_{11}+m_{n_i}^2 C_{12}+(m_{\ell_k}^2-2m_H^2)(C_{11}-C_{12})+2m_{n_i}^2 C_0\Big\},$$

where $C_{0,11,12}=C_{0,11,12}(m_{\ell_k}^2,m_H^2,m_{n_i}^2,m_W^2,m_W^2)$ and $\tilde{C}_0=\tilde{C}_0(m_{\ell_k}^2,m_H^2,m_{n_i}^2,m_W^2,m_W^2)$.

$$F_L^{(5)} = \frac{g^2}{4m_W}\frac{1}{16\pi^2}B_{\ell_k n_i}B_{\ell_m n_i}^* m_{\ell_k}\Big\{\tilde{C}_0+2m_{n_i}^2 C_0+(m_{n_i}^2+2m_{\ell_k}^2)C_{11}+(m_{\ell_m}^2-m_{n_i}^2-2m_H^2)C_{12}\Big\},$$

$$F_R^{(5)} = -\frac{g^2}{4m_W}\frac{1}{16\pi^2}B_{\ell_k n_i}B_{\ell_m n_i}^* m_{\ell_m}\Big\{m_{n_i}^2 C_0+m_{\ell_k}^2 C_{11}+(m_{\ell_k}^2-m_{n_i}^2)C_{12}\Big\},$$

where $C_{0,11,12}=C_{0,11,12}(m_{\ell_k}^2,m_H^2,m_{n_i}^2,m_W^2,m_W^2)$ and $\tilde{C}_0=\tilde{C}_0(m_{\ell_k}^2,m_H^2,m_{n_i}^2,m_W^2,m_W^2)$.

$$F_L^{(6)} = \frac{g^2}{4m_W^3}\frac{1}{16\pi^2}B_{\ell_k n_i}B_{\ell_m n_i}^* m_{\ell_k}m_H^2\Big\{m_{n_i}^2(C_0+C_{11})+(m_{\ell_m}^2-m_{n_i}^2)C_{12}\Big\},$$

$$F_R^{(6)} = \frac{g^2}{4m_W^3}\frac{1}{16\pi^2}B_{\ell_k n_i}B_{\ell_m n_i}^* m_{\ell_m}m_H^2\Big\{m_{n_i}^2(C_0+C_{12})+m_{\ell_k}^2(C_{11}-C_{12})\Big\},$$

where $C_{0,11,12}=C_{0,11,12}(m_{\ell_k}^2,m_H^2,m_{n_i}^2,m_W^2,m_W^2)$.

$$F_L^{(7)} = \frac{g^2}{2m_W}\frac{1}{16\pi^2}B_{\ell_k n_i}B_{\ell_m n_i}^* \frac{m_{\ell_m}^2 m_{\ell_k}}{m_{\ell_k}^2-m_{\ell_m}^2}B_1,$$

$$F_R^{(7)} = \frac{g^2}{2m_W} \frac{1}{16\pi^2} B_{\ell_k n_i} B_{\ell_m n_i}^* \frac{m_{\ell_k}^2 m_{\ell_m}}{m_{\ell_k}^2 - m_{\ell_m}^2} B_1 \,,$$

$$F_L^{(8)} = \frac{g^2}{4m_W^3} \frac{1}{16\pi^2} B_{\ell_k n_i} B_{\ell_m n_i}^* \frac{m_{\ell_k}}{m_{\ell_k}^2 - m_{\ell_m}^2} \left\{ m_{\ell_m}^2 (m_{\ell_k}^2 + m_{n_i}^2) B_1 + 2m_{n_i}^2 m_{\ell_m}^2 B_0 \right\} ,$$

$$F_R^{(8)} = \frac{g^2}{4m_W^3} \frac{1}{16\pi^2} B_{\ell_k n_i} B_{\ell_m n_i}^* \frac{m_{\ell_m}}{m_{\ell_k}^2 - m_{\ell_m}^2} \left\{ m_{\ell_k}^2 (m_{\ell_m}^2 + m_{n_i}^2) B_1 + m_{n_i}^2 (m_{\ell_k}^2 + m_{\ell_m}^2) B_0 \right\} ,$$

where $B_{0,1} = B_{0,1}(m_{\ell_k}^2, m_{n_i}^2, m_W^2)$.

$$F_L^{(9)} = \frac{g^2}{2m_W} \frac{1}{16\pi^2} B_{\ell_k n_i} B_{\ell_m n_i}^* \frac{m_{\ell_m}^2 m_{\ell_k}}{m_{\ell_m}^2 - m_{\ell_k}^2} B_1 \,,$$

$$F_R^{(9)} = \frac{g^2}{2m_W} \frac{1}{16\pi^2} B_{\ell_k n_i} B_{\ell_m n_i}^* \frac{m_{\ell_k}^2 m_{\ell_m}}{m_{\ell_m}^2 - m_{\ell_k}^2} B_1 \,,$$

$$F_L^{(10)} = \frac{g^2}{4m_W^3} \frac{1}{16\pi^2} B_{\ell_k n_i} B_{\ell_m n_i}^* \frac{m_{\ell_k}}{m_{\ell_m}^2 - m_{\ell_k}^2} \left\{ m_{\ell_m}^2 (m_{\ell_k}^2 + m_{n_i}^2) B_1 + m_{n_i}^2 (m_{\ell_k}^2 + m_{\ell_m}^2) B_0 \right\} ,$$

$$F_R^{(10)} = \frac{g^2}{4m_W^3} \frac{1}{16\pi^2} B_{\ell_k n_i} B_{\ell_m n_i}^* \frac{m_{\ell_m}}{m_{\ell_m}^2 - m_{\ell_k}^2} \left\{ m_{\ell_k}^2 (m_{\ell_m}^2 + m_{n_i}^2) B_1 + 2m_{n_i}^2 m_{\ell_k}^2 B_0 \right\} ,$$

where $B_{0,1} = B_{0,1}(m_{\ell_m}^2, m_{n_i}^2, m_W^2)$.

Appendix D

Form factors for the LFVHD in the SUSY-ISS model

In this Appendix we present the form factors that correspond to the diagrams of Fig. 3.12, together with the relevant couplings needed for performing the computation. The original calculation in the SUSY type I seesaw was done in Ref. [82] in the mass basis and in the Feynman-'t Hooft gauge, which we have adapted them to the SUSY-ISS model. In order to do that, we have derived the new relevant couplings with respect to the SUSY type-I seesaw model, which we give in the following.

When compared with the SUSY type I seesaw, only the coupling factors $A_{R\alpha j}^{(\ell)}$ and $g_{H_x \tilde\nu_\alpha \tilde\nu_\beta}$ are modified. In the SUSY inverse seesaw, they are defined in the mass basis with diagonal charged leptons by

$$
A_{R\alpha j}^{(e,\mu,\tau)} = \tilde{U}_{(1,2,3)\alpha} V_{j1} - \frac{m_{D(1,2,3)k}}{\sqrt{2}m_W \sin\beta} \tilde{U}_{k+9,\alpha} V_{j2} \,,
$$

$$
g_{H_x \tilde\nu_\alpha \tilde\nu_\beta} = -ig \Bigg[(g_{LL,\nu}^{(x)})_{ik} \tilde{U}_{i\alpha}^* \tilde{U}_{k\beta} + (g_{RR,\nu}^{(x)})_{ik} \tilde{U}_{i+9,\alpha}^* \tilde{U}_{k+9,\beta} + (g_{LR,\nu}^{(x)})_{ik} \tilde{U}_{i,\alpha}^* \tilde{U}_{k+9,\beta}
$$

$$
+ (g_{LR,\nu}^{(x)})_{ik}^* \tilde{U}_{k+9,\alpha}^* \tilde{U}_{i,\beta} + (g_{LX,\nu}^{(x)})_{ik} \tilde{U}_{i,\alpha}^* \tilde{U}_{k+12,\beta} + (g_{LX,\nu}^{(x)})_{ik}^* \tilde{U}_{k+12,\alpha}^* \tilde{U}_{i,\beta} \Bigg] \,,
$$

$$
(g_{LL,\nu}^{(x)})_{ik} = -\frac{m_Z}{2\cos\theta_W} \sigma_3^{(x)} \delta_{ik} + \frac{(m_D m_D^\dagger)_{ik}}{m_W \sin\beta} \sigma_6^{(x)} \,,
$$

$$
(g_{RR,\nu}^{(x)})_{ik} = \frac{(m_D^\dagger m_D)_{ik}}{m_W \sin\beta} \sigma_6^{(x)} \,,
$$

$$
(g_{LR,\nu}^{(x)})_{ik} = \frac{(m_D A_\nu^\dagger)_{ik}}{2m_W \sin\beta} \sigma_2^{(x)} + \frac{\mu}{2m_W \sin\beta} (m_D)_{ik} \sigma_7^{(x)} \,,
$$

$$
(g_{LX,\nu}^{(x)})_{ik} = \frac{(m_D M_R^*)_{ik}}{2m_W \sin\beta} \sigma_2^{(x)} \,,
\tag{D.1}
$$

which are summed over the internal indices, with $i, k = 1, \ldots, 3$. We reproduced below the unmodified coupling factors from Ref. [82] (correcting a typo in $W_{Rij}^{(x)}$) for completeness in the mass basis with diagonal charged leptons

$$A_{L\alpha j}^{(e,\mu,\tau)} = -\frac{m_{e,\mu,\tau}}{\sqrt{2}m_W cos\beta} U_{j2}^* \tilde{U}_{(1,2,3)\alpha} \,,$$

$$B_{L\alpha a}^{(e,\mu,\tau)} = \sqrt{2} \left[\frac{m_{e,\mu,\tau}}{2m_W cos\beta} N_{a3}^* R_{(1,3,5)\alpha}^{(\ell)} + \left[\sin\theta_W N_{a1}'^* - \frac{\sin^2\theta_W}{cos\theta_W} N_{a2}'^* \right] R_{(2,4,6)\alpha}^{(\ell)} \right] \,,$$

$$B_{R\alpha a}^{(e,\mu,\tau)} = \sqrt{2} \left[\left(-\sin\theta_W N_{a1}' - \frac{1}{\cos\theta_W}(\frac{1}{2} - \sin^2\theta_W)N_{a2}' \right) R_{(1,3,5)\alpha}^{(\ell)} + \frac{m_{e,\mu,\tau}}{2m_W \cos\beta} N_{a3} R_{(2,4,6)\alpha}^{(\ell)} \right] \,,$$

$$W_{Lij}^{(x)} = \frac{1}{\sqrt{2}} \left(-\sigma_1^{(x)} U_{j2}^* V_{i1}^* + \sigma_2^{(x)} U_{j1}^* V_{i2}^* \right) \,,$$

$$W_{Rij}^{(x)} = \frac{1}{\sqrt{2}} \left(-\sigma_1^{(x)*} U_{i2} V_{j1} + \sigma_2^{(x)*} U_{i1} V_{j2} \right) \,,$$

$$D_{Lab}^{(x)} = \frac{1}{2\cos\theta_W} \left[(\sin\theta_W N_{b1}^* - \cos\theta_W N_{b2}^*)(\sigma_1^{(x)} N_{a3}^* + \sigma_2^{(x)} N_{a4}^*) \right.$$
$$\left. + (\sin\theta_W N_{a1}^* - \cos\theta_W N_{a2}^*)(\sigma_1^{(x)} N_{b3}^* + \sigma_2^{(x)} N_{b4}^*) \right] \,,$$

$$D_{Rab}^{(x)} = D_{Lab}^{(x)*} \,,$$

$$S_{L,\ell}^{(x)} = -\frac{m_\ell}{2m_W \cos\beta} \sigma_1^{(x)*} \,,$$

$$S_{R,\ell}^{(x)} = S_{L,\ell}^{(x)*} \,,$$

$$g_{H_x \tilde{\ell}_\alpha \tilde{\ell}_\beta} = -ig \left[g_{LL,e}^{(x)} R_{1\alpha}^{*(\ell)} R_{1\beta}^{(\ell)} + g_{RR,e}^{(x)} R_{2\alpha}^{*(\ell)} R_{2\beta}^{(\ell)} + g_{LR,e}^{(x)} R_{1\alpha}^{*(\ell)} R_{2\beta}^{(\ell)} + g_{RL,e}^{(x)} R_{2\alpha}^{*(\ell)} R_{1\beta}^{(\ell)} \right.$$
$$+ g_{LL,\mu}^{(x)} R_{3\alpha}^{*(\ell)} R_{3\beta}^{(\ell)} + g_{RR,\mu}^{(x)} R_{4\alpha}^{*(\ell)} R_{4\beta}^{(\ell)} + g_{LR,\mu}^{(x)} R_{3\alpha}^{*(\ell)} R_{4\beta}^{(\ell)} + g_{RL,\mu}^{(x)} R_{4\alpha}^{*(\ell)} R_{3\beta}^{(\ell)}$$
$$\left. + g_{LL,\tau}^{(x)} R_{5\alpha}^{*(\ell)} R_{5\beta}^{(\ell)} + g_{RR,\tau}^{(x)} R_{6\alpha}^{*(\ell)} R_{6\beta}^{(\ell)} + g_{LR,\tau}^{(x)} R_{5\alpha}^{*(\ell)} R_{6\beta}^{(\ell)} + g_{RL,\tau}^{(x)} R_{6\alpha}^{*(\ell)} R_{5\beta}^{(\ell)} \right] \,,$$

$$g_{LL,\ell}^{(x)} = \frac{m_Z}{\cos\theta_W} \sigma_3^{(x)} \left(\frac{1}{2} - \sin^2\theta_W \right) + \frac{m_\ell^2}{m_W \cos\beta} \sigma_4^{(x)} \,,$$

$$g_{RR,\ell}^{(x)} = \frac{m_Z}{\cos\theta_W} \sigma_3^{(x)} \left(\sin^2\theta_W \right) + \frac{m_\ell^2}{m_W \cos\beta} \sigma_4^{(x)} \,,$$

$$g_{LR,\ell}^{(x)} = \left(-\sigma_1^{(x)} A_\ell - \sigma_5^{(x)} \mu \right) \frac{m_\ell}{2m_W \cos\beta} \,,$$

$$g_{RL,\ell}^{(x)} = g_{LR,\ell}^{(x)*} \,, \tag{D.2}$$

with

$$\sigma_1^{(x)} = \begin{pmatrix} \sin\alpha \\ -\cos\alpha \\ i\sin\beta \end{pmatrix}, \quad \sigma_2^{(x)} = \begin{pmatrix} \cos\alpha \\ \sin\alpha \\ -i\cos\beta \end{pmatrix}, \quad \sigma_3^{(x)} = \begin{pmatrix} \sin(\alpha+\beta) \\ -\cos(\alpha+\beta) \\ 0 \end{pmatrix}, \quad \sigma_4^{(x)} = \begin{pmatrix} -\sin\alpha \\ \cos\alpha \\ 0 \end{pmatrix},$$

$$\sigma_5^{(x)} = \begin{pmatrix} \cos\alpha \\ \sin\alpha \\ i\cos\beta \end{pmatrix}, \quad \sigma_6^{(x)} = \begin{pmatrix} \cos\alpha \\ \sin\alpha \\ 0 \end{pmatrix}, \quad \sigma_7^{(x)} = \begin{pmatrix} \sin\alpha \\ -\cos\alpha \\ -i\sin\beta \end{pmatrix}, \quad \text{for } H_x = \begin{pmatrix} h^0 \\ H^0 \\ A^0 \end{pmatrix}. \tag{D.3}$$

Besides using these new couplings, the only changes required to adapt the original form factors to the SUSY-ISS model are the sum over sneutrinos that has to be extended to the 18 mass eigenstates. In the following formulas, summation over all indices corresponding to internal propagators is understood, meaning $\alpha\,,\beta = 1\,,...\,,18$ for the sneutrinos, $i\,,j = 1\,,2$ for the charginos, $\alpha\,,\beta = 1\,,...\,,6$ for the charged sleptons and $a\,,b = 1\,,...\,,4$ for the neutralinos.

$$\begin{aligned}
F_{L,x}^{(1)} =& -\frac{g^2}{16\pi^2}\bigg[\Big(B_0 + m_{\tilde\nu_\alpha}^2 C_0 + m_{\ell_m}^2 C_{12} + m_{\ell_k}^2 (C_{11} - C_{12})\Big) \kappa_{L1}^{x,\tilde\chi^-} \\
&+ m_{\ell_k} m_{\ell_m} (C_{11} + C_0) \kappa_{L2}^{x,\tilde\chi^-} + m_{\ell_k} m_{\tilde\chi_j^-} (C_{11} - C_{12} + C_0) \kappa_{L3}^{x,\tilde\chi^-} + m_{\ell_m} m_{\tilde\chi_j^-} C_{12} \kappa_{L4}^{x,\tilde\chi^-} \\
&+ m_{\ell_k} m_{\tilde\chi_i^-} (C_{11} - C_{12}) \kappa_{L5}^{x,\tilde\chi^-} + m_{\ell_m} m_{\tilde\chi_i^-} (C_{12} + C_0) \kappa_{L6}^{x,\tilde\chi^-} + m_{\tilde\chi_i^-} m_{\tilde\chi_j^-} C_0 \kappa_{L7}^{x,\tilde\chi^-} \bigg],
\end{aligned}$$

$$F_{L,x}^{(2)} = -\frac{igg_{H_x\tilde\nu_\alpha\tilde\nu_\beta}}{16\pi^2}\Big[-m_{\ell_k}(C_{11} - C_{12})\,\iota_{L1}^{x,\tilde\chi^-} - m_{\ell_m} C_{12}\,\iota_{L2}^{x,\tilde\chi^-} + m_{\tilde\chi_i^-} C_0\,\iota_{L3}^{x,\tilde\chi^-} \Big],$$

$$F_{L,x}^{(3)} = \frac{-S_{L,\ell_m}^{(x)}}{m_{\ell_k}^2 - m_{\ell_m}^2}\Big[m_{\ell_k}^2 \Sigma_R^{\tilde\chi^-}(m_{\ell_k}^2) + m_{\ell_k}^2 \Sigma_{Rs}^{\tilde\chi^-}(m_{\ell_k}^2) + m_{\ell_m}\Big(m_{\ell_k}\Sigma_L^{\tilde\chi^-}(m_{\ell_k}^2) + m_{\ell_k}\Sigma_{Ls}^{\tilde\chi^-}(m_{\ell_k}^2)\Big)\Big],$$

$$F_{L,x}^{(4)} = \frac{-S_{L,\ell_k}^{(x)}}{m_{\ell_m}^2 - m_{\ell_k}^2}\Big[m_{\ell_m}^2 \Sigma_L^{\tilde\chi^-}(m_{\ell_m}^2) + m_{\ell_m} m_{\ell_k} \Sigma_{Rs}^{\tilde\chi^-}(m_{\ell_m}^2) + m_{\ell_k}\Big(m_{\ell_m}\Sigma_R^{\tilde\chi^-}(m_{\ell_m}^2) + m_{\ell_k}\Sigma_{Ls}^{\tilde\chi^-}(m_{\ell_m}^2)\Big)\Big],$$

$$\tag{D.4}$$

$$\begin{aligned}
F_{L,x}^{(5)} =& -\frac{g^2}{16\pi^2}\bigg[\Big(B_0 + m_{\tilde\ell_\alpha}^2 C_0 + m_{\ell_m}^2 C_{12} + m_{\ell_k}^2 (C_{11} - C_{12})\Big) \kappa_{L1}^{x,\tilde\chi^0} \\
&+ m_{\ell_k} m_{\ell_m} (C_{11} + C_0) \kappa_{L2}^{x,\tilde\chi^0} + m_{\ell_k} m_{\tilde\chi_b^0} (C_{11} - C_{12} + C_0) \kappa_{L3}^{x,\tilde\chi^0} + m_{\ell_m} m_{\tilde\chi_b^0} C_{12} \kappa_{L4}^{x,\tilde\chi^0} \\
&+ m_{\ell_k} m_{\tilde\chi_a^0} (C_{11} - C_{12}) \kappa_{L5}^{x,\tilde\chi^0} + m_{\ell_m} m_{\tilde\chi_a^0} (C_{12} + C_0) \kappa_{L6}^{x,\tilde\chi^0} + m_{\tilde\chi_a^0} m_{\tilde\chi_b^0} C_0 \kappa_{L7}^{x,\tilde\chi^0} \bigg],
\end{aligned}$$

$$F_{L,x}^{(6)} = -\frac{igg_{H_x\tilde\ell_\alpha\tilde\ell_\beta}}{16\pi^2}\Big[-m_{\ell_k}(C_{11} - C_{12})\,\iota_{L1}^{x,\tilde\chi^0} - m_{\ell_m} C_{12}\,\iota_{L2}^{x,\tilde\chi^0} + m_{\tilde\chi_a^0} C_0\,\iota_{L3}^{x,\tilde\chi^0} \Big],$$

$$F_{L,x}^{(7)} = \frac{-S_{L,\ell_m}^{(x)}}{m_{\ell_k}^2 - m_{\ell_m}^2}\Big[m_{\ell_k}^2 \Sigma_R^{\tilde\chi^0}(m_{\ell_k}^2) + m_{\ell_k}^2 \Sigma_{Rs}^{\tilde\chi^0}(m_{\ell_k}^2) + m_{\ell_m}\Big(m_{\ell_k}\Sigma_L^{\tilde\chi^0}(m_{\ell_k}^2) + m_{\ell_k}\Sigma_{Ls}^{\tilde\chi^0}(m_{\ell_k}^2)\Big)\Big],$$

$$F_{L,x}^{(8)} = \frac{-S_{L,\ell_k}^{(x)}}{m_{\ell_m}^2 - m_{\ell_k}^2}\Big[m_{\ell_m}^2 \Sigma_L^{\tilde\chi^0}(m_{\ell_m}^2) + m_{\ell_m} m_{\ell_k} \Sigma_{Rs}^{\tilde\chi^0}(m_{\ell_m}^2) + m_{\ell_k}\Big(m_{\ell_m}\Sigma_R^{\tilde\chi^0}(m_{\ell_m}^2) + m_{\ell_k}\Sigma_{Ls}^{\tilde\chi^0}(m_{\ell_m}^2)\Big)\Big],$$

$$\tag{D.5}$$

where,

$$
B_0 = \begin{cases} B_0(m_{H_x}^2, m_{\tilde{\chi}_i^-}^2, m_{\tilde{\chi}_j^-}^2) \text{ in } F_{L,x}^{(1)}, \\ B_0(m_{H_x}^2, m_{\tilde{\chi}_a^0}^2, m_{\tilde{\chi}_b^0}^2) \text{ in } F_{L,x}^{(5)}, \end{cases}
$$

and

$$
C_{0,11,12} = \begin{cases} C_{0,11,12}(m_{\ell_k}^2, m_{H_x}^2, m_{\tilde{\nu}_\alpha}^2, m_{\tilde{\chi}_i^-}^2, m_{\tilde{\chi}_j^-}^2) \text{ in } F_{L,x}^{(1)}, \\ C_{0,11,12}(m_{\ell_k}^2, m_{H_x}^2, m_{\tilde{\chi}_i^-}^2, m_{\tilde{\nu}_\alpha}^2, m_{\tilde{\nu}_\beta}^2) \text{ in } F_{L,x}^{(2)}, \\ C_{0,11,12}(m_{\ell_k}^2, m_{H_x}^2, m_{\tilde{l}_\alpha}^2, m_{\tilde{\chi}_a^0}^2, m_{\tilde{\chi}_b^0}^2) \text{ in } F_{L,x}^{(5)}, \\ C_{0,11,12}(m_{\ell_k}^2, m_{H_x}^2, m_{\tilde{\chi}_a^0}^2, m_{\tilde{l}_\alpha}^2, m_{\tilde{l}_\beta}^2) \text{ in } F_{L,x}^{(6)}. \end{cases}
$$

The couplings and self-energies from the neutralino contributions to the form factors were defined as

$$
\kappa_{L1}^{x,\tilde{\chi}^0} = B_{L\alpha a}^{(\ell_k)} D_{Rab}^{(x)} B_{R\alpha b}^{(\ell_m)*}, \qquad \iota_{L1}^{x,\tilde{\chi}^0} = B_{R\alpha a}^{(\ell_k)} B_{R\beta a}^{(\ell_m)*},
$$

$$
\kappa_{L2}^{x,\tilde{\chi}^0} = B_{R\alpha a}^{(\ell_k)} D_{Lab}^{(x)} B_{L\alpha b}^{(\ell_m)*}, \qquad \iota_{L2}^{x,\tilde{\chi}^0} = B_{L\alpha a}^{(\ell_k)} B_{L\beta a}^{(\ell_m)*},
$$

$$
\kappa_{L3}^{x,\tilde{\chi}^0} = B_{R\alpha a}^{(\ell_k)} D_{Lab}^{(x)} B_{R\alpha b}^{(\ell_m)*}, \qquad \iota_{L3}^{x,\tilde{\chi}^0} = B_{L\alpha a}^{(\ell_k)} B_{R\beta a}^{(\ell_m)*},
$$

$$
\kappa_{L4}^{x,\tilde{\chi}^0} = B_{L\alpha a}^{(\ell_k)} D_{Rab}^{(x)} B_{L\alpha b}^{(\ell_m)*},
$$

$$
\kappa_{L5}^{x,\tilde{\chi}^0} = B_{R\alpha a}^{(\ell_k)} D_{Rab}^{(x)} B_{R\alpha b}^{(\ell_m)*},
$$

$$
\kappa_{L6}^{x,\tilde{\chi}^0} = B_{L\alpha a}^{(\ell_k)} D_{Lab}^{(x)} B_{L\alpha b}^{(\ell_m)*},
$$

$$
\kappa_{L7}^{x,\tilde{\chi}^0} = B_{L\alpha a}^{(\ell_k)} D_{Lab}^{(x)} B_{R\alpha b}^{(\ell_m)*},
$$

$$
\begin{aligned}
\Sigma_L^{\tilde{\chi}^0}(k^2) &= -\frac{g^2}{16\pi^2} B_1(k^2, m_{\tilde{\chi}_a^0}^2, m_{\tilde{\ell}_\alpha}^2) B_{R\alpha a}^{(\ell_k)} B_{R\alpha a}^{(\ell_m)*}, \\
m_{\ell_k} \Sigma_{Ls}^{\tilde{\chi}^0}(k^2) &= \frac{g^2 m_{\tilde{\chi}_a^0}}{16\pi^2} B_0(k^2, m_{\tilde{\chi}_a^0}^2, m_{\tilde{\ell}_\alpha}^2) B_{L\alpha a}^{(\ell_k)} B_{R\alpha a}^{(\ell_m)*}.
\end{aligned} \tag{D.6}
$$

The couplings and self energies from the chargino contributions to the form factors, $\kappa^{x,\tilde{\chi}^-}$, $\iota^{x,\tilde{\chi}^-}$, and $\Sigma^{\tilde{\chi}^-}$ can be obtained from the previous expressions $\kappa^{x,\tilde{\chi}^0}$, $\iota^{x,\tilde{\chi}^0}$ and $\Sigma^{\tilde{\chi}^0}$ by using the following replacement rules $m_{\tilde{\chi}_a^0} \to m_{\tilde{\chi}_i^-}$, $m_{\tilde{\ell}_\alpha} \to m_{\tilde{\nu}_\alpha}$, $B^{(l)} \to A^{(l)}$, $D^{(x)} \to W^{(x)}$, $a \to i$, and $b \to j$.

The form factors $F_{R,x}^{(i)}, i = 1, ..., 8$ can be obtained from $F_{L,x}^{(i)}, i = 1, ..., 8$ through the exchange $L \leftrightarrow R$ in all places.

Appendix E

Formulas for the MIA computation

In this Appendix we give the technical details of our MIA computation of the LFV Higgs decay rates in Section 3.3 More concretely, we explain the derivation of the *fat propagators*, used in our MIA computation in the Feynman-'t Hooft and Unitary gauges. We give our results for the form factors, up to (Y_ν^4) order in the MIA expansion, showing explicitly that we obtain the same in both gauges. Furthermore, we explore the large M_R limit and derive useful approximate expressions for the loop integrals needed for computing the $H\ell_k\ell_m$ effective vertex of Eq. (3.34).

E.1 Modified neutrino propagators

In this section we derive the right-handed neutrino *fat propagators* used for the computations in this work. The idea is to resum all possible large flavor diagonal M_R mass insertions, which we denote with a dot in order to distinguish them from the flavor off-diagonal ones, in a way such that the large mass appears effectively in the denominator of the propagators of the new states.

In order to make a MIA computation in the electroweak basis $(\nu_L^c,\ \nu_R,\ X)$, we need to take into account all the propagators and mass insertions given by the neutrino mass matrix. In the ISS model we are considering, this mass matrix is given by Eq. (1.35), which we repeat here for completeness:

$$M_{\mathrm{ISS}} = \begin{pmatrix} 0 & m_D & 0 \\ m_D^T & 0 & M_R \\ 0 & M_R^T & \mu_X \end{pmatrix}.$$

(E.1)

From this mass matrix, we obtain the propagators and mass insertions summarized in Fig. E.1. It is important to notice the presence of the P_L and P_R projectors for the chi-
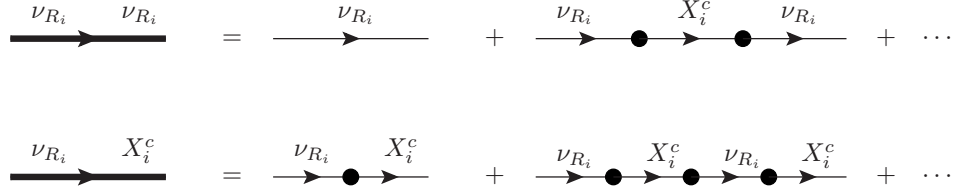
Figure E.1: Propagators and mass insertions in the electroweak basis. Crosses denote mass insertions that can change flavor, while big black dots are for flavor diagonal ones.

ral fields, which have been properly added according to:

$$
\begin{aligned}
\nu_L^c, \nu_R, X &\longrightarrow \textbf{RH fields}, \\
\nu_L, \nu_R^c, X^c &\longrightarrow \textbf{LH fields}.
\end{aligned}
\tag{E.2}
$$

As previously mentioned, there are three types of mass insertions and they are controlled by the matrices m_D, M_R and μ_X. The mass insertions M_R that relate ν_R and X fields are taken to be flavor diagonal in this work and are denoted by a big dot in Fig. E.1. On the other hand, crosses indicate flavor non-diagonal insertions coming from m_D (big cross) and μ_X (small cross), which connect the fields ν_L-ν_R and two X's respectively. Nevertheless, given that we work under the assumption that μ_X is a tiny scale, we neglect μ_X mass insertions for our LFVHD computations and, therefore, we consider m_D as the only relevant LFV insertion.

Since our motivation in this work is to make a MIA computation for LFV H decays by perturbatively inserting LFV mass insertions, we find convenient to take into account first the effects of all possible flavor diagonal M_R insertions. Moreover, this procedure allows us to consider M_R also as a heavy scale so we can define an effective vertex for the H-ℓ_i-ℓ_j interaction. This can be done by defining two types of modified propagators, one for same initial and final state consisting of all possible even number of M_R insertions (which we call *fat propagator*), and one for different initial and final states with an odd number of M_R insertions, as it is schematically shown in Fig. E.2. We can then define two modified propagators starting with ν_R by adding the corresponding series:

$$
\begin{aligned}
\text{Prop}_{\nu_{R_i} \to \nu_{R_i}} &= P_R \frac{i}{\slashed{p}} P_L + P_R \frac{i}{\slashed{p}} P_L \left(-i M_{R_i}^* P_L \right) P_L \frac{i}{\slashed{p}} P_R \left(-i M_{R_i} P_R \right) P_R \frac{i}{\slashed{p}} P_L + \cdots \\
&= P_R \frac{i}{\slashed{p}} \sum_{n \geq 0} \left(\frac{|M_{R_i}|^2}{p^2} \right)^n P_L = P_R \frac{i \slashed{p}}{p^2 - |M_{R_i}|^2} P_L,
\end{aligned}
\tag{E.3}
$$

156

$$\xrightarrow[\nu_{L_i}]{\quad\quad} \qquad P_L \frac{i}{\not p} P_R \qquad\qquad \xrightarrow[\nu_{R_i}]{\quad\quad} \qquad P_R \frac{i}{\not p} P_L \qquad\qquad \xrightarrow[X_i]{\quad\quad} \qquad P_R \frac{i}{\not p} P_L$$

$$\xrightarrow[\nu_{R_j}]{}\times\xrightarrow[\nu_{L_i}]{} \quad -i\, m_{D_{ij}} P_R \qquad \xrightarrow[\nu_{R_i}]{}\bullet\xrightarrow[X_i^c]{} \quad -i\, M_{R_{ii}} P_R \qquad \xrightarrow[X_j]{}\times\xrightarrow[X_i^c]{} \quad -i\, \mu_{X_{ij}} P_R$$
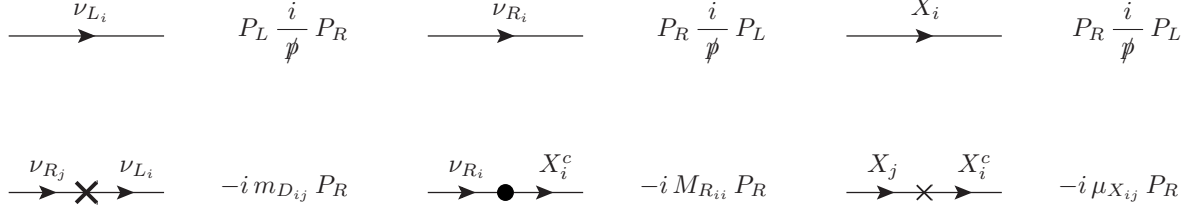
Figure E.2: Modified neutrino propagators after resuming an infinite number of M_R mass insertions, denoted here by big black dots. We use fat arrow lines with same (different) initial and final states to denote that all possible even (odd) number of M_R insertions have been considered. The fat lines with same initial and final ν_R states are referred to in this work as *fat propagators*.

$$
\begin{aligned}
\mathrm{Prop}_{\nu_{R_i}\to X_i^c} &= P_L \frac{i}{\not p} P_R \left(-iM_{R_i}P_R\right) P_R \frac{i}{\not p} P_L \\
&+ P_L \frac{i}{\not p} P_R \left(-iM_{R_i}P_R\right) P_R \frac{i}{\not p} P_L \left(-iM_{R_i}^*P_L\right) P_L \frac{i}{\not p} P_R \left(-iM_{R_i}P_R\right) P_R \frac{i}{\not p} P_L + \cdots \\
&= P_L \frac{iM_{R_i}}{p^2} \sum_{n\geq 0} \left(\frac{|M_{R_i}|^2}{p^2}\right)^n P_L = P_L \frac{iM_{R_i}}{p^2-|M_{R_i}|^2} P_L \, .
\end{aligned}
\tag{E.4}
$$

And we can similarly define other modified propagators considering also the ν_R^c and X states. In the present study of LFVHD, it happens that the X fields do not interact with any of the external legs involved in the LFV process we want to compute. Consequently, to take into account the effects from X in the LFVHD, it is enough to consider the *fat propagator* in Eq. (E.3) when computing the one-loop contributions to $H \to \ell_k \bar{\ell}_m$.

E.2 MIA Form Factors in the Feynman-'t Hooft gauge

Here we present the analytical results for the form factors $F_{L,R}$ involved in the computation of the LFVHD decay rates when computed with the MIA to one-loop order and considering the leading order corrections, $\mathcal{O}(Y_\nu^2)$, and the next to leading corrections, $\mathcal{O}(Y_\nu^4)$, as explained in the text. This means the computation of all the one-loop diagrams in Figs. 3.18, 3.19, 3.20 and 3.21. They are written in terms of the usual one-loop functions for the two-point $B's$, three-point $C's$, and four-point $D's$ functions. We follow these definitions and conventions:

$$
\mu^{4-D} \int \frac{d^D k}{(2\pi)^D} \frac{\{1; k^\mu\}}{[k^2-m_1^2][(k+p_1)^2-m_2^2]} = \frac{i}{16\pi^2} \{B_0; p_1^\mu B_1\}(p_1, m_1, m_2),
\tag{E.5}
$$

$$\mu^{4-D} \int \frac{d^D k}{(2\pi)^D} \frac{\{1; k^2; k^\mu\}}{[k^2 - m_1^2][(k+p_1)^2 - m_2^2][(k+p_1+p_2)^2 - m_3^2]}$$
$$= \frac{i}{16\pi^2} \left\{ C_0; \tilde{C}_0; p_1^\mu C_{11} + p_2^\mu C_{12} \right\} (p_1, p_2, m_1, m_2, m_3), \tag{E.6}$$

$$\mu^{4-D} \int \frac{d^D k}{(2\pi)^D} \frac{\{1; k^2; k^\mu\}}{[k^2 - m_1^2][(k+p_1)^2 - m_2^2][(k+p_1+p_2)^2 - m_3^2][(k+p_1+p_2+p_3)^2 - m_4^2]}$$
$$= \frac{i}{16\pi^2} \left\{ D_0; \tilde{D}_0; p_1^\mu D_{11} + p_2^\mu D_{12} + p_3^\mu D_{13} \right\} (p_1, p_2, p_3, m_1, m_2, m_3, m_4). \tag{E.7}$$

We start with the left-handed form factors and present the contributions diagram by diagram following the notation explained in the text and $m_{k,m} \equiv m_{\ell_{k,m}}$. We will restrict ourselves to the dominant contributions, meaning those that will provide $\mathcal{O}(v^2/M_R^2)$ terms when doing the large M_R expansion, as explained in the next appendix. For instance, contributions from loop functions of type D_i where M_R appears in two of the mass arguments go as $1/M_R^4$ and provide subdominant corrections that are not considered here.

The results of the $\mathcal{O}(Y_\nu^2)$ contributions are:

$$F_L^{\text{MIA}(1)\,(Y^2)} = \frac{1}{32\pi^2} \frac{m_k}{m_W} \left(Y_\nu Y_\nu^\dagger \right)^{km} \left((\tilde{C}_0 + m_k^2(C_{11} - C_{12}) + m_m^2 C_{12})_{(1a)} \right.$$
$$\left. + m_m^2(C_0 + C_{11})_{(1b)} - m_m^2(C_{12})_{(1c)} - m_m^2(C_0 + C_{12})_{(1d)} \right),$$

$$F_L^{\text{MIA}(2)\,(Y^2)} = \frac{-1}{16\pi^2} m_k m_W \left(Y_\nu Y_\nu^\dagger \right)^{km} \left((C_0 + C_{11} - C_{12})_{(2a)} + (C_{11} - C_{12})_{(2b)} \right),$$

$$F_L^{\text{MIA}(3)\,(Y^2)} = \frac{1}{8\pi^2} m_k m_W^3 \left(Y_\nu Y_\nu^\dagger \right)^{km} (D_{12} - D_{13})_{(3a)},$$

$$F_L^{\text{MIA}(4)\,(Y^2)} = \frac{-1}{32\pi^2} m_k m_W \left(Y_\nu Y_\nu^\dagger \right)^{km} \left((C_0 - C_{11} + C_{12})_{(4a)} + m_m^2(2D_{12} - D_{13})_{(4b)} \right),$$

$$F_L^{\text{MIA}(5)\,(Y^2)} = \frac{1}{32\pi^2} m_k m_W \left(Y_\nu Y_\nu^\dagger \right)^{km} \left((2C_0 + C_{11} - C_{12})_{(5a)} \right.$$
$$\left. + (C_0 + 2m_k^2 D_{12} - (2m_H^2 - m_m^2)D_{13})_{(5b)} \right),$$

$$F_L^{\text{MIA}(6)\,(Y^2)} = \frac{1}{32\pi^2} \frac{m_k}{m_W} m_H^2 \left(Y_\nu Y_\nu^\dagger \right)^{km} \left((C_{11} - C_{12})_{(6a)} + (C_0)_{(6c)} + m_m^2(D_{13})_{(6d)} \right),$$

$$F_L^{\text{MIA}(7)\,(Y^2)} = \frac{1}{16\pi^2} m_k m_W \frac{m_m^2}{m_k^2 - m_m^2} \left(Y_\nu Y_\nu^\dagger \right)^{km} (C_{12})_{(7a)},$$

$$F_L^{\text{MIA}(8)\,(Y^2)} = \frac{1}{32\pi^2} \frac{m_k}{m_W} \frac{m_m^2}{m_k^2 - m_m^2} \left(Y_\nu Y_\nu^\dagger \right)^{km} \left((B_1)_{(8a)} + (B_0)_{(8b)} + (B_0)_{(8c)} + m_k^2(C_{12})_{(8d)} \right),$$

$$F_L^{\text{MIA}(9)\,(Y^2)} = \frac{-1}{16\pi^2} m_k m_W \frac{m_m^2}{m_k^2 - m_m^2} \left(Y_\nu Y_\nu^\dagger \right)^{km} (C_{12})_{(9a)},$$

158

$$F_L^{\text{MIA(10) (Y}^2)} = \frac{-1}{32\pi^2} \frac{m_k}{m_W} \frac{m_m^2}{m_k^2 - m_m^2} \left(Y_\nu Y_\nu^\dagger\right)^{km} \left((B_1)_{(10a)} + (B_0)_{(10b)} + \frac{m_k^2}{m_m^2}(B_0)_{(10c)} + m_k^2(C_{12})_{(10d)}\right).$$

$$(E.8)$$

The results of the dominant $\mathcal{O}(Y_\nu^4)$ contributions are:

$$F_L^{\text{MIA(1) (Y}^4)} = \frac{1}{32\pi^2} \frac{m_k}{m_W} \left(Y_\nu Y_\nu^\dagger Y_\nu Y_\nu^\dagger\right)^{km} v^2 \Big(-(C_{11} - C_{12})_{(1e)} - (C_{11} - C_{12} + C_0)_{(1f)}$$
$$+ (\tilde{D}_0)_{(1g)} + (\tilde{D}_0)_{(1h)} + (C_0)_{(1j)} \Big),$$

$$F_L^{\text{MIA(8) (Y}^4)} = \frac{1}{32\pi^2} \frac{m_k}{m_W} \frac{m_m^2}{m_k^2 - m_m^2} \left(Y_\nu Y_\nu^\dagger Y_\nu Y_\nu^\dagger\right)^{km} v^2 \Big((C_{12})_{(8e)} + (C_0)_{(8f)} + (C_0)_{(8g)}\Big),$$

$$F_L^{\text{MIA(10) (Y}^4)} = \frac{-1}{32\pi^2} \frac{m_k}{m_W} \frac{m_m^2}{m_k^2 - m_m^2} \left(Y_\nu Y_\nu^\dagger Y_\nu Y_\nu^\dagger\right)^{km} v^2 \Big((C_{12})_{(10e)} + (C_0)_{(10f)} + \frac{m_k^2}{m_m^2}(C_0)_{(10g)}\Big).$$

$$(E.9)$$

Next, we present the right-handed form factors. The results of the $\mathcal{O}(Y_\nu^2)$ contributions are:

$$F_R^{\text{MIA(1) (Y}^2)} = \frac{1}{32\pi^2} \frac{m_m}{m_W} \left(Y_\nu Y_\nu^\dagger\right)^{km} \Big(m_k^2(C_0 + C_{11})_{(1a)} + (\tilde{C}_0 + m_k^2(C_{11} - C_{12}) + m_m^2 C_{12})_{(1b)}$$
$$- m_k^2(C_0 + C_{11} - C_{12})_{(1c)} - m_k^2(C_{11} - C_{12})_{(1d)} \Big),$$

$$F_R^{\text{MIA(2) (Y}^2)} = \frac{-1}{16\pi^2} m_m m_W \left(Y_\nu Y_\nu^\dagger\right)^{km} \Big((C_{12})_{(2a)} + (C_0 + C_{12})_{(2b)}\Big),$$

$$F_R^{\text{MIA(3) (Y}^2)} = \frac{1}{8\pi^2} m_m m_W^3 \left(Y_\nu Y_\nu^\dagger\right)^{km} (D_{13})_{(3a)},$$

$$F_R^{\text{MIA(4) (Y}^2)} = \frac{1}{32\pi^2} m_m m_W \left(Y_\nu Y_\nu^\dagger\right)^{km} \Big((2C_0 + C_{12})_{(4a)}$$
$$+ \left(C_0 + 2m_m^2 D_{12} - (2m_H^2 - m_k^2)(D_{12} - D_{13})\right)_{(4b)}\Big),$$

$$F_R^{\text{MIA(5) (Y}^2)} = \frac{-1}{32\pi^2} m_m m_W \left(Y_\nu Y_\nu^\dagger\right)^{km} \Big((C_0 - C_{12})_{(5a)} + m_k^2(D_{12} + D_{13})_{(5b)}\Big),$$

$$F_R^{\text{MIA(6) (Y}^2)} = \frac{1}{32\pi^2} \frac{m_m}{m_W} m_H^2 \left(Y_\nu Y_\nu^\dagger\right)^{km} \Big((C_{12})_{(6a)} + (C_0)_{(6b)} + m_k^2(D_{12} - D_{13})_{(6d)}\Big),$$

$$F_R^{\text{MIA(7) (Y}^2)} = \frac{1}{16\pi^2} m_m m_W \frac{m_k^2}{m_k^2 - m_m^2} \left(Y_\nu Y_\nu^\dagger\right)^{km} (C_{12})_{(7a)},$$

$$F_R^{\text{MIA(8) (Y}^2)} = \frac{1}{32\pi^2} \frac{m_m}{m_W} \frac{m_k^2}{m_k^2 - m_m^2} \left(Y_\nu Y_\nu^\dagger\right)^{km} \Big((B_1)_{(8a)} + \frac{m_m^2}{m_k^2}(B_0)_{(8b)} + (B_0)_{(8c)} + m_m^2(C_{12})_{(8d)}\Big),$$

$$F_R^{\text{MIA(9) (Y}^2)} = \frac{-1}{16\pi^2} m_m m_W \frac{m_k^2}{m_k^2 - m_m^2} \left(Y_\nu Y_\nu^\dagger\right)^{km} (C_{12})_{(9a)},$$

$$F_R^{\text{MIA}(10)\ (\text{Y}^2)} = \frac{-1}{32\pi^2} \frac{m_m}{m_W} \frac{m_k^2}{m_k^2 - m_m^2} \left(Y_\nu Y_\nu^\dagger\right)^{km} \left((B_1)_{(10a)} + (B_0)_{(10b)} + (B_0)_{(10c)} + m_m^2 (C_{12})_{(10d)}\right).$$

$$\text{(E.10)}$$

The results of the dominant $\mathcal{O}(Y_\nu^4)$ contributions are:

$$F_R^{\text{MIA}(1)\ (\text{Y}^4)} = \frac{1}{32\pi^2} \frac{m_m}{m_W} \left(Y_\nu Y_\nu^\dagger Y_\nu Y_\nu^\dagger\right)^{km} v^2 \Big(-(C_0 + C_{12})_{(1e)} - (C_{12})_{(1f)}$$
$$+ (C_0)_{(1i)} + (\tilde{D}_0)_{(1k)} + (\tilde{D}_0)_{(1l)} \Big),$$

$$F_R^{\text{MIA}(8)\ (\text{Y}^4)} = \frac{1}{32\pi^2} \frac{m_m}{m_W} \frac{m_k^2}{m_k^2 - m_m^2} \left(Y_\nu Y_\nu^\dagger Y_\nu Y_\nu^\dagger\right)^{km} v^2 \Big((C_{12})_{(8e)} + \frac{m_m^2}{m_k^2}(C_0)_{(8f)} + (C_0)_{(8g)} \Big),$$

$$F_R^{\text{MIA}(10)\ (\text{Y}^4)} = \frac{-1}{32\pi^2} \frac{m_m}{m_W} \frac{m_k^2}{m_k^2 - m_m^2} \left(Y_\nu Y_\nu^\dagger Y_\nu Y_\nu^\dagger\right)^{km} v^2 \Big((C_{12})_{(10e)} + (C_0)_{(10f)} + (C_0)_{(10g)} \Big).$$

$$\text{(E.11)}$$

The arguments of the above one-loop integrals are the following:

$$\begin{aligned}
\tilde{C}_0, C_i &= \tilde{C}_0, C_i(p_2, p_1, m_W, 0, M_R) && \text{in } (1a), (1c), (2a) \\
\tilde{C}_0, C_i &= \tilde{C}_0, C_i(p_2, p_1, m_W, M_R, 0) && \text{in } (1b), (1d), (2b) \\
C_i &= C_i(p_2, p_1, m_W, M_R, M_R) && \text{in } (1e), (1f), (1i), (1j) \\
\tilde{D}_0 &= \tilde{D}_0(p_2, 0, p_1, m_W, 0, M_R, M_R) && \text{in } (1g) \\
\tilde{D}_0 &= \tilde{D}_0(p_2, p_1, 0, m_W, 0, M_R, M_R) && \text{in } (1h) \\
\tilde{D}_0 &= \tilde{D}_0(p_2, p_1, 0, m_W, M_R, M_R, 0) && \text{in } (1k) \\
\tilde{D}_0 &= \tilde{D}_0(p_2, 0, p_1, m_W, M_R, M_R, 0) && \text{in } (1l) \\
D_i &= D_i(0, p_2, p_1, 0, M_R, m_W, m_W) && \text{in } (3a), (4b), (5b), (6d) \\
C_i &= C_i(p_2, p_1, M_R, m_W, m_W) && \text{in } (4a), (4b), (5a), (5b), (6a), (6b), (6c) \\
C_{12} &= C_{12}(0, p_2, 0, M_R, m_W) && \text{in } (7a), (8d) \\
B_i &= B_i(p_2, M_R, m_W) && \text{in } (8a), (8b), (8c) \\
C_i &= C_i(0, p_2, M_R, M_R, m_W) && \text{in } (8e), (8f), (8g) \\
C_{12} &= C_{12}(0, p_3, 0, M_R, m_W) && \text{in } (9a), (10d) \\
B_i &= B_i(p_3, M_R, m_W) && \text{in } (10a), (10b), (10c) \\
C_i &= C_i(0, p_3, M_R, M_R, m_W) && \text{in } (10e), (10f), (10g).
\end{aligned}$$

We want to remark that the above formulas are valid for the degenerate $M_{R_i} = M_R$ case. Nevertheless, they can be easily generalized to the non-degenerate case by properly including the summation indices. For example, it would be enough to change

$$\left(Y_\nu Y_\nu^\dagger\right)^{km} C_\alpha(p_2, p_1, m_W, 0, M_R) \rightarrow \left(Y_\nu^{ka} Y_\nu^{\dagger am}\right) C_\alpha(p_2, p_1, m_W, 0, M_{R_a}),$$
$$\left(Y_\nu Y_\nu^\dagger Y_\nu Y_\nu^\dagger\right)^{km} C_\alpha(p_2, p_1, m_W, M_R, M_R) \rightarrow \left(Y_\nu^{ka} Y_\nu^{\dagger ai} Y_\nu^{ib} Y_\nu^{\dagger bm}\right) C_\alpha(p_2, p_1, m_W, M_{R_a}, M_{R_b}),$$

$$\text{(E.12)}$$

and similarly for all the terms.

E.3 The large M_R expansion

Here we present our analytical results for the loop-functions and form factors involved in our computation of LFVHD rates in the large M_R limit. To reach this limit we perform a systematic expansion of the amplitude in powers of (v^2/M_R^2). Generically, the first order in this expansion is $\mathcal{O}(v^2/M_R^2)$ the next order is $\mathcal{O}(v^4/M_R^4)$, etc. The logarithmic dependence with M_R is left unexpanded. In the final expansion we will keep just the dominant terms in the form factors of $\mathcal{O}(v^2/M_R^2)$ which will be shown to be sufficient to describe successfully the final amplitude for LFVHD in the heavy right-handed neutrino mass region of our interest, $M_R \gg v$.

We first calculate the large M_R expansions of all one-loop functions and second we plug these expansions in the form factors formulas. To do this, we perform first the integration of Feynman's parameters and next we expand them for large $M_R \gg v$. Since we have the mass of W boson in the mass argument of the one-loop functions, we cannot take the most used approximation of neglecting external momentum particles (because the mass of the Higgs boson enters here). In fact our expansions presented in this work will apply to the present case of on-shell Higgs boson, i.e. with $p_1^2 = m_H^2$ and m_H being the realistic Higgs boson mass. Furthermore, it should be noticed that in principle there are three very different scales of masses involved in the computation: the lepton sector masses (m_{ℓ_m} and m_{ℓ_k}), the electroweak sector masses (m_W and m_H) and the new physics scale M_R. As we said, in a good approximation we can neglect the lepton masses in the one-loop functions at the beginning. However, both electroweak masses m_W and m_H must be retained in order to calculate the $\mathcal{O}(M_R^{-2})$ terms of the one-loop functions. Actually, in practice we consider the vacuum expectation value v, which is the common scale entering in both electroweak masses within the SM, and as we said above, we perform a well defined expansion in powers of an unique dimensionless parameter that is given by the ratio v^2/M_R^2.

At the numerical level, we have checked that all expansions presented in the following are in very good accordance with the numerical results from *LoopTools* [266]. The analytical expansions that we get for the dominant terms of the loop functions, i.e. up to $\mathcal{O}(M_R^{-2})$, are summarized next:

$$
B_0\left(p, M_R, m_W\right) = \Delta + 1 - \log\left(\frac{M_R^2}{\mu^2}\right) + \frac{m_W^2 \log\left(\frac{m_W^2}{M_R^2}\right)}{M_R^2} + \frac{p^2}{2M_R^2},
$$

$$
C_0\left(p_2, p_1, m_W, 0, M_R\right) = C_0\left(p_2, p_1, m_W, M_R, 0\right) = \frac{\log\left(\frac{m_W^2}{M_R^2}\right)}{M_R^2},
$$

$$
C_0\left(p_2, p_1, M_R, m_W, m_W\right) = \frac{2\sqrt{4\lambda - 1}\arctan\left(\sqrt{\frac{1}{4\lambda-1}}\right) - 1 + \log\left(\frac{m_W^2}{M_R^2}\right)}{M_R^2},
$$

$$C_0\left(p_2, p_1, m_W, M_R, M_R\right) = -\frac{1}{M_R^2},$$

$$C_0\left(0, p_{lep}, M_R, M_R, m_W\right) = -\frac{1}{M_R^2},$$

$$\tilde{C}_0\left(p_2, p_1, m_W, M_R, 0\right) = \tilde{C}_0\left(p_2, p_1, m_W, 0, M_R\right)$$

$$= \Delta + 1 - \log\left(\frac{M_R^2}{\mu^2}\right) + \frac{m_W^2 \log\left(\frac{m_W^2}{M_R^2}\right)}{M_R^2} + \frac{m_H^2}{2M_R^2},$$

$$\tilde{D}_0\left(p_2, 0, p_1, m_W, 0, M_R, M_R\right) = \tilde{D}_0\left(p_2, p_1, 0, m_W, 0, M_R, M_R\right) = -\frac{1}{M_R^2},$$

$$\tilde{D}_0\left(p_2, 0, p_1, m_W, M_R, M_R, 0\right) = \tilde{D}_0\left(p_2, p_1, 0, m_W, M_R, M_R, 0\right) = -\frac{1}{M_R^2},$$

$$B_1\left(p, M_R, m_W\right) = -\frac{\Delta}{2} - \frac{3}{4} + \frac{1}{2}\log\left(\frac{M_R^2}{\mu^2}\right) - \frac{m_W^2\left(2\log\left(\frac{m_W^2}{M_R^2}\right)+1\right)}{2M_R^2} - \frac{p^2}{3M_R^2},$$

$$C_{11}\left(p_2, p_1, m_W, 0, M_R\right) = \frac{1 - \log\left(\frac{m_W^2}{M_R^2}\right)}{2M_R^2},$$

$$C_{12}\left(p_2, p_1, m_W, 0, M_R\right) = \frac{1}{2M_R^2},$$

$$C_{11}\left(p_2, p_1, m_W, M_R, 0\right) = \frac{1 - \log\left(\frac{m_W^2}{M_R^2}\right)}{2M_R^2},$$

$$C_{12}\left(p_2, p_1, m_W, M_R, 0\right) = -\frac{\log\left(\frac{m_W^2}{M_R^2}\right)}{2M_R^2},$$

$$C_{11}\left(p_2, p_1, M_R, m_W, m_W\right) = 2C_{12}\left(p_2, p_1, M_R, m_W, m_W\right)$$

$$= -\frac{4\sqrt{4\lambda - 1}\arctan\left(\sqrt{\frac{1}{4\lambda-1}}\right) + 2\log\left(\frac{m_W^2}{M_R^2}\right) - 1}{2M_R^2},$$

$$C_{11}\left(p_2, p_1, m_W, M_R, M_R\right) = 2C_{12}\left(p_2, p_1, m_W, M_R, M_R\right) = \frac{1}{2M_R^2},$$

$$C_{12}\left(0, p_{lep}, 0, M_R, m_W\right) = \frac{-\log\left(\frac{m_W^2}{M_R^2}\right) - 1}{2M_R^2},$$

$$C_{12}\left(0, p_{lep}, M_R, M_R, m_W\right) = \frac{1}{2M_R^2},$$

$$D_{12}\left(0, p_2, p_1, 0, M_R, m_W, m_W\right) = 2D_{13}\left(0, p_2, p_1, 0, M_R, m_W, m_W\right)$$

$$= \frac{2\left(-4\lambda \arctan^2\left(\sqrt{\frac{1}{4\lambda-1}}\right) + 2\sqrt{4\lambda-1}\arctan\left(\sqrt{\frac{1}{4\lambda-1}}\right) - 1\right)}{M_R^2 m_H^2}.$$

(E.13)

where we have used the usual definitions in dimensional regularization, $\Delta = 2/\epsilon - \gamma_E + \mathrm{Log}(4\pi)$ with $D = 4 - \epsilon$ and μ the usual scale, and we have denoted the mass ratio $\lambda = \frac{m_W^2}{m_H^2}$ to shorten the result.

Taking into account the formulas above in Eq. (E.13), plugging them into the results of the form factors in the App. E.2, neglecting the tiny terms with lepton masses, and pairing diagrams conveniently, we finally get the results for the dominant terms of the various type diagrams (i) of the MIA form factors valid in the large $M_R \gg v$ regime:

$$
\begin{aligned}
F_L^{(1)} &= \frac{1}{32\pi^2}\frac{m_k}{m_W}\left[\left(Y_\nu Y_\nu^\dagger\right)^{km}\left(\Delta + 1 - \log(\frac{M_R^2}{\mu^2}) + \frac{m_W^2 \log\left(\frac{m_W^2}{M_R^2}\right)}{M_R^2} + \frac{m_H^2}{2M_R^2}\right)\right. \\
&\quad \left. -\frac{5}{2}\frac{v^2}{M_R^2}\left(Y_\nu Y_\nu^\dagger Y_\nu Y_\nu^\dagger\right)^{km}\right], \\
F_L^{(2)} &= -\frac{1}{32\pi^2}\frac{m_k}{m_W}\left(Y_\nu Y_\nu^\dagger\right)^{km}\frac{m_W^2}{M_R^2}\left(1 + \log\left(\frac{m_W^2}{M_R^2}\right)\right), \\
F_L^{(3)} &= \frac{1}{8\pi^2}\frac{m_k}{m_W}\left(Y_\nu Y_\nu^\dagger\right)^{km}\frac{\lambda m_W^2}{M_R^2}\left(-4\lambda \arctan^2\left(\frac{1}{\sqrt{4\lambda-1}}\right)\right. \\
&\quad \left. +2\sqrt{4\lambda-1}\arctan\left(\frac{1}{\sqrt{4\lambda-1}}\right) - 1\right), \\
F_L^{(4+5)} &= \frac{1}{32\pi^2}\frac{m_k}{m_W}\left(Y_\nu Y_\nu^\dagger\right)^{km}\frac{m_W^2}{M_R^2}\left(8\lambda \arctan^2\left(\frac{1}{\sqrt{4\lambda-1}}\right)\right. \\
&\quad \left. -2\sqrt{4\lambda-1}\arctan\left(\frac{1}{\sqrt{4\lambda-1}}\right) + \frac{1}{2} + \log\left(\frac{m_W^2}{M_R^2}\right)\right), \\
F_L^{(6)} &= \frac{1}{32\pi^2}\frac{m_k}{m_W}\left(Y_\nu Y_\nu^\dagger\right)^{km}\frac{m_H^2}{M_R^2}\left(\sqrt{4\lambda-1}\arctan\left(\frac{1}{\sqrt{4\lambda-1}}\right) - \frac{3}{4} + \frac{\log\left(\frac{m_W^2}{M_R^2}\right)}{2}\right), \\
F_L^{(7+9)} &= 0, \\
F_L^{(8+10)} &= -\frac{1}{32\pi^2}\frac{m_k}{m_W}\left[\left(Y_\nu Y_\nu^\dagger\right)^{km}\left(\Delta + 1 - \log(\frac{M_R^2}{\mu^2}) + \frac{m_W^2 \log\left(\frac{m_W^2}{M_R^2}\right)}{M_R^2}\right)\right. \\
&\quad \left. -\frac{v^2}{M_R^2}\left(Y_\nu Y_\nu^\dagger Y_\nu Y_\nu^\dagger\right)^{km}\right].
\end{aligned}
$$

(E.14)

And similar formulas can be obtained for the F_R form factors. Notice that in the results above we have included all the relevant contributions, i.e. up to $\mathcal{O}(Y_\nu^2 + Y_\nu^4)$ and it turns out, as announced in the text, that they are just the diagrams (1)+(8)+(10) that provide contributions of $\mathcal{O}(Y_\nu^4)$ with a v^2/M_R^2 dependence. The other diagrams will also give $\mathcal{O}(Y_\nu^4)$ contributions but they will be suppressed since they go with a v^4/M_R^4 dependence, and we do not keep these small contributions in our expansions.
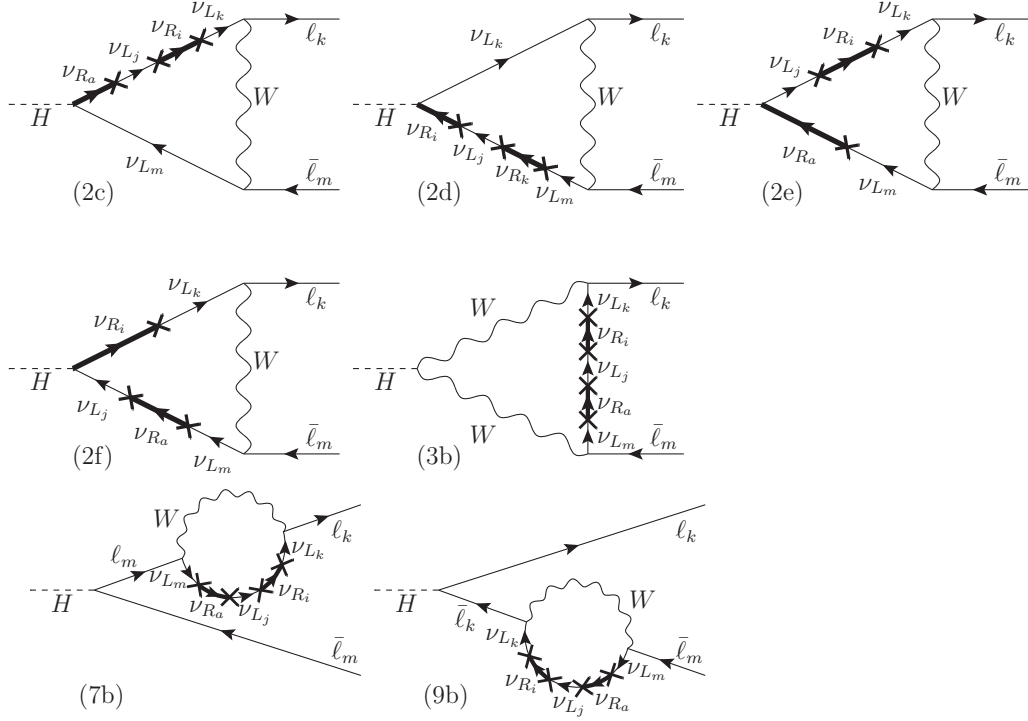
E.4 MIA Form Factors in the Unitary gauge

In order to check the gauge invariance of our results for the LFVHD form factors (and therefore the partial width) that we have computed in the MIA by using the Feynman-'t Hooft gauge, we are going to present here the computation of these same form factors but using a different gauge choice, in particular the Unitary gauge (UG). We will demonstrate that when computing the MIA form factor F_L to $\mathcal{O}(Y_\nu^2 + Y_\nu^4)$ we get the same result as in Eq. (3.30). A similar demonstration can be done for F_R but we do not include it here for shortness. For this exercise, we ignore the tiny terms suppressed by factors of the lepton masses as we did in Eq. (3.30).

First, we list the relevant one-loop diagrams contributing to the form factor F_L in the UG. Since, in this gauge there are not Goldstone bosons, there will be just diagrams of type: (2), (3), (7) and (9). Generically, each of these diagrams will get contributions of $\mathcal{O}(Y_\nu^2)$ and $\mathcal{O}(Y_\nu^4)$. Second, we write the propagator of the W gauge boson in the UG, P_W^{UG}, by splitting it into two parts, P_W^a and P_W^b:

$$P_W^{\mathrm{UG}} = P_W^a + P_W^b = -\frac{ig_{\mu\nu}}{p^2 - m_W^2} + \frac{ip_\mu p_\nu}{m_W^2(p^2 - m_W^2)}\,, \tag{E.15}$$

such that, P_W^a coincides with the W propagator in the Feynman-'t Hooft gauge. Then, each diagram of type (i), i=2,3,7,9, will receive three kind of contributions: 1) from the part P_W^a one gets the same contributions to $\mathcal{O}(Y_\nu^2)$ as those we got in the Feynman-'t Hooft gauge from the five diagrams (2a), (2b), (3a), (7a) and (9a) in Figs. 3.18 and 3.19; 2) new contributions to $\mathcal{O}(Y_\nu^2)$ that come from considering the new propagator term P_W^b in these same diagrams (2a), (2b), (3a), (7a) and (9a) ; 3) contributions to $\mathcal{O}(Y_\nu^4)$ that come from new diagrams which were not relevant in the Feynman-'t Hooft gauge, but they are relevant in the UG. By relevant we mean leading to dominant $\mathcal{O}(M_R^{-2})$ contributions in the large M_R expansion. These new diagrams contributing to order $\mathcal{O}(Y_\nu^4)$ in the UG are the seven diagrams shown in figure E.3. Thus, we get in total twelve one-loop diagrams contributing in the UG: (2a), (2b), (2c), (2d), (2e), (2f), (3a), (3b), (7a), (7b), (9a) and (9b).

Next we present the results in the UG for each type of diagram (i), specifying the various contributions explained above, which for clarity we present correspondingly ordered

Figure E.3: Relevant diagrams for the Form Factors to $\mathcal{O}(Y_\nu^4)$ in the Unitary gauge

in three lines, the first line is for kind 1), the second line is for kind 2) and the third line is for kind 3). The UG F_L form factors to $\mathcal{O}(Y_\nu^2 + Y_\nu^4)$ that we get are, as follows:

$$
\begin{aligned}
F_L^{\mathrm{UG}(2)} &= -\frac{1}{16\pi^2} m_k m_W \left(Y_\nu Y_\nu^\dagger\right)^{km} \left((C_0 + C_{11} - C_{12})_{(2a)} + (C_{11} - C_{12})_{(2b)}\right) \\
&\quad + \frac{1}{32\pi^2}\frac{m_k}{m_W}\left[\left(Y_\nu Y_\nu^\dagger\right)^{km}\left((\tilde{C}_0)_{(2a)} - (B_1)_{(2b)}\right)\right. \\
&\quad \left. + \left(Y_\nu Y_\nu^\dagger Y_\nu Y_\nu^\dagger\right)^{km} v^2 \left(-(C_{11})_{(2c)} + (\tilde{D}_0)_{(2d)} + (\tilde{D}_0 - (C_{11} - C_{12}))_{(2e)} - (C_{11} - C_{12})_{(2f)}\right)\right], \\
F_L^{\mathrm{UG}(3)} &= \frac{1}{8\pi^2} m_k m_W^3 \left(Y_\nu Y_\nu^\dagger\right)^{km}(D_{12} - D_{13})_{(3a)} \\
&\quad - \frac{1}{32\pi^2}\left(Y_\nu Y_\nu^\dagger\right)^{km}\frac{m_k}{m_W}\left[2B_0 + B_1 - (2m_W^2 + m_H^2)(C_0 + C_{11} - C_{12}) + 2m_W^2 m_H^2 D_{13}\right]_{(3a)} \\
&\quad - \frac{1}{32\pi^2}\left(Y_\nu Y_\nu^\dagger Y_\nu Y_\nu^\dagger\right)^{km}\frac{m_k}{m_W} v^2 \left[2C_0 + C_{12}\right]_{(3b)},
\end{aligned}
$$

$$
\begin{aligned}
F_L^{\mathrm{UG}(7)} \;=\; & \frac{1}{16\pi^2} m_k m_W \frac{m_m^2}{m_k^2 - m_m^2} \left(Y_\nu Y_\nu^\dagger\right)^{km} (C_{12})_{(7a)} , \\
& \frac{1}{32\pi^2} \frac{m_k m_m^2}{m_W(m_k^2 - m_m^2)} \left[\left(Y_\nu Y_\nu^\dagger\right)^{km} (2B_0 + B_1)_{(7a)}\right. \\
& \left. + \left(Y_\nu Y_\nu^\dagger Y_\nu Y_\nu^\dagger\right)^{km} v^2 (2C_0 + C_{12})_{(7b)}\right] \\
F_L^{\mathrm{UG}(9)} \;=\; & -\frac{1}{16\pi^2} m_k m_W \frac{m_m^2}{m_k^2 - m_m^2} \left(Y_\nu Y_\nu^\dagger\right)^{km} (C_{12})_{(9a)} , \\
& -\frac{1}{32\pi^2} \frac{m_k m_m^2}{m_W(m_k^2 - m_m^2)} \left[\left(Y_\nu Y_\nu^\dagger\right)^{km} (2B_0 + B_1)_{(9a)}\right. \\
& \left. + \left(Y_\nu Y_\nu^\dagger Y_\nu Y_\nu^\dagger\right)^{km} v^2 (2C_0 + C_{12})_{(9b)}\right] ,
\end{aligned}
\tag{E.16}
$$

where the arguments of the one-loop functions are:

$$
\begin{aligned}
\tilde{C}_0, C_i \;=\; & \tilde{C}_0, C_i(p_2, p_1, m_W, 0, M_R) && \text{in } (2a) \\
B_i \;=\; & B_i(p_{lep}, m_W, M_R) && \text{in } (2b) \\
C_i \;=\; & C_i(p_2, p_1, m_W, M_R, 0) && \text{in } (2b) \\
C_i \;=\; & C_i(p_{lep}, 0, m_W, M_R, M_R) && \text{in } (2c) \\
\tilde{D}_0 \;=\; & \tilde{D}_0(p_2, p_1, 0, m_W, 0, M_R, M_R) && \text{in } (2d) \\
C_i \;=\; & C_i(p_2, p_1, m_W, M_R, M_R) && \text{in } (2e), (2f) \\
\tilde{D}_0 \;=\; & \tilde{D}_0(p_2, 0, p_1, m_W, 0, M_R, M_R) && \text{in } (2e) \\
B_i \;=\; & B_i(p_{lep}, M_R, m_W) && \text{in } (3a), (7a), (9a) \\
C_i \;=\; & C_i(p_2, p_1, M_R, m_W, m_W) && \text{in } (3a) \\
D_i \;=\; & D_i(0, p_2, p_1, 0, M_R, m_W, m_W) && \text{in } (3a) \\
C_i \;=\; & C_i(0, p_{lep}, M_R, M_R, m_W) && \text{in } (3b), (7b), (9b) \\
C_i \;=\; & C_i(0, p_{lep}, 0, M_R, m_W) && \text{in } (7a), (9a) .
\end{aligned}
$$

The comparison of the previous results with that in Eq. (??) then goes as follows. First, it is clear from the above results, that once again the contributions from diagrams (7) and (9) cancel out fully, as it happened in the Feynman-'t Hooft gauge. Therefore, $F_L^{\mathrm{UG}} = F_L^{\mathrm{UG}(2)} + F_L^{\mathrm{UG}(3)}$. Then, the first line in $F_L^{\mathrm{UG}(2)}$ and the first line in $F_L^{\mathrm{UG}(3)}$ match correspondingly with the contributions from (2) and (3) in the Feynman-'t Hooft gauge. Next, by using the relation,

$$
B_0(p_{lep}, M_R, m_W) + B_1(p_{lep}, M_R, m_W) + B_1(p_{lep}, m_W, M_R) = 0 ,
\tag{E.17}
$$

we get that the sum of the second line in $F_L^{\mathrm{UG}(2)}$ and the second line in $F_L^{\mathrm{UG}(3)}$ gives exactly the contributions to $\mathcal{O}(Y_\nu^2)$ from (1)+(8)+(10)+(4)+(5)+(6) in the Feynman-'t Hooft gauge. Finally, by using the relation

$$
C_{11}(p_{lep}, 0, m_W, M_R, M_R) + (C_0 + C_{12})(0, p_{lep}, M_R, M_R, m_W) = 0 ,
\tag{E.18}
$$

166

we get that the sum of the third line in $F_L^{\mathrm{UG}(2)}$ and the third line in $F_L^{\mathrm{UG}(3)}$ gives exactly the contributions to $\mathcal{O}(Y_\nu^4)$ from (1)+(8)+(10). Therefore, in summary, we get the identity of the total result for F_L computed in both gauges, leading to the gauge invariant result of Eq. (3.30).

Appendix F

Form factors for LFVZD in the ISS model

In this Appendix we give the analytical expressions for the form factors contributing to $Z \to \ell_k \bar{\ell}_m$, as they are defined in Eqs. (4.1) and (4.2). In the Feynman-t'Hooft gauge, they are obtained by computing the diagrams shown in Fig. 4.1. We take the results from [49, 80] and adapt them to our notation and to the convection of *LoopTools* [266] for the loop functions.

The form factors of the different diagrams are

$$\mathcal{F}_Z^{(1)} = \frac{1}{2} B_{\ell_k n_i} B_{\ell_m n_j}^* \left\{ -C_{n_i n_j} x_i x_j m_W^2 C_0 + C_{n_i n_j}^* \sqrt{x_i x_j} \left[m_Z^2 C_{12} - 2C_{00} + \frac{1}{2} \right] \right\}, \quad \text{(F.1)}$$

where $C_{0,12,00} \equiv C_{0,12,00}(0, m_Z^2, 0, m_W^2, m_{n_i}^2, m_{n_j}^2)$;

$$\mathcal{F}_Z^{(2)} = B_{\ell_k n_i} B_{\ell_m n_j}^* \left\{ -C_{n_i n_j} \left[m_Z^2 \left(C_0 + C_1 + C_2 + C_{12} \right) - 2C_{00} + 1 \right] + C_{n_i n_j}^* \sqrt{x_i x_j} \, m_W^2 C_0 \right\}, \quad \text{(F.2)}$$

where $C_{0,1,2,12,00} \equiv C_{0,1,2,12,00}(0, m_Z^2, 0, m_W^2, m_{n_i}^2, m_{n_j}^2)$;

$$\mathcal{F}_Z^{(3)} = 2c_W^2 B_{\ell_k n_i} B_{\ell_m n_i}^* \left\{ m_Z^2 \left(C_1 + C_2 + C_{12} \right) - 6C_{00} + 1 \right\}, \quad \text{(F.3)}$$

where $C_{1,2,12,00} \equiv C_{1,2,12,00}(0, m_Z^2, 0, m_{n_i}^2, m_W^2, m_W^2)$;

$$\mathcal{F}_Z^{(4)} + \mathcal{F}_Z^{(5)} = -2s_W^2 \, B_{\ell_k n_i} B_{\ell_m n_i}^* \, x_i \, m_W^2 C_0, \quad \text{(F.4)}$$

where $C_0 \equiv C_0(0, m_Z^2, 0, m_{n_i}^2, m_W^2, m_W^2)$;

$$\mathcal{F}_Z^{(6)} = -(1 - 2s_W^2) \, B_{\ell_k n_i} B_{\ell_m n_i}^* \, x_i \, C_{00}, \quad \text{(F.5)}$$

where $C_{00} \equiv C_{00}(0, m_Z^2, 0, m_{n_i}^2, m_W^2, m_W^2)$;

$$\mathcal{F}_Z^{(7)} + \mathcal{F}_Z^{(8)} + \mathcal{F}_Z^{(9)} + \mathcal{F}_Z^{(10)} = \frac{1}{2}(1 - 2c_W^2)\, B_{\ell_k n_i} B_{\ell_m n_i}^* \left\{ (2 + x_i)B_1 + 1 \right\}, \qquad \text{(F.6)}$$

where $B_1 \equiv B_1(0, m_{n_i}^2, m_W^2)$.

In all these formulas, sum over neutrino indices, $i, j = 1, ..., 9$ has to be understood, $x_i \equiv m_{n_i}^2 / m_W^2$ and the charged lepton masses have been neglected.

Bibliography

[1] G. Aad *et al.* (ATLAS), Phys. Lett. **B716**, 1 (2012), arXiv:1207.7214 [hep-ex]

[2] S. Chatrchyan *et al.* (CMS), Phys. Lett. **B716**, 30 (2012), arXiv:1207.7235 [hep-ex]

[3] S. L. Glashow, Nucl. Phys. **22**, 579 (1961)

[4] M. Gell-Mann, Phys. Lett. **8**, 214 (1964)

[5] S. Weinberg, Phys. Rev. Lett. **19**, 1264 (1967)

[6] A. Salam, *8th Nobel Symposium Lerum, Sweden, May 19-25, 1968*, Conf. Proc. **C680519**, 367 (1968)

[7] P. W. Higgs, Phys. Lett. **12**, 132 (1964)

[8] F. Englert and R. Brout, Phys. Rev. Lett. **13**, 321 (1964)

[9] G. S. Guralnik, C. R. Hagen, and T. W. B. Kibble, Phys. Rev. Lett. **13**, 585 (1964)

[10] P. W. Higgs, Phys. Rev. **145**, 1156 (1966)

[11] S. L. Glashow, J. Iliopoulos, and L. Maiani, *Meeting of the Italian School of Physics and Weak Interactions Bologna, Italy, April 26-28, 1984*, Phys. Rev. **D2**, 1285 (1970)

[12] N. Cabibbo, *Meeting of the Italian School of Physics and Weak Interactions Bologna, Italy, April 26-28, 1984*, Phys. Rev. Lett. **10**, 531 (1963), [,648(1963)]

[13] M. Kobayashi and T. Maskawa, Prog. Theor. Phys. **49**, 652 (1973)

[14] Y. Fukuda *et al.* (Super-Kamiokande), Phys. Rev. Lett. **81**, 1562 (1998), arXiv:hep-ex/9807003 [hep-ex]

[15] Q. R. Ahmad *et al.* (SNO), Phys. Rev. Lett. **87**, 071301 (2001), arXiv:nucl-ex/0106015 [nucl-ex]

[16] Q. R. Ahmad *et al.* (SNO), Phys. Rev. Lett. **89**, 011301 (2002), arXiv:nucl-ex/0204008 [nucl-ex]

[17] P. Minkowski, Phys. Lett. **B67**, 421 (1977)

[18] M. Gell-Mann, P. Ramond, and R. Slansky, *Supergravity Workshop Stony Brook, New York, September 27-28, 1979*, Conf. Proc. **C790927**, 315 (1979), arXiv:1306.4669 [hep-th]

[19] T. Yanagida, *Proceedings: Workshop on the Unified Theories and the Baryon Number in the Universe: Tsukuba, Japan, February 13-14, 1979*, Conf. Proc. **C7902131**, 95 (1979)

[20] R. N. Mohapatra and G. Senjanovic, Phys. Rev. Lett. **44**, 912 (1980)

[21] J. Schechter and J. W. F. Valle, Phys. Rev. **D22**, 2227 (1980)

[22] R. N. Mohapatra, Phys. Rev. Lett. **56**, 561 (1986)

[23] R. N. Mohapatra and J. W. F. Valle, *Proceedings, 23RD International Conference on High Energy Physics, JULY 16-23, 1986, Berkeley, CA*, Phys. Rev. **D34**, 1642 (1986)

[24] J. Bernabeu, A. Santamaria, J. Vidal, A. Mendez, and J. W. F. Valle, Phys. Lett. **B187**, 303 (1987)

[25] G. 't Hooft, *Recent Developments in Gauge Theories. Proceedings, Nato Advanced Study Institute, Cargese, France, August 26 - September 8, 1979*, NATO Sci. Ser. B **59**, 135 (1980)

[26] A. Abada, D. Das, A. M. Teixeira, A. Vicente, and C. Weiland, JHEP **02**, 048 (2013), arXiv:1211.3052 [hep-ph]

[27] A. Abada, A. M. Teixeira, A. Vicente, and C. Weiland, JHEP **02**, 091 (2014), arXiv:1311.2830 [hep-ph]

[28] A. Abada and T. Toma, JHEP **02**, 174 (2016), arXiv:1511.03265 [hep-ph]

[29] A. Abada and T. Toma, JHEP **08**, 079 (2016), arXiv:1605.07643 [hep-ph]

[30] A. Abada, V. De Romeri, and A. M. Teixeira, JHEP **09**, 074 (2014), arXiv:1406.6978 [hep-ph]

[31] C.-Y. Chen and P. S. B. Dev, Phys. Rev. **D85**, 093018 (2012), arXiv:1112.6419 [hep-ph]

[32] P. S. Bhupal Dev, R. Franceschini, and R. N. Mohapatra, Phys. Rev. **D86**, 093010 (2012), arXiv:1207.2756 [hep-ph]

172

[33] A. Das and N. Okada, Phys. Rev. **D88**, 113001 (2013), arXiv:1207.3734 [hep-ph]

[34] A. Das, P. S. Bhupal Dev, and N. Okada, Phys. Lett. **B735**, 364 (2014), arXiv:1405.0177 [hep-ph]

[35] G. Bambhaniya, S. Goswami, S. Khan, P. Konar, and T. Mondal, Phys. Rev. **D91**, 075007 (2015), arXiv:1410.5687 [hep-ph]

[36] G. Bambhaniya, S. Khan, P. Konar, and T. Mondal, Phys. Rev. **D91**, 095007 (2015), arXiv:1411.6866 [hep-ph]

[37] A. Das and N. Okada, Phys. Rev. **D93**, 033003 (2016), arXiv:1510.04790 [hep-ph]

[38] A. Das, P. Konar, and S. Majhi, JHEP **06**, 019 (2016), arXiv:1604.00608 [hep-ph]

[39] A. Abada, G. Arcadi, and M. Lucente, JCAP **1410**, 001 (2014), arXiv:1406.6556 [hep-ph]

[40] J. Garayoa, M. C. Gonzalez-Garcia, and N. Rius, JHEP **02**, 021 (2007), arXiv:hep-ph/0611311 [hep-ph]

[41] A. Abada, G. Arcadi, V. Domcke, and M. Lucente, JCAP **1511**, 041 (2015), arXiv:1507.06215 [hep-ph]

[42] F. Deppisch and J. W. F. Valle, Phys. Rev. **D72**, 036001 (2005), arXiv:hep-ph/0406040 [hep-ph]

[43] F. Deppisch, T. S. Kosmas, and J. W. F. Valle, Nucl. Phys. **B752**, 80 (2006), arXiv:hep-ph/0512360 [hep-ph]

[44] P. S. B. Dev and R. N. Mohapatra, Phys. Rev. **D81**, 013001 (2010), arXiv:0910.3924 [hep-ph]

[45] M. Hirsch, T. Kernreiter, J. C. Romao, and A. Villanova del Moral, JHEP **01**, 103 (2010), arXiv:0910.2435 [hep-ph]

[46] A. Abada, D. Das, and C. Weiland, JHEP **03**, 100 (2012), arXiv:1111.5836 [hep-ph]

[47] A. Abada, D. Das, A. Vicente, and C. Weiland, JHEP **09**, 015 (2012), arXiv:1206.6497 [hep-ph]

[48] M. Hirsch, F. Staub, and A. Vicente, Phys. Rev. **D85**, 113013 (2012), [Erratum: Phys. Rev.D91,no.5,059902(2015)], arXiv:1202.1825 [hep-ph]

[49] A. Abada, V. De Romeri, S. Monteil, J. Orloff, and A. M. Teixeira, JHEP **04**, 051 (2015), arXiv:1412.6322 [hep-ph]

[50] A. Abada, M. E. Krauss, W. Porod, F. Staub, A. Vicente, and C. Weiland, JHEP **11**, 048 (2014), arXiv:1408.0138 [hep-ph]

[51] A. Abada, V. De Romeri, and A. M. Teixeira, JHEP **02**, 083 (2016), arXiv:1510.06657 [hep-ph]

[52] A. Abada, V. De Romeri, J. Orloff, and A. M. Teixeira, Eur. Phys. J. **C77**, 304 (2017), arXiv:1612.05548 [hep-ph]

[53] G. Aad *et al.* (ATLAS, CMS), *Proceedings, Meeting of the APS Division of Particles and Fields (DPF 2015): Ann Arbor, Michigan, USA, 4-8 Aug 2015*, Phys. Rev. Lett. **114**, 191803 (2015), arXiv:1503.07589 [hep-ex]

[54] Yu. A. Golfand and E. P. Likhtman, JETP Lett. **13**, 323 (1971), [Pisma Zh. Eksp. Teor. Fiz.13,452(1971)]

[55] D. V. Volkov and V. P. Akulov, Phys. Lett. **46B**, 109 (1973)

[56] J. Wess and B. Zumino, Nucl. Phys. **B70**, 39 (1974)

[57] H. E. Haber and G. L. Kane, Phys. Rept. **117**, 75 (1985)

[58] J. F. Gunion and H. E. Haber, Nucl. Phys. **B272**, 1 (1986), [Erratum: Nucl. Phys.B402,567(1993)]

[59] J. F. Gunion and H. E. Haber, *Proceedings, 23RD International Conference on High Energy Physics, JULY 16-23, 1986, Berkeley, CA*, Nucl. Phys. **B278**, 449 (1986), [Erratum: Nucl. Phys.B402,569(1993)]

[60] L. Girardello and M. T. Grisaru, Nucl. Phys. **B194**, 65 (1982)

[61] A. M. Baldini *et al.* (MEG), Eur. Phys. J. **C76**, 434 (2016), arXiv:1605.05081 [hep-ex]

[62] W. H. Bertl *et al.* (SINDRUM II), Eur. Phys. J. **C47**, 337 (2006)

[63] Y. Kuno (COMET), PTEP **2013**, 022C01 (2013)

[64] B. Aubert *et al.* (BaBar), Phys. Rev. Lett. **104**, 021802 (2010), arXiv:0908.2381 [hep-ex]

[65] T. Aushev *et al.*, (2010), arXiv:1002.5012 [hep-ex]

[66] V. Khachatryan *et al.* (CMS), Phys. Lett. **B763**, 472 (2016), arXiv:1607.03561 [hep-ex]

[67] CMS Collaboration, "Search for lepton flavour violating decays of the Higgs boson to $\mu\tau$ and eτ in proton-proton collisions at $\sqrt{s} = 13$ TeV," (2017), CMS-PAS-HIG-17-001

[68] G. Aad *et al.* (ATLAS), Eur. Phys. J. **C77**, 70 (2017), arXiv:1604.07730 [hep-ex]

[69] V. Khachatryan *et al.* (CMS), Phys. Lett. **B749**, 337 (2015), arXiv:1502.07400 [hep-ex]

[70] G. Aad *et al.* (ATLAS), Phys. Rev. **D90**, 072010 (2014), arXiv:1408.5774 [hep-ex]

[71] R. Akers *et al.* (OPAL), Z. Phys. **C67**, 555 (1995)

[72] P. Abreu *et al.* (DELPHI), Z. Phys. **C73**, 243 (1997)

[73] G. Wilson, "Neutrino oscillations: are lepton-flavor violating Z decays observable with the CDR detector?" (Nov 1998), dESY-ECFA LC Workshops held at Frascati

[74] G. Wilson, "Update on experimental aspects of lepton-flavour violation," (March 1999), dESY-ECFA LC Workshops held at Oxford

[75] A. Blondel, E. Graverini, N. Serra, and M. Shaposhnikov (FCC-ee study Team), in *Proceedings, 37th International Conference on High Energy Physics (ICHEP 2014): Valencia, Spain, July 2-9, 2014*, Vol. 273-275 (2016) pp. 1883–1890, arXiv:1411.5230 [hep-ex]

[76] A. Pilaftsis, Phys. Lett. **B285**, 68 (1992)

[77] J. G. Korner, A. Pilaftsis, and K. Schilcher, Phys. Rev. **D47**, 1080 (1993), arXiv:hep-ph/9301289 [hep-ph]

[78] J. G. Korner, A. Pilaftsis, and K. Schilcher, Phys. Lett. **B300**, 381 (1993), arXiv:hep-ph/9301290 [hep-ph]

[79] A. Ilakovac, Phys. Rev. **D62**, 036010 (2000), arXiv:hep-ph/9910213 [hep-ph]

[80] J. I. Illana, M. Jack, and T. Riemann, in *5th Workshop of the 2nd ECFA - DESY Study on Physics and Detectors for a Linear Electron - Positron Collider Obernai, France, October 16-19, 1999* (1999) pp. 490–524, [,490(1999)], arXiv:hep-ph/0001273 [hep-ph]

[81] J. I. Illana and T. Riemann, Phys. Rev. **D63**, 053004 (2001), arXiv:hep-ph/0010193 [hep-ph]

[82] E. Arganda, A. M. Curiel, M. J. Herrero, and D. Temes, Phys. Rev. **D71**, 035011 (2005), arXiv:hep-ph/0407302 [hep-ph]

[83] E. Arganda and M. J. Herrero, Phys. Rev. **D73**, 055003 (2006), arXiv:hep-ph/0510405 [hep-ph]

[84] S. Antusch, E. Arganda, M. J. Herrero, and A. M. Teixeira, JHEP **11**, 090 (2006), arXiv:hep-ph/0607263 [hep-ph]

[85] E. Arganda, M. J. Herrero, and A. M. Teixeira, JHEP **10**, 104 (2007), arXiv:0707.2955 [hep-ph]

[86] E. Arganda, M. J. Herrero, and J. Portoles, JHEP **06**, 079 (2008), arXiv:0803.2039 [hep-ph]

[87] A. Ilakovac and A. Pilaftsis, Phys. Rev. **D80**, 091902 (2009), arXiv:0904.2381 [hep-ph]

[88] M. J. Herrero, J. Portoles, and A. M. Rodriguez-Sanchez, Phys. Rev. **D80**, 015023 (2009), arXiv:0903.5151 [hep-ph]

[89] D. N. Dinh, A. Ibarra, E. Molinaro, and S. T. Petcov, JHEP **08**, 125 (2012), [Erratum: JHEP09,023(2013)], arXiv:1205.4671 [hep-ph]

[90] R. Alonso, M. Dhen, M. B. Gavela, and T. Hambye, JHEP **01**, 118 (2013), arXiv:1209.2679 [hep-ph]

[91] A. Ilakovac, A. Pilaftsis, and L. Popov, Phys. Rev. **D87**, 053014 (2013), arXiv:1212.5939 [hep-ph]

[92] J. Herrero-Garcia, N. Rius, and A. Santamaria, JHEP **11**, 084 (2016), arXiv:1605.06091 [hep-ph]

[93] A. Pilaftsis, Z. Phys. **C55**, 275 (1992), arXiv:hep-ph/9901206 [hep-ph]

[94] A. Datta, M. Guchait, and A. Pilaftsis, Phys. Rev. **D50**, 3195 (1994), arXiv:hep-ph/9311257 [hep-ph]

[95] F. del Aguila, J. A. Aguilar-Saavedra, and R. Pittau, JHEP **10**, 047 (2007), arXiv:hep-ph/0703261 [hep-ph]

[96] A. Atre, T. Han, S. Pascoli, and B. Zhang, JHEP **05**, 030 (2009), arXiv:0901.3589 [hep-ph]

[97] E. Arganda, M. J. Herrero, X. Marcano, and C. Weiland, Phys. Rev. **D91**, 015001 (2015), arXiv:1405.4300 [hep-ph]

[98] E. Arganda, M. J. Herrero, X. Marcano, and C. Weiland, Phys. Rev. **D93**, 055010 (2016), arXiv:1508.04623 [hep-ph]

[99] E. Arganda, M. J. Herrero, X. Marcano, and C. Weiland, Phys. Lett. **B752**, 46 (2016), arXiv:1508.05074 [hep-ph]

[100] V. De Romeri, M. J. Herrero, X. Marcano, and F. Scarcella, Phys. Rev. **D95**, 075028 (2017), arXiv:1607.05257 [hep-ph]

[101] E. Arganda, M. Herrero, X. Marcano, R. Morales, and A. Szynkman, Phys. Rev. **D95**, 095029 (2017), arXiv:1612.09290 [hep-ph]

[102] E. Arganda, M. J. Herrero, X. Marcano, and C. Weiland, in *Proceedings, 49th Rencontres de Moriond on Electroweak Interactions and Unified Theories: La Thuile, Italy, March 15-22, 2014* (2014) pp. 401–406, arXiv:1406.0384 [hep-ph]

[103] E. Arganda, M. J. Herrero, X. Marcano, and C. Weiland, *Proceedings, 37th International Conference on High Energy Physics (ICHEP 2014): Valencia, Spain, July 2-9, 2014*, Nucl. Part. Phys. Proc. **273-275**, 1685 (2016), arXiv:1410.5779 [hep-ph]

[104] E. Arganda, M. J. Herrero, X. Marcano, and C. Weiland, in *Neutrino Cross section Future* (2016) arXiv:1605.05660 [hep-ph]

[105] V. De Romeri, M. J. Herrero, X. Marcano, and F. Scarcella, in *16th Hellenic School and Workshops on Elementary Particle Physics and Gravity (CORFU2016) Corfu, Corfu Island, Greece, August 31-September 19, 2016* (2017) arXiv:1705.00485 [hep-ph]

[106] B. Pontecorvo, Sov. Phys. JETP **6**, 429 (1957), [Zh. Eksp. Teor. Fiz.33,549(1957)]

[107] Z. Maki, M. Nakagawa, and S. Sakata, Prog. Theor. Phys. **28**, 870 (1962)

[108] C. Giunti and W. C. Kim, *Fundamentals of Neutrino Physics and Astrophysics* (Oxford University Press, 2007)

[109] C. Patrignani *et al.* (Particle Data Group), Chin. Phys. **C40**, 100001 (2016)

[110] C. Kraus *et al.*, Eur. Phys. J. **C40**, 447 (2005), arXiv:hep-ex/0412056 [hep-ex]

[111] V. N. Aseev *et al.* (Troitsk), Phys. Rev. **D84**, 112003 (2011), arXiv:1108.5034 [hep-ex]

[112] P. A. R. Ade *et al.* (Planck), Astron. Astrophys. **571**, A16 (2014), arXiv:1303.5076 [astro-ph.CO]

[113] L. Wolfenstein, Phys. Rev. **D17**, 2369 (1978)

[114] L. Wolfenstein, Phys. Rev. **D20**, 2634 (1979)

[115] S. P. Mikheev and A. Yu. Smirnov, Sov. J. Nucl. Phys. **42**, 913 (1985), [Yad. Fiz.42,1441(1985)]

[116] S. P. Mikheev and A. Yu. Smirnov, Nuovo Cim. **C9**, 17 (1986)

177

[117] S. P. Mikheev and A. Yu. Smirnov, Sov. Phys. JETP **64**, 4 (1986), [Zh. Eksp. Teor. Fiz.91,7(1986)], arXiv:0706.0454 [hep-ph]

[118] J. D. Vergados, H. Ejiri, and F. Simkovic, Rept. Prog. Phys. **75**, 106301 (2012), arXiv:1205.0649 [hep-ph]

[119] S. Dell'Oro, S. Marcocci, M. Viel, and F. Vissani, Adv. High Energy Phys. **2016**, 2162659 (2016), arXiv:1601.07512 [hep-ph]

[120] C. Jarlskog, Z. Phys. **C29**, 491 (1985)

[121] S. Davidson, E. Nardi, and Y. Nir, Phys. Rept. **466**, 105 (2008), arXiv:0802.2962 [hep-ph]

[122] M. A. Acero, C. Giunti, and M. Laveder, Phys. Rev. **D78**, 073009 (2008), arXiv:0711.4222 [hep-ph]

[123] C. Giunti and M. Laveder, Phys. Rev. **C83**, 065504 (2011), arXiv:1006.3244 [hep-ph]

[124] T. A. Mueller *et al.*, Phys. Rev. **C83**, 054615 (2011), arXiv:1101.2663 [hep-ex]

[125] P. Huber, Phys. Rev. **C84**, 024617 (2011), [Erratum: Phys. Rev.C85,029901(2012)], arXiv:1106.0687 [hep-ph]

[126] G. Mention, M. Fechner, T. Lasserre, T. A. Mueller, D. Lhuillier, M. Cribier, and A. Letourneau, Phys. Rev. **D83**, 073006 (2011), arXiv:1101.2755 [hep-ex]

[127] A. Aguilar-Arevalo *et al.* (LSND), Phys. Rev. **D64**, 112007 (2001), arXiv:hep-ex/0104049 [hep-ex]

[128] A. A. Aguilar-Arevalo *et al.* (MiniBooNE), Phys. Rev. Lett. **98**, 231801 (2007), arXiv:0704.1500 [hep-ex]

[129] A. A. Aguilar-Arevalo *et al.* (MiniBooNE), Phys. Rev. Lett. **105**, 181801 (2010), arXiv:1007.1150 [hep-ex]

[130] A. A. Aguilar-Arevalo *et al.* (MiniBooNE), Phys. Rev. Lett. **110**, 161801 (2013), arXiv:1303.2588 [hep-ex]

[131] I. Esteban, M. C. Gonzalez-Garcia, M. Maltoni, I. Martinez-Soler, and T. Schwetz, JHEP **01**, 087 (2017), arXiv:1611.01514 [hep-ph]

[132] E. Akhmedov (2014) arXiv:1412.3320 [hep-ph]

[133] S. Weinberg, Phys. Rev. Lett. **43**, 1566 (1979)

[134] A. Abada, C. Biggio, F. Bonnet, M. B. Gavela, and T. Hambye, JHEP **12**, 061 (2007), arXiv:0707.4058 [hep-ph]

[135] J. A. Casas and A. Ibarra, Nucl. Phys. **B618**, 171 (2001), arXiv:hep-ph/0103065 [hep-ph]

[136] M. Magg and C. Wetterich, Phys. Lett. **B94**, 61 (1980)

[137] C. Wetterich, Nucl. Phys. **B187**, 343 (1981)

[138] G. Lazarides, Q. Shafi, and C. Wetterich, Nucl. Phys. **B181**, 287 (1981)

[139] R. N. Mohapatra and G. Senjanovic, Phys. Rev. **D23**, 165 (1981)

[140] A. Arhrib, R. Benbrik, M. Chabab, G. Moultaka, M. C. Peyranere, L. Rahili, and J. Ramadan, Phys. Rev. **D84**, 095005 (2011), arXiv:1105.1925 [hep-ph]

[141] R. Foot, H. Lew, X. G. He, and G. C. Joshi, Z. Phys. **C44**, 441 (1989)

[142] A. Zee, Nucl. Phys. **B264**, 99 (1986)

[143] K. S. Babu, Phys. Lett. **B203**, 132 (1988)

[144] C. S. Aulakh and R. N. Mohapatra, Phys. Lett. **B119**, 136 (1982)

[145] L. J. Hall and M. Suzuki, Nucl. Phys. **B231**, 419 (1984)

[146] R. Barbier *et al.*, Phys. Rept. **420**, 1 (2005), arXiv:hep-ph/0406039 [hep-ph]

[147] R. N. Mohapatra *et al.*, Rept. Prog. Phys. **70**, 1757 (2007), arXiv:hep-ph/0510213 [hep-ph]

[148] E. Ma, *Proceedings, 15th Hellenic School and Workshops on Elementary Particle Physics and Gravity (CORFU2015): Corfu, Greece, September 1-25, 2015*, PoS **CORFU2015**, 009 (2016)

[149] E. K. Akhmedov, M. Lindner, E. Schnapka, and J. W. F. Valle, Phys. Lett. **B368**, 270 (1996), arXiv:hep-ph/9507275 [hep-ph]

[150] E. K. Akhmedov, M. Lindner, E. Schnapka, and J. W. F. Valle, Phys. Rev. **D53**, 2752 (1996), arXiv:hep-ph/9509255 [hep-ph]

[151] A. Abada and M. Lucente, Nucl. Phys. **B885**, 651 (2014), arXiv:1401.1507 [hep-ph]

[152] M. C. Gonzalez-Garcia and J. W. F. Valle, Phys. Lett. **B216**, 360 (1989)

179

[153] E. Ma, Mod. Phys. Lett. **A24**, 2161 (2009), arXiv:0904.1580 [hep-ph]

[154] H. E. Haber, in *Theoretical Advanced Study Institute (TASI 92): From Black Holes and Strings to Particles Boulder, Colorado, June 3-28, 1992* (1993) pp. 0589–688, arXiv:hep-ph/9306207 [hep-ph]

[155] S. P. Martin, Adv. Ser. Direct. High Energy Phys **21**, 1 (2010), [Adv. Ser. Direct. High Energy Phys.18,1(1998)], arXiv:hep-ph/9709356 [hep-ph]

[156] J. Hisano, T. Moroi, K. Tobe, and M. Yamaguchi, Phys. Rev. **D53**, 2442 (1996), arXiv:hep-ph/9510309 [hep-ph]

[157] S. Bravar and O. B. O. T. T. M. Collaboration, *Proceedings, 38th International Conference on High Energy Physics (ICHEP 2016): Chicago, IL, USA, August 3-10, 2016*, PoS **ICHEP2016**, 552 (2016)

[158] E. P. Hincks and B. Pontecorvo, Phys. Rev. **73**, 257 (1948)

[159] Y. Kuno and Y. Okada, Rev. Mod. Phys. **73**, 151 (2001), arXiv:hep-ph/9909265 [hep-ph]

[160] R. H. Bernstein and P. S. Cooper, Phys. Rept. **532**, 27 (2013), arXiv:1307.5787 [hep-ex]

[161] A. M. Baldini *et al.*, (2013), arXiv:1301.7225 [physics.ins-det]

[162] U. Bellgardt *et al.* (SINDRUM), Nucl. Phys. **B299**, 1 (1988)

[163] A. Blondel *et al.*, (2013), arXiv:1301.6113 [physics.ins-det]

[164] K. Hayasaka *et al.*, Phys. Lett. **B687**, 139 (2010), arXiv:1001.3221 [hep-ex]

[165] K. Hayasaka, in *22nd Rencontres de Blois on Particle Physics and Cosmology Blois, Loire Valley, France, July 15-20, 2010* (2010) arXiv:1010.3746 [hep-ex]

[166] C. Dohmen *et al.* (SINDRUM II), Phys. Lett. **B317**, 631 (1993)

[167] A. Alekou *et al.*, in *Proceedings, 2013 Community Summer Study on the Future of U.S. Particle Physics: Snowmass on the Mississippi (CSS2013): Minneapolis, MN, USA, July 29-August 6, 2013* (2013) arXiv:1310.0804 [physics.acc-ph]

[168] R. M. Carey *et al.* (Mu2e), *Proposal to search for $\mu^- N \to e^- N$ with a single event sensitivity below* 10^{-16}, Tech. Rep. (2008)

[169] D. F. Measday, Phys. Rept. **354**, 243 (2001)

[170] Y. Amhis *et al.*, (2016), arXiv:1612.07233 [hep-ex]

180

[171] R. Aaij *et al.* (LHCb), JHEP **02**, 121 (2015), arXiv:1409.8548 [hep-ex]

[172] E. Abouzaid *et al.* (KTeV), Phys. Rev. Lett. **100**, 131803 (2008), arXiv:0711.3472 [hep-ex]

[173] D. Ambrose *et al.* (BNL), Phys. Rev. Lett. **81**, 5734 (1998), arXiv:hep-ex/9811038 [hep-ex]

[174] A. Sher *et al.*, Phys. Rev. **D72**, 012005 (2005), arXiv:hep-ex/0502020 [hep-ex]

[175] R. Appel *et al.*, Phys. Rev. Lett. **85**, 2877 (2000), arXiv:hep-ex/0006003 [hep-ex]

[176] J. R. Batley *et al.* (NA48/2), Phys. Lett. **B697**, 107 (2011), arXiv:1011.4817 [hep-ex]

[177] R. Aaij *et al.* (LHCb), Phys. Rev. Lett. **108**, 101601 (2012), arXiv:1110.0730 [hep-ex]

[178] R. Harnik, J. Kopp, and J. Zupan, JHEP **03**, 026 (2013), arXiv:1209.1397 [hep-ph]

[179] G. Blankenburg, J. Ellis, and G. Isidori, Phys. Lett. **B712**, 386 (2012), arXiv:1202.5704 [hep-ph]

[180] S. Davidson and P. Verdier, Phys. Rev. **D86**, 111701 (2012), arXiv:1211.1248 [hep-ph]

[181] S. Bressler, A. Dery, and A. Efrati, Phys. Rev. **D90**, 015025 (2014), arXiv:1405.4545 [hep-ph]

[182] The ATLAS collaboration, *Projections for measurements of Higgs boson cross sections, branching ratios and coupling parameters with the ATLAS detector at a HL-LHC*, Tech. Rep. ATL-PHYS-PUB-2013-014 (CERN, 2013)

[183] The CMS Collaboration (CMS), Proceedings, Community Summer Study 2013: Snowmass on the Mississippi (CSS2013) (2013), arXiv:1307.7135 [hep-ex]

[184] A. De Roeck, "Higgs Physics at the LHC, experimental review," (2014), talk at Physics Challenges in the face of LHC-14, IFT, Madrid

[185] H. Baer, T. Barklow, K. Fujii, Y. Gao, A. Hoang, S. Kanemura, J. List, H. E. Logan, A. Nomerotski, M. Perelstein, *et al.*, (2013), arXiv:1306.6352 [hep-ph]

[186] M. Bicer *et al.* (TLEP Design Study Working Group), *Proceedings, 2013 Community Summer Study on the Future of U.S. Particle Physics: Snowmass on the Mississippi (CSS2013): Minneapolis, MN, USA, July 29-August 6, 2013*, JHEP **01**, 164 (2014), arXiv:1308.6176 [hep-ex]

[187] A. Ilakovac and A. Pilaftsis, Nucl. Phys. **B437**, 491 (1995), arXiv:hep-ph/9403398 [hep-ph]

[188] T. Appelquist and J. Carazzone, Phys. Rev. **D11**, 2856 (1975)

[189] V. Cirigliano and I. Rosell, Phys. Rev. Lett. **99**, 231801 (2007), arXiv:0707.3439 [hep-ph]

[190] M. Finkemeier, *2nd Workshop on Physics and Detectors for DAPHNE (DAPHNE 95) Frascati, Italy, April 4-7, 1995*, Phys. Lett. **B387**, 391 (1996), arXiv:hep-ph/9505434 [hep-ph]

[191] E. Goudzovski (NA48/2, NA62), *Proceedings, 21st International Europhysics Conference on High energy physics (EPS-HEP 2011): Grenoble, France, July 21-27, 2011*, PoS **EPS-HEP2011**, 181 (2011), arXiv:1111.2818 [hep-ex]

[192] C. Lazzeroni *et al.* (NA62), Phys. Lett. **B719**, 326 (2013), arXiv:1212.4012 [hep-ex]

[193] K. A. Olive *et al.* (Particle Data Group), Chin. Phys. **C38**, 090001 (2014)

[194] E. Fernandez-Martinez, J. Hernandez-Garcia, J. Lopez-Pavon, and M. Lucente, JHEP **10**, 130 (2015), arXiv:1508.03051 [hep-ph]

[195] P. Benes, A. Faessler, F. Simkovic, and S. Kovalenko, Phys. Rev. **D71**, 077901 (2005), arXiv:hep-ph/0501295 [hep-ph]

[196] M. Blennow, E. Fernandez-Martinez, J. Lopez-Pavon, and J. Menendez, JHEP **07**, 096 (2010), arXiv:1005.3240 [hep-ph]

[197] M. Agostini *et al.* (GERDA), Phys. Rev. Lett. **111**, 122503 (2013), arXiv:1307.4720 [nucl-ex]

[198] M. Auger *et al.* (EXO-200), Phys. Rev. Lett. **109**, 032505 (2012), arXiv:1205.5608 [hep-ex]

[199] J. B. Albert *et al.* (EXO-200), Nature **510**, 229 (2014), arXiv:1402.6956 [nucl-ex]

[200] A. Gando *et al.* (KamLAND-Zen), Phys. Rev. Lett. **110**, 062502 (2013), arXiv:1211.3863 [hep-ex]

[201] M. E. Peskin and T. Takeuchi, Phys. Rev. **D46**, 381 (1992)

[202] E. Akhmedov, A. Kartavtsev, M. Lindner, L. Michaels, and J. Smirnov, JHEP **05**, 081 (2013), arXiv:1302.1872 [hep-ph]

[203] D. V. Forero, M. Tortola, and J. W. F. Valle, Phys. Rev. **D86**, 073012 (2012), arXiv:1205.4018 [hep-ph]

[204] G. L. Fogli, E. Lisi, A. Marrone, D. Montanino, A. Palazzo, and A. M. Rotunno, Phys. Rev. **D86**, 013012 (2012), arXiv:1205.5254 [hep-ph]

[205] D. V. Forero, M. Tortola, and J. W. F. Valle, Phys. Rev. **D90**, 093006 (2014), arXiv:1405.7540 [hep-ph]

[206] M. Drewes *et al.*, JCAP **1701**, 025 (2017), arXiv:1602.04816 [hep-ph]

[207] J. Baglio and C. Weiland, JHEP **04**, 038 (2017), arXiv:1612.06403 [hep-ph]

[208] T. Han and D. Marfatia, Phys. Rev. Lett. **86**, 1442 (2001), arXiv:hep-ph/0008141 [hep-ph]

[209] A. M. Curiel, M. J. Herrero, and D. Temes, Phys. Rev. **D67**, 075008 (2003), arXiv:hep-ph/0210335 [hep-ph]

[210] J. L. Diaz-Cruz, JHEP **05**, 036 (2003), arXiv:hep-ph/0207030 [hep-ph]

[211] A. M. Curiel, M. J. Herrero, W. Hollik, F. Merz, and S. Penaranda, Phys. Rev. **D69**, 075009 (2004), arXiv:hep-ph/0312135 [hep-ph]

[212] A. Brignole and A. Rossi, Phys. Lett. **B566**, 217 (2003), arXiv:hep-ph/0304081 [hep-ph]

[213] A. Brignole and A. Rossi, Nucl. Phys. **B701**, 3 (2004), arXiv:hep-ph/0404211 [hep-ph]

[214] J. K. Parry, Nucl. Phys. **B760**, 38 (2007), arXiv:hep-ph/0510305 [hep-ph]

[215] J. L. Diaz-Cruz, D. K. Ghosh, and S. Moretti, Phys. Lett. **B679**, 376 (2009), arXiv:0809.5158 [hep-ph]

[216] A. Crivellin, Phys. Rev. **D83**, 056001 (2011), arXiv:1012.4840 [hep-ph]

[217] P. T. Giang, L. T. Hue, D. T. Huong, and H. N. Long, Nucl. Phys. **B864**, 85 (2012), arXiv:1204.2902 [hep-ph]

[218] A. Arhrib, Y. Cheng, and O. C. W. Kong, Europhys. Lett. **101**, 31003 (2013), arXiv:1208.4669 [hep-ph]

[219] A. Arhrib, Y. Cheng, and O. C. W. Kong, Phys. Rev. **D87**, 015025 (2013), arXiv:1210.8241 [hep-ph]

[220] M. Arana-Catania, E. Arganda, and M. J. Herrero, JHEP **09**, 160 (2013), [Erratum: JHEP10,192(2015)], arXiv:1304.3371 [hep-ph]

[221] E. Arganda, M. J. Herrero, R. Morales, and A. Szynkman, JHEP **03**, 055 (2016), arXiv:1510.04685 [hep-ph]

[222] D. Aloni, Y. Nir, and E. Stamou, JHEP **04**, 162 (2016), arXiv:1511.00979 [hep-ph]

[223] A. Vicente, Adv. High Energy Phys. **2015**, 686572 (2015), arXiv:1503.08622 [hep-ph]

[224] C. Alvarado, R. M. Capdevilla, A. Delgado, and A. Martin, Phys. Rev. **D94**, 075010 (2016), arXiv:1602.08506 [hep-ph]

[225] A. Hammad, S. Khalil, and C. S. Un, Phys. Rev. **D95**, 055028 (2017), arXiv:1605.07567 [hep-ph]

[226] K. Agashe and R. Contino, Phys. Rev. **D80**, 075016 (2009), arXiv:0906.1542 [hep-ph]

[227] S. Davidson and G. J. Grenier, Phys. Rev. **D81**, 095016 (2010), arXiv:1001.0434 [hep-ph]

[228] D. Aristizabal Sierra and A. Vicente, Phys. Rev. **D90**, 115004 (2014), arXiv:1409.7690 [hep-ph]

[229] Y. Omura, E. Senaha, and K. Tobe, JHEP **05**, 028 (2015), arXiv:1502.07824 [hep-ph]

[230] N. Bizot, S. Davidson, M. Frigerio, and J. L. Kneur, JHEP **03**, 073 (2016), arXiv:1512.08508 [hep-ph]

[231] F. J. Botella, G. C. Branco, M. Nebot, and M. N. Rebelo, Eur. Phys. J. **C76**, 161 (2016), arXiv:1508.05101 [hep-ph]

[232] J. Herrero-García, T. Ohlsson, S. Riad, and J. Wirén, JHEP **04**, 130 (2017), arXiv:1701.05345 [hep-ph]

[233] A. Dery, A. Efrati, G. Hiller, Y. Hochberg, and Y. Nir, JHEP **08**, 006 (2013), arXiv:1304.6727 [hep-ph]

[234] A. Dery, A. Efrati, Y. Nir, Y. Soreq, and V. Susič, Phys. Rev. **D90**, 115022 (2014), arXiv:1408.1371 [hep-ph]

[235] X.-G. He, J. Tandean, and Y.-J. Zheng, JHEP **09**, 093 (2015), arXiv:1507.02673 [hep-ph]

[236] S. Baek and J. Tandean, Eur. Phys. J. **C76**, 673 (2016), arXiv:1604.08935 [hep-ph]

[237] G. Perez and L. Randall, JHEP **01**, 077 (2009), arXiv:0805.4652 [hep-ph]

184

[238] A. Azatov, M. Toharia, and L. Zhu, Phys. Rev. **D80**, 035016 (2009), arXiv:0906.1990 [hep-ph]

[239] J. L. Diaz-Cruz and J. J. Toscano, Phys. Rev. **D62**, 116005 (2000), arXiv:hep-ph/9910233 [hep-ph]

[240] L. de Lima, C. S. Machado, R. D. Matheus, and L. A. F. do Prado, JHEP **11**, 074 (2015), arXiv:1501.06923 [hep-ph]

[241] M. Buschmann, J. Kopp, J. Liu, and X.-P. Wang, JHEP **06**, 149 (2016), arXiv:1601.02616 [hep-ph]

[242] A. Falkowski, D. M. Straub, and A. Vicente, JHEP **05**, 092 (2014), arXiv:1312.5329 [hep-ph]

[243] A. Dery, A. Efrati, Y. Hochberg, and Y. Nir, JHEP **05**, 039 (2013), arXiv:1302.3229 [hep-ph]

[244] J. Heeck, M. Holthausen, W. Rodejohann, and Y. Shimizu, Nucl. Phys. **B896**, 281 (2015), arXiv:1412.3671 [hep-ph]

[245] M. D. Campos, A. E. Cárcamo Hernández, H. Päs, and E. Schumacher, Phys. Rev. **D91**, 116011 (2015), arXiv:1408.1652 [hep-ph]

[246] I. Doršner, S. Fajfer, A. Greljo, J. F. Kamenik, N. Košnik, and I. Nišandžic, JHEP **06**, 108 (2015), arXiv:1502.07784 [hep-ph]

[247] A. Crivellin, G. D'Ambrosio, and J. Heeck, Phys. Rev. Lett. **114**, 151801 (2015), arXiv:1501.00993 [hep-ph]

[248] A. E. Cárcamo Hernández, I. de Medeiros Varzielas, and E. Schumacher, Phys. Rev. **D93**, 016003 (2016), arXiv:1509.02083 [hep-ph]

[249] W. Altmannshofer, M. Carena, and A. Crivellin, Phys. Rev. **D94**, 095026 (2016), arXiv:1604.08221 [hep-ph]

[250] K. Huitu, V. Keus, N. Koivunen, and O. Lebedev, JHEP **05**, 026 (2016), arXiv:1603.06614 [hep-ph]

[251] S. Baek, T. Nomura, and H. Okada, Phys. Lett. **B759**, 91 (2016), arXiv:1604.03738 [hep-ph]

[252] A. Di Iura, J. Herrero-Garcia, and D. Meloni, Nucl. Phys. **B911**, 388 (2016), arXiv:1606.08785 [hep-ph]

185

[253] S. Heinemeyer, W. Hollik, and G. Weiglein, Comput. Phys. Commun. **124**, 76 (2000), arXiv:hep-ph/9812320 [hep-ph]

[254] S. Heinemeyer, W. Hollik, and G. Weiglein, Eur. Phys. J. **C9**, 343 (1999), arXiv:hep-ph/9812472 [hep-ph]

[255] G. Degrassi, S. Heinemeyer, W. Hollik, P. Slavich, and G. Weiglein, Eur. Phys. J. **C28**, 133 (2003), arXiv:hep-ph/0212020 [hep-ph]

[256] A. Dedes, M. Paraskevas, J. Rosiek, K. Suxho, and K. Tamvakis, JHEP **06**, 151 (2015), arXiv:1504.00960 [hep-ph]

[257] J. Rosiek, Comput. Phys. Commun. **201**, 144 (2016), arXiv:1509.05030 [hep-ph]

[258] E. Fernandez-Martinez, J. Hernandez-Garcia, and J. Lopez-Pavon, JHEP **08**, 033 (2016), arXiv:1605.08774 [hep-ph]

[259] G. Mann and T. Riemann, Annalen Phys. **40**, 334 (1984)

[260] M. Dittmar, A. Santamaria, M. C. Gonzalez-Garcia, and J. W. F. Valle, Nucl. Phys. **B332**, 1 (1990)

[261] M. A. Perez, G. Tavares-Velasco, and J. J. Toscano, Int. J. Mod. Phys. **A19**, 159 (2004), arXiv:hep-ph/0305227 [hep-ph]

[262] A. Flores-Tlalpa, J. M. Hernandez, G. Tavares-Velasco, and J. J. Toscano, Phys. Rev. **D65**, 073010 (2002), arXiv:hep-ph/0112065 [hep-ph]

[263] D. Delepine and F. Vissani, Phys. Lett. **B522**, 95 (2001), arXiv:hep-ph/0106287 [hep-ph]

[264] S. Davidson, S. Lacroix, and P. Verdier, JHEP **09**, 092 (2012), arXiv:1207.4894 [hep-ph]

[265] A. Abada, D. Bečirević, M. Lucente, and O. Sumensari, Phys. Rev. **D91**, 113013 (2015), arXiv:1503.04159 [hep-ph]

[266] T. Hahn and M. Perez-Victoria, Comput. Phys. Commun. **118**, 153 (1999), arXiv:hep-ph/9807565 [hep-ph]

[267] S. Antusch, C. Biggio, E. Fernandez-Martinez, M. B. Gavela, and J. Lopez-Pavon, JHEP **10**, 084 (2006), arXiv:hep-ph/0607020 [hep-ph]

[268] E. Fernandez-Martinez, M. B. Gavela, J. Lopez-Pavon, and O. Yasuda, Phys. Lett. **B649**, 427 (2007), arXiv:hep-ph/0703098 [hep-ph]

186

[269] F. del Aguila, J. de Blas, and M. Perez-Victoria, Phys. Rev. **D78**, 013010 (2008), arXiv:0803.4008 [hep-ph]

[270] S. Antusch, J. P. Baumann, and E. Fernandez-Martinez, Nucl. Phys. **B810**, 369 (2009), arXiv:0807.1003 [hep-ph]

[271] S. Antusch and O. Fischer, JHEP **10**, 094 (2014), arXiv:1407.6607 [hep-ph]

[272] F. del Aguila and J. A. Aguilar-Saavedra, Nucl. Phys. **B813**, 22 (2009), arXiv:0808.2468 [hep-ph]

[273] D. Alva, T. Han, and R. Ruiz, JHEP **02**, 072 (2015), arXiv:1411.7305 [hep-ph]

[274] P. S. B. Dev, A. Pilaftsis, and U.-k. Yang, Phys. Rev. Lett. **112**, 081801 (2014), arXiv:1308.2209 [hep-ph]

[275] A. Alloul, N. D. Christensen, C. Degrande, C. Duhr, and B. Fuks, Comput. Phys. Commun. **185**, 2250 (2014), arXiv:1310.1921 [hep-ph]

[276] J. Alwall, R. Frederix, S. Frixione, V. Hirschi, F. Maltoni, O. Mattelaer, H. S. Shao, T. Stelzer, P. Torrielli, and M. Zaro, JHEP **07**, 079 (2014), arXiv:1405.0301 [hep-ph]

[277] G. Aad *et al.* (ATLAS), Phys. Rev. Lett. **115**, 031801 (2015), arXiv:1503.04430 [hep-ex]

[278] S. Bray, J. S. Lee, and A. Pilaftsis, Nucl. Phys. **B786**, 95 (2007), arXiv:hep-ph/0702294 [HEP-PH]

[279] T. Golling *et al.*, Submitted to: Phys. Rept. (2016), arXiv:1606.00947 [hep-ph]

[280] G. Passarino and M. J. G. Veltman, Nucl. Phys. **B160**, 151 (1979)